Ultra-cold atom interferometer for a space test of the weak equivalence principle

Célia Pelluet

THÈSE PRÉSENTÉE

POUR OBTENIR LE GRADE DE

DOCTEUR
DE L'UNIVERSITÉ DE BORDEAUX

Ecole Doctorale des Sciences Physiques et de l'Ingénieur

Spécialité Lasers, Matière et Nanosciences

par

Célia PELLUET

Ultra-cold atom interferometer for a space test of the weak equivalence principle

---

Interféromètre atomique à sources ultra-froides pour le test du principe d'équivalence faible depuis l'espace

Sous la direction de : **Baptiste BATTELIER**

Soutenue le 17 Novembre 2023
devant le jury composé de:

Franck Pereira Dos Santos	Directeur de recherche	LNE-SYRTE	Président du Jury
Pierre Lemonde	Directeur de recherche	Institut Néel	Rapporteur
Eric Charron	Professeur des Universités	Université Paris-Saclay	Rapporteur
Juliette Billy	Maîtresse de conférence	LCAR	Examinatrice
Wolf Von Klitzing	Chargé de recherche	IESL-FORTH	Examinateur
M. Baptiste Battelier	Ingénieur de Recherche	LP2N	Directeur de Thèse

Interféromètre atomique à sources ultra-froides pour le test du principe d'équivalence faible depuis l'espace

Résumé : Les révolutions quantiques du XXe siècle ont vu l'émergence de nouveaux capteurs de haute précision, appelés senseurs inertiels à onde de matière. L'utilisation de ces senseurs pour étudier le champ gravitationnel terrestre pourrait contribuer à résoudre l'un des grands mystères de la physique fondamentale : le principe d'équivalence faible, qui postule que la masse des corps n'affecte pas leur chute. Cependant, ce postulat fondamental de la relativité générale est remis en question par certaines théories cherchant à unifier la mécanique quantique et la gravité.

La réalisation d'un test expérimental pour examiner cette question est essentielle, mais elle nécessite un long temps de chute libre, qui n'est réalisable que depuis l'espace. La conception d'un démonstrateur spatial nécessite une avancée technologique significative. Cette thèse s'inscrit dans le cadre du projet ICE, qui consiste en un prototype de laboratoire pour de futures missions spatiales. Cette expérience est testée à bord de l'avion Zéro-G ainsi que sur un simulateur de microgravité au sein du laboratoire.

L'objectif principal est de mesurer l'accélération subie par deux espèces atomiques différentes, le rubidium 87 et le potassium 39, en utilisant une méthode interférométrique. Ces atomes sont utilisés comme masses d'épreuve. Pour réaliser la mesure avec une grande précision, il est nécessaire d'abaisser la température des nuages atomiques avec des techniques de refroidissement laser. Le présent manuscrit présente les premiers résultats obtenus concernant la production de nuages d'atomes ultra-froids à bord de l'avion Zéro-G, grâce à des techniques de refroidissement évaporatif tout-optique. De plus, notre simulateur de microgravité, doté d'un accès illimité et d'un taux de répétition élevé, nous a permis d'obtenir des résultats en interférométrie atomique avec de longs temps d'interrogation. Ces résultats ouvrent la voie à la réalisation d'un test de haute sensibilité du principe d'équivalence sur cette plateforme.
Mots-clés : Microgravité, Intreférométrie atomique, Atomes ultra-froids, Principe d'équivalence faible

---

Ultra-cold atom interferometer for a space test of the weak equivalence principle

Abstract: The quantum revolutions of the 20th century have given rise to new high-precision sensors known as matter-wave inertial sensors. Utilizing these sensors to study the Earth's gravitational field holds the potential to address one of the grand mysteries of fundamental physics: the weak equivalence principle (WEP), which postulates that the mass of an object does not affect its fall. However, this foundational postulate of general relativity is challenged by certain theories aiming to unify quantum mechanics and gravity.

Conducting an experimental test is paramount, yet it necessitates a prolonged period of free fall achievable only in space. The development of a space-based demonstrator requires significant technological advancement. This thesis is situated within the ICE (Interférométrie à source Cohérente pour l'Espace) project, which serves as a laboratory prototype for future space missions. This experiment is tested aboard the Zero-G aircraft as well as on a microgravity simulator within the laboratory.

The primary objective is to measure the acceleration experienced by two different atomic species, rubidium 87 and potassium 39, using an interferometric method. These atoms serve as test masses. Achieving precise measurements requires lowering the temperature of the atomic clouds through laser cooling techniques. This manuscript presents the initial results concerning the production of ultra-cold atomic clouds aboard the Zero-G aircraft, achieved through all-optical evaporative cooling techniques. Furthermore, our microgravity simulator, equipped with unlimited access and a high repetition rate, has enabled us to obtain atomic interferometry results with extended interrogation times. These outcomes pave the way for conducting a highly sensitive test of the equivalence principle using this platform.
Keywords: Atom Interferometry, Ultra-cold atoms, Microgravity, Weak Equivalence Principle

---

Laboratoire Photonique, Numérique et Nanosciences
UMR 5298, Université de Bordeaux, 33400 Talence, France.

Remerciements

Ce manuscrit retrace le travail effectué au Laboratoire Photonique, Numérique et Nanosciences (LP2N) entre octobre 2020 et septembre 2023. Il est le résultat d'un effort collectif sur le projet ICE, débuté bien avant mon arrivée au laboratoire, et qui ouvre la voie vers de belles expériences à venir. Entre ces lignes se cachent des heures de réparations d'une expérience complexe qui relèvent parfois du bricolage, du montage de racks (je considère d'ailleurs ajouter une ligne concernant le montage de meubles en kits à mon CV) ou encore de prises de données qui semblent infinies "pour les statistiques". Il m'a été notifié qu'à la description de ces travaux manquait la première personne du singulier : ce ne serait pas rendre justice à la réalité du laboratoire, qui est un partage constant. Je souhaite ici remercier les personnes qui m'ont permis de profiter de ce moment particulier de la thèse.

Mes premiers et plus sincères remerciements s'adresseront à mon directeur de thèse, Baptiste Battelier, qui supervise ICE depuis plusieurs années et a été un excellent encadrant pendant ces trois ans ainsi que mon stage de fin d'étude. J'ai rencontré Baptiste et ICE alors que je réalisais mon stage de césure de Supoptique au CNES, en 2018. J'ai immédiatement été fascinée par la passion de Baptiste pour cette expérience hors du commun, au croisement entre physique fondamentale, technologies spatiales, bricolage et sport extrême. C'est donc avec deux ans d'avance que j'ai postulé pour participer à cette belle aventure sans aucune hésitation. Pendant ma thèse, Baptiste a été très présent pour répondre à mes questionnements concernant les phénomènes physiques, les difficultés expérimentales, ou encore le monde de la recherche et les choix de carrière. Il est sur tous les fronts pour offrir à ses doctorantes la meilleure expérience de cet apprentissage par la recherche, et m'a enseigné la rigueur et l'honnêteté intellectuelle qui font la beauté des sciences. Alors pour tout cela, et tout ce que j'oublie probablement, merci infiniment !

À mon arrivée, j'ai été accueillie par Romain Arguel et Vincent Jarlaud, alors doctorant et post-doctorant sur l'expérience. Je mesure la chance que j'ai eue d'être formée au quotidien sur ce dispositif qui me semblait alors chaotique et incompréhensible. Tous deux m'ont initiée aux manipulations des atomes, aux phénomènes surprenants à observer et aux curiosités de Cicero qui décidément aura mérité son surnom (que je tairai ici par souci de décence, tout comme celui de la Ximea). À travers les montages de lasers et les campagnes de vols, ils ont su me faire prendre confiance en mes capacités malgré quelques déboires à mes débuts (et par la suite...). Je ne peux qu'être reconnaissante pour le travail minutieux de Romain quand il s'agit de documenter ses travaux, et de Vincent qui m'a inculqué une gestion rigoureuse du cahier de manip, au stylo plume noir avec les dates soulignées, s'il vous plaît. Je me souviendrai avec émotions des heures à relever des données, accompagnées des fidèles Sporcle et GeoGuesser pour occuper ces longues soirées. J'ai même eu la chance de croiser dans les couloirs du laboratoire certains anciens de ICE, Martin Rabault, Gabriel Condon et Vincent Ménoret, qui ont su me conseiller et me partager leurs anecdotes, créant ainsi un « folklore » de ICE qui, je l'espère, perdurera. Je fais confiance à mon successeur Clément Métayer pour reprendre les rênes du projet, ce qu'il fait déjà avec une main de maître depuis que je l'ai lâchement abandonné pour rédiger le présent manuscrit. Clément m'a impressionnée pour avoir, seulement quelques mois après son arrivée, été capable de piloter l'expérience en Zéro G, réalignement de faisceaux dipolaires inclus, mal-

gré la présence de Thomas Pesquet qui pilotait alors l'avion (personnellement, j'étais un peu déconcentrée). Puisse-tu prendre soin d'Alex(périence) et du simulateur (zé)Roger !

Le LP2N a été un cadre idéal, avec son groupe Atomes Froids sous la direction de Philippe Bouyer qui a été un soutien et un mentor inspirant. Je tiens également à remercier Laurent Cognet, qui a pris la suite de Philippe à la direction du laboratoire au cours de ma thèse. Les équipes administratives ont été indispensables et je tiens à remercier Stéphanie Schultze, Laurent Porcel, Fabien Lehoux et Elysabeth Hortolland. Un dispositif comme le nôtre ne pourrait exister sans le travail minutieux de Philippe Teulat à l'atelier mécanique, qui a su nous aider en des temps records quand nous préparions les campagnes de vols. Je remercie également Jordan, Jean-Hugues et Cyril pour leur support.

Merci à l'ESA et au CNES de soutenir ce travail de recherche et particulièrement à mes référents Eamonn Murphy et Thomas Lévêque. Thomas m'a permis pendant mon stage de césure de découvrir les enjeux passionnants des technologies quantiques pour l'espace, vers lesquels je pense aujourd'hui orienter ma carrière, en commençant par participer à l'ambitieux projet CARIOQA.

Merci à toute l'équipe de Novespace, Anne-Clothilde, Frédéric, Alexis. Si ces derniers ne manquent pas de me taquiner quand mon visage devient blême après 15 paraboles ou mes jambes tremblantes quand j'aperçois un astronaute, ils ont avant tout garanti la réussite des deux campagnes auxquelles j'ai eu l'immense chance de participer. Merci à Thomas Pesquet d'avoir non seulement piloté l'avion mais également de m'avoir inspiré mon sketch phare, et pour la discussion sur mon orientation professionnelle entre deux paraboles (tu as gagné Frédéric, j'ai signé pour le postdoc).

Merci à la gravité d'exister, car je sais désormais que sans elle je passerais mes journées à vomir.

Un mot également pour l'équipe de Symétrie qui a su pendant ma thèse relever le défi de réparer et remettre à niveau le simulateur. Leur disponibilité pour répondre à nos questions en temps records a été précieuse et nous a permis d'obtenir de beaux résultats.

Vielen Dank an das Primus-Team von Zarm für die Einladung, ihr Experimentiergerät und den beeindruckenden Freifallturm zu entdecken !

Merci à la fondation l'Oréal-Unesco pour les Femmes et la Science de m'avoir sélectionnée pour faire partie des lauréates du Prix Jeunes Talents 2023. Merci à Alain Aspect de m'avoir fait l'honneur de m'aider dans ma candidature grâce à une belle lettre de recommandation. C'était une grande fierté de se voir ainsi récompensée et de prendre confiance en ce début de carrière de chercheuse. Je sors changée de la semaine de remise des prix et de la formation For Women in Science. Elle m'a permis des rencontres incroyables avec l'équipe de la fondation et les 34 autres lauréates, toutes plus inspirantes les unes que les autres. Merci les filles pour la sororité, les moments de partage et la cure intense de motivation ! Dans le contexte de ce prix, merci à Elodie Chabrol et Lucie Clarysse d'avoir réalisé la superbe illustration qu'elles m'ont autorisé à présenter à la suite de ces remerciements.

La thèse présente ses hauts et ses bas, à l'image des paraboles de l'avion, et on peut se retrouver un peu secouée (voire nauséeuse...), mais j'ai bénéficié d'un soutien moral sans faille de la part de mes collègues et amis. Merci à toute l'équipe des doctorantes de « Cold Photonics » sans qui les pauses cafés ne seraient pas aussi chaleureuses. A special thanks to Dylan, who helped me several times and also managed to gather us around a good cup of coffee or a drink after work. I know he will be rolling his eyes while reading these lines, so I will deliberately be even more cheesy: we miss you a lot since you left to escape our noisy environment, and I hope I can

work with you again in the future. Merci à Luisa, grâce à qui je ne suis pas la seule à chanter à tue-tête en manipulant au laboratoire, et qui est sûrement une des plus belles rencontres de ces dernières années. Merci à mes amis en dehors du laboratoire, spécialement à Avotra qui m'a non seulement initiée à ma carrière parallèle de saltimbanque, mais m'a surtout aidé à prendre confiance en moi en général, supporté plusieurs heures de messages vocaux, toujours été là dans les moments importants et m'offre les plus grands fous-rires possibles. Merci à toutes celles et tous ceux qui ont été là pour moi pendant toutes ces années, notamment les ami • es incroyables que j'ai rencontré pendant mes années à Supoptique sur qui je sais pouvoir compter : Arnaud, Anouk, Perrine, Elodie, Ceryse, Magui, Mathal, Lucas, Solène, Coco, JB, Etienne, Paul... j'en oublie sûrement. Merci Lucas de supporter mon emploi du temps impossible - qu'il s'agisse de la rédaction éprouvante ou des Comedy Clubs et concerts qui s'enchaînent - tout en gardant une confiance en moi qui m'a fait tenir à travers les différentes épreuves. Et merci tout simplement d'être toi.

Ces remerciements se concluent sur celles et ceux qui ont cru en moi littéralement depuis les premiers instants : ma famille. Merci à mes grandes sœurs, Joanna et Angelina, mes meilleures amies, d'être dans ma vie. Merci à mes parents qui nous ont offert la possibilité et le luxe de rêver loin, de nous avoir éduqués avec exigence mais surtout avec amour et en musique.

L'UNIVERSALITÉ DE LA CHUTE LIBRE AFFIRME QUE LA CHUTE D'UN CORPS DANS LE VIDE EST INDÉPENDANTE DE SA MASSE ET DE SA COMPOSITION.

CE PRINCIPE EST FONDAMENTAL POUR L'ÉTUDE DE NOTRE UNIVERS ET DE SES ORIGINES.

DE NOUVELLES THÉORIES REMETTENT EN QUESTION CE PRINCIPE. IL FAUT DONC TESTER SUR DES TEMPS TRÈS LONGS DE CHUTE LIBRE… CE QUI NE PEUT ÊTRE RÉALISÉ QUE … DANS L'ESPACE !

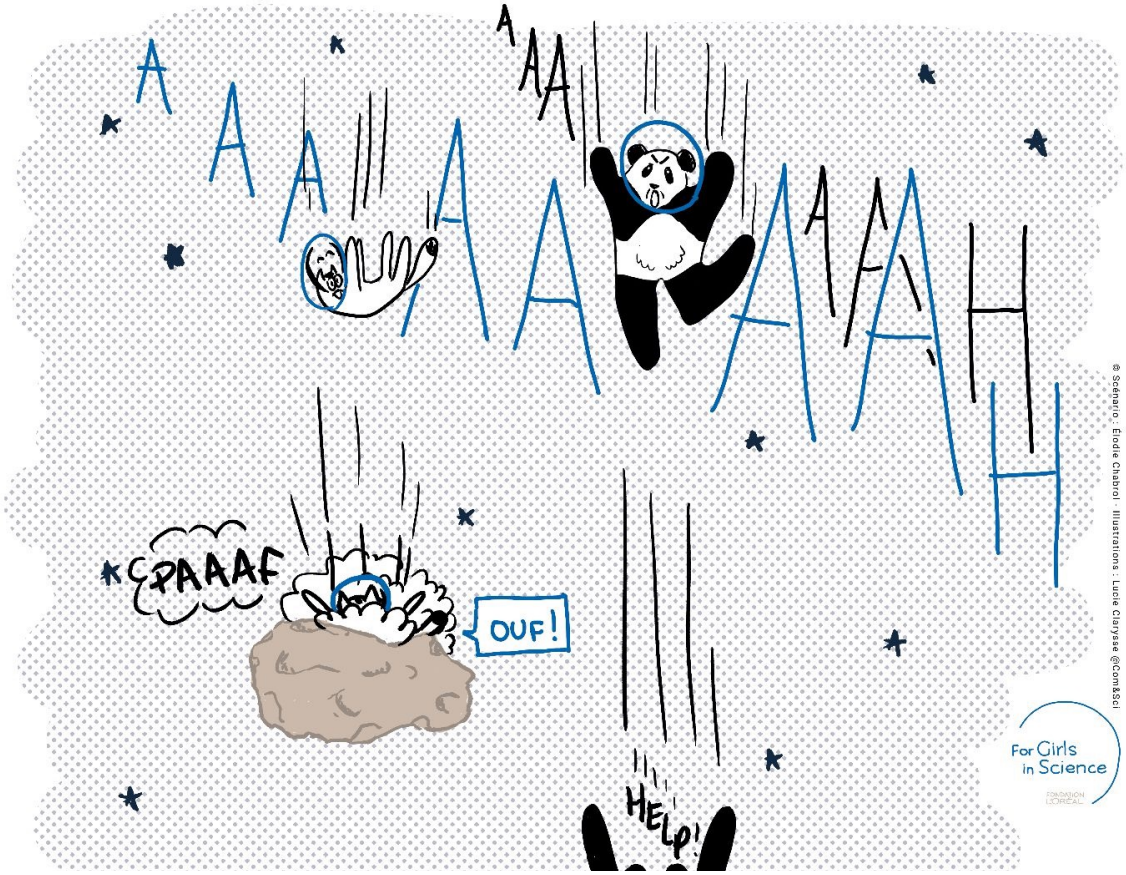

© Scénario : Élodie Chabrol - Illustrations : Lucie Clarysse @Com&Sci

Table of contents

Table of contents 9

List of Figures 13

List of Tables 17

Résumé de la thèse en français 18

Introduction 28
- 0.1 The Weak Equivalence Principle . . . 30
  - 0.1.1 The Universality of Free Fall . . . 30
  - 0.1.2 The Einstein equivalence principle . . . 31
  - 0.1.3 Why testing the WEP? . . . 32
  - 0.1.4 State of the art . . . 32
- 0.2 Cold Atoms inertial measurements . . . 33
  - 0.2.1 Wave-particle duality . . . 33
  - 0.2.2 Atom interferometer . . . 34
- 0.3 Towards space tests with cold atoms interferometry . . . 35
  - 0.3.1 Gravity gradient mapping space mission . . . 36
  - 0.3.2 WEP test space mission . . . 36
  - 0.3.3 Pathfinder mission CARIOQA . . . 36
- 0.4 Microgravity platforms . . . 37
  - 0.4.1 Overview of microgravity platforms for atom intreferometry . . . 38
  - 0.4.2 Einstein Elevator in Bordeaux . . . 39
  - 0.4.3 Zero G parabolic flights . . . 45

1 Experimental setup 49
- 1.1 Laser sources . . . 50
  - 1.1.1 Performances . . . 50
  - 1.1.2 Laser systems for rubidium . . . 51
  - 1.1.3 Laser systems for potassium . . . 56
  - 1.1.4 Dipole trap . . . 61
- 1.2 Sensor head . . . 62
  - 1.2.1 Ultra-high vacuum chamber . . . 63
  - 1.2.2 Collimators and optical systems . . . 64
  - 1.2.3 2D MOT chamber . . . 64
  - 1.2.4 Magnetic field control . . . 66
  - 1.2.5 Detection systems . . . 67
  - 1.2.6 Microwave antenna . . . 75
  - 1.2.7 Classical inertial sensors . . . 75
  - 1.2.8 Breadboard . . . 76
  - 1.2.9 Optical set-up for the dipole trap . . . 77

1.3 Radiofrequency and microwave sources . . . 80
1.3.1 RF chain for rubidium . . . 81
1.3.2 RF chain for potassium . . . 82
1.4 Control and acquisition system . . . 82
1.4.1 Hardware structure . . . 82
1.4.2 Software structure . . . 83
1.5 Constraints linked to microgravity operation . . . 83
1.5.1 Racks . . . 84
1.5.2 Safety requirements for the plane . . . 84

2 Atomic sources of rubidium and potassium 86
2.1 Measuring the temperature of the atomic samples . . . 88
2.1.1 Time of flight method . . . 88
2.1.2 Counter-propagating Raman spectrum method . . . 88
2.2 Laser cooling of rubidium and potassium . . . 91
2.2.1 Magneto-optical trap . . . 91
2.2.2 Red molasses . . . 93
2.3 Gray molasses of rubidium and potassium . . . 96
2.3.1 Theoretical study of gray molasses . . . 96
2.3.2 Gray molasses of ^{39}K . . . 99
2.3.3 Gray molasses of ^{87}Rb . . . 100
2.4 Dipole trap and ultra-cold atoms . . . 102
2.4.1 The dipole potential . . . 102
2.4.2 Evaporative cooling . . . 106
2.4.3 Bose-Einstein condensation . . . 110
2.5 Implementation of loading and evaporative cooling in standard gravity . . . 112
2.5.1 Lightshift due to the dipole trap . . . 112
2.5.2 Loading rubidium and potassium in the dipole trap . . . 114
2.5.3 Evaporation in standard gravity . . . 117
2.6 Ultra-cold atoms of ^{87}Rb in microgravity . . . 123
2.6.1 Condensation on the microgravity simulator . . . 123
2.6.2 Ultra-cold atoms in the Zero G plane . . . 126
2.7 State preparation . . . 130
2.7.1 Microwave state preparation for ^{87}Rb cold atoms . . . 130
2.7.2 State preparation for ^{39}K cold atoms . . . 132
2.7.3 Spin distillation technique for ultra-cold atoms . . . 133
2.8 Conclusion . . . 136

3 Atom interferometry in standard gravity 137
3.1 Principles of a light-pulse atom interferometer . . . 138
3.1.1 Raman transition . . . 138
3.1.2 Atomic beam-splitter and mirror . . . 141
3.1.3 Considering Atom Velocity in Raman Transitions . . . 142
3.1.4 Mach-Zehnder interferometer in the single-diffraction regime . . . 143
3.1.5 Sensitivity of the interferometer to accelerations . . . 144
3.2 Experimental results and characterization of the Atom Interferometer . . . 147
3.2.1 Raman spectroscopy and Rabi oscillations . . . 147
3.2.2 Scanning the phase of the atom interferometer . . . 148
3.2.3 Scanning the chirp of the atom interferometer . . . 150
3.2.4 Atomic accelerometer . . . 151

4 Atom interferometry in microgravity **156**
4.1 Theory of Atom Interferometry in microgravity . . . 157
4.1.1 Raman transition in the low velocity and acceleration regime . . . 157
4.1.2 Interferometry in the Double-single diffraction regime . . . 165
4.1.3 Interferometry in the Double Diffraction regime . . . 166
4.2 Experimental realization of atom interferometry in microgravity . . . 167
4.2.1 Raman spectroscopy in microgravity . . . 169
4.2.2 Ramsey fringes in microgravity . . . 170
4.2.3 Atom interferometry in Double Single Diffraction regime in the Einstein elevator . . . 172
4.3 Double Diffraction in microgravity . . . 178
4.3.1 Raman spectroscopy with ultra-cold atoms in microgravity . . . 178
4.3.2 Double diffraction interferometer in the horizontal configuration . . . 180
4.3.3 Interferometry on the simulator : latest results . . . 182

5 Testing the Weak Equivalence Principle with Atom Interferometry **185**
5.1 Dual-species atomic accelerometer . . . 187
5.1.1 Ellipse fitting method . . . 188
5.1.2 Generalized Bayesian Analysis . . . 189
5.1.3 Differential FRAC method . . . 191
5.2 Weak Equivalence Principle test on ICE . . . 192
5.2.1 WEP test onboard the Zero G aircraft . . . 192
5.2.2 WEP test in standard gravity and study of the systematic errors . . . 194
5.3 Strategy for a test on the simulator . . . 199
5.3.1 Case $\kappa = 1$ . . . 200
5.3.2 Case $\kappa = 1.018$ . . . 201
5.3.3 Convergence of the algorithm as a function of the common phase range . . . 203
5.3.4 Impact of the phase noise . . . 204
5.3.5 Importance of the knowledge of the phase scan . . . 204

Bibliography **209**

List of Figures

1 Plateformes d'accès à la microgravité : avion Zéro G et ascenceur d'Einstein au laboratoire . . . 19
2 Dispositif expérimental complet à bord de l'avion Zéro G . . . 20
3 Tête de senseur : Enceinte à vide et instruments pour le refroidissement, l'interférométrie et la détection des atomes. . . . 20
4 Principe du piégeage magnéto-optique et du refroidissement d'atomes . . . 21
5 Atomes ultra-froids obtenus à bord de l'avion Zéro G . . . 22
6 Schéma de l'interféromètre atomique en gravité standard . . . 23
7 Schéma de l'interféromètre atomique en double simple diffraction. . . . 24
8 Résultats obtenus avec l'interféromètre en double simple diffraction sur le simulateur de microgravité . . . 24
9 Schéma de l'interféromètre atomique en double diffraction . . . 25
10 Nuages atomiques après la première impulsion séparatrice pour différents temps de vol. . . . 25
11 Principe de l'interféromètre double-espèce . . . 26
12 Pictures taken during microgravity phase in the Zero G plane . . . 29
13 Principle of Galileo thought experiment . . . 30
14 Principle of the Einstein Elevator thought experiment . . . 31
15 Principle of an Atom Interferometer . . . 35
16 Space missions projects involving atom accelerometers . . . 35
17 CARIOQA pathfinder mission preparation program . . . 37
18 ZARM Drop Tower in Bremen . . . 39
19 Einstein elevator in Bordeaux . . . 40
20 Mobile part of the simulator . . . 41
21 Ballistic trajectory profile on the simulator . . . 43
22 The various trajectories on the simulator . . . 43
23 Vibrations on the simulator . . . 44
24 Residual rotations on the simulator . . . 45
25 Zero G plane during the entry phase . . . 46
26 Parabolic flight . . . 47
27 Vibrations and rotations on the Zero G plane . . . 48

1.1 Full experimental setup onboard the Zero G aircraft . . . 49
1.2 Internal structure of rubidium ^{87}Rb and potassium ^{39}K . . . 50
1.3 Functional diagram presenting the six laser sources used on the ICE experiment . 51
1.4 Architecture of the laser for the D_2 transition of rubidium . . . 52
1.5 PPLN housing and performance of the temperature regulation . . . 54
1.6 Micro-optical bench for combining and splitting . . . 55
1.7 Architecture of the laser for the D_2 transition of potassium . . . 57
1.8 Saturated absorption spectra of D_2 and D_1 transitions of K . . . 58
1.9 Architecture of the laser for the D_1 transition of potassium . . . 59
1.10 Architecture of the laser for the 2D MOT PotaMOT2D . . . 60

1.11 Solidworks model of the potassium 2D MOT laser at 767 nm laser 3U rack box . 61
1.12 Repartition of the optical power inside the Shäfter-Kirschoff dichroic 2×6 beam splitter . . . 61
1.13 Solidworks model of the science chamber . . . 62
1.14 Vacuum chamber . . . 64
1.15 Cross section of the ColdQuanta 2D MOT (Source : ColdQuanta PICAS Datasheet) 65
1.16 Picture of the installation of the 2D MOT . . . 66
1.17 Picture of the installation of the 2D MOT . . . 67
1.18 Schematic of the detectors on the science chamber . . . 68
1.19 Normalized detection signal as a function of the time of flight for two detectors in standard and micro-gravity . . . 69
1.20 Detection zone and temperature of the atoms . . . 70
1.21 Fluorescence detection sequence for estimating the population ratio between the ground state $|F = 1\rangle$ and the excited state $|F = 2\rangle$ . . . 71
1.22 Schematic of the absorption imaging setup . . . 72
1.23 Rear view of the vacuum chamber and the different detection systems . . . 74
1.24 Calibration of the imaging system . . . 76
1.25 Structure of the CFRP breadboard . . . 77
1.26 Spatial modulation of the dipole trap beam . . . 78
1.27 Top view of the dipole trap configuration . . . 79
1.28 Acceleration profile along the z direction during the parabola and absorption images of the trapped atoms taken at different moments of the parabola . . . 80
1.29 Functional diagram of Rubidium and Potassium radiofrequency chains . . . 81
1.30 Solidworks model of a rack . . . 84

2.1 Time of flight method for the estimation of the atomic cloud temperature . . . 89
2.2 Counter-propagating Raman spectrum for cold atoms and Gaussian fits for temperature estimation . . . 90
2.3 Atomic transitions and potential created by the lightshift leading to Sisyphus cooling . . . 93
2.4 Red molasses cooling sequence for ^{87}Rb . . . 95
2.5 Red molasses cooling sequence for ^{39}K . . . 96
2.6 Atomic transitions and potential created by the lightshift leading to gray Sisyphus cooling . . . 98
2.7 Gray molasses cooling sequence for ^{39}K . . . 99
2.8 Number of atoms in the potassium gray molasses as a function of the detuning Δ_{cool} of the D_1 laser . . . 100
2.9 Counter-propagating Raman spectra obtained with red and gray molasses on potassium . . . 101
2.10 Gray molasses cooling sequence for ^{87}Rb . . . 101
2.11 Simulated profile of a crossed beam dipole trap with an angle of 70° . . . 105
2.12 Simulations of the modulated intensity in 1D . . . 106
2.13 Principle of forced evaporative cooling . . . 107
2.14 Principle of Bose-Einstein Condensation . . . 111
2.15 Lightshift due to the FORT on the D_2 transition of Rb . . . 113
2.16 Lightshift due to the FORT on the D_1 transition of K . . . 113
2.17 Loading efficiency as a function of the detuning for ^{87}Rb . . . 114
2.18 ^{39}K compressed MOT . . . 115
2.19 Loading efficiency in the dipole trap as a function of the detuning for ^{39}K . . . 116
2.20 Absorption images of ^{87}Rb and ^{39}K in the dipole trap . . . 116
2.21 ^{87}Rb and ^{39}K loaded in the dipole trap as a function of the optical power . . . 117
2.22 Temporal evolutions during the process of forced evaporation . . . 119

2.23 Efficiency of evaporation in 1 g . . . 119
2.24 Absorption image of atoms for different stages of evaporation . . . 120
2.25 Parametric heating method for trap frequency measurement . . . 121
2.26 Trap frequencies . . . 121
2.27 BEC Lifetime . . . 122
2.28 Experimental sequence for ultra-cold atoms on the microgravity simulator . . . 124
2.29 Experimental sequence for ultra-cold atoms on the microgravity simulator during the pull-up phase . . . 125
2.30 Atom loss and misalignment of the dipole trap during the parabola on the Einstein Elevator . . . 126
2.31 Fluorescence images of the atoms on the simulator . . . 126
2.32 Temperature estimation on the simulator by time of flight method . . . 127
2.33 Acceleration profile along the z direction during the parabola and position of the dipole trap beams . . . 128
2.34 Fluorescence images of the ultra-cold atoms onboard the Zero-G plane . . . 129
2.35 Ultra-cold atoms of ^{87}Rb in the Zero-G plane . . . 129
2.36 Fluorescence image of the residual tweezer after 1 s time of flight on the Zero G plane . . . 130
2.37 State preparation sequence for thermal samples of ^{87}Rb . . . 131
2.38 Rabi Oscillation due to the microwave source between the hyperfine levels $|F = 1\rangle$, $|F = 2\rangle$ . . . 131
2.39 State preparation sequence for thermal samples of ^{39}K . . . 132
2.40 Principle of condensate state preparation . . . 134
2.41 State preparation efficiency for ultra-cold samples of ^{87}Rb . . . 135
2.42 Additional microwave state preparation for ultra-cold ^{87}Rb samples . . . 135

3.1 Energy-momentum diagram of a stimulated Raman transition . . . 138
3.2 Diagram of the retro-reflected laser configuration used to create Raman pulses . . . 139
3.3 Atom beam splitters and mirrors . . . 142
3.4 Mach-Zehnder interferometer in the single diffraction regime . . . 143
3.5 Response of an Atomic Mach-Zehnder Interferometer . . . 147
3.6 Counter-propagating Raman spectrum for Rb cold and ultra-cold atoms . . . 148
3.7 Counter-propagating Rabi oscillations for Rb cold and ultra-cold atoms . . . 149
3.8 Detection signal for cold and ultra-cold atoms . . . 149
3.9 Phase scan for cold and ultra-cold atoms and noise due to the detection system . . . 150
3.10 Atomic interferometer fringes obtained with phase scan in standard gravity with ^{87}Rb . . . 150
3.11 Atomic interferometer fringes obtained with chirp scan in standard gravity with ^{87}Rb . . . 151
3.12 Principle of the FRAC method . . . 152
3.13 Atomic interferometer fringes obtained with FRAC method with ^{87}Rb . . . 153
3.14 Principle of the BAT method . . . 154

4.1 Diagram of the retro-reflected configuration used without Doppler effect . . . 157
4.2 5-level system for a stimulated Raman transition in microgravity . . . 158
4.3 Numerical simulations of Rabi oscillations in the Double Diffraction regime . . . 160
4.4 Simulations of Raman spectra in the regime of low velocity and low acceleration 161
4.5 10-level system for a stimulated Raman transition in microgravity . . . 162
4.6 Simulations of Raman spectra in the regime of low velocity and low acceleration with co-propagating transitions . . . 165
4.7 Space-time diagram of an interferometer in the Double Single Diffraction regime 166
4.8 Space-time diagram of an interferometer in the Double Diffraction regime . . . 167

4.9 Simulated Rabi oscillation for a mirror pulse in double diffraction . . . 168
4.10 Simulated efficiency of atomic mirror and beam-splitter as a function of the temperature of the atoms . . . 168
4.11 Raman spectra obtained in microgravity with cold ^{87}Rb and simulated spectra . 169
4.12 Principle of Ramsey fringes . . . 170
4.13 Ramsey fringes obtained in microgravity . . . 171
4.14 Experimental sequence in the Double Single Diffraction regime on the Einstein Elevator . . . 172
4.15 Results of interferometry obtained in the regime of double-single diffraction in microgravity . . . 173
4.16 Sensitivity estimation using BAT method for two different datasets of interferometry in microgravity . . . 175
4.17 Contrast loss for the Ramsey fringes versus the interrogation time . . . 176
4.18 Estimation of the contrast loss induced by residual rotations of the simulator . . 177
4.19 Rabi oscillations and Raman spectrum obtained on the simulator with ultra-cold atoms . . . 179
4.20 Absorption imaging of the diffracted atoms in 0g as a function of the time of flight after the Raman pulse . . . 179
4.21 Rabi oscillations for a mirror pulse in double diffraction . . . 180
4.22 Double Diffraction interference fringes in the horizontal configuration . . . 181
4.23 Space-time diagram of an interferometer in the Double Diffraction regime when starting in the F=2 excited state . . . 181
4.24 Raman spectrum obtained in horizontal configuration when starting the sequence in the excited state . . . 182
4.25 Double Diffraction interference fringes in the horizontal configuration when starting the sequence in the excited state . . . 183
4.26 Absorption imaging of the diffracted atoms in 0g as a function of the time of flight after the first and second Raman pulses . . . 183

5.1 Principle of the simultaneous dual-species interferometer . . . 187
5.2 Diagram of the algorithm of Bayesian estimation of the differential phase . . . 189
5.3 Bayesian estimation of the differential phase from data following a Lissajous curve 191
5.4 Bayesian method on simulated data for $\kappa = 1$ . . . 200
5.5 Statistical and systematic error in the Bayesian phase estimator as a function of the number of measurements N for $\kappa = 1$ . . . 201
5.6 Bayesian simulations to extract the differential phase ϕ_d and errors on the estimation for two interrogation times . . . 202
5.7 Error on the Bayesian estimate as a function of the common phase scanned by the simulated data . . . 203
5.8 Error on the Bayesian estimate as a function of the differential phase noise . . . 204
5.9 Error on the Bayesian estimate as a function of the unknown part of the scanning phase range . . . 205

List of Tables

1 State of the Art of WEP Tests . . . 33
2 Microgravity platforms . . . 38

1.1 Performances for laser sources . . . 51
1.2 Characteristics of the magnetic pairs of coils . . . 67
1.3 Material comparison for the breadboard . . . 77

2.1 Different steps of evaporative cooling . . . 117
2.2 Summary of Projects and Achieved Minimum Temperatures . . . 123

5.1 Quantum tests of the weak-equivalence principle using dual-species atomic interferometers . . . 185
5.2 Contributions of systematic effects to the measurement. . . . 196

Résumé de la thèse en français

Introduction

Réaliser des mesures inertielles précises et exactes représente un enjeu important pour différentes applications, allant de l'étude du champ de gravité terrestre (géodésie) aux expériences de physique fondamentale comme la détection d'ondes gravitationnelles ou le test de l'universalité de la chute libre (UCL). L'UCL, également appelée "Principe d'Équivalence Faible" (PEF), a été formulé par Albert Einstein comme l'un des piliers de sa théorie de la relativité restreinte en 1907. Il stipule l'équivalence entre la masse inertielle et la masse gravitationnelle. Il en résulte que la chute libre d'un corps est indépendante de sa masse et sa composition. Certaines théories cherchant à unifier la physique quantique et la relativité générale prédisent une violation de ce principe, et les tests expérimentaux permettent de contraindre ces modèles, offrant ainsi une nouvelle perspective sur la physique fondamentale. Les tests consistent à mesurer précisément la chute de deux masses d'épreuve A et B et à estimer le paramètre d'Eötvös, défini par :

$$\eta = 2\frac{a_A - a_B}{a_A + a_B} = 2\frac{\left(\frac{m_g}{m_i}\right)_A - \left(\frac{m_g}{m_i}\right)_B}{\left(\frac{m_g}{m_i}\right)_A + \left(\frac{m_g}{m_i}\right)_B}$$

Actuellement, la mesure la plus précise de ce principe a été réalisée par la mission MICROSCOPE, qui a comparé l'accélération subie par deux cylindres de platine et de titane à bord d'un satellite avec $\eta = 10^{-15}$[[102]]. Cependant, les accéléromètres classiques présentent des limites fondamentales dues à leurs dérives sur le long terme. Le développement récent des technologies quantiques a permis la conception d'accéléromètres utilisant des nuages d'atomes comme masses d'épreuve, bénéficiant ainsi de leur caractère absolu. En utilisant deux espèces d'atomes de masses différentes, l'expérience ICE (Interférométrie à source Cohérente pour l'Espace) présentée dans cette thèse propose de comparer leur chute pour tester le principe d'équivalence faible.

Pour gagner deux ordres de grandeur sur l'état de l'art et atteindre la précision à laquelle une violation pourrait intervenir, cette mesure doit être faite avec de très longs temps de chute libre. Seul l'espace offre un environnement de chute libre suffisamment long et peu perturbé pour réaliser cette mesure. Des missions spatiales sont envisagées [[1]], mais elles seront précédées d'une mission de démonstration technologique avec un accéléromètre atomique à une espèce à bord d'un satellite (projet Carioqa)[[66]].

L'expérience ICE en est un démonstrateur terrestre et elle est transportable pour être mise en oeuvre sur des plateformes reproduisant l'apesanteur. Nous avons accès à deux plateformes : un simulateur de microgravité au laboratoire et l'avion Zéro-G. Le simulateur de microgravité, ou ascenceur d'Einstein, fonctionne sur le principe d'un plateau sur lequel repose la partie de l'expérience qui contient les atomes (appelée tête de senseur), mis en mouvement parabolique selon l'axe vertical. Quatre vérins pneumatiques et deux moteurs linéaires asservis en position offrent une demie seconde de zéro-gravité toutes les 12 secondes. Cet appareil de trois mètres de haut est unique au monde et permet d'observer les atomes en chute libre de manière répétable, dans l'espace du laboratoire. Pour avoir accès à des temps de chute libre plus longs, nous avons

participé à deux campagnes de vols Zéro-G du CNES en Mars 2022 et Mars 2023. A bord de l'avion Zéro G opéré par la société Novespace, les expériences et leurs expérimentateurs sont en chute libre dans un avion qui effectue des mouvements paraboliques, offrant 22 secondes d'apesanteur. Le principe de ces deux plateformes de microgravité est présenté dans la figure 1.

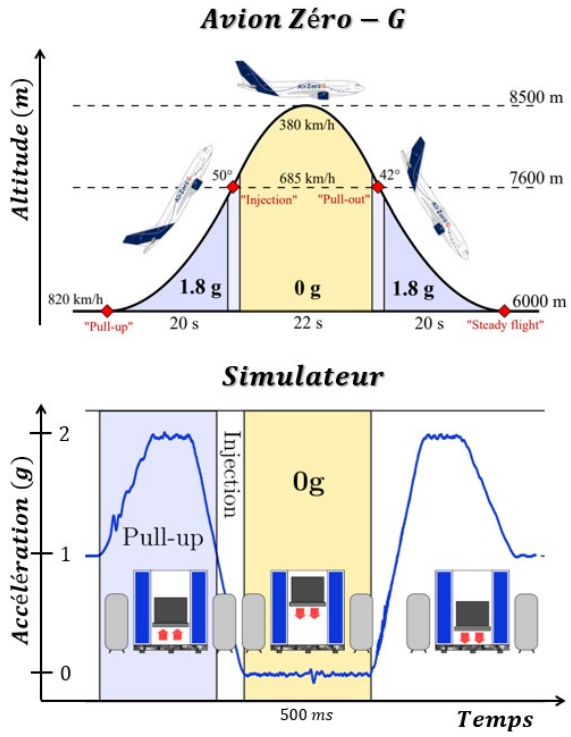

Figure 1: ***Plateformes d'accès à la microgravité : avion Zéro G et ascenceur d'Einstein au laboratoire***

Ce manuscrit présente les premières sources atomiques ultra-froides dans cet avion et les premiers pas vers des mesures inertielles avec ces sources en zéro-gravité sur le simulateur. Ce travail sur le démonstrateur ICE permet à la fois l'étude des phénomènes physiques propres à l'environnement de microgravité; mais aussi de relever le défi technologique que représente la réalisation d'une expérience de laboratoire transportable et robuste.

Chapitre 1 - Dispositif expérimental

Le dispositif expérimental doit être compact, robuste et compatible avec les contraintes de sécurité de la société Novespace qui opère l'avion Zéro-G. Il est composé de 10 racks d'instruments, avec plus d'une tonne de matériel dans les normes aéronautiques (voir Figure 2).
Diverses sources laser sont employées pour le refroidissement et l'interférométrie des atomes de rubidium et de potassium, ainsi que pour la mesure de leur accélération. Le système laser repose entièrement sur des technologies d'optique fibrée, utilisant des composants télécom, un domaine d'expertise développé au sein de notre groupe pour assurer la portabilité de l'expérience sur le terrain. Pour le test du principe d'équivalence, nous utilisons le rubidium (Rb) et le potassium (K). Ces atomes présentent des transitions atomiques avantageuses autour de 780 nm et 767 nm de longueur d'onde, nous permettant d'utiliser des lasers fibrés dont la fréquence est doublée dans des cristaux non linéaires. Grâce à des architectures laser innovantes, ces sources sont accordables en longueur d'onde, ce qui permet d'effectuer les séquences expérimentales. Les faisceaux réalisant l'interaction avec les deux espèces atomiques passent à travers les mêmes

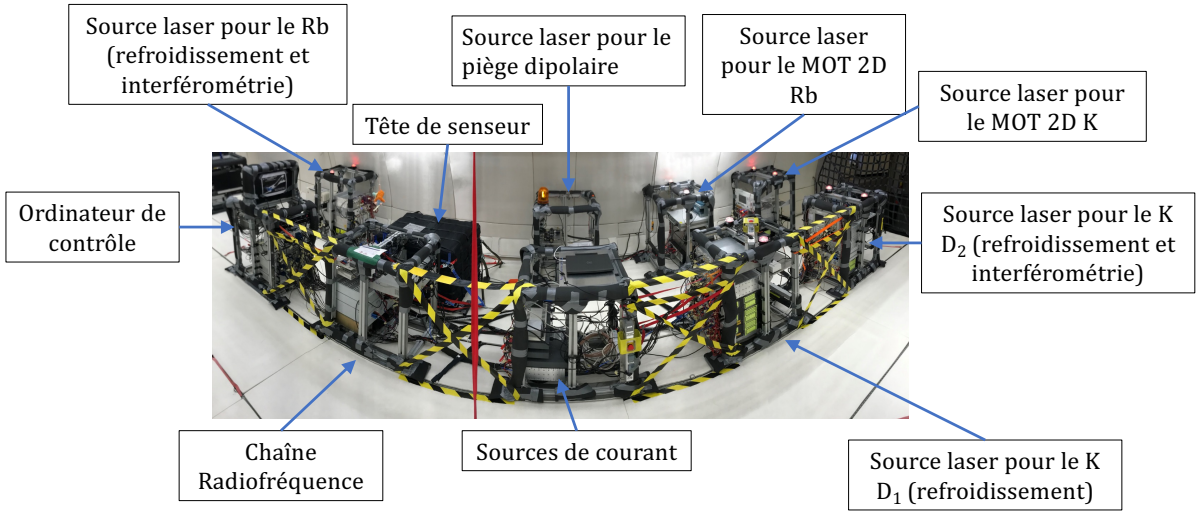

Figure 2: ***Dispositif expérimental complet à bord de l'avion Zéro G***

fibres et composants optiques, facilitant l'intégration de l'instrument.

Les expériences sont menées dans une enceinte à vide présentée en Figure 3, où les atomes de rubidium et de potassium sont introduits par le biais de dispensers métalliques chauffés par un courant électrique. Les atomes sont éclairés par la lumière des lasers à travers les hublots de l'enceinte à vide, grâce à des collimateurs. Un ensemble de bobines est utilisé pour créer un gradient de champ magnétique, permettant à la fois de piéger et de refroidir les atomes, tout en compensant les champs magnétiques extérieurs. Un blindage magnétique en mu-métal protège l'expérience des perturbations magnétiques extérieures qui pourraient varier au cours de l'expérience. La détection des atomes s'effectue à l'aide de deux détecteurs et deux caméras, tandis que des accéléromètres et des gyromètres classiques sont utilisés pour réaliser une hybridation des mesures quantiques.

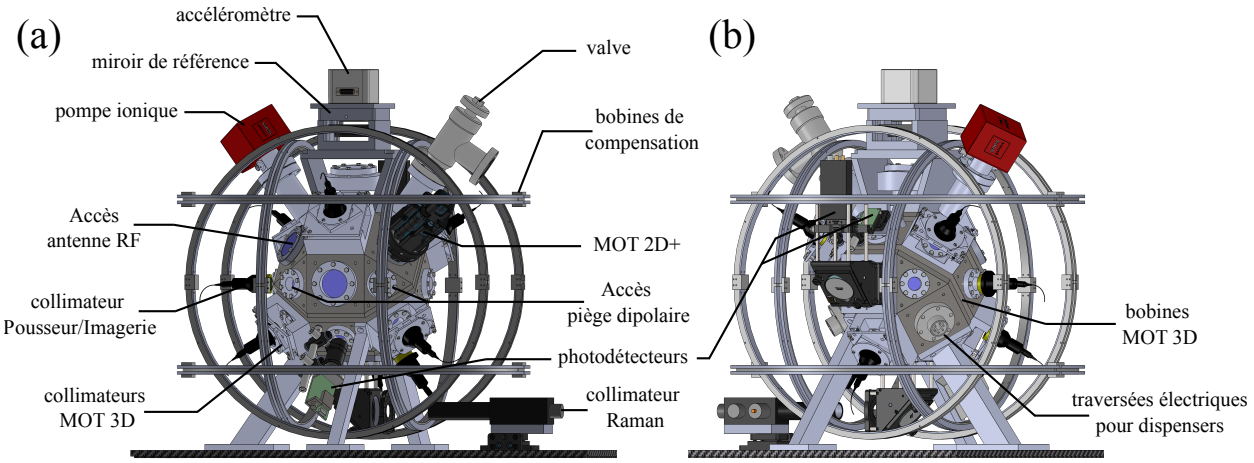

Figure 3: ***Tête de senseur : Enceinte à vide et instruments pour le refroidissement, l'interférométrie et la détection des atomes.***

Des sources radio-fréquences sont indispensables pour assurer le verrouillage des fréquences des lasers et pour interagir directement avec les atomes au moyen d'une antenne radio-fréquence. L'ensemble de l'expérience est soigneusement synchronisé par l'ordinateur de contrôle.

Chapitre 2 - Sources atomiques de rubidium et potassium

La méthode de l'interférométrie atomique (IA) tire profit du caractère ondulatoire de la matière à basse énergie, dans notre cas un nuage d'atomes sous forme gazeux. Placés dans un environnement d'ultra-vide, les atomes (en orange sur la figure 4) sont piégés au centre de faisceaux lasers qui illuminent les atomes dans les 3 directions de l'espace (en bleu). Grâce à la connaissance de la structure énergétique des atomes et leur interaction avec le champ électro-magnétique produit par les lasers, des méthodes de refoidissement permettent d'abaisser la température des atomes à quelques dizaines de nanokelvin au dessus du zéro absolu. Notamment, un laser puissant nommé pince optique (en jaune) utilise la force dite dipolaire de la lumière sur les atomes pour les confiner en un nuage très dense.

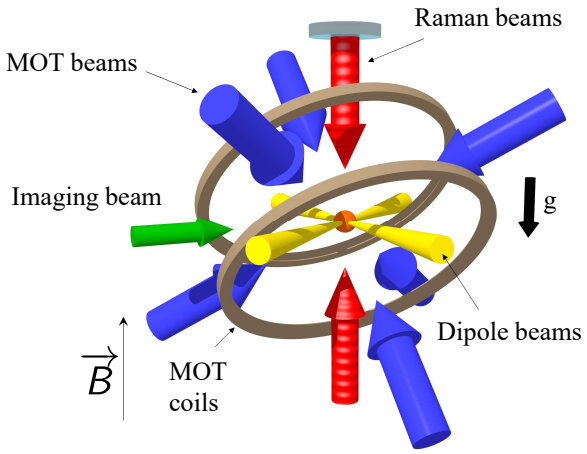

Figure 4: ***Principe du piégeage magnéto-optique et du refroidissement d'atomes***

Dans ce piège dipolaire, la température des atomes est abaissée grâce à une méthode d'évaporation forcée. Le potentiel créé par la pince optique est progressivement réduit pour éliminer les atomes les plus énergétiques, tandis que les atomes restants se thermalisent à une température plus basse. Lorsque cette température descend en dessous d'un certain seuil, les atomes ne sont plus considérés comme formant un nuage composé d'individus distincts, chacun décrit par une fonction d'onde séparée, mais comme un unique système quantique macroscopique décrit par une seule fonction d'onde. Cette transition de phase est connue sous le nom de condensation de Bose-Einstein (BEC). Une signature typique de cet état se caractérise par la présence d'une double structure : une partie des atomes du nuage demeure "thermique", tandis qu'une autre partie du nuage est condensée. En gravité standard, nous parvenons à obtenir des condensats de rubidium avec des températures équivalentes d'environ 40 nanokelvins. Le potassium est également piégé dans le piège dipolaire, et des travaux sont actuellement en cours pour le refroidir à des températures similaires à celles du rubidium, en vue de la réalisation d'interféromètres à double espèce.

Le fonctionnement du refroidissement évaporatif en l'absence de gravité présente des particularités qui nécessitent une étude approfondie en prévision de futures missions spatiales.
Sur le simulateur, une séquence spécifique permet d'utiliser les phases de gravité standard et d'hypergravité pour les étapes de refroidissement laser. Ensuite, ces sources sont "lancées" en microgravité pour réaliser la suite des expériences. À bord de l'avion Zero G, nous avons réussi à créer les premières sources atomiques ultra-froides avec une séquence entièrement en microgravité en utilisant des méthodes tout-optiques (voir Figure 5). Ces sources atteignent des

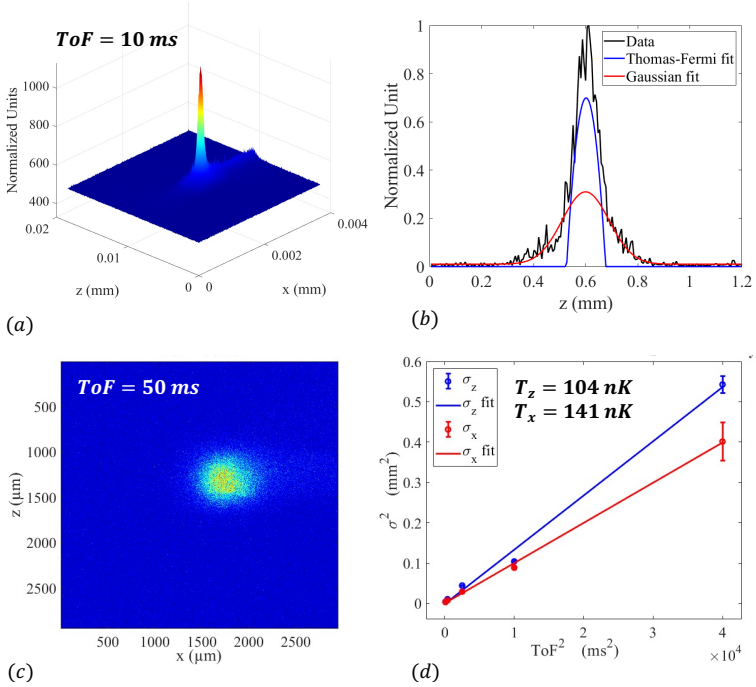

Figure 5: ***Atomes ultra-froids obtenus à bord de l'avion Zéro G*** *- (a) et (c) Images par fluorescence du nuage ultra-froid pour différents temps de vol. (b) Vue en coupe du profil du signal par fluorescence. On peut distinguer une partie condensée (ajustée par une parabole inversée) et une partie thermique (ajustée par une fonction gaussienne) dans ce nuage. (d) Mesure de la température par la méthode du temps de vol.*

températures proches de 100 nanokelvins, mesurées en étudiant l'expansion spatiale du nuage pour différents temps de vol lorsque les atomes ne sont pas piégés.

Chapitre 3 - Interférométrie atomique en gravité standard

Pour mesurer l'accélération des atomes par interférométrie atomique, nous utilisons un laser d'interrogation (représenté en rouge sur la figure 4), appelé faisceau Raman, qui est rétro-réfléchi sur un miroir pour créer une référence de phase. La séquence d'interférométrie se déroule de la manière suivante : une première impulsion d'environ 20 microsecondes de ce faisceau d'interrogation sépare le nuage d'atomes. Pendant cette séparation, une partie des atomes acquiert une quantité de mouvement dans une direction, passant également d'un état interne fondamental à un état excité. Deux autres impulsions les recombinent en un seul point. En utilisant le phénomène de fluorescence des atomes, nous estimons le nombre d'atomes dans l'état interne excité (correspondant aux atomes "déviés") ainsi que le nombre total d'atomes présents dans le nuage. Nous calculons ensuite le ratio des populations en sortie de l'interféromètre. Ce processus nous permet d'observer le comportement ondulatoire des atomes, se traduisant par une figure d'interférences quantiques sous la forme de franges sinusoïdales. Le déphasage de cette sinusoïde est directement proportionnel à l'accélération subie par le système, avec un facteur k_{laser} lié à la longueur d'onde du laser et au temps d'interrogation T au carré, soit $\delta\phi = k_{laser} a T^2$.
Le faisceau Raman comprend deux fréquences laser et est rétro-réfléchi par le miroir de référence. Deux paires de faisceaux interagissent ainsi avec les atomes. En gravité standard, les atomes tombent par rapport au miroir, ce qui provoque un effet Doppler modifiant la fréquence du laser d'interrogation "perçue" par les atomes. Dans cette configuration, les atomes sont en résonance avec l'une des deux paires de faisceaux Raman, permettant ainsi d'imprimer la phase du laser

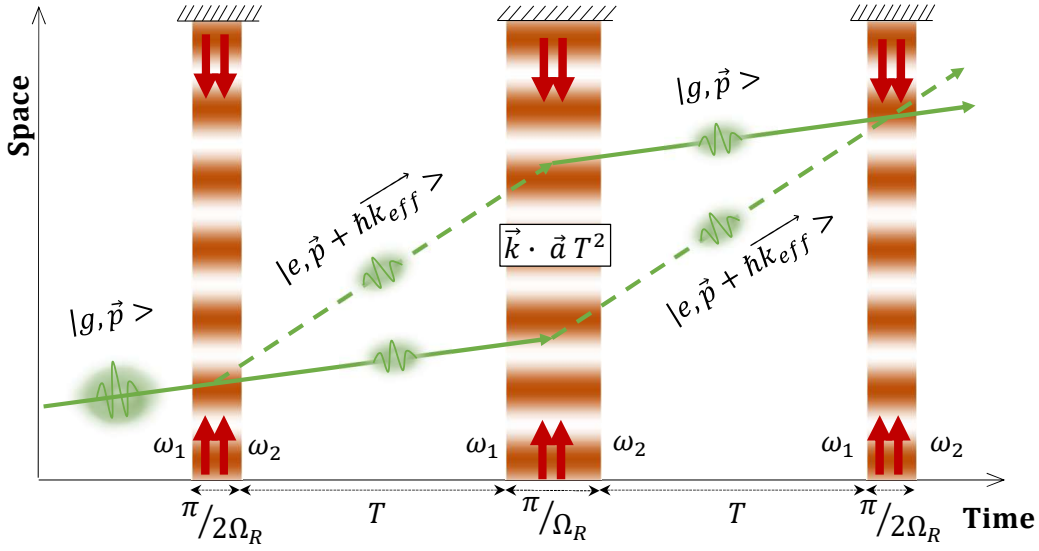

Figure 6: ***Schéma de l'interféromètre atomique en gravité standard***

sur une seule partie des atomes. Les atomes restants ne sont pas déviés, créant un schéma d'interférométrie similaire à un interféromètre optique de Mach-Zehnder, présenté en Figure 6. Différents effets inertiels peuvent perturber la stabilité des franges de l'interféromètre, notamment les niveaux élevés de vibrations, ce qui complique l'observation de la figure sinusoidale. Pour reconstruire avec précision les franges, nous employons une méthode d'hybridation avec un accéléromètre classique, connue sous le nom de méthode FRAC (Fringe Reconstruction using Accelerometer Correction). Les opérations réalisées en gravité standard nous permettent de caractériser notre dispositif de mesure.

Chapitre 4 - Interférométrie atomique en microgravité

Le principe de l'expérience est de mesurer des accélérations sur de longues périodes de chute libre des atomes. Cependant, la durée de cette chute est limitée par la taille de l'enceinte à vide. Pour surmonter cette limitation, nous avons opté pour une approche où la tête du capteur est mise en chute libre, une réalisation que nous avons réussie avec notre ascenseur d'Einstein. Lorsqu'il n'y a pas de chute relative des atomes par rapport au miroir de référence, les atomes sont en résonance avec les deux paires de faisceaux Raman simultanément. Dans le cas où la distribution des impulsions des atomes est large, comme c'est le cas pour les atomes dits "froids", la configuration d'interférométrie connue sous le nom de "double simple diffraction" permet de réaliser des mesures où deux interféromètres atomiques en simple diffraction coexistent simultanément, comme illustré sur la figure 7.

Cette configuration a permis la réalisation d'interféromètres en microgravité pour des temps d'interrogation allant jusqu'à T=100 ms. Pour différents temps d'interrogation T, 300 points de mesure de ratio des atomes en sortie d'interféromètres sont réalisés. Cependant, pour ces durées étendues, la reconstruction des franges à l'aide de la méthode FRAC est rendue impossible en raison des bruits intrinsèques des accélérations classiques. Nous confirmons la réalisation de l'interférométrie en observant des structures appelées "batman" et en vérifiant que la distribution des points de mesure suit la statistique d'une sinusoïde. L'ajustement de ces structures bimodales nous permet d'extraire un contraste et un rapport signal/bruit (SNR), ce qui nous permet de déduire la sensibilité de la mesure de l'accélération de 5×10^{-8}g.

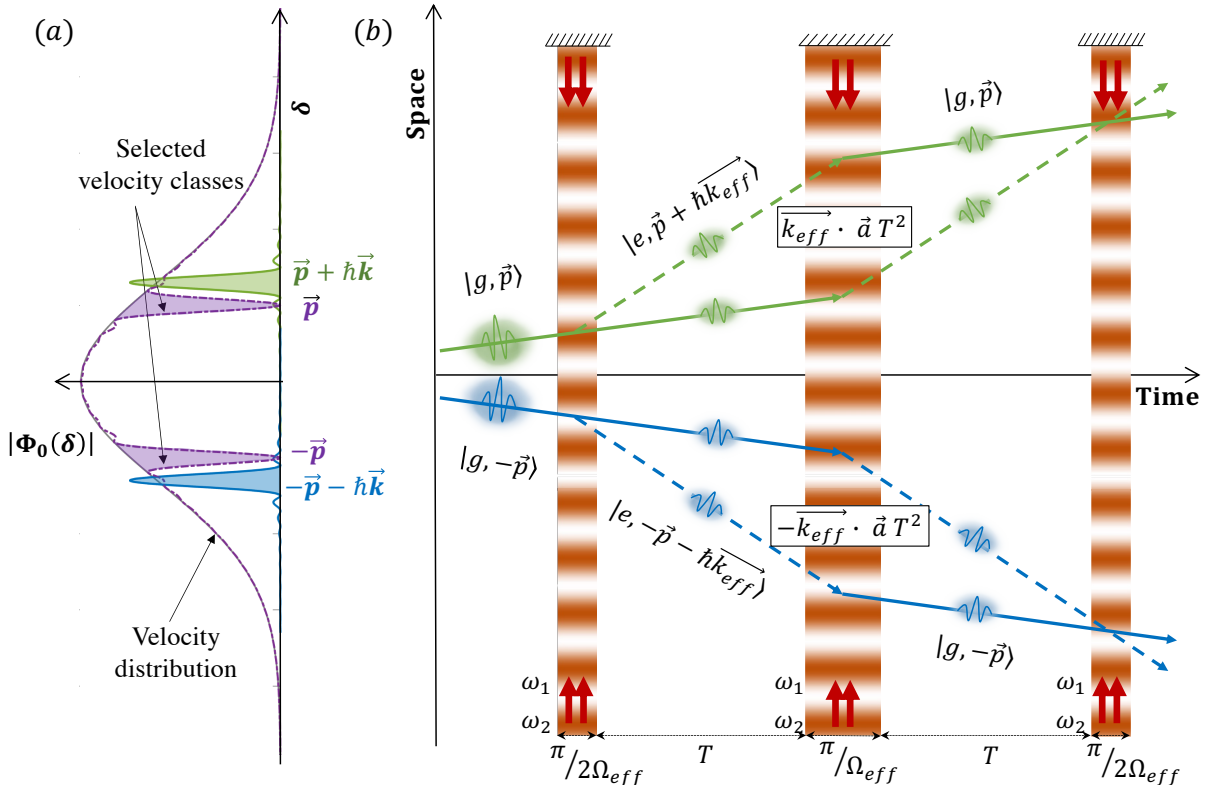

Figure 7: ***Schéma de l'interféromètre atomique en double simple diffraction.***

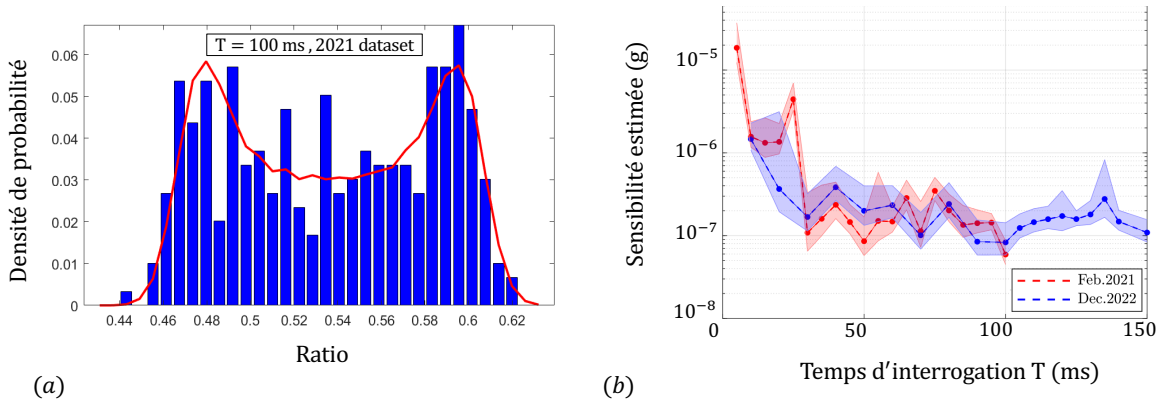

Figure 8: ***Résultats obtenus avec l'interféromètre en double simple diffraction sur le simulateur de microgravité*** *- (a) Histogramme des ratios obtenus expérimentalement avec ajustement (méthode BAT). (b) Sensibilités estimées pour différents temps d'interrogation à partir des données expérimentales (chaque point correspond à 300 mesures).*

Ces résultats sont très prometteurs, mais ils sont limités par des facteurs tels que les rotations résiduelles de notre simulateur, qui sont dues à la température élevée des atomes. Par conséquent, il est nécessaire de réaliser les mesures avec les sources ultra-froides décrites précédemment pour améliorer la précision de nos expériences.

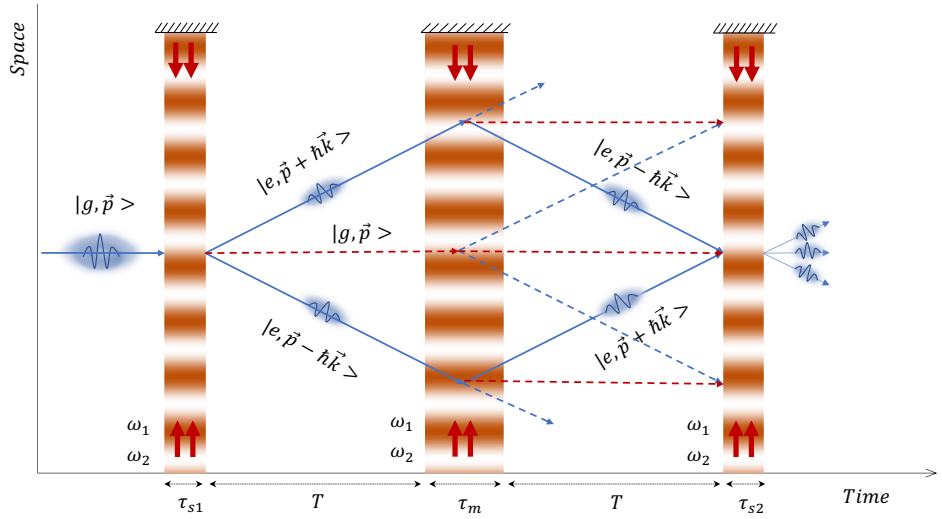

Figure 9: ***Schéma de l'interféromètre atomique en double diffraction***

En ce qui concerne les sources ultra-froides, la distribution en impulsion est trop étroite pour permettre l'émergence du régime de double simple diffraction. Lors du premier pulse, les atomes résonnent avec les deux paires de faisceaux, ce qui entraîne la déviation des atomes dans les deux directions. Cela crée un interféromètre avec une aire deux fois plus grande, conformément à la configuration illustrée à la Figure 9, communément appelée la configuration de Double Diffraction.

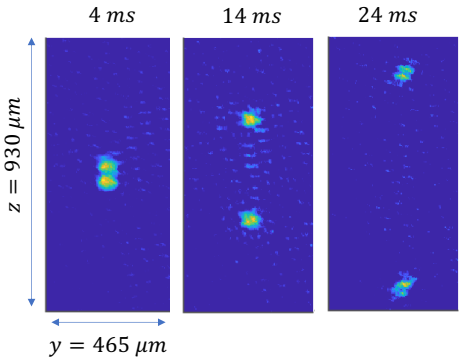

Figure 10: ***Nuages atomiques après la première impulsion séparatrice pour différents temps de vol.***

Dans cette configuration, nous avons réalisé avec succès la première étape de la séquence intreferéométrique (la séparatrice) avec des atomes ultra-froids à une température équivalente d'environ 40 nK sur notre simulateur de micrgravité (voire figure 10).

Chapitre 5 - Test du Principe d'Equivalence Faible

Le test du PEF est réalisé par un interféromètre double-espèce présenté dans la figure 11.

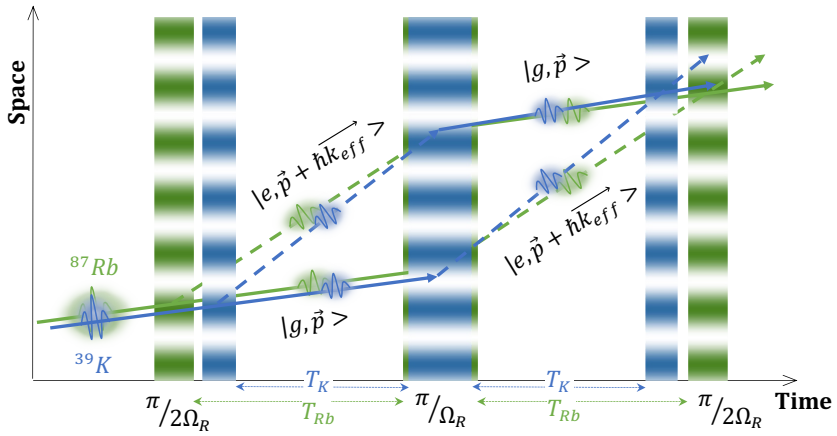

Figure 11: ***Principe de l'interféromètre double-espèce***

Le paramètre d'Eötvös, figure de mérite essentielle pour le test de l'universalité de la chute libre, est défini ici comme $\eta = 2 \times (a_{\mathrm{Rb}} - a_{\mathrm{K}})/(a_{\mathrm{Rb}} + a_{\mathrm{K}})$. Une déviation de ce paramètre par rapport à zéro serait indicative d'une violation du principe d'équivalence, et sa mesure précise doit prendre en compte divers effets systématiques. Ces effets systématiques ont été minutieusement répertoriés et quantifiés dans l'étude présentée dans [[17]]. Grâce à notre interféromètre double-espèce, nous avons réussi à effectuer le premier test en microgravité[[15]] ainsi qu'un test au sol avec une sensibilité atteignant 10^{-8} sur ce paramètre [[14]]. Plusieurs méthodes ont été développées pour extraire l'accélération différentielle de cet interféromètre double espèce[[12]], dont la méthode double FRAC, une méthode basée sur l'ajustement des données expérimentales pour les deux espèces par une ellipse, ainsi qu'une méthode faisant appel à une analyse bayésienne des données. Cette dernière méthode fait l'objet de nos investigations en réalisant des simulations visant à évaluer la sensibilité que nous pourrions atteindre pour le test du PEF sur notre simulateur.

Avec notre configuration actuelle, qui utilise des atomes thermiques, nous sommes en mesure de réaliser des interféromètres pour des temps d'interrogation allant jusqu'à 200 ms. Grâce à une approche bayésienne, nos simulations prédisent que nous pourrions mesurer la phase différentielle entre les deux interféromètres corrélés avec une incertitude de moins de 10 mrad, en effectuant seulement 300 mesures (équivalent à environ une heure de mesures sur notre simulateur). Cela se traduirait par $\delta\eta^{\mathrm{sys}} = 1.9 \times 10^{-8}$ g et $\delta\eta^{\mathrm{stat}} = 6.3 \times 10^{-9}$ g.

En augmentant le nombre de mesures à 1000, il serait possible d'améliorer ces valeurs, dépassant ainsi le seuil de 10^{-10} pour le paramètre d'Eötvös. Toutefois, la durée d'interrogation est principalement limitée par la température des atomes, qui les rend sensibles aux rotations. En utilisant des atomes ultra-froids, nous pourrions potentiellement atteindre des temps d'interrogation plus longs, bien que des ajustements soient nécessaires pour améliorer la méthode d'analyse.

Conclusion

Le travail de cette thèse représente trois années d'efforts pour avancer notre compréhension de la production de sources ultra-froides et de l'interférométrie en microgravité. Notre objectif est

de préparer des missions spatiales pour tester le Principe d'Équivalence Faible (WEP) et les missions préliminaires.

Notre configuration expérimentale est polyvalente, conçue pour le laboratoire et l'avion Zero G, et offre une grande robustesse et transportabilité. Nous avons réalisé les premières sources ultra-froides de rubidium en microgravité, atteignant des températures inégalées par évaporation tout-optique.

Les travaux sur l'interféromètre à deux espèces offrent une exploration complète des mesures d'accélération en utilisant des atomes froids et ultra-froids en gravité standard et en microgravité, ouvrant la voie à des mesures très sensibles.

Nous avons également étudié la possibilité d'extension de cette interférométrie à deux espèces atomiques, avec des simulations montrant la capacité d'atteindre une sensibilité de meilleure que 10^{-10} g pour le WEP. Des améliorations futures sont envisagées pour renforcer nos capacités, notamment en réduisant les désalignements du faisceau du piège dipolaire par un asservissement actif.

En résumé, cette thèse représente une contribution significative à la préparation de missions spatiales pour l'interférométrie atomique telle que la mission Carioqa financée par l'union européenne. Le potentiel de notre appareil s'étend bien au-delà du test du WEP. Par exemple, l'ascenseur d'Einstein et notre connaissance des pièges dipolaires tout optiques ouvrent la voie à l'étude de nouvelles formes de pièges dipolaires optiques. Des géométries telles que les bulles de condensats de Bose-Einstein suscitent un grand intérêt en raison de leurs propriétés topologiques uniques, et des études théoriques sont déjà en cours. Notre appareil transportable, aux côtés de l'ascenseur d'Einstein, représente un outil unique pour étudier la physique des atomes ultra-froids en microgravité.

Introduction

In the vast cosmos, where the forces of nature shape the dance of celestial bodies, one force stands out as both omnipresent and enigmatic: gravity. From the tragic fall of a cellphone to the orbits of planets, its influence is undeniable, and we experience its effect on a daily basis. Yet, it is perhaps the most mysterious of the four fundamental forces, with its true nature remaining a subject of debate. At the core of this debate lies the Einstein Equivalence Principle, and one of its consequences known as the Universality of Free Fall or the Weak Equivalence Principle. But the answers to these fundamental questions may lie at the level of atoms, within the realms of quantum physics.

The development of technologies stemming from the first quantum revolution have forever changed society and daily life, introducing innovations like lasers and transistors. Quantum technologies are fundamental components of modern electronic devices, including computers and smartphones. These advancements ushered humanity into a new era, characterized by an information-driven society [[9]]. The second quantum revolution has paved the way for groundbreaking experiments leveraging quantum principles such as entanglement and superposition[[21]]. This has given rise to quantum clocks, quantum simulations, quantum computing, cryptography, and quantum sensing. In our pursuit of unraveling the mysteries of the universe and comprehending its fundamental laws, precise measurement tools serve as the key to unlocking nature's deepest secrets. Quantum sensors, employing clouds of atoms as test masses for precise inertial measurements, offer these tools, benefitting from their inherent accuracy.

To achieve two orders of magnitude improvement over the state of the art and reach the precision at which a violation might occur, this measurement must be conducted over very long free fall times. Space missions are being considered[[1, 2]], and they will be preceded by a technology demonstration mission featuring an atomic accelerometer with a single species on board a satellite (the CARIOQA project). The experiment described in this manuscript serves as a terrestrial demonstrator and is transportable for use on platforms that replicate weightlessness conditions. The ICE project ('Interférométrie à sources Cohérentes pour l'Espace'), proposes to compare the free fall of two different species of atoms to test the weak equivalence principle. We currently have access to two such platforms: a microgravity simulator in the laboratory and the Zero-G aircraft. In this aircraft, we have successfully generated ultra-cold atomic sources. In the zero-gravity environment provided by our simulator, we have demonstrated state-of-the art inertial measurements using cold atoms. Our work on the ICE demonstrator allows for both the study of physical phenomena specific to the microgravity environment and addressing the technological challenge of creating a portable and robust laboratory experiment.

Figure 12: ***Pictures taken during microgravity phase in the Zero G plane*** *- The ICE experiment and the experimenters : Baptiste Battelier, Vincent Jarlaud, Dylan Sabulsky and Celia Pelluet during the 62nd and 64th CNES flight campaigns in 2022 and 2023. Credits : Novespace.*

The initial chapter of this manuscript serves as an introductory section, where we will provide the context and principles that underlie the ICE experiment. This first chapter aims to be accessible to a wide audience, so certain fundamental concepts will be explained, and contextual elements will be elaborated upon. We will discuss the need for a quantum test of the Weak Equivalence Principle in space. Additionally, we will explore how cold atoms can facilitate such precise measurements. Furthermore, we will delve into the crucial aspect of achieving microgravity, which is essential for advancing quantum sensors aboard satellites. Lastly, we will offer an overview of the envisioned space missions in this context.

0.1 The Weak Equivalence Principle

0.1.1 The Universality of Free Fall

The concept of the Weak Equivalence Principle has a rich history rooted in the foundations of physics. Aristotle, in his treatise 'On the Heavens', postulated that gravity was an inherent property of objects, suggesting that objects naturally moved toward ground : their designated place. This idea prevailed for centuries, primarily based on observations rather than experimental evidence. It was observed that heavier objects seemed to fall faster, and Aristotle stated that the time of descent appeared to be inversely proportional to weight, leading to the belief that the velocity of descent was directly proportional to mass. This Aristotelian framework held sway for about two millennia.

However, Galileo Galilei[[50]] dared to cast doubt on the validity of this proportional law. He conducted experiments, including those involving objects moving through water and molasses, envisioning a realm devoid of resistance—a realm akin to pure thought : vacuum. In doing so, he pronounced a law that directly contradicted the commonly held observations. Though emblematic, the veracity of Galileo's experiment at the Leaning Tower of Pisa is debated : we know he used tilted plans and rolling spheres to test the principle. But the strength of Galileo stands in the thought experiment he pursued, presented in Figure 13. He considered an intriguing hypothesis involving two stones: one heavy and the other light, connected by a rope. According to Aristotle's understanding, the heavy stone should fall faster than the lighter stone, and the ensemble should fall faster than the heavy stone. However, due to the lighter stone, the heavy stone should be slowed down in its fall. Galileo's genius lay in recognizing this paradox : how could it fall both faster and slower simultaneously? The resolution was found in equality rather than proportionality.

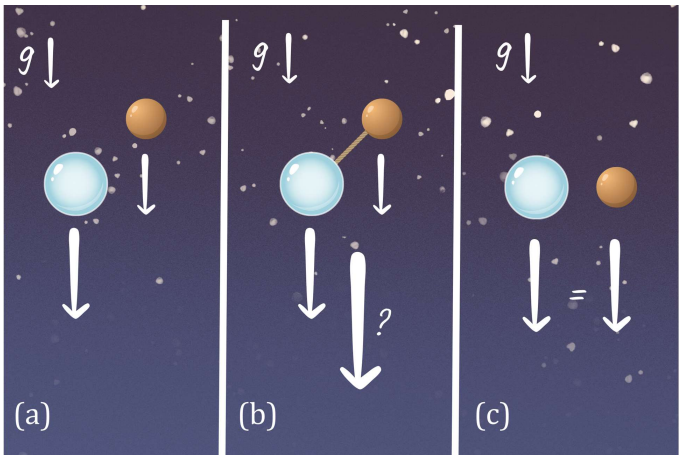

Figure 13: ***Principle of Galileo thought experiment*** *- We consider two stones falling under gravity in a vacuum environment: (a) According to Aristotle, the heavier stone experiences a greater acceleration due to gravity. (b) When the two stones are connected by a rope, the expectation is that the lighter stone should slow down the fall of the heavier one. However, the system comprising the heavy stone, the light stone, and the rope should fall faster than the heavy stone alone, creating a paradox. (c) The only resolution to this paradox lies in the equivalence of the accelerations experienced by the two stones.*

The torchbearer of this new understanding was Sir Isaac Newton, who formalized the laws of motion and universal gravitation. His formalism reveals two fundamental quantities: gravitational mass m_g and inertial mass m_i. The former determines the weight of an object in a gravitational field, while the latter relates the force applied to an object to the resulting acceleration. Newton

deduced like Galileo an equivalence between them. This equality immediately led to the Principle of Universality of Free Fall, which asserts that the acceleration of an object subject solely to gravity is independent of its mass or composition.

At the dawn of 20th century, Albert Einstein presented his theory of special relativity that states that laws of physics are invarient in all inertial frames of reference and that the speed of light is an absolute constant. When later generalizing this theory to include gravitation, he based his model on what he initially called 'Hypothesis of equivalence'.

0.1.2 The Einstein equivalence principle

In the spirit of Galileo, Einstein dared to envision the consequences of this equivalence for experiments in environments that did not exist in his time, such as an elevator in free fall, subjected solely to gravity. He proposed a compelling thought experiment depicted in Figure 14, involving an observer within this elevator.

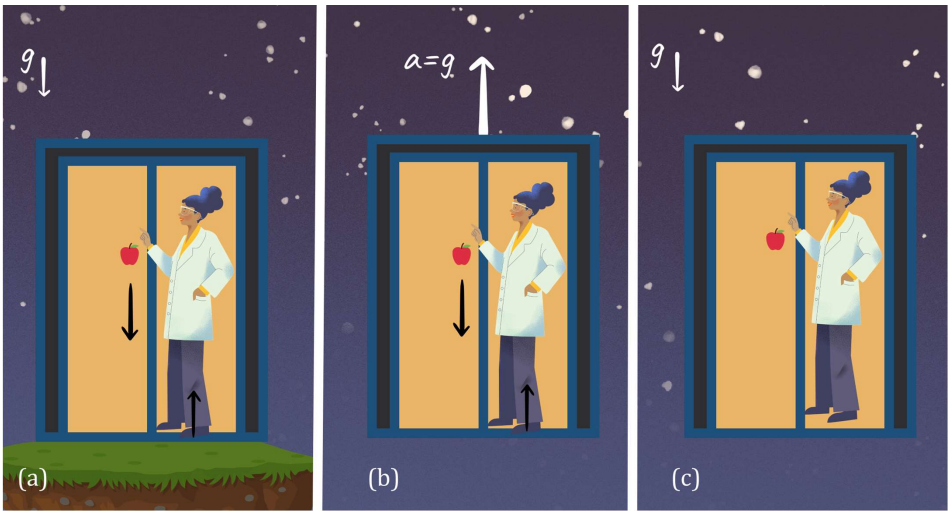

Figure 14: ***Principle of the Einstein Elevator thought experiment*** *- (a) The elevator is at rest on the ground in Earth's gravitational field. The observer sees the apple accelerated by Earth's gravity, causing it to hit the floor of the elevator.(b) A force of the same order of magnitude as gravity accelerating the elevator upwards. The apple falls to the floor in the exact same way, and the observer cannot tell the difference between the two situations.(c) The elevator is in free fall: in the absence of an additional force, the observer considers herself as weightless, and the apple floats alongside her.*

In one scenario, the elevator is at rest on Earth: the reaction of the Earth's ground compensates for the gravitational acceleration, and the observer only perceives this reaction force. In the second scenario, the elevator accelerated upwards with the same magnitude of acceleration as gravity, possibly by a rope pulling the elevator upwards. Remarkably, the observer cannot distinguish between these two situations, and the trajectories of objects within the elevator remain identical. This reasoning can be extended to a reference frame in free fall: if the elevator experiences only gravitational acceleration, the observer perceives no sensation of weight, and any loose objects within the elevator would appear to float alongside them.

This thought experiment gave birth to the Einstein Equivalence Principle (EEP), that can be divided into three sub-principles :

- The Weak Equivalence Principle (WEP) or Universality of Free Fall (UFF) asserts that an uncharged test body's trajectory in space-time, after being placed at an initial event

with an initial velocity, remains unaffected by its internal structure and composition. It is commonly tested by measuring the relative acceleration of two test bodies with different internal structures and compositions in free fall within the same gravitational field, where the satisfaction of WEP implies their differential acceleration is zero.

- The Local Lorentz Invariance (LLI) asserts that the results of local experiments not influenced by gravity remain consistent regardless of the velocity or orientation of the apparatus involved. Experiments testing LLI are primarily based on comparing the oscillation frequency of two clocks with different velocities and/or orientations, with LLI being confirmed if the experiment's outcome remains unchanged despite these variations[[73, 91]].

- The Local Position Invariance (LPI) states that the outcomes of local experiments unaffected by gravity remain consistent regardless of where or when they are conducted in the Universe, often involving experiments in various locations and/or times to test this principle. These tests can involve altering the local gravitational potential to search for potential anomalous connections between gravity and the fields within the experiment, with a specific example being gravitational red-shift tests comparing clocks at different locations to confirm LPI when the measured relative frequency difference corresponds to the gravitational potential difference divided by the square of the speed of light.

0.1.3 Why testing the WEP?

The EEP presents an intriguing aspect of gravity by making it fundamentally different from other known interactions, as it posits that gravity results from the curvature of space-time itself rather than acting as a field over space-time. This distinction emphasizes the uniqueness of gravitation. Surprisingly, experiments consistently uphold EEP, despite its counterintuitive nature. Many theories in quantum gravity and unification predict violations of EEP, often necessitating tuning mechanisms to align with existing limits on EEP. The absence of EEP violations poses a significant constraint on the development of new theories. EEP tests are vital in this regard, as they investigate the universal coupling of gravity to Standard Model fields and anomalous couplings. These experiments impact both particle physics and cosmology, revealing insights into dark energy, dark matter, and particle interactions. Moreover, quantum tests of EEP differ from classical ones, requiring consideration of quantum mechanics' unique features and their interplay with gravity, offering the potential for deeper insights into the fundamental nature of these couplings.

0.1.4 State of the art

The history of experimental tests for the UFF dates back to the Renaissance, with documented experiments conducted by figures like Simon Stevin, Galileo Galilei, and later Newton, Bessel, Eotvös, Dicke, Braginsky, and Adelberger, among others. These experiments primarily employed two methods: dropping objects and using torsion balances, with torsion balances providing the best uncertainties on Earth but being limited by local gravity gradients. In space, the recent mission MICROSCOPE has significantly improved upon ground experiments, and further advancements are anticipated.

A critical parameter for evaluating UFF/WEP tests is the Eotvös ratio η, which compares the gravitational acceleration of two test objects A and B relative to a specified source mass of the gravitational field.

$$\eta = 2\frac{a_A - a_B}{a_A + a_B} = 2\frac{\left(\frac{m_g}{m_i}\right)_A - \left(\frac{m_g}{m_i}\right)_B}{\left(\frac{m_g}{m_i}\right)_A + \left(\frac{m_g}{m_i}\right)_B} \tag{1}$$

While η is valuable for comparing different experiments, it cannot account for the diversity of underlying theories, including variations in couplings depending on source and test objects or couplings to space-time-varying background fields. Therefore, achieving both high-performance results in terms of the Eotvös ratio and diversity in test objects and source masses is essential.

η	**Elements**	**Method**	**Reference**	**Comments**
10^{-15}	Pt-Ti	Space test	[[102]]	Classical
10^{-13}	Be-Ti	Torsion balance	[[93]]	Classical
10^{-12}	^{87}Rb-^{85}Rb	8.2 meter atomic fountain	[[8]]	Quantum
10^{-9}	^{133}Cs-Corner Cube	Atoms, ground	[[80]]	Hybrid
10^{-9}	^{87}Rb-Corner Cube	Atoms, ground	[[75]]	Hybrid

Table 1: ***State of the Art of WEP Tests***

Table 1 illustrates the current state of UFF/WEP tests, categorized by the type of test masses used, distinguishing between quantum tests and classical or hybrid tests.

Results from the MICROSCOPE mission (MICROSatellite for Compensated Drag-free Equivalence Principle Test) in a controlled space environment demonstrate the potential of extended free-fall durations. To this day, it is the most sensitive test of the weak equivalence principle. The payload, mounted on a satellite in heliosynchronous orbit, consisted of two concentric cylinders with different masses and compositions (titanium and platinum) serving as test masses. These two masses were held in position by applying an electrostatic force, and the objective was to verify that the force required to maintain their equilibrium was equivalent in both cases. In this manner, the mission was able to demonstrate a precision on the order of 10^{-15} [[102]] on the parameter η, not witnessing any violation of the WEP.

0.2 Cold Atoms inertial measurements

While state-of-the-art tests are currently conducted using classical test masses, freely falling atoms present an opportunity to improve previous results to reach $\eta = 10^{-17}$[[18]]. Although the precision of quantum measurements is currently several orders of magnitude lower than that of MICROSCOPE, they offer real complementarity to classical methods and have a strong potential for improvement.

Accessing the measurement of the Eötvös parameter through atomic interferometry methods allows not only for confirming these results on a microscopic scale but also for directly comparing the laws of gravitation with those of quantum mechanics. Manipulating the intrinsic degrees of freedom of atoms (internal states, spin, etc.) also opens up the possibility of a greater diversity of experimental parameters.

0.2.1 Wave-particle duality

Before the twentieth century, physical phenomena could be interpreted according to different models: a corpuscular vision, in which phenomena were imagined as involving small 'balls' that followed very precise trajectories; or a wave vision, in which events were thought to be associated with waves moving through a material medium, like waves on the surface of the ocean. While Newton initially presented light as a tiny body in order to explain its linear trajectory, defended by geometric optics, this vision was abandoned in the 19th century in favour of the undulating idea of light: phenomena specific to waves were observed experimentally, phenomena of interference that could not be explained by visualising light as made up of 'balls'. This led to

the theorisation of a medium in which the wave travels, the luminiferous ether. At the beginning of the 20th century, the idea of "quanta" appeared in an attempt to explain the mystery of blackbody radiation, and Einstein took up the idea to apply it to light and understand the photoelectric phenomenon. This led to the discovery of the paradox of the double behaviour of light: both a wave and a small quantity of energy, a particle: the photon. The idea of a luminous ether was abandoned. Both theories, despite their seemingly divergent foundations, elegantly explained the same experimental observations.

In his thesis[[25]], Louis de Broglie argues that the apparent conflict between the idea of light being associated with a quantum, an "atom of light," and its wave-like description can indeed be resolved. Building on the concept from special relativity that a profound connection exists between frequency and energy, he postulates 'the existence of a periodic phenomenon of an undetermined nature that would be associated with any isolated portion of energy and would correlate with its intrinsic mass according to the Planck-Einstein equation'. De Broglie thus introduces the idea of the matter wave: every material particle has a wave-particle duality, just like light.The wavelength associated with this particle is given by :

$$\lambda_{dB} = \frac{h}{p} = \frac{h}{mv} \tag{2}$$

with h Planck's constant, p , v and m the impulse, velocity and mass of the particle.

This behavior of matter can only be observed under specific conditions. If we consider a cloud of atoms at room temperature for example, the atoms can be modeled by 'marbles' and the behaviour is classical. Velocities of the atoms within the cloud follow a large distribution, reflecting their thermal motion. When lowering the velocity distribution, the temperature of the cloud decreases and the quantum wave-like behaviour appears. This cooling can be performed with methods called 'laser cooling' that will be described in Chapter 2 of this manuscript.

If this temperature is low enough, it is possible to attain a phase transition to a particular state of matter known as 'Bose-Einstein Condensate' (BEC). The cloud is no longer considered as an ensemble of individual particles but as one macroscopic quantum object.

The wave behavior of matter has enabled explained experiments such as the diffraction of electrons[[42]], but it has also opened up entirely new fields of physics. For instance, it allows us to use matter as sources for interferometry, enabling precise measurements much like we do with light.

0.2.2 Atom interferometer

In an optical interferometer, light is split into two paths and then recombined to create an interference pattern. This pattern reflects the phase difference between the two paths, allowing for precise measurements of parameters like the index of a medium or the difference in path length between the arms.

Following De Broglie's work, the same principle is applied to particles other than photons, such as atoms. In an atom interferometer, the role of light and matter is reversed: matter waves replace interfering light, and light pulses from lasers are used to split and recombine atoms instead of mirrors and beam splitters, as presented in Figure 15.
At the output of this interferometer, we can measure a quantum interference pattern: a sinusoidal pattern whose phase contains information about the accelerations experienced by the

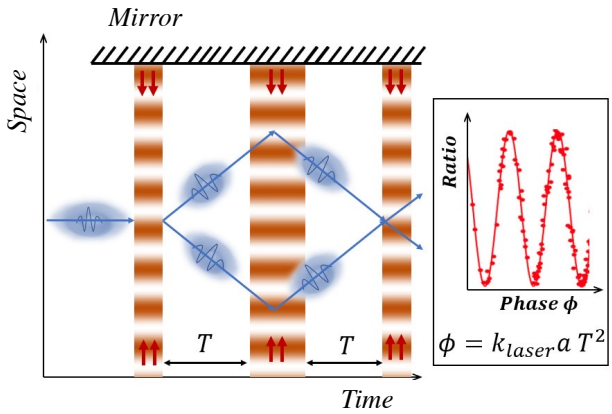

Figure 15: ***Principle of an Atom Interferometer*** *- The representation is a space-time diagram. The cloud of atoms is cooled down to create a wave packet. Three laser pulses are used to split and recombine the matter wave. This results in a sinusoidal interference pattern whose phase is proportional to inertial effects, such as acceleration.*

system.

To test the Weak Equivalence Principle, this method can be applied to two clouds of different atomic species simultaneously to compare their accelerations. The precision of the measurement increases with the interrogation time in the interferometer. To achieve high sensitivities, only space provides the long free-fall durations required.

0.3 Towards space tests with cold atoms interferometry

Utilizing a high earth orbit offers distinct advantages, including minimal vibrations and freedom from external disturbances. Space missions envisaged include gravity gradient studies (GRICE mission [[68]]) and WEP tests (STE-QUEST proposal[[1]]).

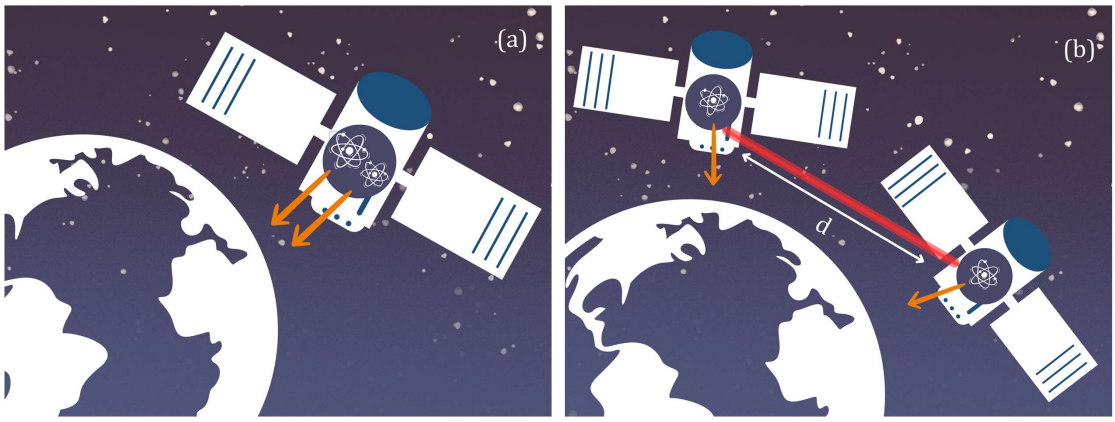

Figure 16: ***Space missions projects involving atom accelerometers*** *- (a) Principle of a WEP test space mission (b) Principle of a gradiometry space mission*

In the context of the growing interest in atom interferometry for space applications, the pathfinder mission preparation CARIOQA PMP has received fundings from European Union.

0.3.1 Gravity gradient mapping space mission

Gravity field mapping from space is a great tool for monitoring changes in Earth's mass distribution, which helps us understand various phenomena, including sea-level rise, ice sheet dynamics, and shifts in the distribution of water resources, all of which are crucial for addressing climate change and natural resource management. The GRACE (Gravity Recovery and Climate Experiment) mission [[99]] involved a pair of satellites flying in tandem 220 kilometers apart in a polar orbit, utilizing precise distance measurements between them via GPS and microwave ranging[1]. Thanks to accelerometers, the non-gravitational accelerations experienced by the satellites are rejected. Launched in March of 2002, the GRACE mission is accurately mapping variations in Earth's gravity field, providing insights into Earth's water distribution and climate changes.

To evaluate the potential of cold atom technologies on a similar space mission for geodesy and its impact on geodetic data users, CNES initiated the GRICE (GRadiométrie à Interféromètres quantiques Corrélés pour l'Espace) study [[68]]. The mission involves a constellation of two satellites orbiting at an altitude of 373 km, each equipped with a cold atom accelerometer. A laser link measures the distance between the two satellites and synchronizes these instruments to produce correlated differential acceleration measurements. The simulations indicate that this concept would yield its best performance for recovering monthly gravity fields with resolutions under 1000 km. This type of mission will benefit from the absolute aspect of atom interferometry to prevent long-term drifts in the acceleration measurement. In the resolution band ranging from 1000 to 222 km, the GRICE gradient approach demonstrates a global improvement of approximately 10 to 25% compared to the traditional range-rate approach.

0.3.2 WEP test space mission

We have established that the WEP is a fundamental cornerstone of our modern understanding of physics. To conduct experiments that could improve the current precision and potentially detect violations of this principle, we require extended periods of free fall with minimal vibration levels, conditions that can only be achieved in space. Notably, the MICROSCOPE space mission, as detailed in [[102]], has provided the most precise test of the WEP to date. A new space mission with higher-sensitivity sensors seems necessary to discover a possible violation of the principle.

The mission proposal STE-QUEST (Space-Time Explorer and Quantum Equivalence Principle Space Test) aims to test the universality of free fall of matter waves. Its goal is to test the Weak Equivalence Principle (WEP) with an uncertainty in the Eötvös ratio of less than 10^{-17}, representing a two-order-of-magnitude improvement over the MICROSCOPE measurement [[18]]. The proposal presented in 2021 [[2, 18]], employs a dual-species atom interferometer with ultracold atoms of ^{41}K and ^{87}Rb to study their relative acceleration. While the project was not chosen for further studies in 2022, efforts towards achieving the technological maturity required for such a space mission continue.

0.3.3 Pathfinder mission CARIOQA

The CARIOQA Quantum Pathfinder mission, funded under the programme Horizon Europe of the European Union aims to launch a space-borne quantum accelerometer based on chip-based rubidium Bose Einstein Condensate compatible with microgravity.
This project involves a consortium comprising 17 European partners, including laboratories and companies, with LP2N as one of the participants. The project will entail producing a

[1]The new version of this mission GRACE-FO uses lasers to perform this measurement.

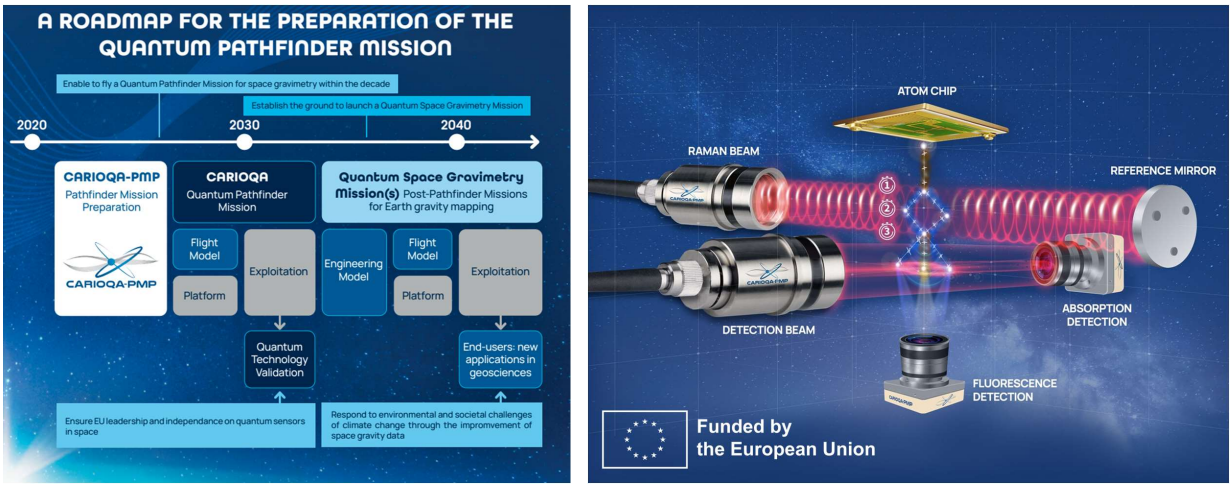

(*a*) (*b*)

Figure 17: ***CARIOQA pathfinder mission preparation program*** *- (a) Roadmap for the preparation of quantum gravimetry mission by European Union (extracted from CARIOQA PMP presentation poster) (b) Artistic view of the atom accelerometer principle (CARIOQA website)*

Bose-Einstein Condensate on an atomic chip, followed by an interferometric sequence in a microgravity regime, which will be detailed in Chapter 4. The goal is to gain one or two orders of magnitude with respect to the best gravimeters on earth.

This pathfinder mission not only paves the way for future space-based gradiometry missions but also facilitates testing the Weak Equivalence WEP in space. The involvement of the ICE experiment in this project includes an extensive study of Bose-Einstein Condensation (BEC) in space and atom interferometry in microgravity. These studies conducted on our microgravity platforms play a pivotal role in preparing the scientific foundation for such an ambitious program.

0.4 Microgravity platforms

Given the high technological maturity demanded by such endeavors, microgravity platforms serve as testbeds for upcoming dedicated space missions.

Microgravity, often referred to as zero gravity or weightlessness, is a state where the referential is subject only to the force of gravitation and no other force. On Earth, various platforms provide a microgravity environment by placing the experiment in a reference frame experiencing trajectories equivalent to free fall. In our laboratory, we have a simulator of this kind: a platform supporting the part of the experiment containing the atoms (referred to as the sensor head) is subjected to parabolic motion along the vertical axis. This three-meter-tall device is unique worldwide and allows us to access microgravity for half a second repeatedly within the laboratory space. To have access to longer free-fall time, our experiment is adapted to Novespace Zero G aircraft. We took part in two CNES Zero-G flight campaigns in March 2022 and March 2023, during which experiments and their researchers experience microgravity in an aircraft performing parabolic maneuvers.

0.4.1 Overview of microgravity platforms for atom intreferometry

In this section we provide an overview of the different ways to perform atom interferometry in a microgravity environment. A summary of the main characteristics of the European platforms is provided in Table 2.

Platform	Experiment	Freefall Duration per shot	Repetition Rate	Residual accelerations	Rotation rate
		Space			
ISS	CAL	∞	/	/	
Sounding rocket[[85]]	MAIUS	6 min	1-2 shots/year	10-1 μg	
		Ground			
Zero G plane[[15]]	ICE	22 s	93 parabola 34 min /campaign	$<$ 50 mg	5°/s
Bremen drop tower[[85]]	QUANTUS PRIMUS	4.5s 9s if catapult	1 to 3 / day	μg	
HITec Einstein Elevator[[85]]		4s	33 min/day		$<$ 8 mrad/s
GraviTower[[85]]	QUANTUS PRIMUS	2.5s	960/day 40 min/day	$\approx 100\mu g$	
Einstein Elevator in Bordeaux	ICE	0.5 s	13s duty cycle 55 min/day	$<$ 50 mg repeat. $<$ 5 mg	5 mrad/s

Table 2: ***Microgravity platforms*** *- A description of some of those platforms can be found in [[85]]*

Placing experiments in orbit offers nearly unlimited durations of free fall. For instance, the Cold Atom Laboratory (CAL), recently installed on the International Space Station (ISS), has demonstrated the achievement of quantum degeneracy [[10]]. While operating on the ISS allows human intervention through astronauts, it suffers from a noisy environment due to the large number of instruments on board and high ambient vibration levels caused by the low-altitude orbit of the ISS, which also results in high rotation rates.

The MAIUS project uses sounding rockets, offering up to 6 minutes of microgravity per launch and a maximum payload of 80 kg for the current generation of rockets. This experiment was the first to demonstrate the production of a Bose-Einstein condensate in space in 2017 [[19]]. Another version of the rockets still under development will offer up to 30 minutes microgravity for a 1000 kg payload[[85]]. Despite the usual constraints regarding robustness and compactness, the main limitation for conducting cold atom experiments on this platform is the very low number of launches performed.

The drop tower in Bremen allows the dropping of a 2.4-meter-long capsule with a diameter of 80 cm, to a height of 110 meters, providing up to 4.5 seconds of microgravity. A catapult mode allows for up to 9 s of microgravity. The experimental setup is made compact and robust to fit inside the capsule and withstand violent accelerations upon landing. This instrument has a low repetition rate, limited to a few launches per day, as it requires over an hour to prepare the tower for vacuum after each trajectory. On this platform, the QUANTUS project performs atom interferometry with ultra-cold sources on atomic chip [[78]] and the PRIMUS

project demonstrated the first evaporation in an all-optical dipole trap in microgravity [[103]].

Figure 18: ***ZARM Drop Tower in Bremen***

The recently-installed 'HiTec Einstein Elevator' in Hannover offers 4 s of microgravity thanks to a 40 m-high facility that imparts vertical parabolic motion to a capsule containing the experiment. A linear drive accelerates the gondola, which houses the integrated experimental setup, providing the required acceleration while precisely controlling its calculated motion and compensating for any rolling and air resistance during rapid movement within the building. The experiment carrier is located in a vacuum atmosphere (10^{-2} mbar) for acoustic decoupling during free fall.

A brand new microgravity platform at ZARM in Bremen called 'GraviTower' offers 2.5 s of microgravity with a repetition rate of 90 s thanks to an airtight slider which is accelerated by an hydraulic winch. Inside the slider, the experiment is free-floating to decouple from the system. The system do not require a vacuum chamber and up to 960 parabola a day can be performed. The residual acceleration during the zero gravity phase is similar to the drop tower performances. No data concerning the rotation rates or the detailed acceleration profiles have been published to our knowledge. This platform is planned to be used by the 'QUANTUS' and 'PRIMUS' German projects [[85]].

The strength of the ICE experiment lies in our convenient access to two microgravity platforms. Our partnership with CNES provides us with access to extended periods of free fall onboard the Zero G aircraft. Meanwhile, our Einstein Elevator has the highest repetition rate among these platforms and is housed within our laboratory, exclusively dedicated to our project.

0.4.2 Einstein Elevator in Bordeaux

We often refer to the Zero-G simulator as an "Einstein elevator" due to the clear analogy between its operating principle and the thought experiment by the physicist explained previously. This simulator allows us to replicate the trajectory of an object in free fall, vertically launched within Earth's gravitational field. To achieve this, the payload we want to place in weightlessness is mounted on a platform with extremely precise vertical motion control. It was designed and built by the French company Symétrie, specializing in the development of hexapods for high-precision positioning and movement. An overall view of the simulator and its various components is presented in Figure 19. This simulator was installed on the experiment during the doctoral studies of M. Rabault (see [[83]] and [[7]]).

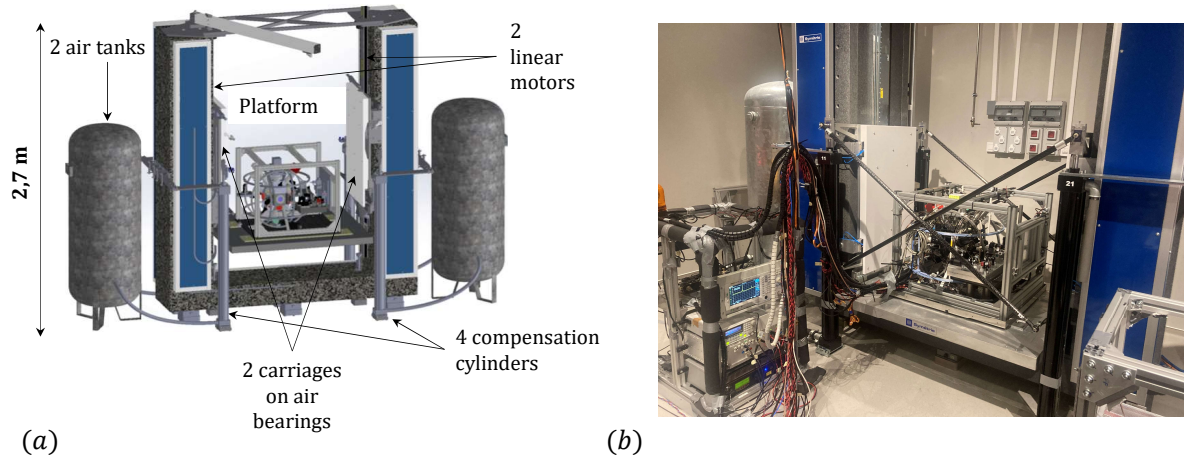

Figure 19: ***Einstein elevator in Bordeaux*** *- (a) Schematic of the structure of the microgravity simulator. (b) Picture of the simulator in the laboratory at LP2N with one of the experimental racks*

Description of the simulator

The payload, which can weigh up to 250 kg, is mounted on a platform that moves vertically between two granite columns, each measuring over 2 meters in height. The two carriages acting as an interface between the platform and the columns are not in direct contact with the granite but are embedded and guided through an air cushion system to avoid friction.

The carriages also integrate linear motors that provide their movement. The substantial force required to counteract gravity and allow the detachment of the moving mass is provided by a set of four air cylinders attached to the carriages. The pressure injected into these cylinders is delivered by a compressed air circuit, including a pressure regulator and two tanks, arranged on either side of the simulator.

This system applies a force that compensates for the weight of the moving elements (payload + platform + carriages) so that the linear motors do not have to fight against gravity and only generate the force required for the acceleration/deceleration of the moving mass. The entire assembly of the simulator and its payload weighs a total of 3900 kg and is supported by six square-shaped feet, each measuring 17 cm on each side.

It is worth noting that tracking the reference trajectory is achieved through position control, which is much more reliable and robust than acceleration control as it is not subject to drift. The granite columns incorporate micrometric rulers to determine the absolute position of the platform using optical read heads placed in each of the carriages facing them. These position measurements are used by the controller to provide feedback on the force of the linear motors and the pressure in the cylinders. Therefore, the system does not require any inertial measurements to function.

The mobile part of the simulator, consisting of the platform and the two carriages, is detailed in Figure 20. The simulator's platform is made of aluminum and has a honeycomb internal structure, giving it a reasonable mass despite its large dimensions (130 by 110 cm). It features several threaded holes, M12 and M8, on its upper surface for securing our experiment and a dedicated interface box for passing electrical cables. It's worth noting that special attention

must be given to centering the experiment on the platform. Ideally, we aim to align the center of mass of the payload with that of the platform to within a few centimeters. This proper centering is crucial as it balances the forces applied to the two carriages and prevents the risk of wear and failures.

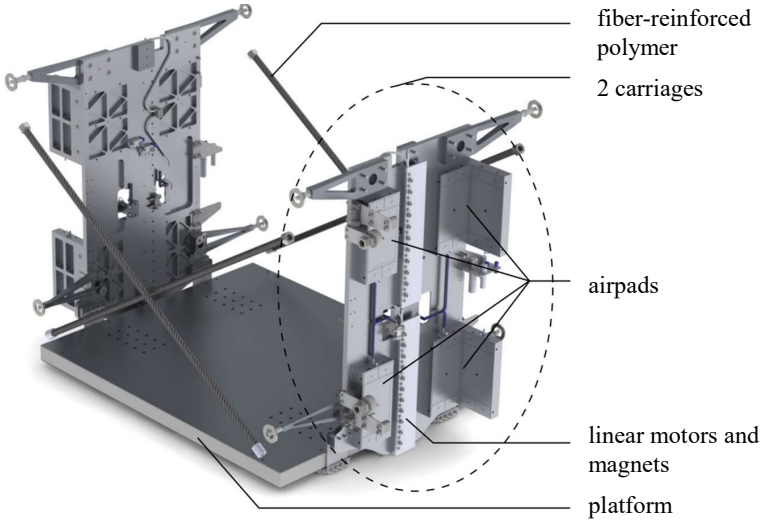

Figure 20: ***Mobile part of the simulator***

In the first version of the system, each air pad injected air around its periphery and aspirated air at its center to create a pressure/depression zone between its surface and the granite. Appropriate adjustment of the injection and aspiration rates produced an air cushion that ensures the air pad sticks within 10 µm of the granite wall, guaranteeing no mechanical contact between the carriage and the column during the trajectory and enabling frictionless sliding when everything is functioning correctly. However, these injection-aspiration pads regularly caused issues, requiring frequent adjustments, which was not convenient for long data-taking sessions. Failures in this system caused a gradual wear of the pads and the simulator's marble, necessitating a complete shutdown for an entire year during maintenance. This time allowed for an upgrade to a more reliable system by refurbishing the marble surface and adding additional pads. Instead of a "pressure-depression" system, porous pad systems placed on both sides of the marbles, forming a kind of jaw, enable frictionless guidance of the platform. This architecture has proven highly reliable, enabling hours of measurements without our intervention.

Under normal loading conditions, achieving the desired acceleration profile requires a maximum force of approximately 4500 N. This force is generated using the linear motors integrated into each of the two carriages. These motors operate within an intense and highly localized magnetic field generated by permanent magnets attached to the granite columns. When subjected to an electrical current, the motors produce a vertical translational force that can reach up to 5000 N. Generating such force necessitates the use of a high current, which can lead to an increase in motor temperature. Thus, a sufficient cooling period is necessary between two trajectories to avoid the risk of overheating. In practice, it is this cooling duration of the linear motors that fundamentally limits the simulator's cycle time to approximately 13 seconds.

The incremental rules used for measuring the position of the platform are vertically aligned along each of the granite columns. During the carriage's movement, the displacement of the optical reading head over the rule generates TTL signals, providing the platform's position with a precision of 0.5 µm. Finally, four transverse carbon fiber bars are used to connect the two carriages. These bars are not essential as the control system ensures the synchronization of both carriages' movements. They primarily serve as a precautionary measure in case of failure and

can be easily removed to facilitate access to the sensor head when the simulator is turned off. The pneumatic "compensation" system opposes the moving part's weight using four air cylinders connected to two reservoirs. A regulator adjusts the pneumatic system's pressure from the building's compressed air supply. Once activated, the regulator fills the cylinders and reservoirs until reaching around 2 bars, enabling platform lift. Afterward, the system, including cylinders and reservoirs, acts as a closed system. Maintaining stable cylinder force during movement is crucial. Carriage height fluctuations cause cylinder volume changes and pressure shifts, roughly 22 liters in total. The 1000-liter reserve volume and short pipelines reduce pressure fluctuations and minimize pressure losses caused by abrupt volume changes, ensuring force stability within 5% during movement.

Trajectories

During the weightlessness phase, the temporal evolution of the platform's position must faithfully reproduce the parabolic profile, which is the solution of the motion equation for an object solely subject to its weight:

$$z(t) = -\frac{1}{2}gt^2 + v_0 t + z_0$$

Here, v_0 and z_0 are the initial conditions for velocity and position. The amplitude of the motion $z_{0g} = z_{\max} - z_0$ and the total weightless time t_{0g} are both related to the injection velocity v_0 by:

$$z_{0g} = \frac{v_0^2}{2g}$$

and

$$t_{0g} = \frac{2v_0}{g} = 2\sqrt{\frac{2z_{0g}}{g}}$$

Here, it's noteworthy that the maximum achievable duration of weightlessness is directly determined by the amplitude of the allowed motion and varies as the square root of it. The weightlessness phase is sandwiched between two hypergravity phases: the input phase, which provides the acceleration required to reach the injection velocity v_0, and the output phase, which decelerates the motion until it reaches a standstill. The resource travel z_{res} of the resource phase is added to that of the weightless phase to form the total amplitude of the motion z_{tot}.
Figure 21 illustrates the theoretical acceleration, velocity, and position profiles used by the simulator to create 400 ms of weightlessness. Both input and output resources, symmetric in time, last 425 ms each, including a phase of constant 2g acceleration. Notably, transitions between different gravity regimes employ relatively gentle acceleration ramps to minimize jolts. The "injection" phase, which transitions from the 2g phase to 0g, lasts 125 ms and achieves an injection velocity of $v_0 = 2$ m/s. In summary, the complete trajectory encompasses an approximate 70 cm range, with associated distances for resource and weightlessness phases being approximately $z_{res} \simeq 50$ cm and $z_{0g} \simeq 20$ cm, respectively.

Various acceleration profiles can be applied depending on the desired microgravity duration. This device can also provide any gravity level between 0 and 1 g. To achieve this, one simply needs to perform a time dilation of the programmed $z(t)$ trajectory. By selecting an appropriate dilation factor, it's possible to simulate partial gravity levels encountered on the Moon (0.17 g) or Mars (0.38 g), for example. We can also choose between pre-programmed trajectories producing between 100 and 500 ms of weightlessness. Figure 22 illustrates the acceleration profiles experienced during trajectories associated with different durations of microgravity. These measurements were conducted using mechanical accelerometers mounted on the experiment. It is apparent that extending the microgravity duration to 500 ms requires a quicker attainment of

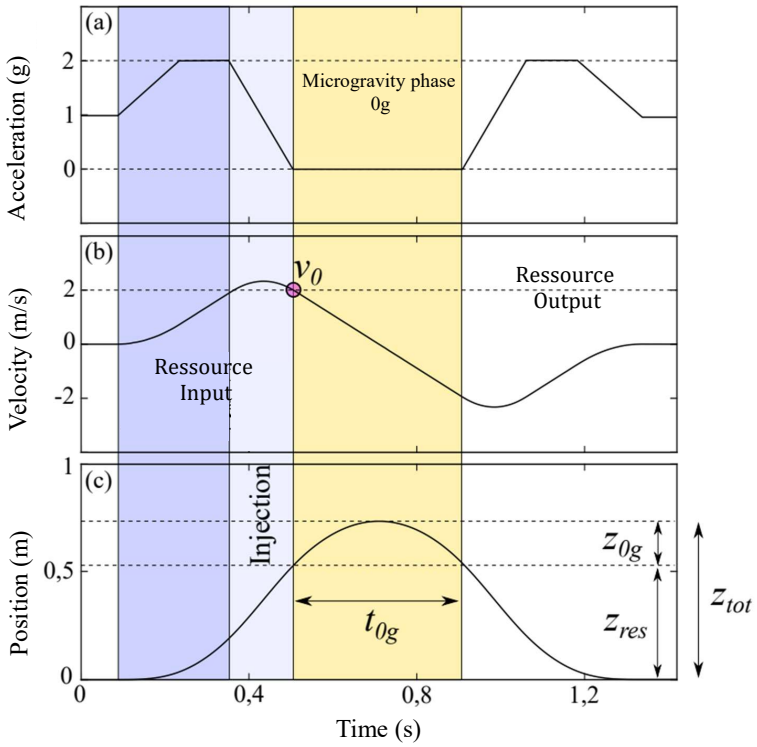

Figure 21: ***Ballistic trajectory profile on the simulator*** *- Acceleration (a), velocity (b), and position (c) profiles of a weightlessness-inducing trajectory. Three phases are discernible: the input phase, which achieves the necessary velocity for microgravity, the 0g phase (here, 400 ms), and the symmetrical output phase to the input. The injection corresponds to the phase between 2g and 0g.*

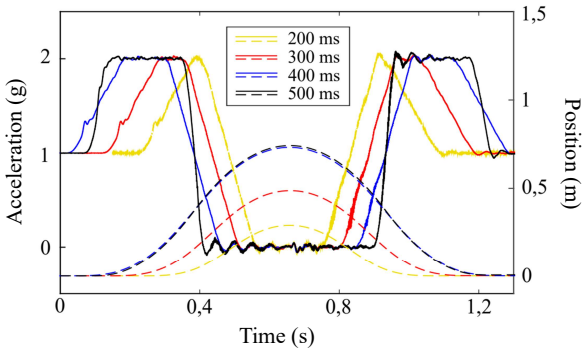

Figure 22: ***The various trajectories on the simulator*** *- Acceleration profiles measured and position profiles (calculated by integrating acceleration) of the platform with the load for different microgravity durations: 200 ms, 300 ms, 400 ms, and 500 ms.*

injection velocity, resulting in a more pronounced jolt during transition phases. This translates to more significant vibrations at the start of the 0G phase. Examining the temporal position changes for these different scenarios reveals that the total movement amplitude naturally increases with the microgravity duration.
The vibration affecting the trajectory for the one capable of generating 400 ms of weightlessness can be recorded[2] on one trajectory to estimate the simulator's performances, the results are presented in Figure 23.

[2]Using Colybris SF300L accelerometer

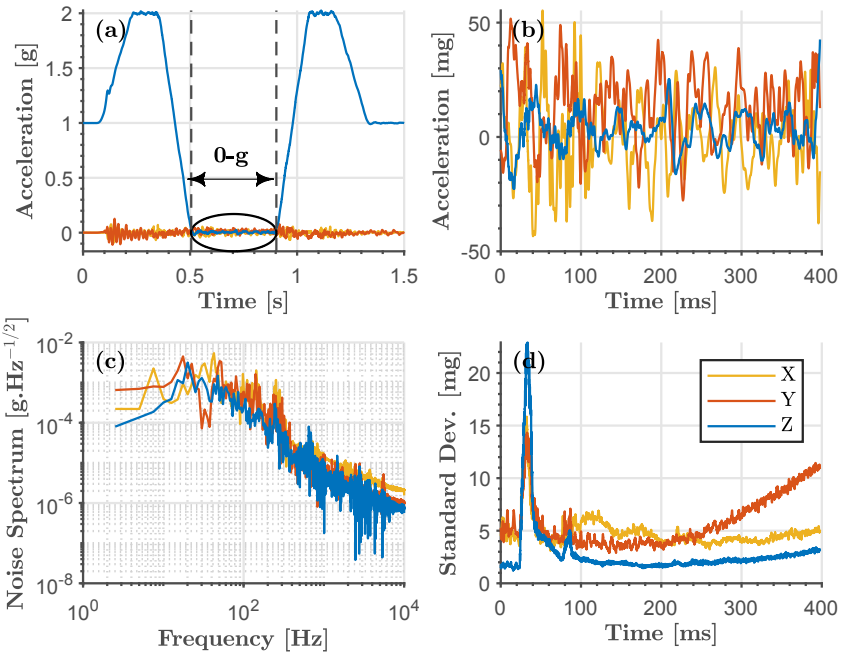

Figure 23: ***Vibrations on the simulator*** *- (a) Acceleration profiles measured with an accelerometer installed on the reference mirror for the dif ferent axes (yellow for X, red for Y , blue for Z). (b) Zoom on the residual acceleration during the microgravity phase. (c) Power Spectral Density of the acceleration profile during a parabola (d) Standard Deviation of the fluctuating component of the acceleration, calculated over a set of 300 parabolas, for each time location t of the microgravity phase.*

The average residual vibrations along the vertical Z-axis are limited to a peak-to-peak amplitude of approximately 40 mg during microgravity. The highest accelerations occur in the middle of the microgravity phase when the platform reaches the apex of its trajectory and changes direction. It's noteworthy that the accelerations along the Z-axis remain significantly lower than those measured in the transverse X and Y directions. It's also worth mentioning that vibration levels are consistently lower during the microgravity phase than during hypergravity phases. Power spectral densities associated with the acceleration signals are provided in Figure 23(c). These plots are not the result of any averaging and are simply calculated from arbitrary vibration time profiles. They give an overview of the frequency components along each of the three axes during the microgravity phase.
The random component of vibrations can be evaluated at each moment of the trajectory by calculating the standard deviation of the 300 associated acceleration measurements. The low values obtained confirm the quasi-deterministic nature of the vibrations. For example, along the vertical axis, the standard deviation remains around 3 mg throughout the microgravity phase. The peaks observed at the beginning of the trajectory are caused by high-frequency noise present in all accelerometer signals at that point in the cycle. This noise is likely due to electromagnetic disturbances caused by the linear motors.

Angular velocities about the transverse X and Y axes were recorded using fiber-optic gyroscopes[3], as presented in Figure 24. During the microgravity phase, it's observed that the residual angular velocities fall within the range of ±5mrad/s. There is still some repeatability, and once again, it's the input and output resources that come with the most significant inertial effects.

[3]KVH-DSP 1750

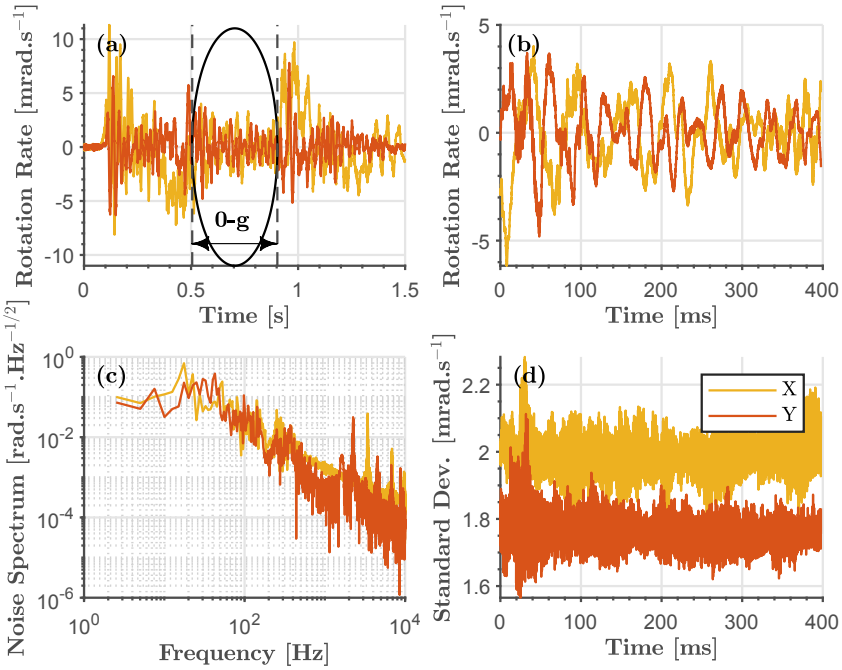

Figure 24: ***Residual rotations on the simulator*** *- (a) Rotation rate measured by a two-axis gyroscope along X (yellow) and Y (orange) during the trajectory. (b) Zoom on the rotation rates during the microgravity phase. (c) Power Spectral Density of the rotation rate profile during one parabola (d) Standard Deviation of the rotation rate, calculated over a set of 300 parabolas, for each instant t of the microgravity phase.*

0.4.3 Zero G parabolic flights

Description of a flight campaign

In addition to having a microgravity simulator in the laboratory, the experiment is intended to be conducted aboard the Zero-G aircraft, which performs parabolic flight maneuvers. Historically, this aircraft was the first microgravity platform on which the ICE experiment was operated. Traditional cold atom experiments are typically conducted within laboratories equipped with large and stable optical tables for free-space optical setups and a controlled air-conditioned environment. The extreme conditions aboard the aircraft impose specific constraints on the experimental setup, requiring it to be compact, robust, and easily transportable.

The parabolic flight campaigns are organized by Novespace, a subsidiary of CNES, on behalf of researchers selected by the scientific committees of the French space agency (CNES), the European Space Agency (ESA), and the German Aerospace Center (DLR). Flights take place aboard the A310 Zero-g aircraft departing from Bordeaux-Mérignac Airport and typically carry around ten scientific experiments. Each campaign consists of three flights, each with 31 parabolas, resulting in approximately 30 minutes of cumulative microgravity. During these campaigns, in which we took part twice within the duration my PhD, the experiment is transported from the laboratory to Novespace's hangar at the airport. The campaign lasts for two weeks and is divided into two parts. The first week involves the transportation and installation of the experiment on the aircraft. In addition to rapid setup, the experiment undergoes numerous safety checks (electrical, mechanical, etc.) by Novespace engineers and civil aviation authorities. The second week is reserved for final ground tests and the three days of flights, which take place on Tuesday, Wednesday, and Thursday mornings. The afternoons are dedicated to data analysis from the flight and addressing any technical issues encountered, as well as preparing for the next flight.

During the flight campaign, our setup remains inside the aircraft on the tarmac of the airport, exposing it to significant temperature fluctuations. The flights commence at 9 A.M., requiring us to heat the experiment and conduct final checks of its proper functioning between 6 and 9 A.M. During take-off, all experiments must remain powered off. Only after several minutes in the air, as the plane reaches its stable flight altitude, can we turn the experiment on. Thus, the entire system must become operational within a very short time frame.

To recreate weightlessness conditions aboard the aircraft, it must trace the trajectory of a free-falling object. Essentially, the aircraft enters a state resembling orbit around the Earth. Three pilots are present in the cockpit to perform the parabolas : One pilot controls the pitching, a second one controls the roll movement (to keep the wings horizontal) and the third pilot, sitting behind them, controls the engine speed (he or she also monitors the flight parameters: warnings, temperatures and pressure). The maneuver consists in serval phases decribed as follows :

- **Entry phase** : Starting from its stationary flight altitude of 6000 meters, the pilots gradually increase the speed of the aircraft to approximately 810 km/h (the maximum allowed speed of the aircraft). Then, the pilots pitch the aircraft up to reach an attitude of about 47° and an altitude of 7500 meters. During this phase, the high speed of the aircraft and the sharp curvature of the trajectory result in hypergravity of 1.8 g.

Figure 25: ***Zero G plane during the entry phase*** *- Credits : Novespace website.*

- **Parabola** : Once the 47° attitude is reached, the pilots significantly reduce the engine power to compensate for the aircraft's drag. This is referred to as the parabola injection phase. In less than two seconds, the local acceleration drops from 1.8 g to 0 g. On its way up, the aircraft continues to gain altitude, reaching the top of the parabola at approximately 8500 meters. Its speed is then 350 km/h. During this time, the pilots control the aircraft's attitude to maintain nearly zero acceleration and the roll angle to keep the wings horizontal. The aircraft is no longer subject to anything but Earth's gravity, it is in orbit: the aircraft and everything on board are in a state of weightlessness.
- **Exit phase** : After 22 seconds of weightlessness, when the aircraft reaches an attitude of -42°, it is leveled and exits its orbit. A phase of hypergravity occurs again for about twenty seconds before the aircraft returns to its initial altitude and speed.

This maneuver, summarized in Figure 26, with a total duration of one minute, is repeated 31 times during a flight, in sets of 5 parabolas separated by one minute. Each set of parabolas is spaced five minutes apart.

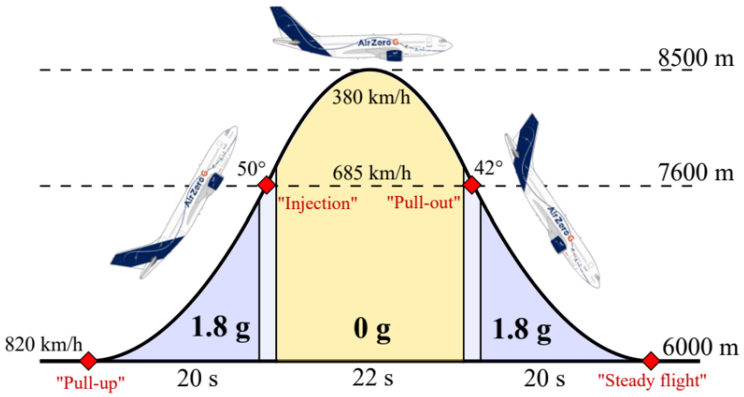

Figure 26: ***Parabolic flight*** *- Three phases follow one another, corresponding to different acceleration regimes: the entry phase, microgravity, and the exit phase. The trajectory has an amplitude of 2.5 km, and the aircraft reaches a pitch angle of 47 degree at the moment of parabola injection.*

Limitations of the platform

This platform serves as a genuine flying laboratory. The presence of operators on board the plane, with the ability to adjust parameters in real-time, presents a significant advantage. Nevertheless, this platform also has its limitations.

One of the main challenges associated with operating a complex atom interferometry experiment during flights is the limited time available during and between parabolic maneuvers. The total duration of our experimental sequence typically ranges from 1 to 3 seconds, depending on the desired temperature regime. During the cumulative 600 seconds of microgravity provided by a parabolic flight, we can perform only a few hundred experimental measurement points at most. The experimental sequences are prepared in advance, and very few adjustments are made during the flights to avoid errors due to the urgency of the moment.

The cabin temperature is not regulated overnight and can drop below 0°C during winter campaigns. Care must be taken when restarting equipment in the morning and sufficient warm-up time should be allowed. However, these large temperature variations put significant stress on components and inevitably increase the risk of damage and failures. During the flight, the cabin temperature is maintained between 17 and 20°C. However, it's worth noting that thermal convection phenomena disappear in a microgravity environment. As a result, the thermalization of heating elements is less efficient, leading to an increased risk of overheating. For this reason, special attention is given to the mechanical ventilation of critical equipment and the addition of heat sinks.

Finally, the inertial effects of the aircraft (residual vibrations and rotation rates) pose a significant challenge for conducting high-sensitivity measurements.
Typical vibration rates of $\sigma^{vib} \approx 40$mg can be measured during the microgravity phase. This vibration level is comparable to that of the microgravity simulator, but the simulator exhibits high repeatability with a standard deviation in the vibration pattern inferior to 5mg from one shot to another.

Due to the trajectory of the plane, large rotation rates of approximately $5° \cdot s^{-1}$ occur during the microgravity phase. They are presented in Figure 27 (b). This represents a significant limitation for performing atom interferometry onboard the plane.

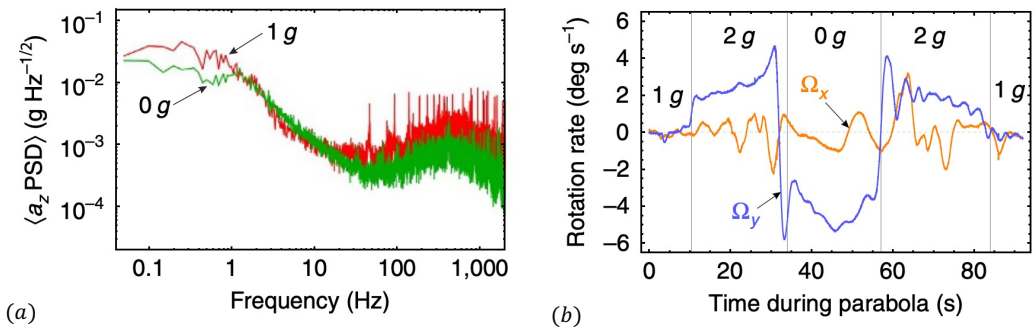

Figure 27: ***Vibrations and rotations on the Zero G plane*** *- (a) Mean power spectral density of vibrations along the z axis of the aircraft during* $1g$ *and* $0g$*. The standard deviation of the vibration noise spectrum is* $\sigma_{vib} \approx 0.055g$ *during* $1g$ *and* $0.038g$ *during* $0g$*. (b) The rotation rates about the x axis (orange line) and y axis (blue line) of the aircraft during a parabola, where* $|\Omega_y| \approx 5°.s^{-1}$ *during parabolic maneuvers. Figure extracted from [[15]].*

Conclusion

The utilization of quantum accelerometers, along with their recent technological advancements, has not only paved the way for groundbreaking fundamental physics experiments but has also significantly enhanced our capabilities for Earth monitoring, particularly in the context of climate studies, marking a profound and far-reaching impact on scientific research and understanding.

The ICE experiments serve as a demonstrator for future space missions, facilitating not only feasibility studies for precise WEP tests but also the technological advancement of portable quantum accelerometers. Specifically, significant progress has been made in developing robust laser sources based on fiber optics technologies over the past decade, and this work has played a crucial role in transferring technology to the company eXail, now a leader in quantum inertial measurements and laser sources for atomic physics experiments. During my PhD journey, I contributed to the development and integration of new fibered laser sources for potassium and rubidium and made enhancements to the experimental setup. We also conducted extended time-of-flight interferometric measurements on the microgravity simulator and achieved the first ultra-cold sources aboard the Zero G aircraft.

This manuscript will detail the collaborative efforts of the ICE team and myself during these three years at the LP2N laboratory in Bordeaux. The first chapter will introduce the complex and transportable experimental setup I worked on. The second chapter will focus on the theoretical background and practical realization of cold and ultra-cold sources of rubidium and potassium, both on the ground and on our microgravity platforms. Subsequently, we will delve into the performance analysis of our interferometer under standard gravity conditions. While the experimental setup is designed for dual-species inertial measurements, my PhD primarily utilized rubidium. Chapter 4 will highlight the achievement of atom interferometry in microgravity, a significant outcome of this thesis. Finally, the last chapter will offer a forward-looking perspective, exploring the potential of the ICE experiment to conduct a WEP test on the microgravity simulator, capitalizing on its exceptionally high repetition rate.

Chapter 1

Experimental setup

Introduction

This chapter presents the experimental setup on which the thesis work was carried out. This device is the result of more than a decade of work, and I contributed to its evolution during my thesis. The ICE experiment is a transportable cold atoms experiment designed to withstand harsh environments such as the Zero G plane. It consists of a sensor head where measurements are performed on the atoms, laser systems, and the necessary electronics for precise control. The laser sources are based on fiber optics telecom technologies with frequency doubling, which imposes constraints on the choice of the atomic species we manipulate. Rubidium-87 and potassium-39 were selected as the test masses for testing the Weak Equivalence Principle (WEP) due to their two-fold difference in mass, but more importantly, because of their favorable atomic transitions. The rubidium D_2 transition corresponds to a wavelength of 780 nm, which can be addressed using frequency-doubled fibered laser diode systems operating at 1560 nm (which belongs to the telecom band). For potassium, two wavelengths are required at the D_1 and D_2 transitions at 767 nm and 770 nm, respectively. These wavelengths are sufficiently close to each other, allowing us to use the same fiber and free space optical systems for both atomic species.

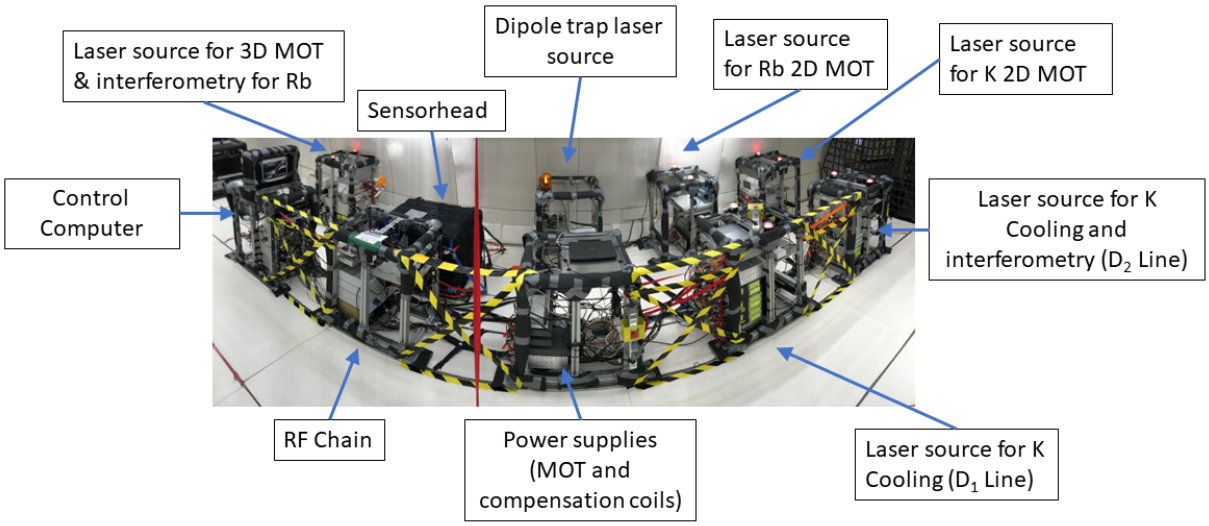

Figure 1.1: ***Full experimental setup onboard the Zero G aircraft during the flight campaign in March 2022***

In order to meet the requirements linked to the Zero G flights, the different elements of the experiment are distributed in 10 different racks built under aeronautical safety constraints. The same experimental set up is operated in the laboratory on the microgravity simulator.

1.1 Laser sources

To trap, cool, manipulate, and interrogate atoms, we rely on the atom-light interaction, which requires the use of several lasers. The laser sources play a critical role, and over the years, significant technological advancements have been made to produce compact, transportable, and robust systems. The highly perturbed environment of the aircraft requires the implementation of particular solutions to cope with these experimental conditions. The laser system, which is very sensitive to temperature variations and vibrations, is the first to be impacted and can thus be subjected to power and frequency fluctuations or even misalignments (fiber injections) in the case of free-space benches. Historically, it was decided to use a laser architecture based on fibered telecom technology and frequency doubling. This solution provides a good alternative to free-space extended cavity diode lasers (ECDL), whose free-space alignment is sensitive to vibrations and thermal variations, especially for embedded applications. For splitting and combining laser lights, micro-optical benches were designed and built with the company Exail (formerly Kylia) to guarantee a high stability of the optical powers even with vibrations and temperature drifts.

This section details the six lasers used in the rubidium and potassium experiment and their architectures, containing more than 10 laser diodes.

1.1.1 Performances

Executing the experimental sequence demands a high degree of tunability from the laser sources, particularly those involved in both cooling and interrogation. Figure 1.2 illustrates the required frequencies for these sources.

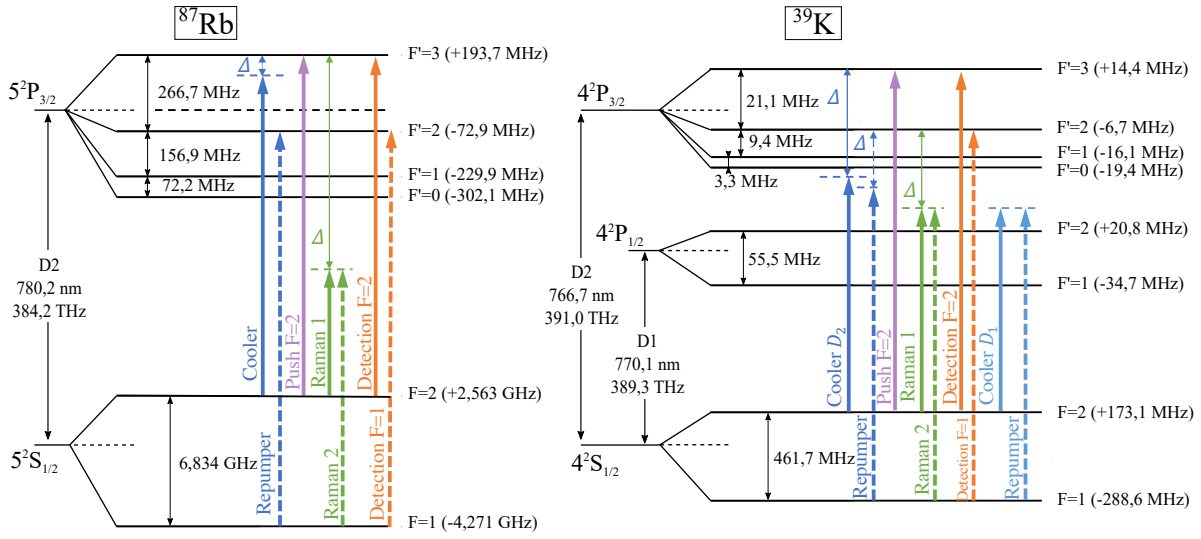

Figure 1.2: ***Internal structure of rubidium*** ^{87}***Rb and potassium*** ^{39}***K*** *- The different frequencies necessary to the experimental sequence are presented [[96, 101]]*

In total, six laser sources are used in the experiment, as shown in the functional diagram in Figure 1.3 :

- 3D MOT cooling and interrogation of the rubidium atoms (referred as "Rb 3D MOT laser")
- 2D MOT for rubidium (referred as "Rb 2D MOT laser")

- 3D MOT cooling and interrogation of the potassium atoms on the D_2 line (referred as "K D_2 laser")
- 3D MOT cooling of the potassium atoms on the D_1 line (referred as "K D_1 laser")
- 2D MOT for potassium (referred as "K 2D MOT Laser")
- Dipole trap (same for potassium and rubidium)

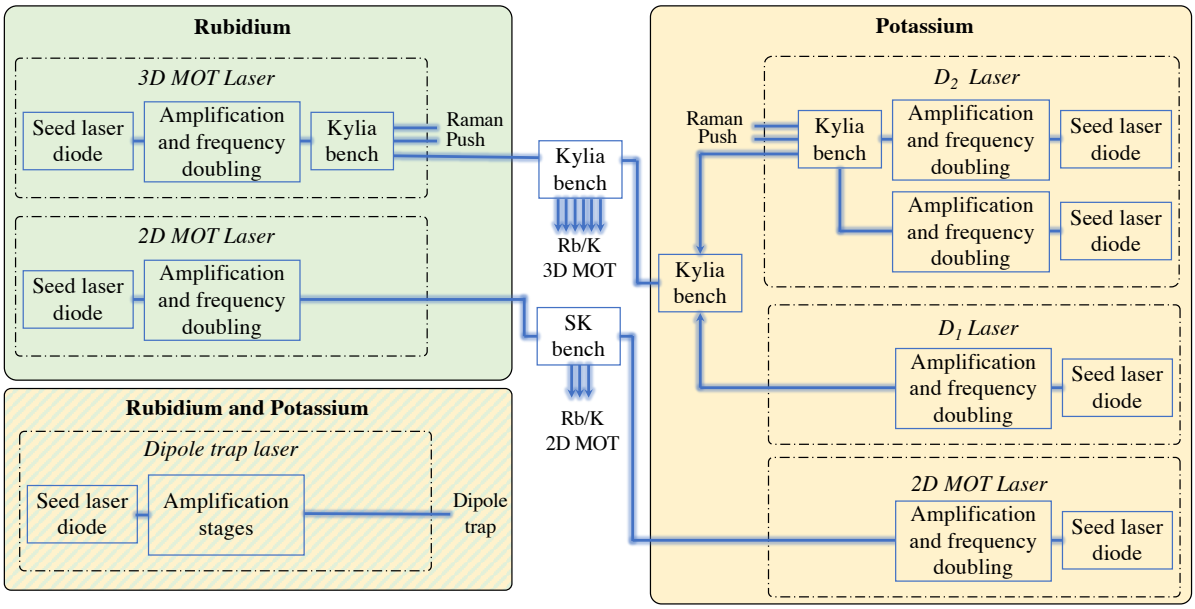

Figure 1.3: ***Functional diagram presenting the six laser sources used on the ICE experiment*** *- The lasers are presented with their function and a simplified view of their architecture. SK: Schäfter-Kirchhoff*

The specifications for each laser are described in the table 1.1.

Laser source	Wavelength (nm)	Detuning Δ (MHz)	Linewidth	Optical power	Power stability
Rb 3D MOT laser	780	0 to -1200	20 kHz	300 mW	1 mw
Rb 2D MOT laser	780	-18	1 MHz	300 mW	$\sim$ 1 mW
K D_2 laser	767	0 to -1260	$\sim$ 1 MHz	300 mW	$\sim$ 1 mW
K D_1 laser	770	0 to 20	$\sim$ 3 MHz	200 mW	$\sim$ 1 mW
K 2D MOT laser	767	-40	2 MHz	200 mW	$\sim$ 1 mW
Dipole trap	1550	/	500 kHz	23 W	1%

Table 1.1: ***Performances for laser sources*** *- The references of the lasers are described in the paragraph 1.1.1 and figure 1.3*

1.1.2 Laser systems for rubidium

We present in the following the rubidium laser system architecture that was integrated by a previous student [[83]]. Our fiber laser architecture for the ^{87}Rb D_2 line, referred as "Rb 3D MOT laser" is divided in two rack boxes. The first stage, known as the "low-power", ensures frequency and phase locking of the different laser beams used during the interferometric sequence. The wavelengths used in this stage are in the telecom C-band, and the optical powers are limited to a few tens of milliwatts at most, which explains its name.

To simplify and make the experimental setup more compact, we use a single laser system for all the steps of our sequence. During the sequence, it is necessary to successively address the different atomic transitions presented in Figure 1.2, and deliver dynamically tunable optical frequencies. In addition to the usual requirements in terms of frequency precision and stability, this first stage must also satisfy important agility constraints. Typically, the output frequencies must be able to be detuned by several hundred megahertz in a few milliseconds. This stage is composed of three laser diodes : a master diode and two slave lasers.

A second "amplification and doubling" stage allows, as the name suggests, for amplification and dynamic control of the optical powers while performing frequency doubling to transfer telecom wavelengths to the visible/near-infrared domain where the atomic transitions occur.

Finally, a third and last "beam combining and splitting" stage is used to dynamically route the laser beams to the different optical accesses we have, respectively dedicated to "MOT", "Raman", and "Push" beams.

The addition of the 2D MOT source made it necessary to use an additional laser, that will also be presented in this section.

Low power stage

The low power stage is a commercial product from the company Exail (formerly MuQuans), it constitutes one of the two 3U element of our laser. Its architecture corresponds to the light blue part in the Figure 1.4.

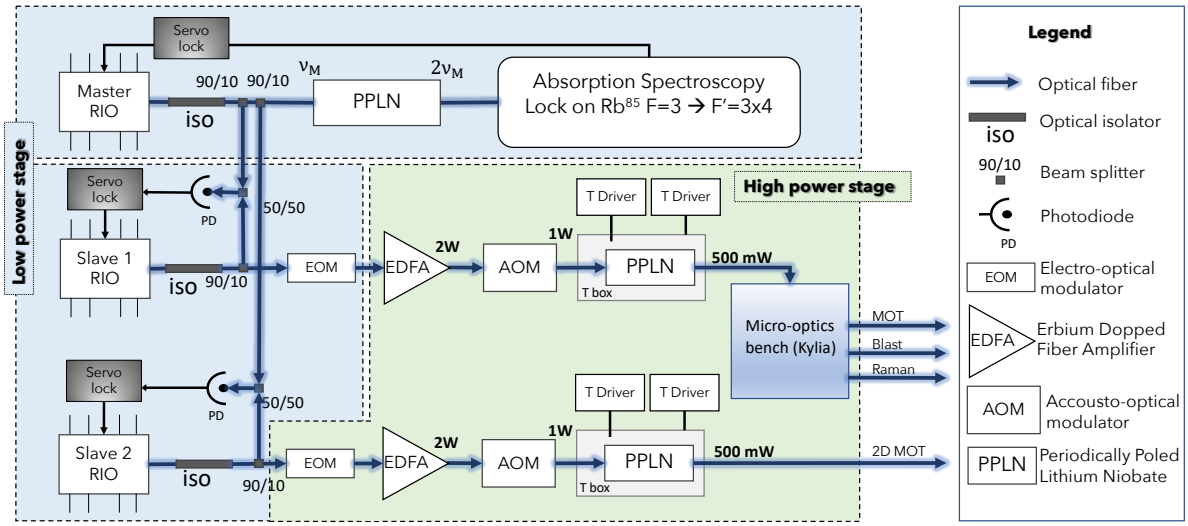

Figure 1.4: ***Architecture of the low and high power stages of the laser for the D_2 transition of rubidium*** *- The light blue part (low power stage) is the MuQuans commercial part, the light green part is the home-made high power stage*

The first stage relies on a Master-Slave architecture comprising three laser sources. The Master diode, locked on an atomic transition, delivers a fixed reference frequency. The output frequencies of the two Slave diodes are phase-locked to the Master frequency. The diodes used in this setup are all from the RIO Planex series and are external cavity lasers (ECDL) with a planar lightwave circuit that includes a Bragg grating. This structure has several advantages over the competing technology of distributed feedback (DFB) lasers, including extremely nar-

row linewidth (typically 15 kHz) and very low phase noise. The lasers emit a single longitudinal mode at a wavelength centered around 1560 nm. The output frequency and power (typically between 10 and 20 mW) can be finely adjusted via temperature or injected current. Temperature control is achieved using an integrated Peltier module, and the diodes are isolated from thermal fluctuations by being placed in temperature-controlled enclosures. Each diode's output is protected from accidental power feedback by an optical isolator. The Master laser's output frequency is first doubled and then frequency locked using a free-space saturated absorption setup containing a rubidium vapor cell. The Slave diodes are phase-locked to the Master (in our case, a frequency lock is sufficient but the commercial system includes only phase-locking electronics). The Master-Slave beat frequencies required for these phase-lockings are obtained by taking a small part of each diode's output and recombining them using fiber components (splitters and couplers). The beat frequencies are sent to phase-locked loops (PLLs) that provide fast feedback on the currents of the Slave diodes. The PLLs also take in radio-frequency signals, which are the set points for the phase-locking, provided by our RF Chain (see section 1.3). As the PLLs have a limited operating range, frequency dividers have been chosen so that the the output frequencies are within the range of interest for the application. When the feedback loop is activated on the "Slave 1" channel, for example, there is a factor of 16 between the beat frequencies and the set point frequency ($f_{beat1} = 16 \times f_{ref1}$). The set point radio frequency f_{ref1} can be anywhere in the range [22 - 65MHz], which offers an agility of 688MHz for the Master-Slave 1 beat frequency, which must be within the range [352 - 1040 MHz]. On the Slave 2 channel, the same locking loop electronics have been installed to use it as the 2D MOT laser.

Finally, it should be noted that Slave 1 and Slave 2 can be phase-modulated through an Electro-Optic Modulator (EOM) with a bandwidth of 12 GHz. For Slave 1, the modulator is integrated to the low power stage and is currently used to generate the sidebands used in our sequence, such as the Repumper frequency at 6.58 GHz or the second Raman frequency at 6.834 GHz. The radio frequency sent to this modulator is directly delivered by the RF chain, which will be presented in detail in section 1.3. It should be recalled that in the case of phase modulation, the sideband is inherently phase-locked to the carrier. The notable disadvantage of this technique is the creation of sidebands at multiples of the RF frequency, which give rise to parasitic interferometers [[28]] introducing an undesirable interferometric phase shift. A phase modulator for Slave 2 generates the repumper for the 2D MOT as well. The radiofrequency of 17 dBm at 6.58 GHz is delivered by a fixed generator from the company Noise XT.

Our system comprises an industrial-grade laser that offers exceptional performance in terms of reliability, stability, agility, and ease of use. Over a characteristic period of 24 hours, the standard deviation of the optical frequency fluctuation is around 20 kHz. The linewidths of each Slave have been measured to be less than 20 kHz with the phase-locked loops, while the settling times of the locks are around 50 µs, regardless of the amplitude of the setpoint jumps. Furthermore, the Master frequency lock has the advantage of being achieved completely automatically: the software installed by MuQuans performs an initial scan of the Master laser frequency, locates the relevant peak in the saturated absorption profile, and then locks onto it during a second scan.

High power stage

The high power stage is presented in light green in the Figure 1.4.

This stage contains two identical paths, associated with the Slave 1 and Slave 2 diodes. Each path is then amplified in a Erbium-Doped Fiber Amplifier (EDFA) from Keopsys[1], delivering 2W of output power. The output of each EDFA is then sent to a fiber-coupled acousto-optic

[1]Keopsys, CEFA-C-PB-HP series

modulator[2] , which acts as a variable power attenuator. Each AOM is driven by a controller capable of generating up to 2.5 W of RF power at an 80 MHz frequency. However, this controller is not housed inside the rack box for thermal reasons; instead, it is located in a dedicated 3U structure that also houses the power supplies for the various components of the high-power stage. The optical power at the output of the AOM can be dynamically controlled by an analog voltage sent to its driver. This AOM model has an insertion and diffraction loss of 3 dB, allowing for a maximum output power of 1 W.

Each path terminates with a frequency-doubling nonlinear crystal that converts 1560 nm to 780 nm. These are made of periodically poled lithium niobate (PPLN) crystals on which an optical waveguide is printed[3]. The conversion efficiency depends on the incident optical intensity and the phase-matching quality between the crystal periodicity and wavelength. Thus, temperature regulation of the PPLN is necessary to maintain the operating point around the phase matching and maximize conversion efficiency. Therefore, each PPLN has a dedicated Peltier module and thermistor for precise crystal temperature regulation. The PPLN is mounted on an aluminum base with a thermistor and Peltier module, which is then integrated into a housing[4] to thermally isolate it from the environment and provide a second level of temperature regulation. The architecture of the Delrin housing and the result of a test concerning the temperature lock are presented in Figure 1.5.

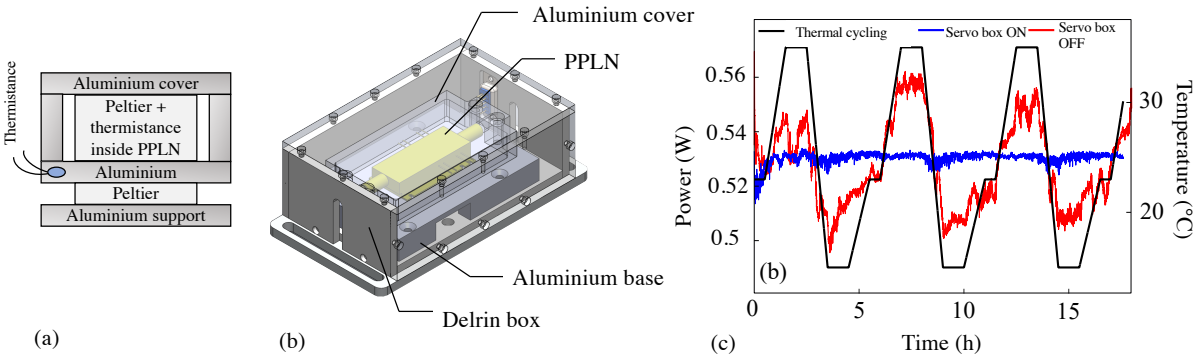

Figure 1.5: ***PPLN housing and performance of the temperature regulation*** *- (a) Schematic view of the PPLN box (side view). The temperature regulation is ensured by two servo-lock loops : one uses the Peltier and thermistance present inside the PPLN packaging, we add the second using an additional Peltier and a thermistance that is placed in a cavity inside the aluminium plate (b) Internal view of the housing allowing temperature control of the PPLN. The component is mounted on an aluminum base, underneath which a Peltier module and a thermistor are integrated. The aluminum cover and Delrin housing provide improved isolation of the system from environmental temperature fluctuations. (b) Results of power stability tests performed under thermal cycling (black) with (blue) and without (red) temperature control of the housing.*

Temperature control of the two PPLNs and their respective housings is provided by temperature controllers[5]. The efficiency of these housings was demonstrated by previous researchers in oven

[2]Gooch & Housego, Fiber-Q series, T-M080-0.4C2J-3-F2P
[3]NTT Electronics, WH-0780-000-F-B-C model
[4]Delrin material: polyoxymethane polymer
[5]Wavelength Electronics, model PTC2.5K-CH

tests, limiting power fluctuations to less than 1% even under significant variations in ambient temperature (between 5 and 35°C) [[83]].
Although the manufacturer specifies a maximum input power of 250 mW, these PPLNs can practically withstand 1 W with good stability, allowing for output powers of up to 500 mW at 780 nm.

Beam Combining and splitting

The third and final stage of our architecture is used to distribute the optical powers among the three physical output paths dedicated to the "MOT", "Raman", and "Push" beams, respectively. It was originally designed to also combine the light of the two lasers but due to the use of the slave 2 for the 2D MOT, the second input of the combiner is not used. This combining/splitting function is performed in free space within a micro-optical bench designed by Baptiste Battelier and built by Exail (formerly Kylia). All of the optical components that make up this stage are glued onto a glass substrate to limit the risk of misalignment due to vibrations. The glass also has a low thermal expansion coefficient (4×10^{-6} K^{-1}), giving the bench good robustness against temperature fluctuations.

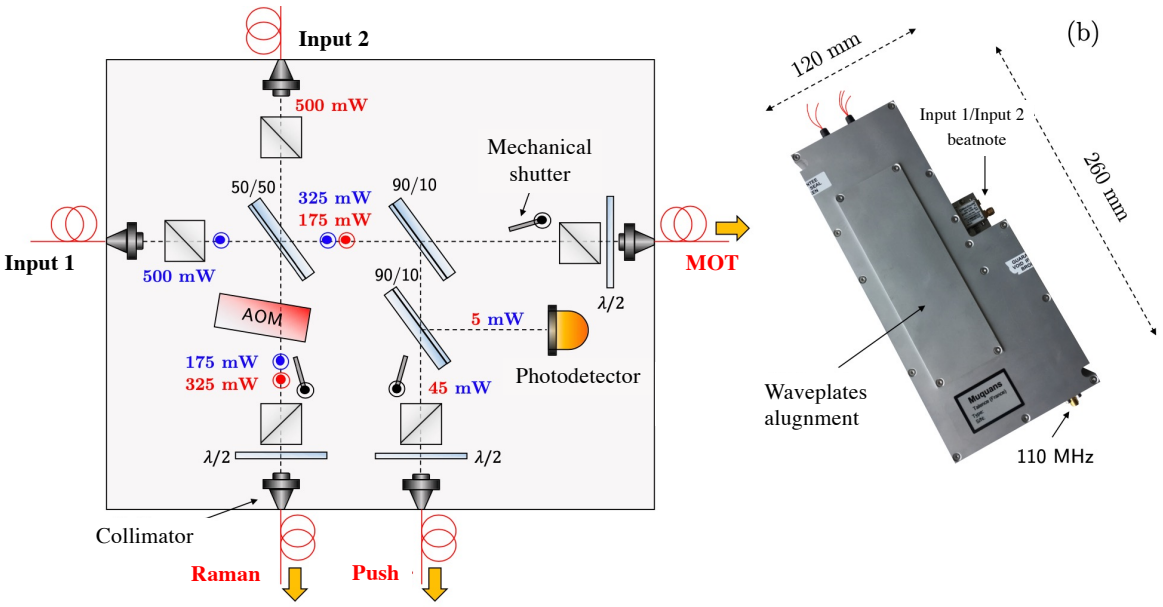

Figure 1.6: ***Micro-optical bench for combining and splitting****- (a) Schematic and (b) picture of the Kylia micro-optical bench that combines two fibered inputs and splits them into three beams that are then reinjected in polarization maintaining optical fibers*

The schematic diagram of the bench is shown in Figure 1.6. On each input path (the slave 1 laser diode light is injected in Input 1, the input 2 is not currently used), the polarization is first filtered by two polarizing cubes. A non-polarizing 50-50 beam splitter is then placed at 45° to each beam to separate the power of each path into two and thus recombine the two frequencies. Each output arm then contains both frequencies in the same polarization state. The first output arm, corresponding to the Raman path, then passes through a free-space AOM[6] controlled by a 110 MHz radio frequency. The -1 diffraction order at the output of this AOM is collected, while the 0 order is directed to a beam dump. This AOM meets the need for extremely rapid switching on and off of the optical power during a Raman pulse. In the other path, the beam

[6] AA Opto Electronic, model MT110-B50A1-IR

is sent to a 90-10 beam splitter, allowing 90 percent of the power to be transmitted to the MOT path and reflecting the remaining 10 percent to the Push path. Finally, a last 90-10 beam splitter on the Push path directs a small portion of the optical power to a photodiode delivering a Input 1/Input 2 beatnote signal. As the beatnote is now performed after doubling (at 780 nm), we use a wideband MSM-type photoconductor (Hamamatsu G4176-03) fed via a bias tee. Mechanical shutters are also present in front of each output collimator. Their opening/closing time is 100 µs, and there is a delay of approximately 2 ms between the digital signal being sent and their effective switching. On the MOT and Push paths, these shutters act as switches to turn the beams on or off. On the Raman path, the mechanical shutter complements the AOM to ensure complete extinction of the parasitic light. The extinction ratio of the AOM we use is approximately 50 dB, which is not sufficient if we wish to avoid any disturbance of the atoms during the sequence. A polarizing cube and a half-wave plate have been placed behind each shutter to allow for adjustment of the output polarization if necessary. This system allows for a significant reduction in optical power losses compared to fiber-based combining and splitting systems. The optimization of opto-mechanical systems also enables low coupling losses between free space and optical fibers, with high robustness against vibrations and thermal fluctuations: no realignment is necessary once the system is in place.

After reinjection into the output optical fibers, the Raman and Push beams are directly directed to their respective collimators, while the MOT path is directed to another micro-optical bench allowing for the combination with the potassium lasers and the distribution of power over the 6 optical access ports of the MOT-3D. This bench is described in section 1.1.3.

1.1.3 Laser systems for potassium

While the internal structure of potassium is similar to rubidium, its hyperfine splitting is significantly smaller (461 MHz), which requires different techniques for cooling and manipulating potassium atoms. This section presents the three lasers required for potassium cooling. The first laser addresses the D_2 line of potassium with a similar architecture to the one described above for rubidium. The second laser addresses the D_1 line, allowing for lower temperatures in the cloud using gray molasses techniques that will be detailed in section 2.3. The final laser is dedicated to the 2D MOT.

Laser for the D_2 transition

The laser architecture for the potassium D_2 line is very similar to that of rubidium. It consists of the same three stages and uses the same components as presented in section 2.2.1, except that they operate at a wavelength of 1534 nm (resp. 767 nm) instead of 1560 nm (resp. 780 nm). The architecture is all-fiber and it was built by the previous PhD student Romain Arguel and an extensive description of this laser is presented in his thesis [[7]]. A schematic view of the laser architecture is presented in Figure 1.7.

Once again, the low-power part is based on three RIO Planex diodes[7] organized in a Master-Slave type architecture. These three diodes are temperature and current-controlled by low-noise electronic cards that were developed as part of the Miniatom project. The Master diode is once again locked to an atomic transition through a saturated absorption spectroscopy setup. Due to the hyperfine splitting of 461 MHz, it is not possible to generate the second Raman frequency through a phase modulator as we do for rubidium. This would create a large number of extremely close frequency spurious lines that would greatly disturb our interferometer and laser cooling. We thus use two slave lasers phase-locked to the master laser to generate those two

[7]Master: RIO 0195-5-01-1-I7; Slave 1: RIO 0195-3-01-1-I7 , Slave 2: RIO 0195-3-01-1-I7

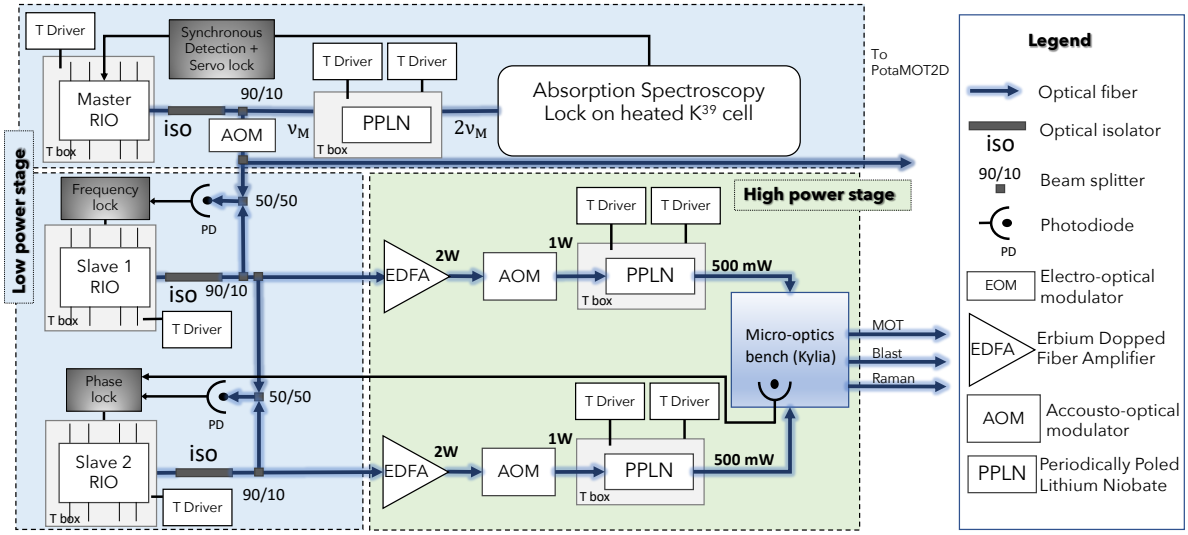

Figure 1.7: ***Architecture of the low and high power stages of the laser for the D_2 transition of potassium*** *- The light blue part is in a first low power stage rack box, the high power stage is in a separated part*

frequencies.

The frequency stabilization of a master diode is achieved through a saturated absorption spectroscopy setup, where a potassium cell is heated to 60°C to observe absorption lines. The atomic transition between the crossover of the ground level and the excited level is used as it corresponds to a sufficiently strong line on which it is possible to lock ($|F = 1 \times 2\rangle \rightarrow |F'\rangle$). The saturated absorption profile with the corresponding transitions is presented in Figure 1.8. We observe that the hyperfine structure of potassium D_2 transition is not resolved for the F' level by saturated absorption, because the splitting between the levels is too small (see Figure 1.2).

The slave diode frequency is servo-locked on the master laser frequency using a frequency divider, frequency-to-voltage converter (CFT), and a Proportional-Integral (PI) type controller. The frequency servo-lock works correctly for any beatnote within the input range of the CFT, which extends from approximately 300 MHz to 1 GHz. The low-power stage includes a second Slave diode, which is phase-locked to Slave diode 1 using a commercial electronics system[8]. The feedback on the diode current is directly done on the fast modulation pin of the RIO diode, and the PLL output voltage is converted into current via a resistor placed in series with the RIO diode. The phase locking box compares two signals corresponding to the beatnote and the reference radiofrequency in relative phase. The output signal is sent to a Proportional-Integral-Derivative (PID) type regulation stage. To optimize the phase stability between the two laser frequencies interacting with the atoms, the Slave 1-Slave 2 beatnote has to be measured as close to the atoms as possible, ideally at the end of the chain. We use a beat photodiode integrated into the Kylia micro-optical bench for this measurement. This servolock after doubling is not trivial because of the large optical path before the measurement, and also because of possible power fluctuations due to the frequency doubling. To maintain lock under all circumstances, the laser contains a second Slave 1-Slave 2 beat photodiode in the low-power stage before frequency doubling and passage through the attenuation AOMs, to have a more stable optical power. We switch from one beatnote to the other during the experimental sequence using a RF switch,

[8]Vescent Photonics, model D2-135

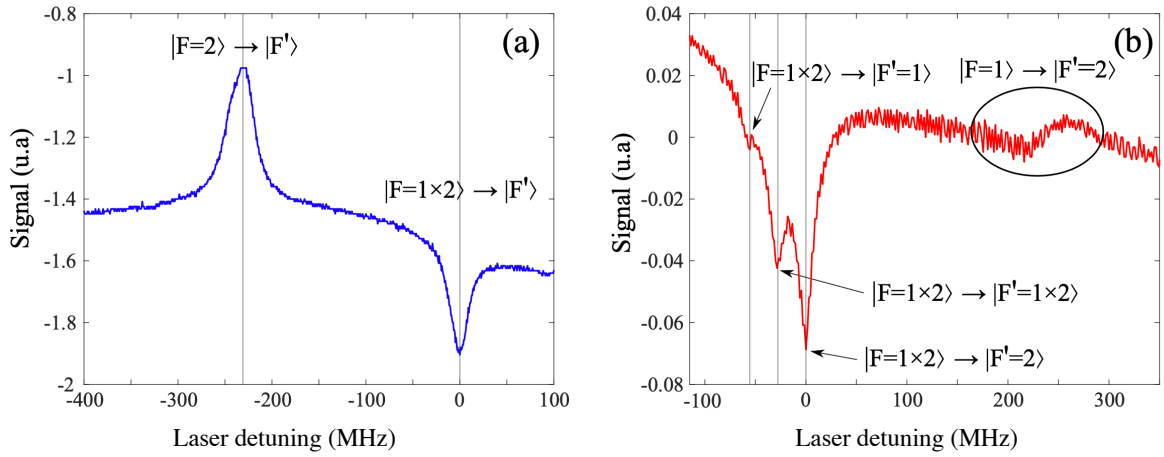

Figure 1.8: ***Saturated absorption spectra of*** D_2 ***(a) and*** D_1 ***(b) transitions of K*** *- Spectra opbtained for potassium cells heated at 60°C. We observe that the hyperfine structure of potassium* D_2 *transition is not resolved for the F' level by saturated absorption.*

controlled by the a digital signal. Two possible setpoints radiofrequencies are provided by the RF chain around 28 and 58 MHz (see section 1.3), another RF switch enables to choose between the two signals, respectively associated with the pre- and post-doubling beat signals.

The two slaves are sent to two distinct 2W fibered amplifiers[9] that are integrated to the laser box. Two fibered AOM[10] enable for the dynamic control of the optical power sent to the fibered PPLNs[11]. The high power combining of the two slaves and the splitting between the three path (MOT, Raman and Push) is ensured by a micro-optical bench that is the exact replica of the one described in section 1.1.2.

Laser for the D_1 transition

In order to improve the cooling of potassium atoms, a laser tuned to the D_1 transition of potassium at 770 nm was added. The use of gray molasses techniques allows for temperature reduction and improved loading into a dipole trap. The corresponding laser source was constructed by a former student [[6]], and its architecture is similar to previously described lasers and is fully fibered. A schematic diagram is presented in the Figure 1.9.
This laser system also relies on a Master-Slave architecture, which consists of two RIO Planex diodes emitting at 1540 nm. Most of the master's power is sent to the saturated absorption spectroscopy setup, while a small part is taken to generate the beatnote with the Slave. The typical spectrum obtained when heating the cell around 60°C is shown in 1.8 (b). The master frequency is servo-locked on the transition $|F = 1\rangle \rightarrow |F' = 2\rangle$. The slave laser frequency is servo-locked on the master frequency in the same way as for the D_2 laser, using a beatnote photodiode, a frequency-to-voltage converter, and a PI controller. The second laser frequency sent to the atoms is generated by a phase modulator that produces the 461 MHz sideband from a radiofrequency signal from our RF chain. The generation of unwanted sidebands is less problematic here, as unlike the D_2 laser, the D_1 laser is not used during Raman pulses of the atom interferometer. At

[9] Keopsys EDFA : CEFA-C-PB-HP series
[10] Gooch and Housego T-M080-0.4C2J-3-F2P
[11] NTT Electronics WH-0767-000-F-B-C

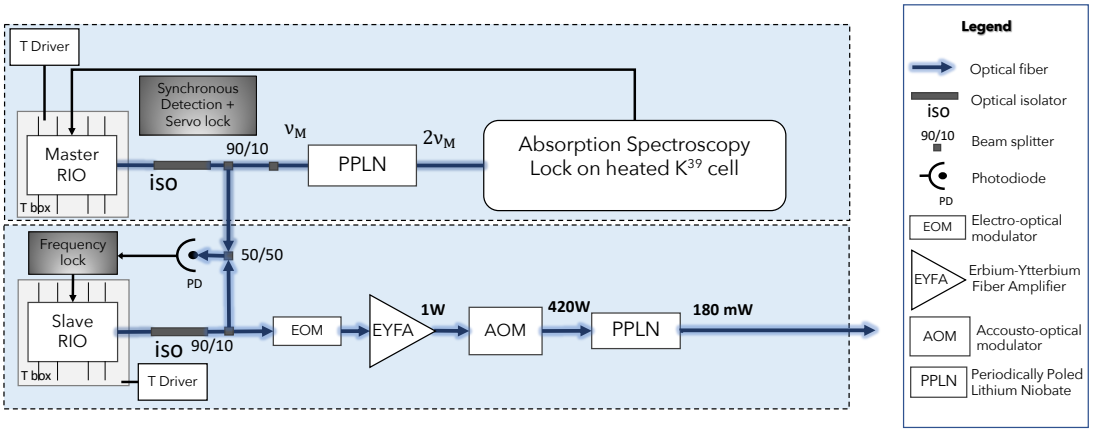

Figure 1.9: ***Architecture of the laser for the D_1 transition of potassium.***

the end of the laser chain, we use the usual setup: Amplifier[12]-AOM[13]-PPLN[14]. We employ an Erbium-Ytterbium Fiber Amplifier (EYFA) from Keopsys, which provides 1W of optical power. Typically, we can maintain up to 420 mW and 180 mW at the output of the AOM and PPLN, respectively. It can be noted that the PPLN of this laser system is not placed in a temperature regulated box.

Combining D_1 and D_2 lasers

The combination of wavelengths at 770 nm and 767 nm is achieved using an interferential filter (dichroic mirror) from Radiant Dyes integrated within a micro-optical bench from Kylia. This type of component has a transmission coefficient dependent on the angle of incidence for a given wavelength, allowing the combination of several wavelengths in the same polarization state. For example, with the model we use, wavelengths at 780 nm, 770 nm, and 767 nm are transmitted for incidence angles of 6°, 17°, and 20°, respectively.
In our first combining stage, the dichroic mirror is placed at an angle of 17° with respect to each of the two incident beams. The 770 nm wavelength is then transmitted, while the 767 nm wavelength is reflected on the opposite face.
The light is injected in polarization maintaining fibers at the bench output. The insertion loss of this system have been measured around 1.5 dB for each input.

Combining and splitting for the 3D MOT

Historically, a Schäfter-Kirchhoff free-space optical system was used to to recombine and split the laser sources. It was located on the side of the sensor head, fixed on its edge. This system showed strong misalignment issues during the parabolic flight resulting in strong losses of power in the 3D MOT due to injection losses. A dedicated micro-optical bench was designed and built, which has proven to be very stable and robust during the flight campaigns.

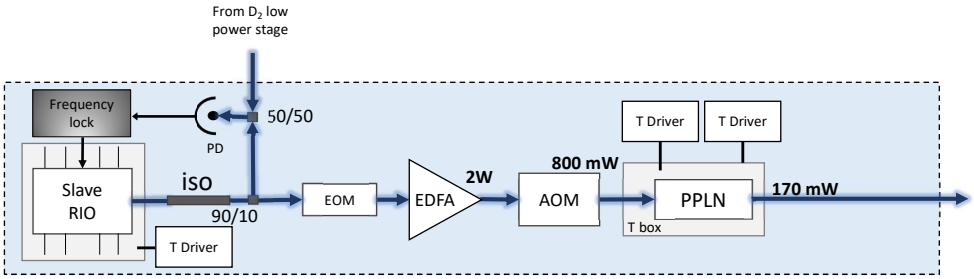

Figure 1.10: ***Architecture of the laser for the potassium 2D MOT PotaMOT2D***

Laser system for the potassium 2D MOT

To operate the potassium 2D MOT, I built a new laser source. Cooling in the 2D MOT is done at the same frequency as the 3D MOT, on the D_2 transition. However, a dedicated laser source was built to provide enough optical power into the 2D MOT. This laser system contains a single diode[15] at 1534 nm and is frequency locked to the potassium D_2 master laser. To do this, a portion of the light from the potassium master laser is sent on an InGaAs photodiode[16] to beat with 10% of the light extracted from the 2D MOT laser diode. The signal is then amplified by a radiofrequency amplifier[17] and sent to a frequency converter module built by our electronics workshop, an exact replica of the box used for the D_1 slave laser lock on the master laser. It contains a 2000-fold frequency divider, a frequency-to-voltage converter, a summing amplifier that receives the analog lock setpoint from the experiment control PC, and a proportional-integral-derivative system that feedbacks on the diode current. The current/temperature controllers used for this laser come from the same laser control commercial device as for the D_1 laser, with a temperature control module[18] and a current control module[19]. The current noise performance of this type of supply is not at the level of the cards used for the D_2 laser, but it is sufficient for the realization of the 2D MOT. The 90% optical power coming from the laser diode is sent to an EOM[20] to create the second frequency necessary for potassium cooling. The light is then sent to an 5W EDFA[21], external to the laser box. This EDFA is used at a 2W maximum output power to avoid damaging the AOM[22] used as a very fast shutter. The frequency doubling is performed thanks to a PPLN[23] which conversion efficiency limits the output power to 180 mW at 767 nm (probably due to previous damages on the component that has been repaired).
A view of the 3U rack box for this laser is presented in Figure 1.11.

Combining and splitting for the 2D MOT

It is necessary to combine the rubidium and potassium lasers for the 2D MOT and then split the beams into two cooling beams and one push beam that will be injected in the optical system

[12]Manlight ML1-EYFA-CW-SLM-P-OEM
[13]Gooch and Housego T-M080-0.4C2J-3-F2P
[14]NTT Electronics WH-0767-000-F-B-C
[15]RIO Planex laser diode RIO 0195-5-01-1-I7
[16]Hamamatsu, model G9801-32
[17]Minicircuits, GALI-74
[18]Thorlabs, model TED 8020
[19]Thorlabs, LDC 8005
[20]iXBlue Photonics MPZ-LN 10
[21]Keopsys KPS-CUS-BT-C-40-SLM series
[22]AA Optoelectronic M80-IIR60-Fio-PM0,5-J1-S
[23]NTT WH-0767-000-F-B-C

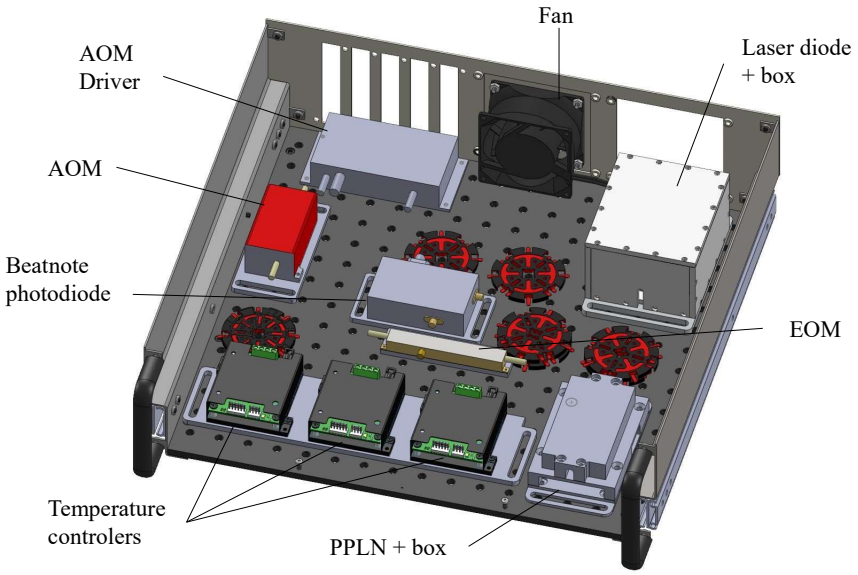

Figure 1.11: ***Solidworks model of the potassium 2D MOT laser at 767 nm 3U rack box*** *- AOM : Acousto-optic modulator ; EOM : Electro-optic modulator*

described in section 1.2.3. The power balance for the 2D MOT source is less critical than for the 3D MOT, because of the retro-reflected optical configuration of the 2D MOT. We thus decided to use the Schäfter-Kirchhoff dichroic 2×6 beam splitter, as a 2×3 beam splitter. To avoid having too strong misalignments due to a lateral position of the bench, it is fixed horizontally on a shelf located on one of the racks of the experiment. This system has been tested during the two flight campaigns and is very satisfying : a fine alignment of the fiber injection was necessary after the installation of the experiment in the plane but remained stable for the rest of the campaign despite the large variations of temperature and the parabolic flights. The power ratios and the configuration of this system are presented in Figure 1.12.

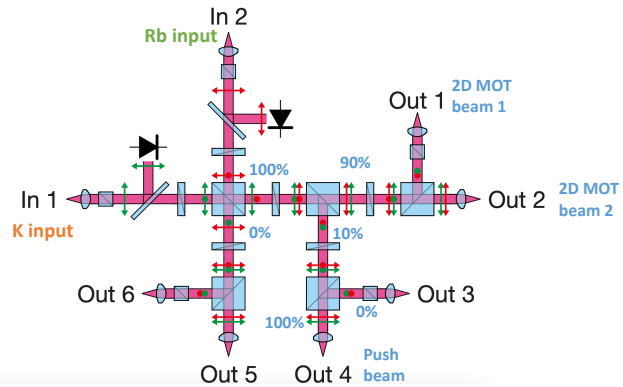

Figure 1.12: ***Repartition of the optical power inside the Shäfter-Kirschoff dichroic*** 2×6 ***beam splitter***

1.1.4 Dipole trap

The laser used for our dipole trap was produced by the French company Keopsys. It is a fiber laser doped with EDFA [24] emitting at a wavelength of 1550nm and capable of delivering up to

[24] Keopsys CEFL-MEGA-30-LP-1550-WT0-SL0-ST0-OM0-B314-C7

23 W of continuous optical power. Its spectral width is estimated to be 500 MHz by the manufacturer. According to measurements taken by the previous PhD student, Martin Rabault [[83]], power fluctuations are limited to about 4% during the heating phase following ignition. After a few tens of minutes, the output power stabilizes even further to reach levels of fluctuations below 1%, which is suitable for our application.

The output of the laser module is in the form of a polarization maintaining optical fiber coupled to a collimator. We obtain a collimated Gaussian beam in spatial TEM00 mode from the laser output, with a diameter of 3.8 mm at $1/e^2$. The linear output polarization corresponds to a polarization extinction ratio (PER) of about 20 dB.

1.2 Sensor head

This section provides an overview of the science chamber and all the components housed within the rack that encloses it. The central component is the vacuum chamber, which is depicted in Figure 1.13, along with all the associated systems.

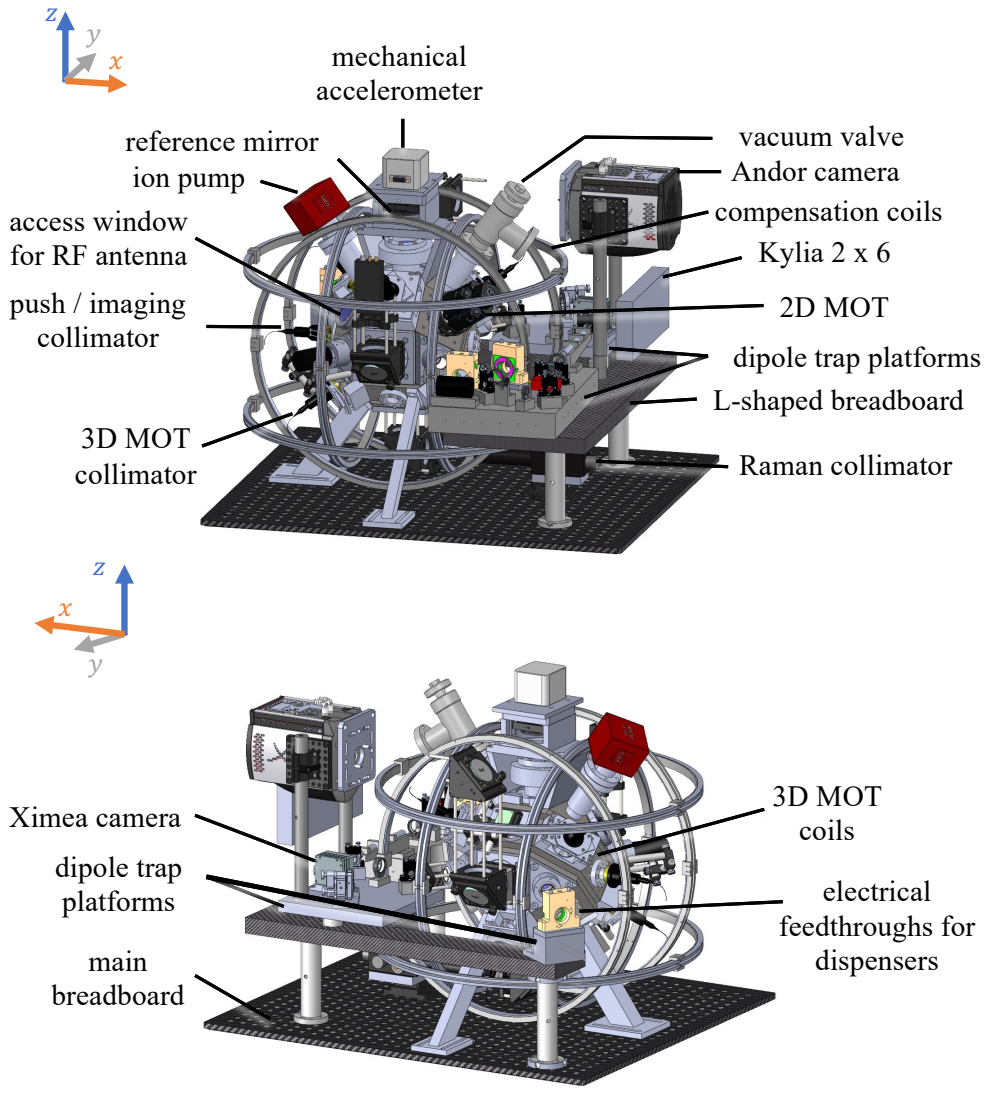

Figure 1.13: ***Solidworks model of the science chamber***

1.2.1 Ultra-high vacuum chamber

The vacuum chamber used in our experiment has 26 faces and resembles a "small rhombicuboctahedron". This geometry can be obtained by truncating the edges of a cube and consists of 18 square faces and 8 triangular faces, each equipped with threaded holes to attach the necessary optomechanical components. The chamber body was machined from a single block of titanium, a material that has the advantages of being non-magnetic, highly resistant to mechanical and thermal stresses, and compatible with ultra-high vacuum environments. Additionally, titanium has a low electrical conductivity, which helps to limit the appearance of unwanted Eddy currents. Finally, its relatively low density in comparison to stainless steel is useful for our onboard application. The final piece weighs 28.5 kg and has an average diameter of about 25 cm. The chamber is supported and fixed to the experiment breadboard via three feet made of an aluminum-copper alloy (AL-2024). Out of the 26 available faces, 20 have optical accesses, 2 are dedicated to the electrical feedthroughs of the dispensers, 2 are used for vacuum purposes (valve and pump), one is dedicated to the 2D-MOT and one allows the attachment of one of the support feet. Ultra-high vacuum compatible flanges are used to connect the different elements to the chamber. The 20 optical accesses are distributed as follows: 6 for the 3D magneto-optical trap beams, 4 for the dipole trap beams, 2 for the vertical Raman beam, 2 for the respective push beams of ^{87}Rb and ^{39}K, 2 for fluorescence detection, one for absorption imaging, one for fluorescence imaging and one for the microwave antenna.
The optical access windows are made of crown-type borosilicate glass (BK7) and have undergone anti-reflection treatment for wavelengths in the range of 725-825 nm, as well as in the range of 1530-1570 nm for the four windows of the dipole trap. The windows are held by titanium flanges and sealed on the chamber with indium gaskets. These flexible and compressible gaskets ensure vacuum tightness and integrity while minimizing stress on the windows and resulting wavefront distortions. This allows us to use high-quality optical windows.

The ultra-high vacuum inside the chamber is produced and maintained by a NEXTorr pump from SAES Getter. This pumping module combines a getter pump and an ion pump. The getter pump adsorbs most gases, while the ion pump is used for inert gases. An angle valve[25] is also integrated into the chamber to break the vacuum or connect an external pumping group during maintenance procedures. Both the pump and the valve are magnetic and are placed as far as possible from the vacuum chamber. Two 10 cm long titanium tubes were added to the chamber body by laser welding to achieve this distance.

During my thesis in March 2021, the last chamber opening took place, allowing the addition of the 2D MOT atomic source and the replacement of a flange with a window, providing an additional optical access. The procedure took one month, including 10 days to bake the chamber at 85°C. Under typical operation conditions, we estimate that the vacuum level stabilizes at less than 10^{-9} mbar according to the measurement made by the ion pump.
An image of the vacuum chamber on its breadboard without the attached elements, with the 2D MOT glass cell under the valve, is shown in Figure 1.14. This image was taken just after the installation of the 2D MOT system in March 2021.
The rubidium and potassium are present in the chamber in a chromate form on metallic wires called dispensers. Electrical connections on the outside of the vacuum chamber enable to run a current through the dispensers and heat them so that the atoms of rubidium or potassium evaporate under their pure form.

[25] VAT 54032-GE02-0002

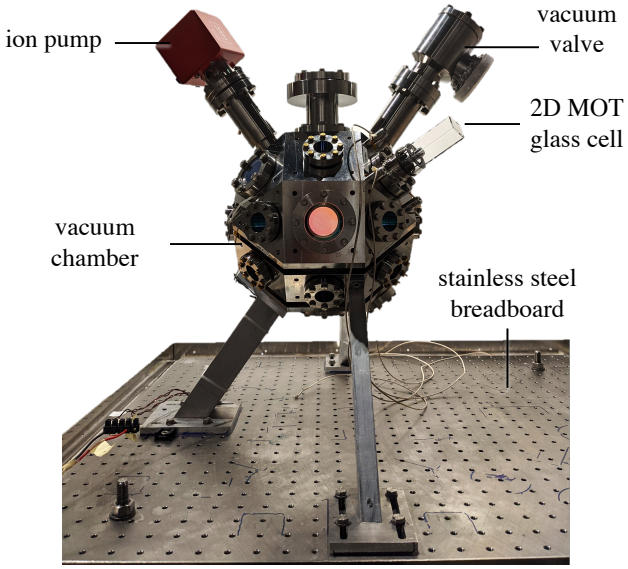

Figure 1.14: ***Vacuum chamber of the ICE experiment***

1.2.2 Collimators and optical systems

The 6 collimators for the MOT beams and their mechanical mounts were specifically designed and produced for our vacuum chamber at SYRTE (Observatoire de Paris). Each collimator incorporates a fixed polarizer and an ajustable quarter-wave plate, which respectively filter the polarization at the output of the optical fiber and make it circularly polarized. The beam at the output of each collimator has a Gaussian profile characterized by a "waist" ($1/e^2$ radius) of 9mm. The mechanical mount of the collimator allows for translation in the plane perpendicular to the beam for fine adjustment of its centering. A ball-and-socket joint also allows for fine control of the beam's orientation.

For the Raman beam, a 1" Schäfter-Kirchhoff collimator is used. The rubidium and potassium laser lights are injected into it through two separate fiber inputs with crossed polarizations. The two beams are then sent to a polarizing cube to be recombined, and a dichroic wave plate is used to put them in the same polarization state. Finally, an adjustable quarter-wave plate is used to adjust the output polarization as desired by the experimenter. As shown in Figure 1.13, the Raman collimator is mounted horizontally under the science chamber. A dielectric reflection mirror placed at a 45° angle is used to direct the beam vertically onto the atoms. The Raman beam is then retro-reflected on the reference mirror placed above the chamber. A final quarter-wave plate is integrated between the upper window and the reference mirror to cross the polarizations of the forward and backward beams. This crossed configuration is essential for the Raman transition we want to perform because of the selection rules. Also, it limits the parasitic optical lattice that introduce parasitic diffraction regimes.

1.2.3 2D MOT chamber

The experiment was originally designed such that the atoms are loaded into the 3D MOT from the dispensers of the main chamber (science chamber). In March 2021, we installed a commercial atom source called "Adjustable Cold Atom Source Cell " (ACASC) from the American company ColdQuanta.

The system is composed of a glass cell connected to the main chamber through a pinhole that creates a differential vacuum between the two chambers (see the glass cell in Figure 1.14). This chamber contains its own set of dispensers, one for rubidium and one for potassium. As the MOTs of rubidium and potassium are loaded from the dispensers inside the 2D MOT chamber, the background pressure should be around 10^{-8} (according to the specifications of the manufacturer), but the pinhole maintains the vacuum in the main chamber.

A compact optical loading system called "PICAS" coupled to a permanent quadrupole magnet called "MAG-2000" allows to load a cigar-shaped cloud of atoms of rubidium or potassium, or the two species simultaneously. Atoms are trapped and cooled in the two transverse directions to the axis of the cell using two pairs of counter-propagating circularly polarized beams. Another beam, oriented along the longitudinal axis of the cell, simultaneously "pushes" the atoms towards the main chamber, producing the directional flow of cold atoms. As they pass from one chamber to the other, the atoms go through an extremely narrow and elongated conduit called a "pinhole", in the form of a cylinder of 750 µm diameter. The metal surface surrounding the pinhole opening acts as a mirror and allows for retro-reflection of the pushing beam on its periphery. This allows for partial cooling of the atoms along a third direction in space, giving the device the rigorous name of "MOT 2D+" . Once in the main chamber, the atoms continue on their path to the center of the 3D MOT, where they are trapped and cooled again. A schematic view of the system is presented in Figure 1.15.

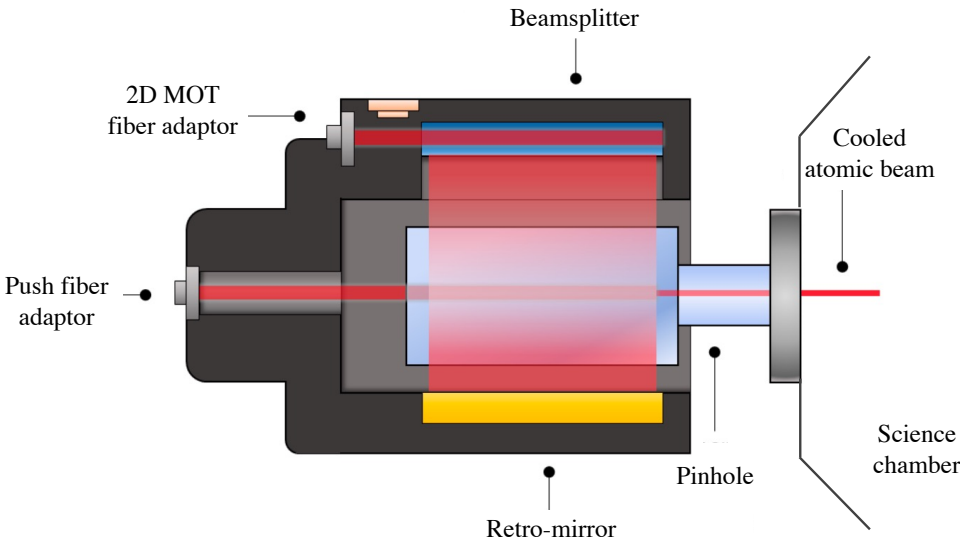

Figure 1.15: ***Cross section of the ColdQuanta 2D MOT (Source : ColdQuanta PICAS Datasheet)***

The installation of the system is made very simple by the fact that the optical system slides onto the permanent magnets to surround the glass cell. Fine alignment screws allow the center of the field to be centered in the cell and ensure proper alignment with the pinhole to maximize atomic flux (see Figure 1.16).

The functioning and performances of this atomic source are described in section 2.2.1.

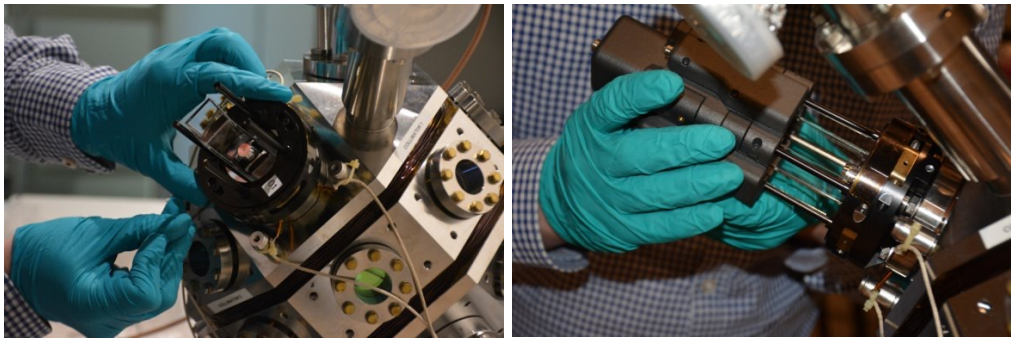

Figure 1.16: ***Installation of the 2D MOT system in March 2021*** *(a) The permanent magnets are fixed around the basis of the glass cell (b) The PICAS optical system is installed around the glasse cell using the permanent magnets as guides to center the system.*

1.2.4 Magnetic field control

MOT Coils

The loading of the magneto-optical trap requires a high magnetic gradient. A pair of coils in anti-Helmoltz configuration is directly integrated around the chamber in two dedicated trenches, allowing them to be close to the atoms. They have a 5.6 cm separation from one another and are powered with a 6A current, the 250 turns that make up the winding generate a gradient of approximately 15 G/cm along the strong axis. This current can be turned on and off rapidly using an electrical circuit based on a power MOFSET transistor.

Magnetic shield

Because atoms are highly sensitive to magnetic field, a precise control of the magnetic field throughout the experimental sequence is required. In order to protect the experiment from external electromagnetic disturbances, the entire sensor head is enclosed within a 1.5mm thick mu-metal magnetic shield. Mu-metal is an alloy composed of 80% nickel, 15% iron, and 5% molybdenum with very high magnetic permeability. This shield deflects magnetic field lines and attenuates external magnetic fields by one to two orders of magnitude within it [[56]].
This magnetic shield, presented in Figure 1.17, was designed in three parts, a bottom plate, a U-shaped and a L-shaped part. It is thus possible for the experimenters to open and close it in the small space that is available onboard the plane. The total weight is 70 kg, its dimensions are 84 × 70 × 74 cm.

Compensation coils

Many systems inside the shield produce magnetic fields that need to be compensated for. For instance the ion pump, the mechanical accelerometer, the cameras or the permanent magnets of the 2D MOT. Three pairs of coils in Helmoltz configuration along the 3 spatial axis are used. They are powered thanks to Delta Elektronika constant current sources. Along the X and Y axis, these power supplies are manually set to a current that is chosen by the experimenter to zero the field at the center of the science chamber. Along the Z axis, the current is controlled using the computer, enabling to change the magnetic fields along this axis during the experimental sequence. An additional pair of anti-Helmoltz coils along the Z axis can be used to compensate for the static vertical gradient.
Table 1.2 presents the characteristics of the coils.

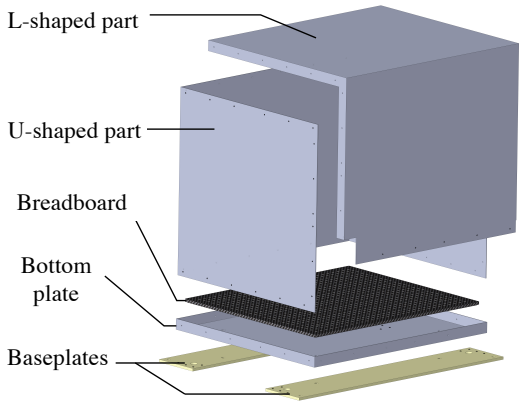

Figure 1.17: ***Exploded view of the magnetic shield structure*** *- It consists of three parts: a bottom plate, a "U" shaped section, and an "L" shaped cover (gray). Its base is fixed between the base plates (gold) and the breadboard (black) using 4 M12 screws. The baseplates are used to fix the experiment to the simulator or on the rails of the plane.*

	R (cm)	a (cm)	Turns	Configuration	Axis	Resistance (Ω)	Conversion
MOT	11	5,6	250	Anti-Helmholtz	$y+z$	4	230 (G/m)/A
Compensation x	21	21	13	Helmholtz	x	1	0,56 G/A
Compensation y	25	21	13	Helmholtz	y	1,5	0,47 G/A
Compensation z	29	21	13	Helmholtz	z	2	0,39 G/A
Gradient z	30	30	72	Anti-Helmholtz	z	60	8,8 (G/m)/A

Table 1.2: ***Characteristics of the pairs of coils on the experiment*** **-** R *is the radius of the coils and* a *the distance between two coils of the same pair.*

1.2.5 Detection systems

We have various detection methods on our experiment, including flux collection and spatial imaging of atoms. These systems complement each other and offer distinct advantages depending on their application.

Fluorescence detection systems

Fluorescence detection of atoms is used to detect and measure the atom number. It works by exciting the atoms, initially in a ground state $|g\rangle$, using laser light causing them to enter an excited energy state $|e\rangle$. By spontaneous emission, the atoms return to a lower energy state, emitting light. This signal is then detected and analyzed to determine the presence and quantity of the atoms in the sample. As the fluorescence of the cloud is not directional, the solid angle of the detection system must be maximized.

Two distinct and complementary detection systems are currently installed on the experiment. Their configuration is presented in Figure 1.18 .
The first detector, located at the top of the chamber, consists of a 3.6 mm sensitive photodiode[26] and its transimpedance circuit. Two lenses, L_1 and L_2, with diameters of 1" and focal lengths of 60 and 30 mm, respectively, are used to collect and focus the fluorescence onto this detector. We estimate a field of view of 8 mm for this detector. Lens L_1 has optical access closest to the atoms (only 6 cm away), which optimizes the collection solid angle and therefore the photodetection signal amplitude : we estimate a Ω_{coll} =0.140 sr solid angle for this system. This privileged optical access is made possible by a recess in the body of the chamber that was provided in its

[26]Hamamatsu, model S1223-01

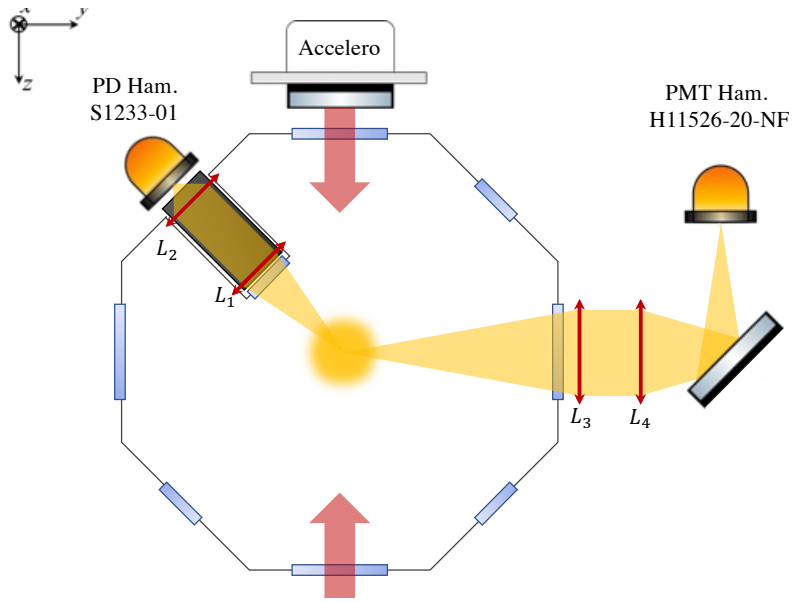

Figure 1.18: ***Side view of the science chamber and the configuration of the detectors*** *- PMT : photomultiplier tube, PD : photodiode, Accelero : Mechanical accelerometer*

design. This optical system, aligned with the position of the atoms during the trapping phase, is optimized for measurements with short flight times (less than 10 ms) in standard gravity or for long-time measurements in microgravity.

The second detection system, located in the middle part of the chamber, consists of two lenses, L_3 and L_4, with focal lengths of 150 mm and 125 mm respectively, a 45° reflecting mirror, an iris, and a photomultiplier tube (PMT) [27]. It consists in a vacuum tube with a photocathode, dynodes, and an anode. Electrons are driven from the cathode to the anode with high voltage. When a photon hits the photocathode, a photoelectron is released and accelerated onto the first dynode, where it's multiplied by secondary electron emission. This multiplication is repeated at each dynode, and the multiplied electrons are collected by the anode. High electron multiplication gains allow for highly sensitive fluorescence detection. This second detection system is positioned in front of a large window and therefore uses 2" diameter lenses. This allows for a collection solid angle comparable to that of the first system despite being twice as far away from the first lens to the atoms : Ω_{coll} =0.090 sr). The optics are maintained by a Thorlabs cage and optomechanics system, allowing for fine adjustments. The iris, placed just before the photomultiplier, minimizes the detection zone around the atoms as much as possible, thus minimizing the level of stray light, which helps improve the signal-to-noise ratio. Although high electron multiplication gain is advantageous for low levels of fluorescence associated with our ultra-cold samples, it has a drawback: the PMT should be exposed to low light levels only; otherwise, it may generate excessive current that saturates and damage the PMT. It is thus not suitable for detecting thermal samples. The solution to this problem is to use time-gating, which protects the PMT from being overexposed. The gate signal is generated by the control computer to acquire the signal. This system is also aligned with the initial position of the cloud after trapping.

At the end of my thesis, just before the the second flight campaign in March 2023, the photomultiplier had an issue and had to be sent back to the manufacturer. It was replaced on the experiment by an avalanche photodiode[28]. This photodiode has both good sensitivity and a

[27] Hamamatsu, model H11526-20-NF
[28] Hamamatsu, model C12703-01

smaller active surface area than the PMT (3 mm in diameter). The optical system to collect the fluorescence was adapted by replacing the lense L_4 by a 2" diameter lense with 75 mm focal length in order to reduce the magnification of the system, keeping the same opto-mechanical mounts. We estimate a field of view of 6 mm for this detector. The two detection systems, the photodiode and the avalanche photodiode, exhibit complementary characteristics. For large atom numbers, the photodiode provides a favorable signal-to-noise ratio within a short time of flight, while the avalanche photodiode tends to saturate under such conditions. Conversely, the avalanche photodiode proves advantageous for smaller sample sizes and longer times of flight due to its higher sensitivity. Figure 1.19 illustrates the normalized detection signals obtained from the photodiode and avalanche photodiode in standard gravity and in a simulated zero-gravity environment.

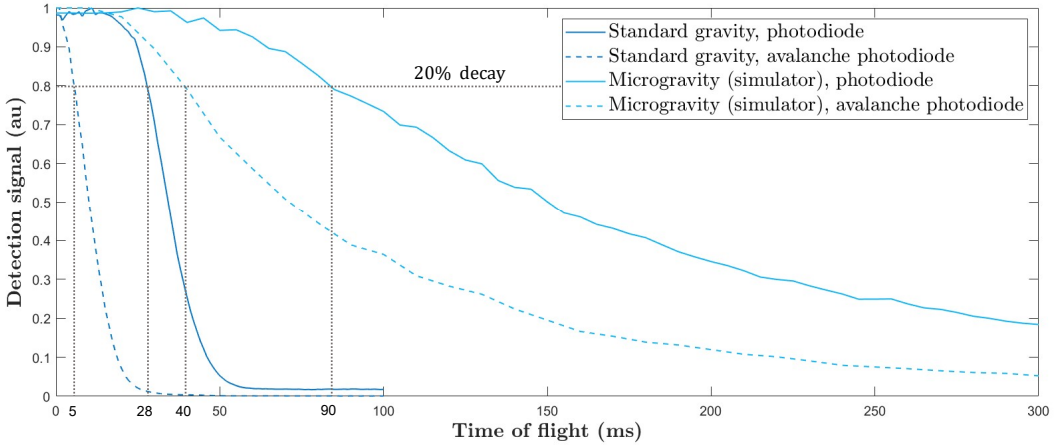

Figure 1.19: ***Normalized detection signal as a function of the time of flight for two detectors in standard and micro-gravity*** *- for cold atoms.In standard gravity, the signal exhibits a rapid decrease due to the gravitational fall of atoms, leading them to leave the detection area. On the other hand, in microgravity conditions, the atomic cloud undergoes expansion, resulting in significant dilution and making it challenging to detect the atoms over long times of flight. The avalanche photodiode exhibits a faster signal decay due to its narrower field of view. However, its higher sensitivity results in a substantially higher absolute detection signal.*

In standard gravity, the detection time is severely limited, and the signal decreases rapidly for both detectors after a few milliseconds. Specifically, the avalanche photodiode experiences a 20% signal loss within just 5 ms, while the photodiode shows a similar drop after 30 ms. This faster signal decay of the avalanche photodiode can be attributed to its lateral position relative to the atom's fall and its narrower field of view. Nonetheless, it is important to emphasize that the absolute detection signal is significantly higher for the avalanche photodiode, enabling work with a higher signal-to-noise ratio. In a zero-gravity setting, the signal's decay occurs at longer times, not due to the falling of atoms but rather due to the expansion of the atom cloud.

Detection zone

The detection zone characterization involves monitoring the fluorescence signal at different times of flight in both standard gravity ($1g$) and microgravity ($0g$) (Fig. 1.20). In $1g$, the atom cloud exits the detection zone before significant expansion occurs. To model the detected signal S_{det}^{1g}, we calculate the overlap of the atom cloud with the detection zone using a 1D model, assuming that the atom cloud is fully detected along the other two directions:

$$S_{det}^{1g}(t) = \int D(z) e^{-(z-z_0(t))^2/\sigma_z(t)^2} dz \tag{1.1}$$

Here, $D(z)$ represents the detection zone in the vertical direction z, and the exponential term corresponds to the 1D Maxwell-Boltzmann distribution of the atom cloud along z. The thermal expansion of the cloud is given by $\sigma_z(t)^2 = \sigma_0^2 + \frac{2k_bT}{m} \cdot t^2$, where σ_0 is the initial size. The atoms fall due to gravity with $z_0(t) = \frac{1}{2}gt^2$ and interact with the detection zone. A satisfactory fit is achieved with a truncated Gaussian top hat having a diameter of approximately 20 mm (see insets in Fig. 1.20).

In $0g$, the atom cloud remains centered in the detection zone, and the detected signal is related to the thermal expansion of the cloud, which exceeds the detection zone in all three spatial directions for long time of flights:

$$S_{det}^{0g}(t) = \int D(x)D(y)D(z) e^{-(x^2+y^2+z^2)/\sigma(t)^2} dxdydz \tag{1.2}$$

Here, we model the detection zone as a cube, with $D(x) = D(y) = D(z)$. The detected signal for long time of flight in microgravity probes the temperature of the atomic sample, yielding a satisfactory agreement for $\mathcal{T} = 6$ μK.

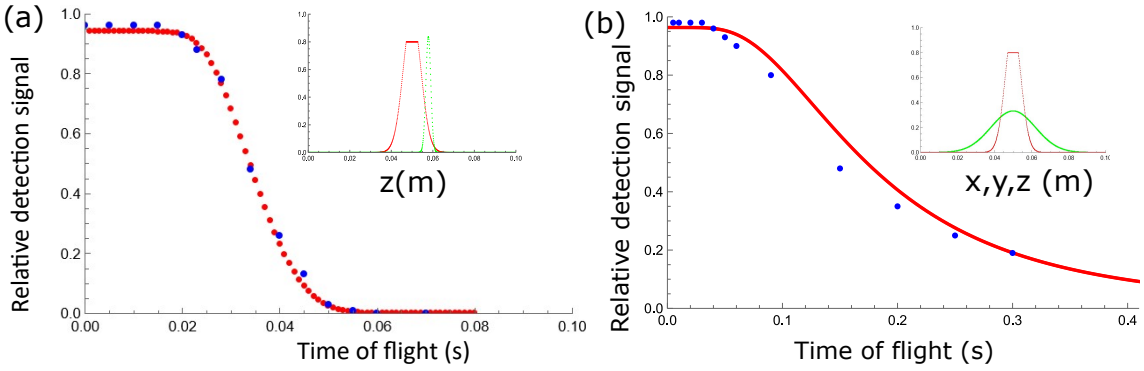

Figure 1.20: ***Detection zone and temperature of the atoms****- Detection signal versus time of flight in (a) standard gravity and (b) microgravity. Each graph shows the measured signal (blue) and a model (red) including the thermal expansion of the atom cloud (inset green) and the detection zone (inset red).*

Populations estimations

To estimate the population of the internal states for each atomic species, our method consists in sequentially detecting the population N_2 of atoms in the state $|F = 2\rangle$, and then the total population $N_{tot} = N_1 + N_2$ in order to determine the population ratio N_2/N_{tot}. For this, we apply two successive laser pulses using the Raman beam: the first pulse contains only the cooler frequency while the second one also contains the repumper frequency. We typically set the duration of these pulses to 50 µs and the delay between them to 20 µs. This fluorescence

detection method is useful because it does not require spatial separation between atoms in the $|F = 1\rangle$ and $|F = 2\rangle$ states.

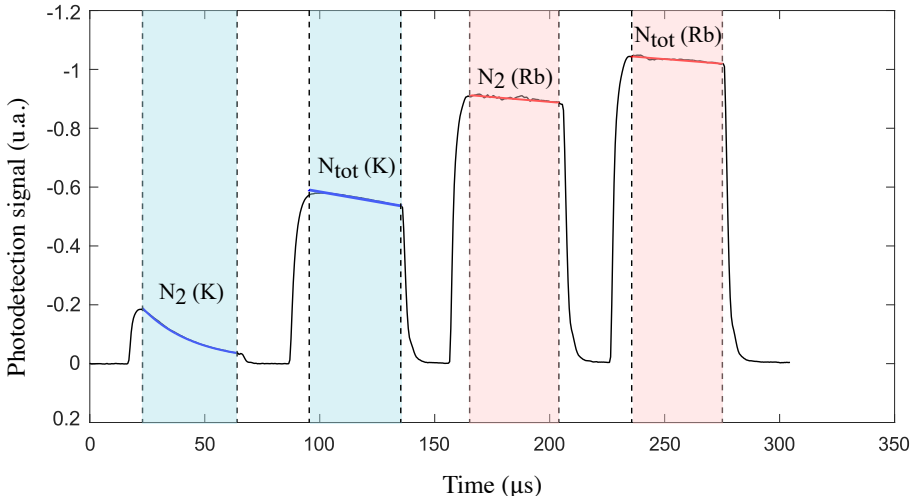

Figure 1.21: ***Fluorescence detection sequence for estimating the population ratio between the ground state*** $|F = 1\rangle$ ***and the excited state*** $|F = 2\rangle$ *- Photodiode signal (black line) and fit used to estimate the atom numbers (blue and red). For each of the two species, the number* N_2 *of atoms in the excited state is sequentially detected, followed by the total number of atoms* N_{tot} *using two laser pulses, with and without a repumper frequency. In the case of potassium, a rapid exponential decay of the detection signal is observed during the first pulse. This is a depumping phenomenon induced by the narrow hyperfine structure of this atomic species.*

This atom detection method suffers from several disadvantages, including difficulties with normalizing the population ratio and the absence of any spatial information. However, this is currently the most efficient method to access the ratio of internal populations of the cloud, which is necessary for both interferometric measurements and diagnostics. The choice of the detector for the measurement and a discussion on the signal to noise ratio (SNR) of this detection systems will be presented in section 3.

To directly access other characteristics of the atom cloud, such as its size, shape, or thermal expansion, it is necessary to use an imaging system in addition to the detection system.

Imaging systems

The ability to image atomic clouds is particularly useful when working with ultra-cold samples. As we will see in the next chapter, spatial imaging is a powerful characterization tool to measure atomic cloud temperatures and trap frequencies or to identify the Bose-Einstein condensation threshold, for example.

It is worth noting that in this regime of very low temperatures, the recoil velocity associated with two-photon transfer exceeds the velocity dispersion of the cloud. The diffraction orders associated with the different output ports of the interferometer thus separate spatially from each other faster than they spread. After a sufficient time-of-flight, typically a few milliseconds, it becomes possible to identify them based on their position rather than their internal state. Interference fringes can thus be obtained by simultaneously estimating the number of atoms in each diffraction order rather than by successive detection of the N_2 and N_{tot} populations. Imaging methods are often based on the scattering of a probe beam through the atomic sam-

ple. Two main categories can be distinguished, which exploit different processes of light-matter interaction: photon absorption and fluorescence re-emission.

Absorption imaging is performed by imaging the shadow of the atomic cloud created by absorption of a collimated resonant beam. It is suitable for high optical densities.

On the other hand, the fluorescence imaging consists in collecting the photon flux due to the phenomenon described in the previous section on a camera to spatially resolve it. This technique is generally preferred when detecting low atomic densities, as they offer a better signal-to-noise ratio (SNR) than absorption methods [[87]]. In these conditions, defects in the camera, optics, and laser beam are indeed predominant and contribute to severely degrading the absorption signal.

Absorption Imaging

To perform an absorption imaging, a laser beam with a wavelength resonant with the absorption transition of the atomic species of interest is directed onto the atomic cloud in the equatorial plane of the experiment. The laser beam is collimated to a thin sheet that illuminates the entire atomic cloud uniformly, using a Schäfter-Kirchhoff collimator. As the laser beam passes through the cloud, atoms that are resonant with the laser will absorb the photons from the beam. The collimated beam is then sent to a CCD camera (Ximea MD120MU-SY) using imaging lenses that form a telescope in $2f$-$2f$ configuration, with two lenses L_1 and L_2 of respectively 150mm and 125mm focal length. The atoms are located in the object plane of L_1 while the camera is in the image plane of L_2. This configuration also requires that the two lenses be spatially separated by the sum of their focal lengths. The choice of lens L_1 was constrained by the atom-aperture distance, while that of L_2 resulted from a compromise between magnification and system size. However, the relatively low magnification we have (0.83) is compensated for by the high resolution of the sensor, which has pixels of only 3.1 µm. Three reflector mirrors also allow for a more compact optical setup. A schematic view of the system is presented in Figure 1.22.

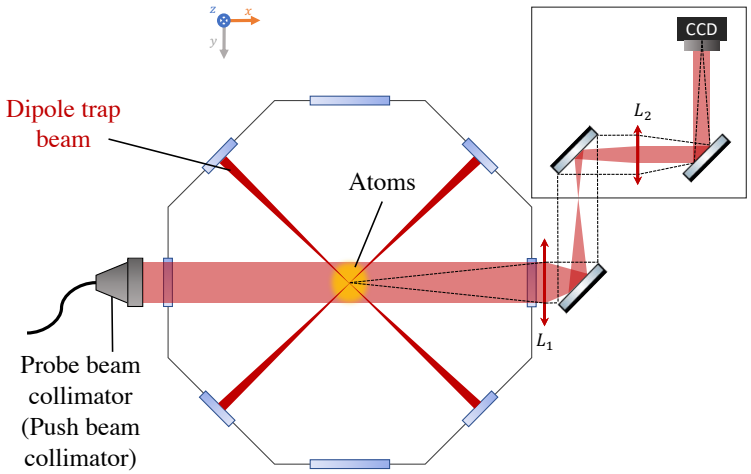

Figure 1.22: ***Top view of the science chamber and the configuration of the optical system and camera for absorption imaging*** *- CCD: Ximea CCD Camera*

The absorption image gives information about the spatial distribution of the atomic cloud, as well as the optical density of the cloud. The optical density is directly proportional to the number of atoms in the cloud.

If we consider a cloud density $n(x, y, z)$, and a collimated resonant probe beam of intensity I_0 propagating along x axis, one can express the transmitted transversal intensity $I_T(y, z)$ using Beer-Lambert's law as

$$I_T(y, z) = I_0(y, z)e^{-\sigma\tilde{n}(y,z)} \tag{1.3}$$

with σ being the absorption cross-section and $\tilde{n}$ the column density (obtained by integrating the density n along the propagation direction).
The camera detects the remaining intensity of the probe beam after it has passed through the atomic cloud. The absorption image is obtained by taking three sequential images : an image after passing through the atoms, an image of the probe beam in the absence of the atomic cloud (no atom image) and a background image (no laser light).

The incident intensity I_0 of the beam being not uniform, we sequentially measure I_T and I_0 by taking two very close successive images: the first with the atomic cloud and the second without it, but still in the presence of the probe beam. In practice, we also take a background image I_B (without laser light) that is substracted to the images to take into account the background noise. The quantity that we then have access to is the optical density OD (for Optical Density) defined as

$$OD(y, z) = \sigma\tilde{n}(y, z) = \ln\left(\frac{I_0(y, z) - I_B(y, z)}{I_T(y, z) - I_B(y, z)}\right) \tag{1.4}$$

To obtain the value of the column density $\tilde{n}(y, z)$ from the optical density $OD(y, z)$, it is necessary to know the value of the proportionality factor σ. This absorption cross section depends on various parameters of the beam and the atomic transition involved, and is expressed as follows:

$$\sigma = \frac{\sigma_0}{1 + 4\delta^2/\Gamma^2 + I_0/I_{sat}} \tag{1.5}$$

with Γ the natural width of the considered atomic transition, I_{sat} the associated saturation intensity, and δ the detuning of the probe beam with respect to the resonance. The parameter σ_0 is the resonant absorption cross-section and depends on the natural width, the saturation intensity and thus the polarization of the light :

$$\sigma_0 = \frac{\hbar\omega\Gamma}{2I_{sat}} \tag{1.6}$$

where ω is the resonance frequency associated with the atomic transition. In our case, for circular polarization, the resonant absorption cross-sections for ^{87}Rb and ^{39}K are respectively 2.9×10^{-13} and 2.8×10^{-13} m^2 [[96, 101]] .

Equation 1.5 reflects the fact that an increase in the detuning δ from the atomic resonance leads to a decrease in the absorption probability. The decrease in the absorption cross-section with increasing incident intensity I_0 is explained by the fact that the latter induces population of the excited level, which in turn tends to favor stimulated emission over spontaneous emission. We generally work with incident intensities that are moderate compared to the saturation intensities in order to maintain an approximately linear relationship between the measured optical density and the effective atomic density. The choice of exposure time is also constrained by the movements of the atoms under the influence of gravity or their thermal expansion. To avoid obtaining blurred images, we limit ourselves to exposure times of the order of 50 µs. We also aim to minimize the time interval between the acquisition of the three images, and we are limited in this regard by the speed of our camera, which imposes a delay of at least 40 ms between successive images. Once the images have been acquired and the column density determined, the total number of atoms in the cloud can be calculated by simple integration of n over the (y, z) plane. In the case of a thermal sample with a Gaussian profile, this total number of atoms N_{at} can also be approximately estimated by:

$$N_{at} = 2\pi \tilde{n}_{pic} \sigma_y \sigma_z \tag{1.7}$$

where $\tilde{n}_{pic}$ represents the peak column density (maximum column density at the center of the cloud) and σ_y and σ_z represent the standard deviations of the Gaussian in the y and z directions, respectively.

Fluorescence imaging

One of the main challenges of the experiment is to be able to detect and image the atoms after long times of flight. It leads to highly diluted atomic clouds characterized by very low atomic densities. Fluorescence imaging techniques are the most suitable for this type of condition, this is why we added a new imaging system during my thesis.

Optical access to the atoms is provided by one of the large 2" windows located in the equatorial plane of the chamber, in order to maximize the solid angle of collection. A new combination of two converging lenses with diameters of 2" and focal lengths of 150 mm and 175 mm, respectively, allows the cloud to be imaged on an EMCCD camera (Andor Ixon Ultra 897 model). A rear view of the experiment in Figure 1.24 shows the Andor camera and the opto-mechanical system along with the other detection systems.

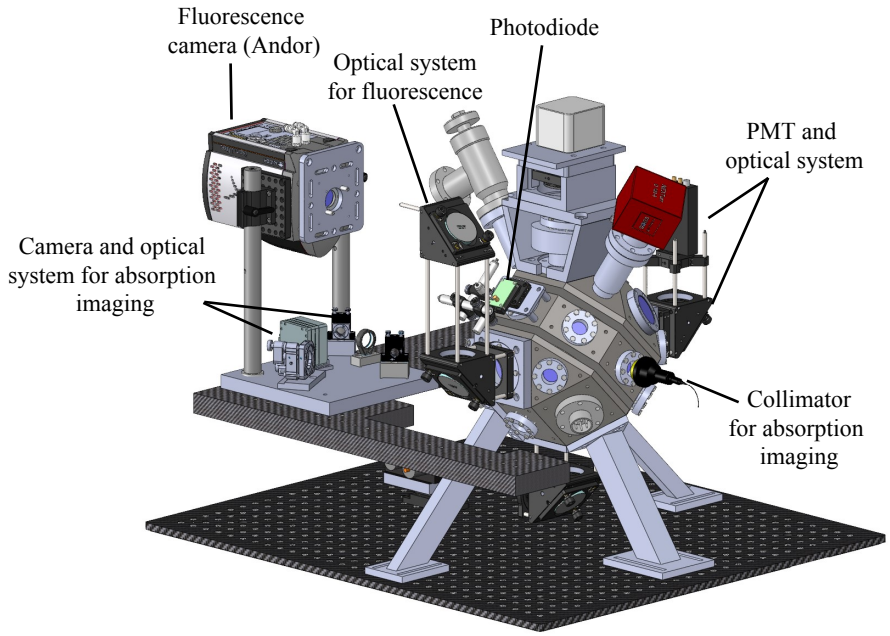

Figure 1.23: ***Rear view of the vacuum chamber and the different detection systems-*** *PMT : photomultiplier tube*

The optical system is characterized by a solid angle of collection of Ω_{coll} =0.090 sr, a magnification of 1.16, and a resolution of 2.8 µm if limited by the diffraction. It is not the case here : the 2" lens used presents spherical aberrations and our opto-mechanicl system makes it difficult to optimize the defocus.

The Andor camera has a pixel matrix that can be cooled by a Peltier effect to -80°C. At this temperature, the dark noise is limited to only 3×10^{-4} electrons per pixel per second. The camera also has a very low read noise (less than 1 electron per pixel) and excellent quantum efficiency ($\eta_q > 75\%$ at 780 nm). The sensor consists of a 512 by 512 pixel array, with each pixel

measuring 16 µm on a side. The size of a pixel, as projected onto the object plane, corresponds to a value of 14 µm, and the resolution is not limited by diffraction here.

The atomic fluorescence is induced by a laser pulse similar to the one we use when we detect the total number of particles N_{tot}. We use the MOT collimators to illuminate the cloud, containing two laser frequencies tuned to the transitions $|F = 1\rangle \rightarrow |F' = 2\rangle$ and $|F = 2\rangle \rightarrow |F' = 3\rangle$, respectively. The exposure time is of the same order of magnitude as that used for absorption imaging.

The total number of atoms N_{at} in our sample can also be estimated using this second imaging device. Assuming that the size of the cloud in the image plane is smaller than that of the sensor, we can write:

$$N_{at} = \frac{4\pi N_{count}}{\Omega_{col}\gamma_{diff}t_{exp}\eta_q G_{EM}} \tag{1.8}$$

where N_{count} is the total number of electronic counts over the entire sensor, t_{exp} is the exposure time, and G_{EM} is the "EM" gain of electron multiplication. The photon diffusion rate (spontaneous emission rate) is given by:

$$\gamma_{diff} = \rho_E \Gamma \tag{1.9}$$

where ρ_E is the probability of occupation of the excited state under the effect of laser excitation, and Γ is the natural linewidth.

Calibration of the imaging systems

For both imaging systems, it is necessary to perform a calibration to have a precise knowledge of the magnification of the system. We use the gravitational fall of the atoms in the field of view to obtain an estimate of the magnification. Figure 1.24 presents an example of this calibration for the absorption and the fluorescence imaging.

1.2.6 Microwave antenna

Performing atom interferometry requires a very good state preparation of the samples (see section 3): the particles must be prepared in a specific internal state F and Zeeman sublevel m_F. To do so, we use a microwave pulse to perform Rabi oscillations between the state $|F = 1, m_F = 0\rangle$ and $|F' = 2, m_F = 0\rangle$. The frequency of this microwave corresponds to the hyperfine transition value of rubidium (6.834 GHz) while the duration of the π pulse, associated with an optimal population transfer, is typically around 600 µs. This pulse is generated using a half-wavelength dipole antenna (measuring 2.2 cm in our case), placed outside the chamber, just in front of one of the windows. This antenna must be firmly attached as the effective power received by the atoms is highly sensitive to its position and orientation.

1.2.7 Classical inertial sensors

One of the features of our experiment is the use of conventional inertial sensors to achieve hybridization with our quantum measurements. As presented in section 3.2.4, the measurement of our reference mirror vibrations as well as the rotations of the experiment are necessary to perform hybridization techniques. The vibrations are measured using a mechanical accelerometer placed on the back of the retro-reflection mirror. The model we use (Colybris SF3000L) is a 3-axis MEMS (Micro Electro Mechanical System) accelerometer. It has a high dynamic range (± 3g), which is essential for our application considering the variations in gravity during 0g flight or on the microgravity simulator. This accelerometer is also characterized by a wide

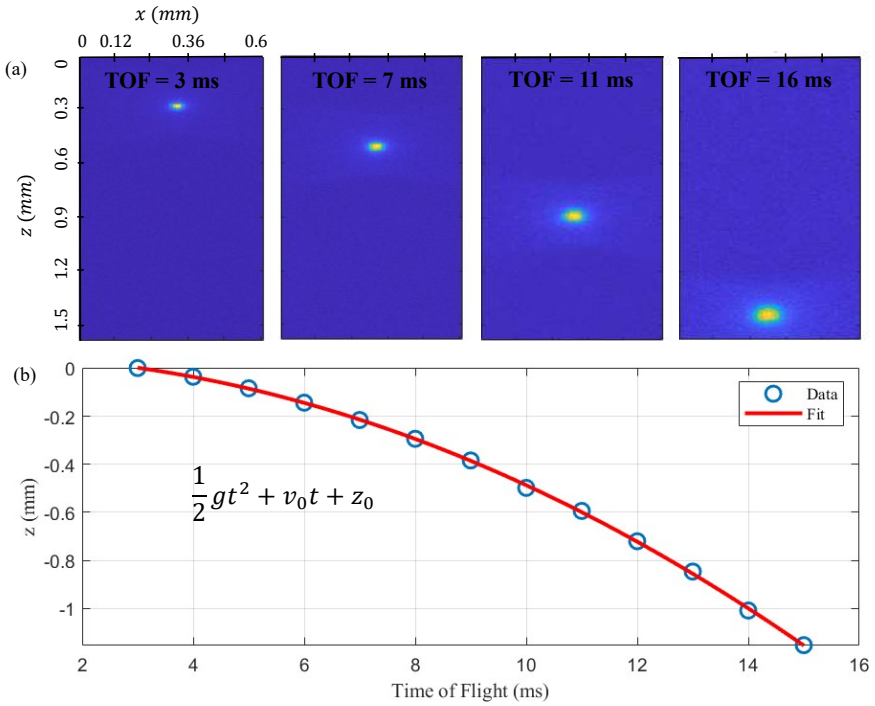

Figure 1.24: ***Calibration of the imaging system****- (a) Fluorescence images of an ultra-cold atomic cloud falling under gravity for different times of flight (b) Position of the cloud along the z axis with respect to time and quadratic fit. Knowing g, we can deduce the magnification of the system.*

bandwidth, extending up to 1kHz, and a low level of intrinsic noise, specified at 500 ng/Hz$^{-1/2}$. The linearity errors are limited to ±0.1% over the entire frequency range. Finally, the axis coupling extinction ratio is greater than 40 dB.

A second accelerometer can be used on the experiment, a low noise sismo-accelerometer (Titan Nanometrics). Its self noise is as low as 30 ng.Hz$^{-1/2}$. Unfortunately, the Titan is a force balance accelerometer designed to have the best sensitivity at 1 g, and a dedicated design for microgravity is required. Moreover, the bandwidth where the sensitivity is optimal [0.1-50 Hz] doesn't match our needs.

The measurement of the rotation rates Ω_x and Ω_y about the transverse axes of the mirror is performed using two fiber optic gyroscopes (model DSP-1750 by KVH). Each gyroscope provides an analog output voltage proportional to the projection of the angular velocity vector $\vec{\Omega}$ along its axis, with a scaling factor of 60 mV/(°/s). These gyroscopes have a bandwidth of 1 kHz, bias instabilities of 2 °/h, and a temperature and angle random walk drift of $0.05°/\sqrt{h}$. They are placed on the main breadboard due to space constraints.

1.2.8 Breadboard

As the sensorhead is the heaviest rack of the experiment, and also the part mounted on the microgravity simulator, efforts have been made to limit its weight. A maximum weight of 250 kg is authorized for the plane, and the same limitation is advised for the simulator to function properly. Therefore, the choice of breadboard material is important, as we want it to be both stiff and light. Previously, an aluminum breadboard was used, but it was replaced with a stainless steel breadboard to reduce the Eddy current linked to time-dependent magnetic fields, which

dissipation is proportional to the product of resistivity and density (see Table 1.3). This material also had the advantage of being stiffer than aluminum but was heavier. We suppose that the mechanical issues experienced by the simulator were due to the heaviness of the sensor head at that time. Hence, we opted for a breadboard made of "Carbon Fiber Reinforced Polymer" (CFRP), manufactured by the German company CarbonVision, which helped us design and build a custom breadboard.

Material	Total weight (kg)	Approximate stiffness (N/m)	Resistivity ($\Omega.m$)	Density (g/cm^3)
Aluminium	16	70.10^9	$2{,}8.10^{-8}$	2,7
Stainless steel (316L)	45	193.10^9	$7{,}6.10^{-8}$	7,9
CFRP	16	140.10^9	/	/

Table 1.3: ***Comparison of different material for the main breadboard***

This composite material is made up of an epoxy resin matrix and high-tensile strength carbon fiber reinforcements. The mechanical, thermal, and magnetic properties of the CFRP make it particularly well-suited for our mobile applications. The breadboard is in fact composed of two CFRP plates. The space in-between the plates is used to integrate the inserts. The load introduction into the board is made by stainless steel inserts which are mounted underneath the upper plate, using a wide flange. The stiffness and strength of the board results from a 10 mm thick upper plate, the lower plate of about 1.0 mm thickness covers the inserts heads (see Figure 1.25).

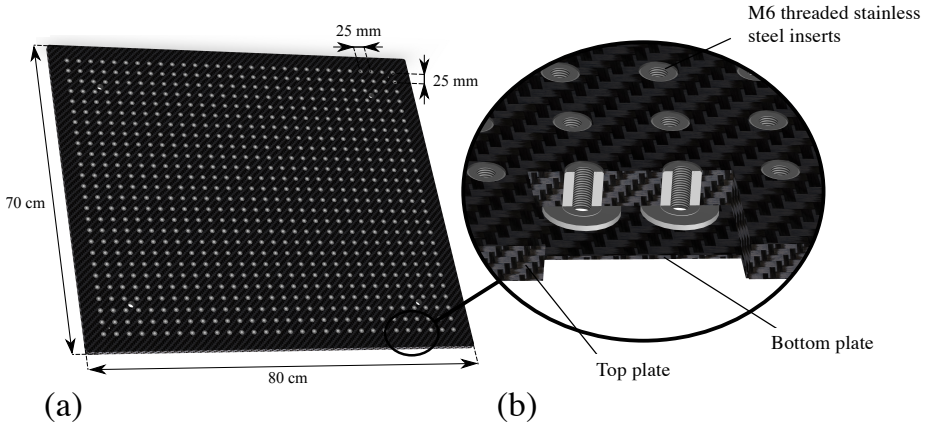

Figure 1.25: ***Carbon fiber-reinforced polymer breadboard*** *- (a) Overall view of the board. (b) Cross-sectional view of the inserts.*

This solution offers a stiffness comparable to stainless steel with a very low weight. As the breadboard is mainly composed of polymer, there are no Eddy current.

1.2.9 Optical set-up for the dipole trap

As we will see in section 2.4, a spatial modulation of the beam creates a time average potential on the atoms that allows us to control the shape of the trap and increase its capture volume. The component that performs this modulation function is a free-space AOM operating at our 1550 nm wavelength, enables an analog control of dipole trap laser power. No mechanical shutter enables for the extinction of the dipole trap, so the extinction is limited by the AOM. As explained in section 2.6, the residual optical tweezer affects the atoms, so we use the AOM the deflect the beam far away from the cloud at the end of the loading.

The modulation is achieved by manipulating the RF frequency sent to the AOM and retrieving the first-order diffraction output. This allows for dynamic control of the beam angle, which varies almost linearly with the value of the applied RF frequency. The optical power transmitted in this first-order diffraction depends on the supplied RF power. We refer to the periodic function describing the desired temporal evolution of the beam position δx in a plane transverse to its propagation direction as the "modulation function." This modulation function is mathematically linked to the shape of the mean potential that we wish to induce on the atoms. The principle of the modulation and the shape of the signal sent to the AOM are presented in Figure 1.26. The details concerning the spatial modulation of the beam can be found in [[83]] and [[37]].

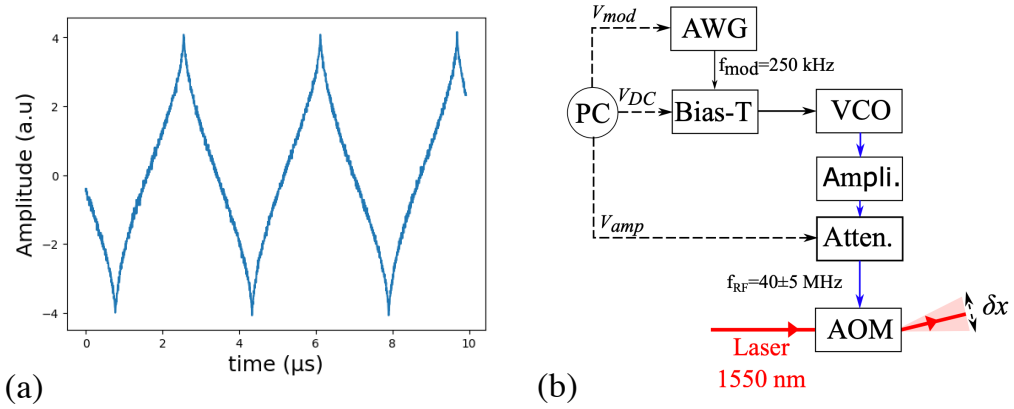

Figure 1.26: ***Spatial modulation of the dipole trap beam*** *- (a) Signal sent to the AOM to spatially modulate the beam in order to have an harmonic potential on the atoms (b) Architecture for the generation of the modulation signal. The commands V_{mod}, V_{DC} and V_{amp} control the amplitude of the modulation, its average position and its intensity. AWG : Arbitrary Wave Generator, VCO : Voltage Control Oscillator, AOM : Accousto-optical modulator.*

The optical set up is presented in Figure 1.27. A first afocal telescope with magnification $\gamma_1 = 0.5$ is used to adapt the beam diameter for the injection of the AOM located downstream. For compactness reasons, this telescope is constructed by combining a plano-convex lens with a plano-concave lens. A half-wave plate is inserted between the two lenses to adjust the polarization direction and thus maximize the efficiency of the AOM. The optimization of the crystal injection is finally completed by a pair of mirrors that allow for fine adjustment of the incident beam position and angle. Under ideal injection conditions, the AOM[29] has a transmission efficiency estimated at 80%. At the output of the AOM, the 0th diffraction order is directed to a beam dump, while the 1st order passes through a second afocal telescope with magnification $\gamma_2 = 3.3$. This telescope is used to obtain an adapted beam diameter (6.3 mm) before focusing on the atoms via lens L_1. Two mirrors placed upstream of this lens allow for very fine alignment of the first beam passage on the atoms.

In our case, the focal length of L_1, which is constrained by the dimensions of the vacuum chamber, is 150 mm. In Gaussian optics, the magnification ratio between the waist w_0 before the focal lens of focal length f (at its object focus) and the waist at its image focus w_i is given by: $w_i = \lambda f/\pi w_0$, where λ is the wavelength of the radiation. In our case, the waist and the theoretical diameter ($2w_0$) at the level of the atoms are thus respectively 23.5 and 47 µm. In practice, we measure a diameter that is about twice as large, which can be explained by a slight error in the telescope adjustments.

[29] AA Optoelectronic, model MTS40-A3-1550

At the output of the first beam passage through the opposite window, the beam is immediately recollimated using a second lens L_2 with a focal length of 150 mm. The beam is then recycled and redirected to the vacuum chamber using two reflecting mirrors. A third and final lens L_3 focuses the second beam passage on the atoms, in order to have the same waist on the atoms than the first path. A half-wave plate is placed just in front of this lens to rotate the polarization by 90° with respect to the first arm, and all the optical power is finally collected in a beam dump located at the output of the second passage.

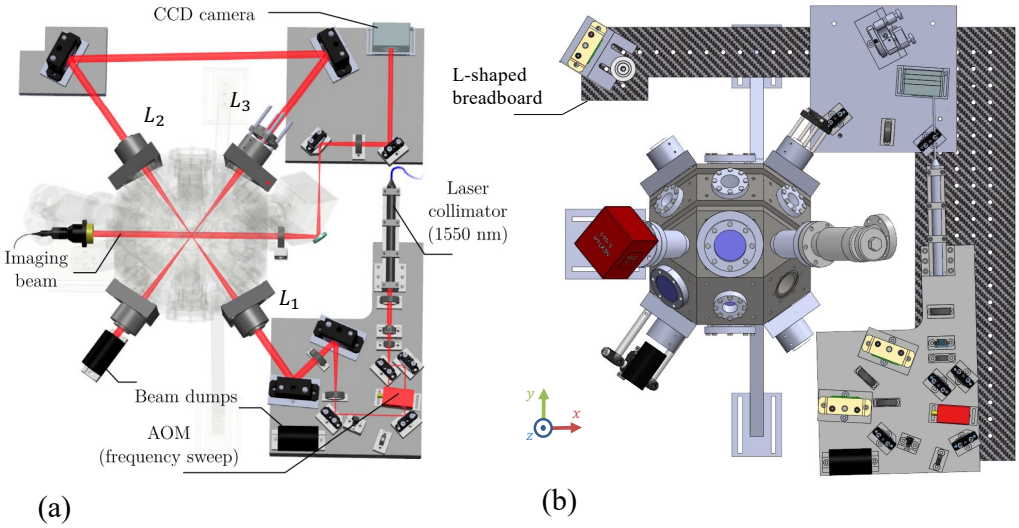

Figure 1.27: ***Top view of the dipole trap configuration****- (a) Optical set up of the dipole trap (b) Top view of the platforms and L-shaped CFRP breadboard*

The two arms of the beam are thus contained in the same horizontal plane and form an angle of 70° imposed by the geometry of the chamber. The good spatial overlap of their respective focal points is particularly critical for obtaining our ultra-cold source, but is difficult to maintain in practice due to the size of the waists. The alignment tends to deteriorate over time due to very slight thermal expansions and/or mechanical deformations. To overcome this difficulty, the reflecting mirror just before the second passage is placed on a pico-motor mount[30]. The position of the mirror can thus be adjusted directly from our PC via a dedicated controller[31]. This system allows real-time alignment adjustment even when the magnetic shield is closed and the experiment is in motion. The pico-motor technology was preferred here because it combines high dynamics (±4° in our case) and good resolution (700 nrad). It also ensures position retention in the absence of electrical power, which is a real advantage compared to piezoelectric technology.

This alignment issue is particularly limiting when operating on the microgravity platforms : due to the changes in gravity, the mechanical constraints change during the experimental sequence. This results in a misalignment of the crossed dipole trap.

Indeed, if the two paths of the dipole trap are overlapped along the vertical (z) axis in standard gravity, it will no longer be the case in microgravity. In the plane, this effect prevented the

[30]New Focus, model 8816-6
[31]New Focus, model 8742

previous experimenters to trap atoms in microgravity. In order to tackle this issue, we worked with the German company CarbonVision to design and build a custom L-shaped breadboard to support the three platforms, mechanically linking them together to limit their relative misalignment. This breadboard is presented in Figure 1.27 (b). It is difficult to estimate the effect of this breadboard on the experiment : during the flight campaigns, we witnessed very strong misalignments. Thanks to a remote control of the mirror's pico-motor, we were able to realign the dipole trap during the microgravity phase by looking at absorption images of the atoms trapped in the two arms of the dipole trap. An overlap of the two clouds of trapped atoms on absorption images is good enough to start evaporation. Fine tuning of the mirror's position is then achieved by maximising the number of atoms in the cloud at different stages of the evaporation process. We typically used the first five parabolas of each flight to make these adjustments. Examples of absorption images showing the atoms trapped in the two arms of the dipole trap are visible in figure 1.28. These images were taken with no time of flight just after the loading step of the dipole trap : the atoms we see are trapped in the arms of the dipole trap, before evaporation. Here the motorised mirror was adjusted so that the two arms are well overlapped in microgravity. During the standard and hypergravity phases, the arms of the dipole trap are separated by several hundred micrometers.

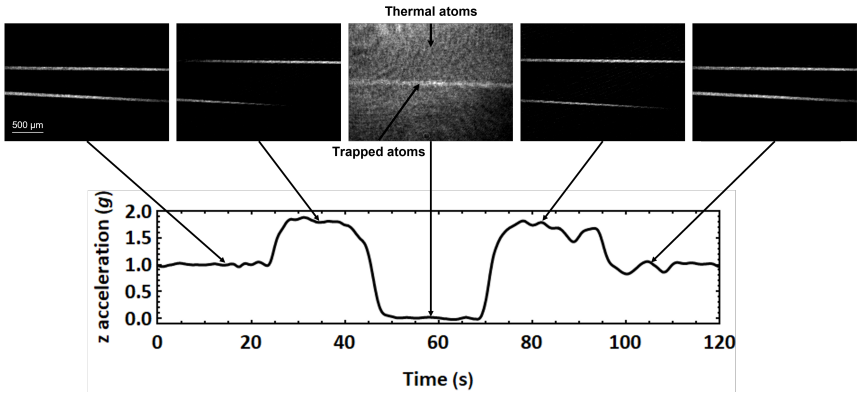

Figure 1.28: ***Acceleration profile along the z direction during the parabola and absorption images of the trapped atoms taken at different moments of the parabola.*** *- Outside of the zero g phase, the two arms of the dipole trap are clearly not overlapped. The pictures are taken 50 ms after turning off the cooling lasers which gives the remaining free atoms ample time to leave the detection zone when a g-force is perceptible (1 g and 2 g phases), and just after the loading in the dipole trap before evaporation. In microgravity however, the atoms outside the dipole trap are still visible, hence the lower contrast in the middle picture*

On the simulator, this issue appeared to be stronger after changing the main breadboard to a CFRP breadboard, probably due to a different distribution of masses on the sensorhead. By adding weights on different parts of the breadboard, this problem was partially resolved. In total, we added about 10 kg on the main breadboard under the mirror after the first pass. We were thus able to capture atoms in the dipole trap with the "new" configuration of the experiment. However, we were not able to reach the same temperature as we did with the previous setup : we consider now installing an active correction on the motorized mirror to solve the problem both on the plane and in the laboratory.

1.3 Radiofrequency and microwave sources

The radio-frequency and microwave signals used in the experiment are generated by a frequency chain whose architecture is presented in Figure 1.29. This frequency chain is divided into

two parts, dedicated respectively to rubidium and potassium. These two architectures share a common reference clock of 10 MHz delivered by an ultra-stable quartz oscillator developed within the framework of the Pharao atomic clock space project [[65]].

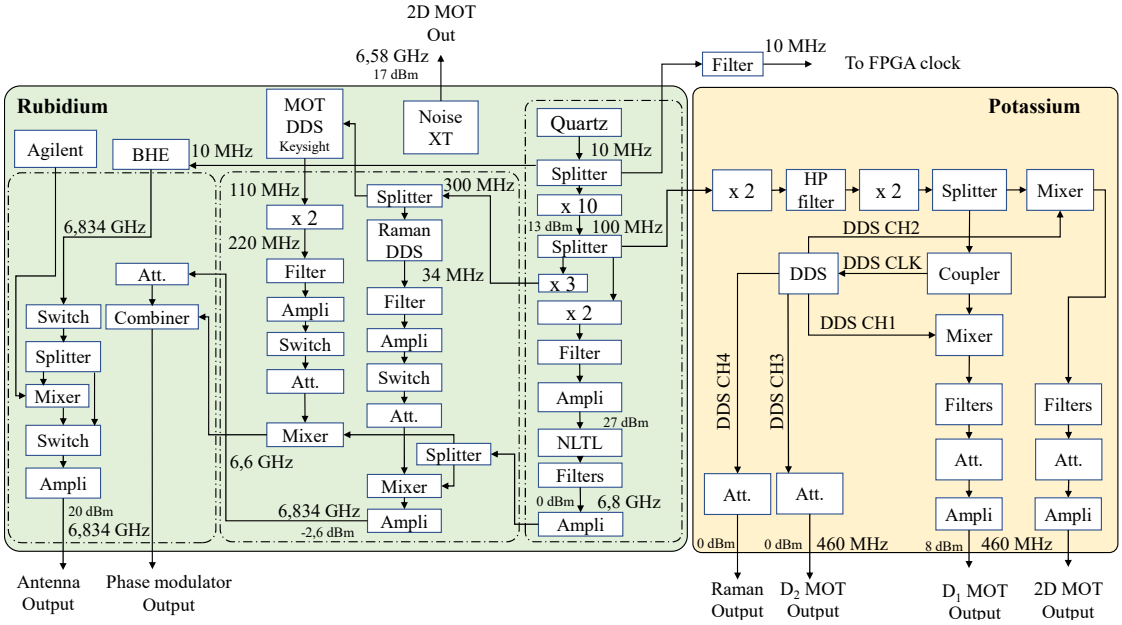

Figure 1.29: ***Functional diagram of Rubidium and Potassium radiofrequency chains*** *- DDS: Direct Digital Synthesizer; Att : Attenuator; NLTL: Nonlinear Transmission Line; AWG: Arbitrary Waveform Generator; EOM: Electro-Optic Modulator; PLL: Phase Locked Loop. The different subsections represent the drawers on the experiment, BHE: Bonn Hungarian Electronics, synthesizer.*

1.3.1 RF chain for rubidium

The Rubidium chain is based on the combination of three essential components: a Non-Linear Transmission Line (NLTL) and two synthesizers : a Keysight function generator corresponding to the "MOT" and a Direct Digital Synthesizers (DDS) fot tthe "Raman" channels. The NLTL generates a frequency comb with harmonics up to 7 GHz from a fundamental frequency of 200 MHz, which is obtained by multiplying the 10 MHz clock frequency. This comb is then filtered to retain only the frequency at 6,8 GHz.

The "MOT" and "Raman" DDS modules retrieve a common 300 MHz clock and generate frequencies around 220 MHz (after doubling) and 34 MHz, respectively. These outputs are then mixed with the 6,8 GHz signal from the NLTL and filtered to obtain the MOT frequency around 6,58 GHz and the Raman frequency around 6,834 GHz.

The two channels are then combined and sent to the electro-optic modulator (EOM) of our laser system to produce the sidebands required during our experimental sequence. The 6,58 GHz frequency, for example, generates the Repumper frequency during the MOT stage, while the 6,834 GHz frequency is used to produce the second Raman frequency during the interferometer pulses. It is worth noting that the Raman DDS module offers a frequency ramp functionality that we utilize to compensate for the Doppler effect when operating in standard gravity. Each of the two channels has its own switches and attenuators for fast switching, turning on/off, or power modulation.

A separated commercial system from Noise XT is used as a synthesizer to provide the RF source at 6,58 GHz for the EOM of the 2D MOT laser.

A synthesizer[32] serves as the microwave source used for atom state preparation. It is clocked by the 10 MHz coming from the Quartz. This source is tuned to the rubidium hyperfine transition (clock transition) and, in the presence of a magnetic field lifting the degeneracy of the Zeeman sublevels, allows for the transfer of atoms in the $m_F = 0$ state, which is insensitive to the magnetic field. This channel can be modulated using an external DDS to create two sidebands for transferring atoms in the $m_F = -1$ and $m_F = +1$ states. The latter option is used to refine the preparation of ultra-cold atoms (see section 2.7.3).

1.3.2 RF chain for potassium

The Potassium RF chain consists of four channels, namely "D1", "MOT", "Raman" and "2D MOT" all controlled by a single DDS with multiple output channels (AD9959 model). We provide this DDS with a 400 MHz clock and obtain output frequencies around 60 MHz, 28 MHz, and 38 MHz, respectively.

In the "D_1" and "2D MOT" channel, we extract the 400 MHz signal and mix it with the 60 MHz signal, which is then filtered to obtain a single frequency around 460 MHz. This radiofrequency signal then passes through an amplifier, a switch, and a variable attenuator before being sent to the electro-optic modulator of the D_1 laser and the 2D MOT laser respectively.

In the "MOT" and "Raman" channel, no specific action is taken except for the usual attenuation and switching steps. Finally, both the "MOT" and "Raman" channels are sent to the phase-locked loop (PLL) that controls the second Slave diode of the Potassium D_2 laser.A switch then allows only one of these two frequencies to be selected simultaneously, depending on the stage of the interferometric sequence.

1.4 Control and acquisition system

Due to the short duration of some steps, as small as a few microseconds, the experimental sequence demands precise synchronization of all the different systems involved.The control computer acts as a conductor to synchronize all systems. A sequencer coupled to a FPGA circuit and a software allows instructions to be sent in an analog manner during the experimental sequence.

1.4.1 Hardware structure

The hardware structure of our control and acquisition system is based on a PXI architecture, which is robust and compact, particularly suited to the field of measurement and instrumentation. We use a National Instrument chassis (model NI PXIe-1078) that offers up to 9 slots for inserting computers and input/output cards. In the current state of the experiment, we are using 6 of these slots.

The entire hardware includes:

- An NI PXIe-8135 controller acting as a computer.
- An NI PXIe-6363 input/output module, offering us 32 digital outputs. Three NI PXIe-6733 analog output modules (8 channels, 16 bits, 1 MS/s).

[32]BHE Bonn Hungarian Electronics, model BSVC14D

- An NI PXIe-6280 acquisition module (16 analog inputs, 18 bits, 625 kS/s).

Therefore, we have a total of 32 digital outputs associated with a TTL voltage level (0 or 5 V) and 24 analog outputs that can deliver a voltage between -10 and +10 V. We also have 16 analog inputs that can be used for acquiring experimental signals from photodetectors and mechanical accelerometers. Finally, digital trigger inputs allow us to synchronize these acquisitions with the rest of the experimental sequence. A "buffer" stage, designed and built by the laboratory's electronics department, serves as an interface between the outputs of the National Instruments cards and the rest of the experimental setup. This stage first physically "breaks out" all control channels to high-quality industrial connectors (LEMO type) located on the front panel, allowing each signal to be individually routed to the corresponding equipment. It also delivers the appropriate current to each physical channel by drawing from its own power supply rather than that of the National Instruments cards.

1.4.2 Software structure

From a software point of view, the management of our experimental sequence is ensured by the "Cicero Word Generator" (CWG) environment [[60]]. Available for free online, this software suite was specifically developed for the control of cold atom experiments by students at the Massachusetts Institute of Technology. The two main entities that make up CWG are "Cicero," the user interface for editing the experimental sequence, and "Atticus," the server responsible for translating the sequence into output buffers. At each new experimental cycle, all these buffers are loaded into a Field Programmable Gate Array (FPGA) circuit which transfers them to the analog and digital outputs of the National Instrument cards. The main disadvantage of CWG is related to the sequence loading time within the FPGA (about 1s), which fundamentally limits the repetition rate of the experimental cycle. However, the CWG environment allows sequencing of all outputs with a temporal resolution of less than a microsecond while offering a particularly clear and intuitive user interface. It also has the advantage of not limiting the number of physical channels that can be controlled simultaneously, and offers many useful features for measurement automation or troubleshooting (variable scanning, generation of a log after each cycle, manual control of physical channels, etc.). Parallel to CWG, we use the LabVIEW development platform to perform two additional functions: retrieving data recorded by the acquisition cards on the one hand, and communicating with the radio frequency (RF) chain's DDS on the other.

The images of the absorption imaging are monitored and saved in the computer using a dedicated LabView program. This program computes the optical density image and estimates the number of atoms and temperature of the clouds for monitoring, but the saved images are raw images and are post-processed using other Matlab programs for analysis.
For fluorescence imaging, we use a laptop and the manufacturer's software to monitor and save the images. This computer is placed on a shelf and attached with velcro for the flight campaigns.

1.5 Constraints linked to microgravity operation

Operating such an experiment on our platforms to access microgravity is a challenge. The experiment has to be transportable, compact and robust, while remaining modular and modifiable. In this section we present the different technical aspects linked to the operation both onboard the place and on our microgravity simulator in the lab.

1.5.1 Racks

The first main specificity of our experiment is the distribution of the different subsystems in several racks. We divided the experiment in 10 racks (when working with both rubidium and potassium), as presented in Figure 1.1. They have to meet a series of requirements to be allowed in the plane, such as a maximum weight of 200 kg per rack and a condition on the center of mass. They are composed of a primary structure made of Rexroth Bosch items (40 mm strut profiles, connecting elements, bolt, screws ...) and machined aluminum plates used as the baseplates ensuring the interface with the aircraft fastening system. The structure of these racks is presented in Figure 1.30.

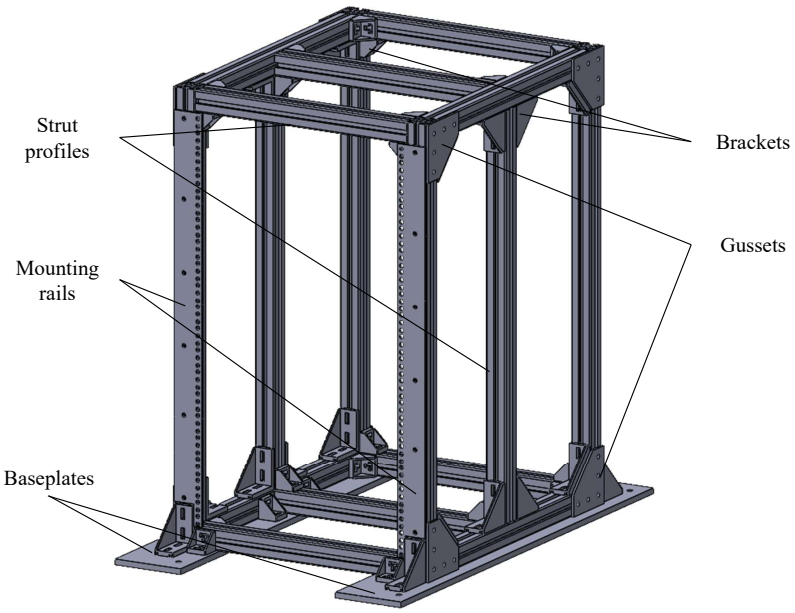

Figure 1.30: ***Solidworks model of a rack on the experiment***

The different sub-systems of the experiment are in the form of 3U drawers or shelves that are fixed on the mounting rails on the front of the rack. One of the challenges of the first flight campaign in March 2022 was to rebuild and adapt all ten racks to the safety requirements, due to the increase on the requirements from Novespace since the last flight campaign in 2019.

1.5.2 Safety requirements for the plane

For each flight campaign, a large document (about 130 pages) must be provided to inform Novespace about the experiment. It exhaustively lists all the systems and subsystems, their operation, power supplies, and electrical connections. It is therefore necessary to be very rigorous and keep track of all changes made to the experiment.

The safety rules for the Zero G flights are the same as those applied to commercial flights. As passengers and experimenters fly with the experiment, numerous safety aspects must be studied : use of lasers, use of heating systems, etc.
In our case, the use of lasers forces us to equip each laser rack with a light signal linked to an interlock and also to have a key switch on every laser systems.
Another aspect that has to be taken into account are the heating systems (Peltier modules) used to keep the laser diodes and PPLN at temperature. To verify that this system did not present any risk even in the event of overheating, we conducted heating tests by simulating a worst-case scenario. To do this, we used a box that allowed us to control the temperature of a

diode's environment. A broken diode was used to utilize its internal Peltier, and the Peltier of the box was continuously supplied with a given current. We concluded that the system remains under the critical temperature for the maximum current allowed by the system, allowing us to use this system in the plane.

Conclusion

In conclusion, the design and implementation of this experimental setup required a careful consideration of the various components and their interactions. From the laser sources to the RF chain and the control system, each element has been optimized for its specific function while ensuring that it is compatible with the harsh operating environment of the Zero G plane. The sensor head has been designed with a focus on precision and robustness, enabling accurate measurements of the target properties. Despite the challenges posed by the environment, the system has been successfully tested and validated both in the lab and during parabolic flights. Overall, this work highlights the importance of the variety of disciplines and skills required for the development of this experiment, which can lead to successful and reliable results even in challenging conditions.

Chapter 2

Atomic sources of rubidium and potassium

Introduction

When conducting measurements using interferometry, the precision strongly depends on the **coherence of the source**. When considering optical interferometry as an analogy, the coherence of the source is linked to its frequency linewidth (temporal coherence) as well as its spatial mode purity (spatial coherence). For atom interferometry, the atomic samples are treated as wavepackets which coherence depends on the so called de Broglie wavelength, defined for a gas of atoms with mass m and temperature $\mathcal{T}$ as :

$$\lambda_{dB} = \frac{\hbar}{\sqrt{2\pi m k_b \mathcal{T}}} \tag{2.1}$$

The coherence is thus linked to the temperature of the cloud i.e. velocity distribution of the atoms; but also on the quality of its preparation in a specific state, insensitive to the magnetic field.

First, it is important to reduce the temperature of atoms to enhance the contrast, as well as to reduce their spatial expansion, which can limit the measurement time. The cooling of atoms using lasers is based on the study of light and matter interaction. It involves two distinct forces: a dissipative force caused by **radiation pressure** and a conservative force associated with the **dipole potential** created by light. Radiation pressure is a dissipative force that arises from the cycle of absorption and spontaneous emission of photons by atoms. During this process, photons are absorbed by atoms, causing their momentum to change, followed by spontaneous emission of photons in random directions, resulting in the atoms' deceleration. On the other hand, the dipole force arises from the interaction between the electric field of the laser light and the electric dipole moment of the atoms. It manifests as an exchange of photons in a specific mode of the laser light, effectively creating a conservative potential that allows for precise control and trapping of atoms.

Methods such as optical molasses use radiation pressure force to achieve temperatures at the order of a few microkelvins above absolute zero for rubidium and potassium, resulting in samples referred to as "cold" or "thermal". Dipole force of a high power laser is then used to reduce the temperature of rubidium samples to a few tens of nanokelvin, employing an evaporative cooling method in an all-optical dipole trap. In the case of these "ultra-cold" atoms, the Bose-Einstein condensation (BEC) threshold can be reached. At this point, the atoms can no longer be considered as a cloud of thermal atoms, and the concept of temperature is no longer associated with the agitation within the cloud. In this manuscript, we will use the term "temperature" for these sources to refer to their "equivalent temperature" measured from the spatial expansion of

the cloud, due to the interactions in the BEC. The application of these techniques in our experiment has allowed us to achieve condensation levels both on the ground and in our microgravity simulator. Despite the technical challenges posed by the microgravity environment, onboard the zero G aircraft, we successfully obtained ultracold atomic samples at 100nK. For potassium, the extension of these method is currently underway as it represents a crucial step towards a high-sensitivity test of the equivalence principle using two ultra-cold atomic sources.

Then, the cold or ultra-cold atom clouds are prepared in a suitable Zeeman sub level. For our applications, we prefer a state that is insensitive to magnetic fields. Techniques involving selective optical pumping or microwave irradiation can be employed on the cold atoms to achieve this. For the ultra-cold atomic sources, we will see that a spin distillation method has been successful in obtaining satisfactory state preparation.

In this section, we describe the different cooling and state preparation techniques and present the atomic samples we obtained on our experiment with both rubidium and potassium in standard gravity and on our microgravity platforms.

2.1 Measuring the temperature of the atomic samples

The temperature of the atomic sources we produce is a crucial parameter of the experiment that needs to be estimated with the highest possible precision. In this section, I present the two complementary and independent measurement methods that we employ to access this physical quantity.

2.1.1 Time of flight method

In the time of flight (TOF) method, the atoms are initially confined in the magneto-optical or in the dipole trap. The trap is then suddenly turned off, allowing the atoms to freely expand in space. The expansion is typically in the form of a cloud that spreads out as the atoms move apart from each other and is directly related to its temperature. By measuring the size of the cloud at different times after the release from the trap, one can determine the velocity distribution of the atoms. From the velocity distribution, the temperature of the atom cloud can be inferred using the principles of kinetic theory.

Each image is adjusted using a two-dimensional Gaussian function to extract the standard deviations in position associated with each transverse direction of the image. By capturing an image along the y axis, for example, we have access to the standard deviations σ_x and σ_z associated with the x and z directions. Finally, the temperatures $\mathcal{T}_x$ and $\mathcal{T}_z$ along each of these axes are determined by fitting the temporal evolutions of the standard deviations using the following functions:

$$\sigma_i(t) = (\sigma_i^2(0) + \frac{2k_B\mathcal{T}_i}{m} \times t^2)^{\frac{1}{2}} \tag{2.2}$$

For thermal atoms, this relation is linked to the Maxwell-Boltzmann distribution of velocities. The TOF method assumes that the expansion for a thermal cloud is adiabatic, meaning that there are no significant interactions or collisions between the atoms during the expansion.

For a BEC, the expansion of the cloud depends on the interactions within the cloud. If the cloud is dilute enough, these interactions remain weak, and fitting the cloud with a Gaussian model is relevant. When the cloud is strongly confined, and the sample is dense, the interactions are not negligible. It has been shown in [[29]] that if the Thomas-Fermi approximation applies, the cloud should be fitted by the sum of an inverted parabola to account for the condensed part and a wider Gaussian for the thermal cloud surrounding it. For our atomic samples, we suspect we are in this regime only for low times of flight; the cloud expands afterwards and becomes more dilute. As we perform the temperature analysis for TOFs varying from 1 to 20 ms, we apply a Gaussian fit that is relevant for the majority of the images.
As seen in Figure 2.1, the temperature of our rubidium sample is estimated using this method to be approximately 50 nK. The reliability of this measurement increases with the duration of the time of flight, but we are practically limited by the finite size of the imaging region. This is particularly true when operating with thermal atoms because of their rapid expansion, especially with potassium atoms, which undergo faster thermal expansion due to their low mass. This method is preferred for ultra-cold atomic samples. It also exhibits a significant limitation in standard gravity, as the cloud typically falls out of the field of view within 20 ms.

2.1.2 Counter-propagating Raman spectrum method

The second method of temperature estimation is based on the study of the spectrum of counter-propagating Raman transitions. We use Raman transitions to perform atom interferometry as well as spectroscopy to probe the energy levels and velocity distribution of the atoms. The

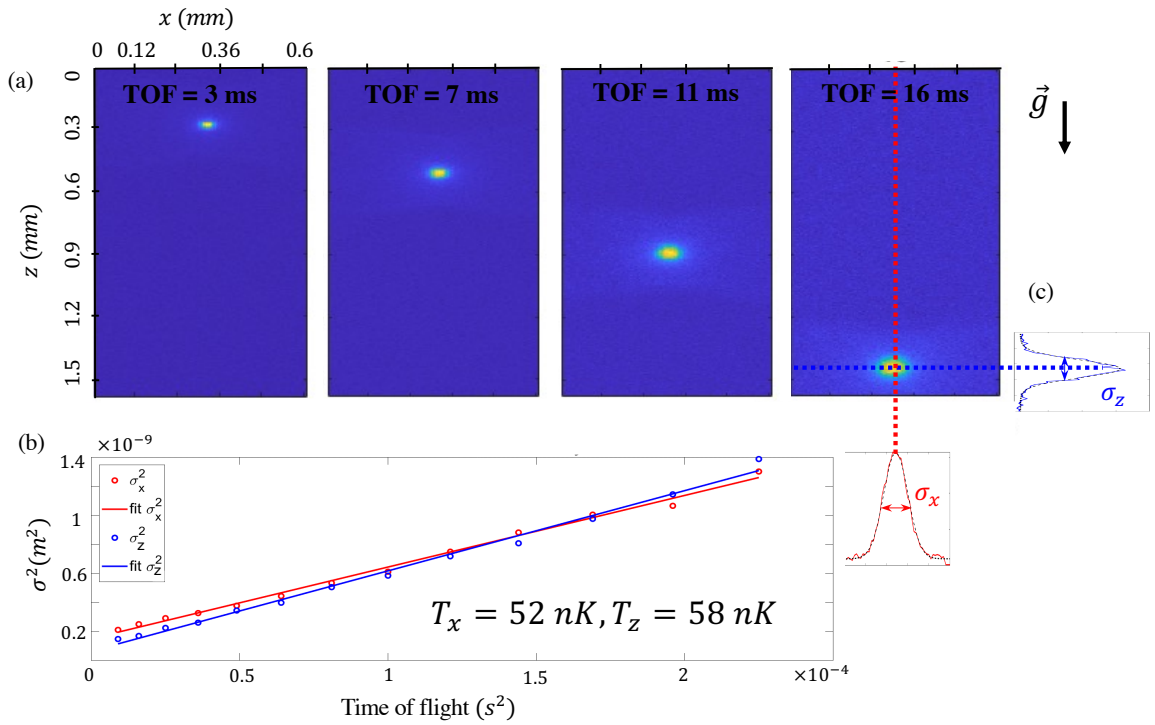

Figure 2.1: ***Time of flight method for the estimation of the atomic cloud temperature*** *- (a) Fluorescence images with the Andor camera of an ultra-cold atomic cloud for different times of flight : 3, 7, 11 and 16 ms. We can see the cloud falling in the gravity field and expanding due to its temperature. (b) A fitting the atomic Gaussian fit of the clouds in the x and z dimension shown in (c) enables to extract the spatial expansion σ_x and σ_z and deduce the temperature associated with the two directions. Here the estimated temperature is about 50 nK.*

two-photon process involved is described in section 3.1.1.

The spectral profile of the scattered light is directly related to the velocity distribution, with broader profiles indicating higher temperatures and narrower profiles indicating lower temperatures : it is given by the convolution of the velocity distribution of the cloud (a Gaussian distribution with standard deviation $\sigma_v = \sqrt{\frac{2k_B\mathcal{T}}{m}}$) and the Fourier transform of the Raman pulse shape. In the case of a "square" pulse with duration τ_π, the Fourier transform is strictly a *sinc* function. However, if we approximate this *sinc* function as a Gaussian with standard deviation σ_{co}, we can consider the convolution with the velocity distribution of the cloud to be a Gaussian as well, with a standard deviation given by :

$$\sigma_{counter} = (k_{eff}^2\sigma_v^2 + \sigma_{co}^2)^{\frac{1}{2}} = (k_{eff}^2\frac{k_B\mathcal{T}}{m} + \sigma_{co}^2)^{\frac{1}{2}} \tag{2.3}$$

After obtaining a Raman frequency scan spectrum, we perform a Gaussian fit of the contra-propagating and the residual co-propagating peaks to determine their respective standard deviations, $\sigma_{counter}$ and σ_{co}. The co-propagating peak is due to an imperfection on the polarization of the Raman beam and is not sensitive to the velocities in the atomic cloud, it is proportional to the Fourier transform of the pulse shape[1]. Finally, we infer the temperature of the sample by inverting the relationship 2.3.

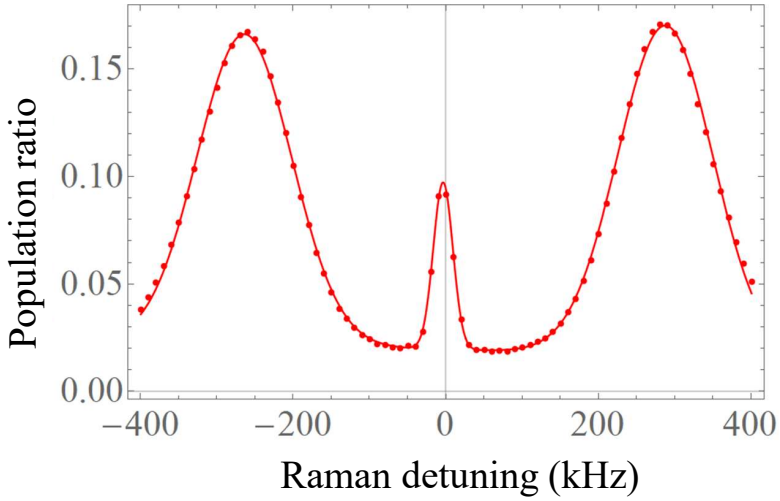

Figure 2.2: ***Counter-propagating Raman spectrum for cold atoms and Gaussian fits for temperature estimation*** *- the fit extracts three parameters for each peak : amplitude, center and width σ. In this example, the co-propagating peaks has a 18 kHz estimated width, and the two counter-propagating peak a 87 and 88 kHz width. The duration of the pulse is 36 μs. The corresponding temperature is 6 μK.*

The figure 2.2 shows an example of this method for recent data taken with a cold sample of rubidium on the experiment. The Raman pulse is not performed at maximum intensity : this way, the π pulse is longer (in comparison to the pulses used for atom interferometry) and the resolution on the spectrum is higher. The estimated temperature with this method is 6 μK, for a pulse of 36 μs duration.

This method is convenient for thermal atoms. For colder atomic sample, the width of the peak is no longer limited by the temperature of the atoms but by the time duration of the Raman

[1]We note that the pulse duration for the Raman spectrum is chosen to satisfy the π condition in the counter-propagating transition (resulting in maximum transfer to the excited state), which is not the same as the duration for the co-propagating pulse.

pulse, which is why we prefer the first method for the temperature estimation of our ultra-cold sources.

2.2 Laser cooling of rubidium and potassium

The generation of our cold atomic samples involves the utilization of magneto-optical trapping (MOT) and optical molasses techniques developed in the 80's[[33, 40]]. In this section, we provide a detailed description of the various steps involved in the preparation of potassium and rubidium samples.

2.2.1 Magneto-optical trap

The initial step in our experimental sequence is the loading of a magneto-optical trap (MOT), which enables both Doppler cooling and trapping of atoms at the center of our vacuum chamber. This type of cooling relies on the radiation pressure force exerted by lasers on atoms through cycles of absorption and spontaneous emission of photons. The atoms experience both a friction force, which cools them by opposing their motion, and a restoring force, which brings them back to the position of zero magnetic field, thus trapping them.

The effectiveness of the MOT relies on the presence of a cycling transition between two atomic levels. For alkali atoms like rubidium ^{87}Rb, a "Cooling" laser beam tuned to the red side of the $|F = 2\rangle \rightarrow |F' = 3\rangle$ transition is typically used. However, there is a non-zero probability for atoms to populate the $|F' = 2\rangle$ level and subsequently decay to $|F = 1\rangle$, rendering them "transparent" to the trapping and cooling forces. To counteract this detrimental optical pumping effect, a second laser frequency, known as "repumping," is tuned to the$|F = 1\rangle \rightarrow |F' = 2\rangle$ transition. It reintroduces atoms into the cycling transition, thereby maintaining the radiation pressure force. This cycling transition allows us to simplify the system to two levels with a fundamental state and an excited state of linewidth Γ, linked to the lifetime of the atoms in this level.

Experimentally, the necessary friction and restoring forces for producing the 3D MOT are generated by the combination of the 6 laser beams (three retro-reflected beams) and gradient coils. The gradient coils are driven by a current of 5.6 A to induce a magnetic field gradient of 15 G/cm at the center of the chamber. For ^{87}Rb, the 6 beams of the 3D MOT generate a total intensity of approximately $I_{cool} = 40 I_{sat}$ on the atoms, where I_{sat} is 1.67 mW/cm^2, the saturation intensity for a circularly polarized light [[96]]. The Cooling frequency is detuned by 18 MHz to the red side of the atomic transition $|F = 2\rangle \rightarrow |F' = 3\rangle$. In our laser system, the repumping is created by modulating the Cooling laser using an EOM (see section 1.1), the amplitude of this modulation sets the intensity ratio with the repumping frequency to $I_{rep}/I_{cool} = 0.1$.

The cooling techniques for potassium ^{39}K are particularly challenging to implement due to its particularly compact atomic structure, as shown in Figure 1.2 from Chapter 1. Defining a cycling transition is difficult because only 33 MHz separates $|F = 0\rangle$ and $|F = 3\rangle$ in the excited state. The terms "Cooling" and "repumping" also lose their meaning, but we will continue to use them to differentiate the optical frequencies inducing transitions from $|F = 2\rangle$ and those based on $|F = 1\rangle$.

During the loading of the magneto-optical trap (MOT), the parameters are fixed at constant values. The detuning of the Cooling laser is 40 MHz from the $|F = 2\rangle \rightarrow |F = 0\rangle$ transition, and the detuning of the repumping laser is 22.6 MHz from the $|F = 1\rangle \rightarrow |F = 0\rangle$ transition. In this situation, both optical frequencies participate to the cooling process here, which is why they are both red-detuned from the transition. As a result, there is an increased need for power,

and at this stage, we deliver the maximum available optical power while attempting to maintain a relatively balanced distribution between the two frequencies. The total intensity at the atom level, taking into account the contribution of the 6 beams, is approximately 22 I_{sat} for the Cooling and 12 I_{sat} for the repumping, where $I_{sat} = 1.75$ mW/cm^2 (for circularly polarized light)[[101]]. Ideally, other groups[[89, 55]] have found an optimum ratio of about 1 between the cooling and repumping light. However in our setup, the distribution of optical powers from the two slave lasers of the D_2 laser system in the micro-optical bench was set during the fabrication process, favoring slave 1 (Cooling) over slave 2 (Repumping). We find a trade off by sending the maximum intensity possible for repumping, resulting in a ratio of one third.

2D MOT atomic source

In our case, the magneto-optical trap in the main chamber is loaded from the directed atomic flux delivered by the recently installed 2D MOT device[2]. This source was custom-made to be used with both rubidium and potassium atoms.

In the case of rubidium, the manufacturer specifies an atomic flux greater than 10^9 atoms/s. In practice, this flux depends on various experimental conditions such as the power and detuning of the MOT and Push beams, as well as the level of vacuum in the cell (rubidium or potassium residual pressure in the cell). We generally work with a detuning of 18 MHz ($\approx 3\Gamma$) in the red of the atomic resonance for the Cooling frequency. The same detuning is applied for the 3D MOT lasers. The optical powers associated with the cooling and repump frequencies are fixed at 50 mW and 5 mW on each MOT path, and at 5 mW and 500 µW on the pusher path, for a dispenser current of 3 A. Under these conditions, we estimate the effective atomic flux to be approximately 10^8 atoms/s. However, this estimate is subject to some variation, as it is based solely on the measurement of the temporal evolution of the fluorescence signal of the 3D MOT in the main chamber. Only the portion of the atomic flux actually loaded into the 3D MOT is thus evaluated. The distance between the pinhole and the 3D MOT is 12.5 cm.
This flux allows us to load a 3D MOT with several tens of millions of atoms in half a second typically, while maintaining a very good vacuum level in the science chamber (of the order of 10^{-10} mbar). It is also still possible to load the 3D MOT from dispensers preset in the main chamber, as it was done in the experiment before the addition of the 2D MOT.

In comparison, before the installation of the 2D MOT, 4 seconds were necessary to load a similar atom number from the main chamber dispensers (for a 4A current). This low residual pressure has a dual interest for our application since it improves both the quality of our ultracold source (by reducing the probability of collision with thermal atoms) and that of our detection (by limiting the level of atomic background noise). The speed of loading induces an improvement in the repetition rate of the experimental sequence, which is a real advantage for operation in 0g aircraft where the durations of microgravity are very limited.

For potassium, no specification was given by the manufacturer because the system is originally designed only for rubidium and is a custom-design (one rubidium dispenser was replaced by a potassium dispenser, the rest of the system is unchanged). We were able to successfully load the 3D MOT from the 2D MOT with both rubidium and potassium, as shown on the detection signal presented in section 1.2.5 in Figure 1.21. We estimate that we have gained at least a factor of 3 in the number of atoms for a fixed loading time in the 3D MOT by loading from the 2D MOT.
The laser sources used for the rubidium and potassium 2D MOT are described in section 1.1.

[2]Commercial 2D MOT device by ColdQuanta CASC (Cold Atoms Source Cell)

For a MOT, the only time constant that is considered is Γ^{-1}, where the associated energy $\hbar\Gamma$ sets the limit for Doppler cooling. This limit affects the achievable temperature reduction and the maximum density of trapped atoms. To overcome this limitation, one must consider transitions with multiple internal ground states to enable the emergence of longer time constants. Additional cooling techniques using these models can be employed, known as 'sub-Doppler cooling'.

2.2.2 Red molasses

Here, we will briefly review a simplified theoretical background of sub-Doppler cooling and its application in our experiment for both rubidium and potassium.

Theoretical approach

When considering a system with different ground states, which is closer to the real atomic structure of our samples, temperatures below the Doppler limit can be obtained using optical molasses technique. In our experiment, we perform "red molasses" cooling, which can be referred as "bright Sisyphus cooling". Red molasses, also known as polarization gradient cooling, involves using a combination of laser beams with detuned frequencies. By carefully tuning the laser frequencies and intensities, it is possible to create a spatially varying light intensity and polarization, which generates a restoring force that counteracts the motion of the atoms. A simplified presentation of the Sysiphus effect will be presented in this section, based on [[41]].

We consider a one-dimensional system with an atomic transition $J_g = 1/2 \rightarrow J_e = 3/2$ and two counter-propagating lasers with a polarization configuration σ_+, σ_-, as shown in figure 2.3.

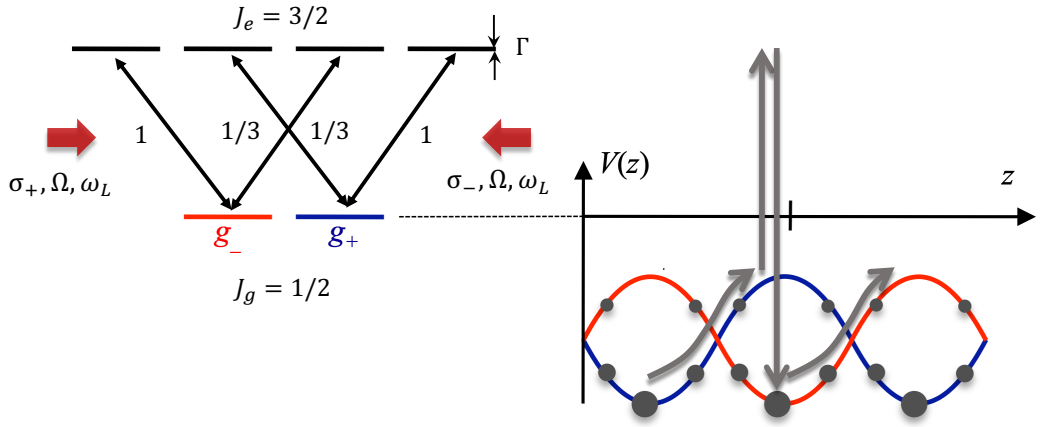

Figure 2.3: ***Atomic transition*** $J_g = 1/2 \rightarrow J_e = 3/2$ ***and potential created by the light-shift on the ground states leading to Sisyphus cooling*** *- with two counter-propagating lasers with polarization* $\sigma_\pm$*, of frequency* ω_L Δ*-detuned from the atomic transition* ω_A *and of Rabi pulsation* Ω*. The Zeeman sublevels are presented with the Clebsch-Gordan coefficients associated with the transitions for this polarization configuration. The gray circles indicate the stationary populations resulting from the optical pumping. The gray arrows represent the typical evolution of the energy of an atom with initial velocity* v *[[41]].*

This optical configuration of the lasers creates a lattice with a gradient of polarization along the propagation axis z. Two major ingredients are necessary to Sysiphus cooling, provided by the interaction of the lasers with the atoms:

- The generation of a bipotential $V_\pm$ created thanks to lightshifts on the ground states $|g_+\rangle$ and $|g_-\rangle$. At a given position z, the energy of the state g_+ is shifted by a quantity

proportional to $I_+(z) + 1/3I_-(z)$, where $I_\pm$(z) are the intensities linked to the $\sigma_\pm$ polarizations. Respectively, the energy of the state g_- is shifted by a quantity proportional to $I_-(z) + 1/3I_+(z)$. The potentials seen by the ground states $g_\pm$ are :

$$\begin{cases} V_+(z) = V_0 cos^2(kz) + cst \\ V_-(z) = V_0 sin^2(kz) + cst \end{cases} \tag{2.4}$$

with the energy $V_0 = \frac{2}{3}\hbar(-\Delta)s_0$, s_0 being the saturation parameter $s_0 = \frac{\Omega^2/2}{\Delta^2+\Gamma^2/4}$, where Ω is the Rabi pulsation linked to each progressive wave for a Clebsh-Gordan coefficient of 1.

- An optical pumping configuration that tends to accumulate the atoms in the ground state of lowest energy. The rate $\gamma_{\pm\to\mp}$ of the transfer between $g_\pm$ and $g_\mp$ is

$$\begin{cases} \gamma_{+\to-}(z) = \gamma_0 \cos^2(kz) \\ \gamma_{-\to+}(z) = \gamma_0 \sin^2(kz) \end{cases} \tag{2.5}$$

with $\gamma_0 = \frac{2}{9}\Gamma s_0$. The optical pumping is correlated to the lightshift of the ground state and one can obtain the stationary populations $P_\pm^{stat}$ of the $g_\pm$ states:

$$\begin{cases} P_{stat,+}(z) = \sin^2(kz) \\ P_{stat,-}(z) = \cos^2(kz) \end{cases} \tag{2.6}$$

The atoms tend to populate the level of lowest energy, going from the top of the "hills" of potential to the bottom.

Considering an atom with velocity v, it will climb the hills of potential and convert its kinetic energy into potential energy. When on top of the hill, the optical pumping process will occur and this energy will be transferred to a photon emitted by fluorescence, and the atom is back to a minimum of potential. The atom more often climbs the potential than it descends, in the manner of Sisyphus in the eponymous Greek myth, carrying his burden up the mountain only to see it fall back down every day. This model can be generalized to three dimensions for a transition $J_g \to J_e = J_g + 1$ and with a detuning $\Delta = \omega_L - \omega_A < 0$, which means the laser is detuned in the red of the transition. In average, the energy of the atom decreases to be transferred to the photons, once again using spontaneous emission phenomenon. The effect on a particle with velocity v in the lattice can be seen as a friction force $F(z, v)$ deriving from the bipotential $V_\pm(z)$, that will slow down the atoms in the cloud resulting in a reduction of the overall temperature.
The multiple diffusion in the cloud linked to the numerous absorption-emission cycles limits the temperature achievable by this technique. By taking advantage of states uncoupled to light called dark states, it is possible to overcome this limit with a technique called gray molasses.

Red molasses on the experiment

For ^{87}Rb, at the end of the MOT loading process, we switch off the magnetic field gradient and linearly increase the detuning of the cooling beam from -3Γ to -24Γ. This 7 ms step, known as the dynamic detuning molasses, is accompanied by a decrease in intensity by a factor of 15, reaching approximately I_{sat}. The temperature at the end of the molasses is around around 6 μK (see figure 2.2). This temperature is sufficient to perform interferometric measurements as we will see in section 3. However, to load atoms in the dipole trap in order to obtain ultra-cold sources, we need to increase the phase space density of the atomic cloud. We turn to gray molasses cooling techniques, which will be discussed in the following section. The experimental sequence for the red molasses cooling of rubidium is presented in Figure 2.4.

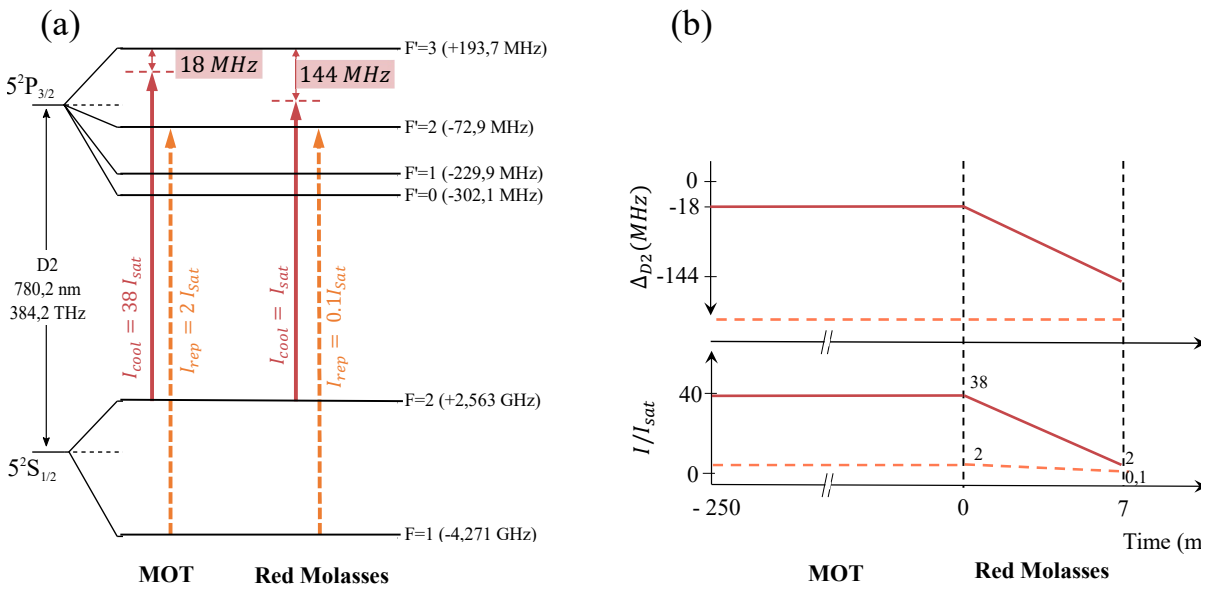

Figure 2.4: ***Red molasses cooling sequence for*** ^{87}***Rb*** *- (a) Hyperfine structure and laser configuration during the MOT and Red Molasses stages. (b) Schematic view of the cooling sequence.* Δ_{D2} *represents the detuning with respect to the transition* $|F = 1, 2\rangle \rightarrow |F' = 3\rangle$ *. The solid red and dashed orange lines correspond to the Cooling and Repumping frequencies, respectively. All the mentioned intensities include the contribution from the 6 beams.*

For ^{39}K, we implement a sequence previously described by a former PhD student in our experiment[[5]]. This sequence includes a red molasses phase lasting 5 ms that starts immediately after turning off the MOT coils. The selection of detunings is based on the studies conducted by [[63]] and [[55]]. The detunings and intensities of the cooling and repumping beams are abruptly reduced to 16 MHz and 7.4 MHz respectively, in the red of the transitions $|F = 2\rangle \rightarrow |F' = 3\rangle$ and $|F = 1\rangle \rightarrow |F' = 2\rangle$, while their respective total intensities are set to approximately 2 and 1 I_{sat}. The experimental sequence for the red molasses cooling of potassium is presented in Figure 2.5.

This red molasses cooling method allows us to achieve a temperature estimated at 12 μK. Although this is already a good result for ^{39}K, we continually strive to further lower this temperature in order to improve the coherence of our atomic source and increase the contrast of our interference fringes. As for ^{87}Rb, to load ^{39}K more efficiently into an optical dipole trap, we implement gray molasses[[90]].

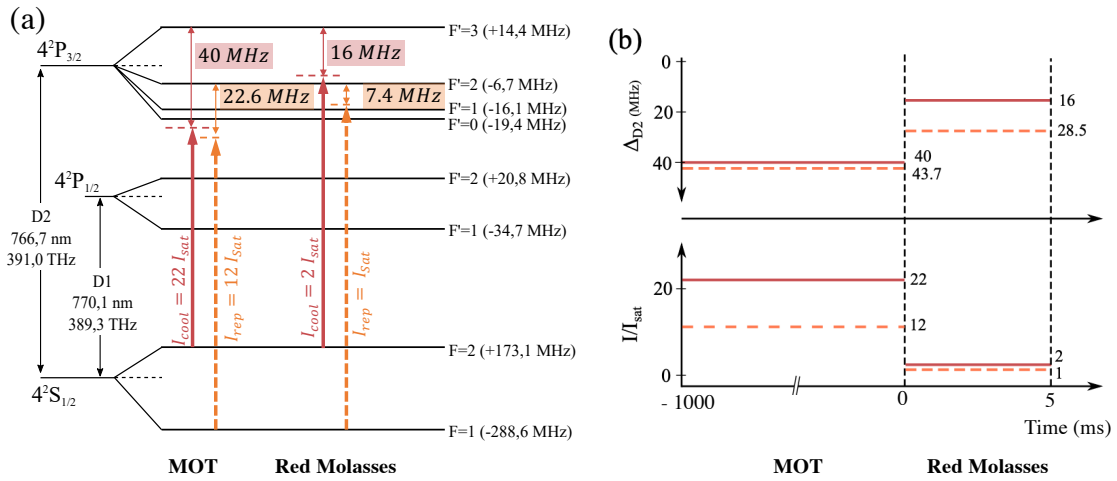

Figure 2.5: ***Red molasses cooling sequence for*** ^{39}K *- (a) Hyperfine structure and laser configuration during the MOT and Red Molasses stages. (b) Schematic view of the cooling sequence.* Δ_{D2} *represents the detuning with respect to the transition* $|F = 1, 2\rangle \rightarrow |F' = 3\rangle$ *. The solid red and dashed orange lines correspond to the Cooling and Repumping frequencies, respectively. All the mentioned intensities include the contribution from the 6 beams.*

2.3 Gray molasses of rubidium and potassium

In order to further improve the cooling capabilities and achieve even lower temperatures and higher densities in our experiment, we implemented a technique known as "gray molasses." Gray molasses is a variation of molasses cooling that offers enhanced cooling efficiency compared to traditional red molasses techniques. In this section, we will explore the principles and implementation of gray molasses in our experimental setup for rubidium and potassium.

2.3.1 Theoretical study of gray molasses

In the previous description of Sisyphus cooling, the general idea lied in the accumulation of atoms in the ground state of lowest energy by optical pumping with a sinusoidal modulation due to the red-detuned lasers. This state is highly coupled to the laser light and the fluorescence was maximized, if J_g<J_e, which is the case for the $|4^2S_{1/2}, F = 1, 2\rangle$ ground state and $|4^2P_{3/2}, F' = 3\rangle$ excited state both for the D_2 line of rubidium and potassium. For gray molasses, we consider a situation where $J_g \geq J_e$. It can be shown that when the coupling from the ground state J_g to the excited state J_e is directed towards a lower-dimensional space, there exists a linear combination of the ground states that is not coupled to the excited state by light. These states are called "dark states" because they are transparent to the laser. In the case of the D_2 line of rubidium, a gray molasses can be performed on $|4^2S_{1/2}, F = 1, 2\rangle \rightarrow |4^2P_{3/2}, F' = 2\rangle$. For potassium, we will see that the gray molasses can be performed on the D_1 line.

The cooling mechanism of gray molasses is based on the association of Velocity Selective Coherent Population Trapping (VSCPT) in the presence of so-called "dark states" and Sisyphus cooling. This section is based on the models detailed in [[41, 35]].

Λ configuration and dark states

Here we provide a simplified description of dark-states cooling in order to understand the mechanism of gray molasses. We consider a 3-level system ($|g_1\rangle, |g_2\rangle, |e\rangle$) as shown in Figure 2.3. We

consider two counter-propagating laser waves along the z-axis, phase-shifted by ϕ, whose linear combination of $\sigma^+ - \sigma^-$ polarization allows for spatial modulation of intensities. For each wave, we define the detuning $\Delta_i = \omega_i - \omega_{0i}$, where ω_i corresponds to the frequency of wave i and ω_{0i} is the frequency of transition $|g\rangle \to |e\rangle$, and the Rabi frequency, dependent on z:

$$\Omega_1(z) = \Omega_1 \cos(kz + \phi) \quad \text{and} \quad \Omega_2(z) = \Omega_2 \cos(kz) \tag{2.7}$$

Initially, we assume the atom has zero velocity. We define the system using the atomic Hamiltonian H_A and the atom-laser coupling V_{AL} in the rotating frame, applying the unitary transformation $T(t) = e^{-i(\omega_1 t|g_1\rangle\langle g_1| + \omega_2 t|g_2\rangle\langle g_2|)}$. We then obtain

$$H_A = \Delta_1|g_1\rangle\langle g_1| + \Delta_2|g_2\rangle\langle g_2| \tag{2.8}$$

and

$$V_{\text{AL}}(z) = \frac{\Omega_1^2}{2}\cos(kz + \phi)|e\rangle\langle g_1| + \frac{\Omega_2^2}{2}\cos(kz)|e\rangle\langle g_2| + \text{h.c.} \tag{2.9}$$

There exists a linear combination of $|g_1\rangle$ and $|g_2\rangle$ that corresponds to an uncoupled state Ψ_{NC} with respect to $|e\rangle$, so that $V_{AL}(z)\Psi_{NC} = 0$:

$$|\Psi_{NC}\rangle = \frac{\Omega_2 \cos(kz)|g_1\rangle - \Omega_1 \cos(kz + \phi)|g_2\rangle}{\sqrt{\Omega_1(z)^2 + \Omega_2(z)^2}} \tag{2.10}$$

We can then express the evolution of the system by taking into account the spontaneous emission due to the lifetime Γ of the excited state. We can write the optical Bloch equations (the detailed calculations can be found in [[35]]), and apply it to the density matrix of the non-coupled state $\rho_{NC} = |\Psi_{NC}\rangle\langle\Psi_{NC}|$. We find that $\dot{\rho}_{NC} = 0$ in the case where $\Delta_2 - \Delta_1 = 0$, which means atoms in $|\Psi_{NC}\rangle$ will not evolve with time. We can see this effect as an interference phenomenon between the two possible paths that can lead from $|\Psi_{NC}\rangle$ to $|e\rangle$: $|g_1\rangle \to |e\rangle$ and $|g_2\rangle \to |e\rangle$.

This means that at the Raman resonance condition, the system exhibits a dark state in which atoms with zero velocity are trapped.

We now assume that the atom has a certain velocity $v = z/t$. For the following analysis, we consider the basis $\{|e\rangle, |\Psi_C\rangle, |\Psi_{NC}\rangle\}$, in which we introduce the coupled state $|\Psi_C\rangle$. This change of basis is represented by passage from the left to right part of Figure 2.6.

$$\begin{cases} |\Psi_C\rangle = \sqrt{\frac{1}{\Omega_1^2(z)+\Omega_2^2(z)}}\left(\Omega_1(z)|g_1\rangle + \Omega_2(z)|g_2\rangle\right) \\ |\Psi_{NC}\rangle = \sqrt{\frac{1}{\Omega_1^2(z)+\Omega_2^2(z)}}\left(\Omega_2(z)|g_1\rangle - \Omega_1(z)|g_2\rangle\right) \end{cases} \tag{2.11}$$

This system reveals a new Hamiltonian, $V_{\text{mot}} = -i\hbar\langle\Psi_C|\frac{d}{dt}|\Psi_{NC}\rangle$, which takes into account the motional coupling terms. By defining a variable $A(z)$ dependent on z that satisfies the equations 2.12:

$$\begin{cases} \frac{d}{dz}(|\Psi_C\rangle) & = A(z)|\Psi_{NC}\rangle \\ \frac{d}{dz}(|\Psi_{NC}\rangle) & = -A(z)|\Psi_C\rangle \end{cases} \tag{2.12}$$

We can then write the motional coupling V_{mot} between the states Ψ_C and Ψ_{NC}:

$$V_{\text{mot}} = -i\hbar v\langle\Psi_C|\frac{d}{dz}|\Psi_{NC}\rangle = i\hbar v A(z) \tag{2.13}$$

where $A(z)$ is in the form $k\sin(\varphi)\frac{\Omega_1(z)\Omega_2(z)}{\Omega_1^2(z)+\Omega_2^2(z)}$. The atom's velocity v induces a new coupling that allows the transfer from the uncoupled state to the coupled state. The coupling rate between these two states is increased with the velocity.

Gray Sysiphus cooling

The modulation of intensities mentioned earlier generates a spatially modulated lightshift ΔE on the coupled state. In order to achieve Sisyphus cooling, this light shift should be positive so that the non coupled state remains the lowest-energy ground state. As observed in Figure 2.6, ΔE is minimized at the troughs of the modulation. Equation 2.14 shows that this condition on the light shift implies a positive laser detuning $\delta = \Delta_1 = \Delta_2$, meaning towards the blue side,

$$\Delta E = \hbar\delta \frac{\Omega_1(z)^2 + \Omega_2(z)^2}{4\delta^2 + \Gamma^2} \quad \text{and} \quad \gamma = \Gamma \frac{\Omega_1(z)^2 + \Omega_2(z)^2}{4\delta^2 + \Gamma^2}. \tag{2.14}$$

The laser light also induces optical pumping processes. Atoms in the coupled state tend to be transferred and accumulate in the uncoupled state. The transfer rate through optical pumping γ, as given in Equation (2.14), is also spatially modulated due to its dependence on the Rabi frequencies.

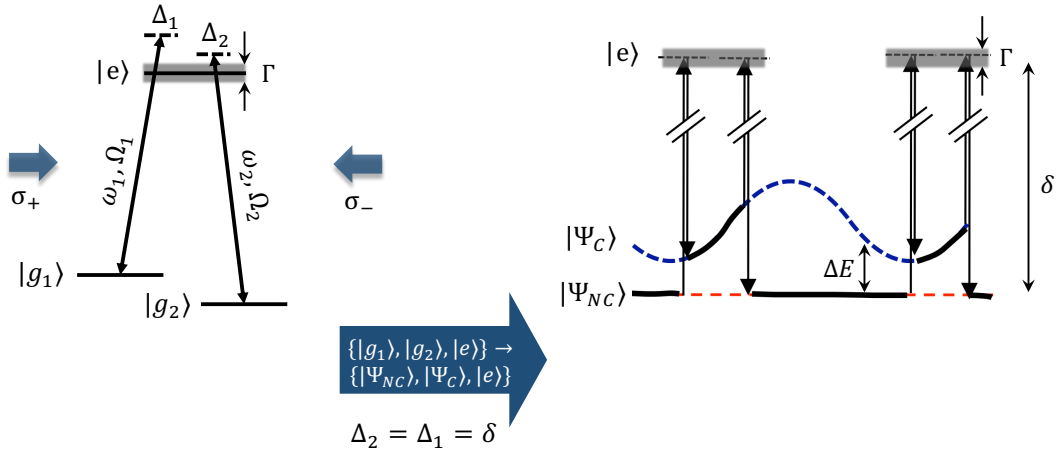

Figure 2.6: ***Atomic transitions and change of basis in the presence of the laser beams that lead to the gray Sisyphus effect*** *- with two counter-propagating lasers with polarization $\sigma_\pm$, of frequency $\omega_{1,2}$ $\Delta_{1,2}$-detuned from the atomic transition ω_A and of Rabi pulsation $\Omega_{1,2}$. The motional coupling enables the transfer from the non coupled state to the coupled state when the energy differnce is at its minimum. When on the top of the hill of the coupled potential, optical pumping transfers the atoms back in the non-coupled state[[41]].*

We now have all the elements to describe the cycle performed by the atom in a gray molasses process, as depicted in Figure 2.6. Let's consider the atom initially in the uncoupled state. When the energy difference between the coupled and uncoupled states is minimal, the probability of the atom being transferred to the coupled state through motion-induced coupling is maximal. Once in the coupled state, the atom climbs the potential hill until it enters an optical pumping cycle that brings it back to the uncoupled state. On average, the atom loses energy if the conditions $\Delta_1 = \Delta_2$ (Raman condition) and $\delta > 0$ are satisfied. In this gray Sisyphus effect, we both create a friction force that reduces the velocity of the atoms but we also selectively accumulate the atoms of zero velocity in a weakly-coupled and thus not completely dark state, a so-called gray state.

More complete descriptions of this phenomenon by taking into account several magnetic states can be done by studying a so called Λ-enhanced system [[79, 83]], we will not explain this model in this manuscript.

2.3.2 Gray molasses of ^{39}K

As seen previously, the hyperfine structure of potassium is highly compact. Detuning the laser to the blue side of the D_2 transition used for potassium MOT is challenging due to the presence of other sublevels. Therefore, for this atom, an additional cooling laser is added, tuned to the D_1 transition of potassium, which does not have the F'=3 level but also exhibits dark states. The laser frequencies are directed onto the atoms through the collimators of the 3D MOT, necessitating a σ_+/σ_- polarization configuration of the counter-propagating beams along each of the three axes. The transition is not closed, each excited sub-level $|F' = 2\rangle$ and $|F' = 1\rangle$ can transfer to the fundamental states. It is thus necessary to consider both sublevels and the two frequencies will not be seen as a cooling and a repumper beams but as two cooling lasers. Our cooling method is based on [[89]]. The "optimized" experimental sequence is presented in Figure 2.7.

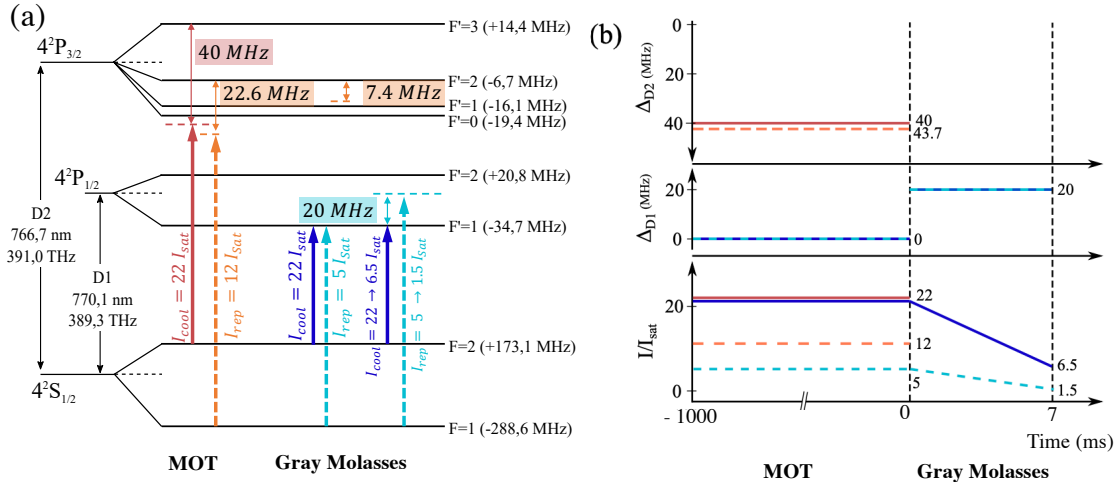

Figure 2.7: ***Gray molasses cooling sequence for ^{39}K*** *- (a) Hyperfine structure and laser configuration during the MOT and Gray Molasses stages. (b) Schematic view of the cooling sequence. The solid red and dashed orange lines correspond, respectively, to the Cooling and Repumper frequencies on the D_2 transition. The solid blue and dashed cyan lines are associated with the Cooling and Repumper frequencies on the D_1 transition. All the intensities mentioned here take into account the contribution from the 6 beams.*

The D_1 laser is turned on during the loading phase of the MOT, with the "Cooling" and "Repumper" optical frequencies resonantly tuned to the transitions $|F = 2\rangle \rightarrow |F' = 2\rangle$ and $|F = 1\rangle \rightarrow |F' = 2\rangle$, respectively. The intensity ratio I_{rep}/I_{cool} is set to 0.2, resulting in a total intensity on the atoms of 27 I_{sat}. It is experimentally verified that the addition of this resonant light on the D_1 transition during the MOT loading phase leads to a slight increase in the total number of captured atoms, on the order of a few tens of percent. This phenomenon, also observed in [[90]], is explained in this reference by a stronger photon re-absorption causing an increase in the MOT size and a lower density, leading to a reduction of the light-assisted two-bodies losses.

The magneto-optical trap is immediately followed by the gray molasses step. The parameters of the gray molasses, such as duration, detunings, and intensities, have been experimentally adjusted to minimize the final temperature of the cloud.

During the 7 ms duration of this step, the "Cooling" and "Repumper" frequencies are detuned by the same amount $\Delta_{cool} = \Delta_{rep} = 20$ MHz in the blue of the transitions $|F = 2\rangle \rightarrow |F' = 2\rangle$ and

$|F = 1\rangle \rightarrow |F' = 2\rangle$ to satisfy the Raman resonance condition. Figure 2.8 shows a normalized number of atoms in the molasses when scanning the detuning Δ_{cool} with respect to the $|F = 2\rangle \rightarrow |F' = 2\rangle$ transition.

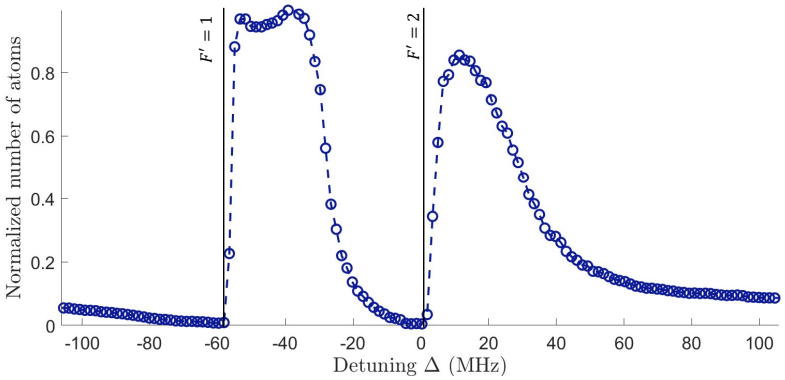

Figure 2.8: ***Number of atoms in the potassium gray molasses as a function of the detuning*** Δ_{cool} ***of the*** D_1 ***laser*** *- The detuning* Δ_{cool} *with respect to the* $|F = 2\rangle \rightarrow |F' = 2\rangle$ *transition is scanned and the evolution of the normalized detected atom number after a time of flight of 20 ms is plotted.*

To explore the frequency ranges where gray molasses exhibits efficient cooling, we need to consider the detection limits of the photodiode after a sufficient flight time (20 ms here). A hot cloud becomes undetectable because of its spatial expansion becomes larger than the detection area, and a larger detected atom number can be associated with a lower molasses temperature. Two functioning zones are observed: one between +15 MHz and 40 MHz from the transition, as predicted by theory, and another between transitions to $|F' = 2\rangle$ and $|F' = 1\rangle$, corresponding to cooling in the blue side of the $|F = 2\rangle \rightarrow |F' = 1\rangle$ transition. In our experiment, we arbitrarily chose the first zone, however the second one could be explored. Therefore, the experiment parameters are set for a detuning of +20 MHz.

The entire available laser power is initially used to maximize the number of captured atoms, resulting in $I_{tot} \sim 27 I_{sat}$. Then, a decreasing ramp is applied to the laser powers, ultimately achieving a total intensity on the atoms of approximately 8 I_{sat}. The I_{rep}/I_{cool} ratio is maintained at a value of 0.2 throughout this step.
This sequence leads to the production of a cloud of approximately 5×10^6 atoms with an estimated temperature of 8 µK. The substantial gain offered by this cooling method is demonstrated in Figure 2.9, which provides a comparison of counter-propagating Raman spectra obtained after the red or gray molasses step. During this last step, a significant narrowing of the velocity distribution is observed, accompanied by an improvement in diffraction efficiency.

2.3.3 Gray molasses of ^{87}Rb

For rubidium, we perform gray molasses when we want to load the atoms in the optical dipole trap. In this section, we will describe the gray molasses sequence, the influence of the dipole trap will be discussed in the next section. The optimized sequence for ^{87}Rb is presented in figure 2.10.
On ICE experiment, it was decided to operate the gray molasses cooling on the D_2 transition in order to avoid adding a new laser source[[83, 37]]. As for potassium, we use the collimators of the 3D MOT, necessitating a σ_+/σ_- polarization configuration of the counter-propagating beams along each of the three axes. Just after the red molasses step, the transition to the gray molasses configuration is achieved by detuning the cooling frequency in the blue of the $|F = 2\rangle \rightarrow |F' = 2\rangle$

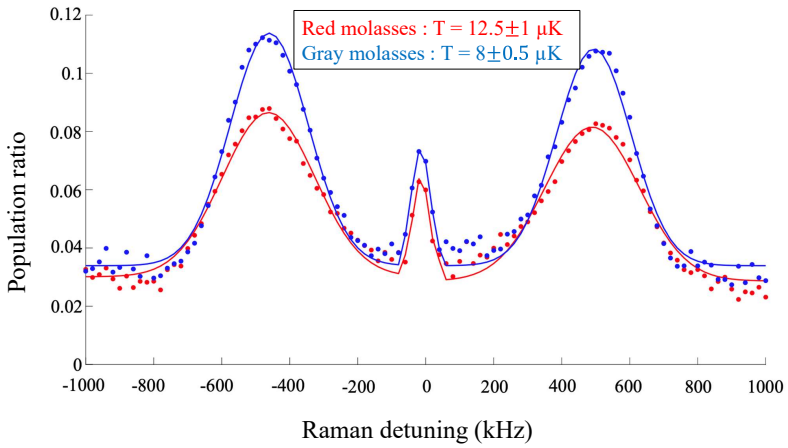

Figure 2.9: ***Counter-propagating Raman spectra obtained with red and gray molasses on potassium***

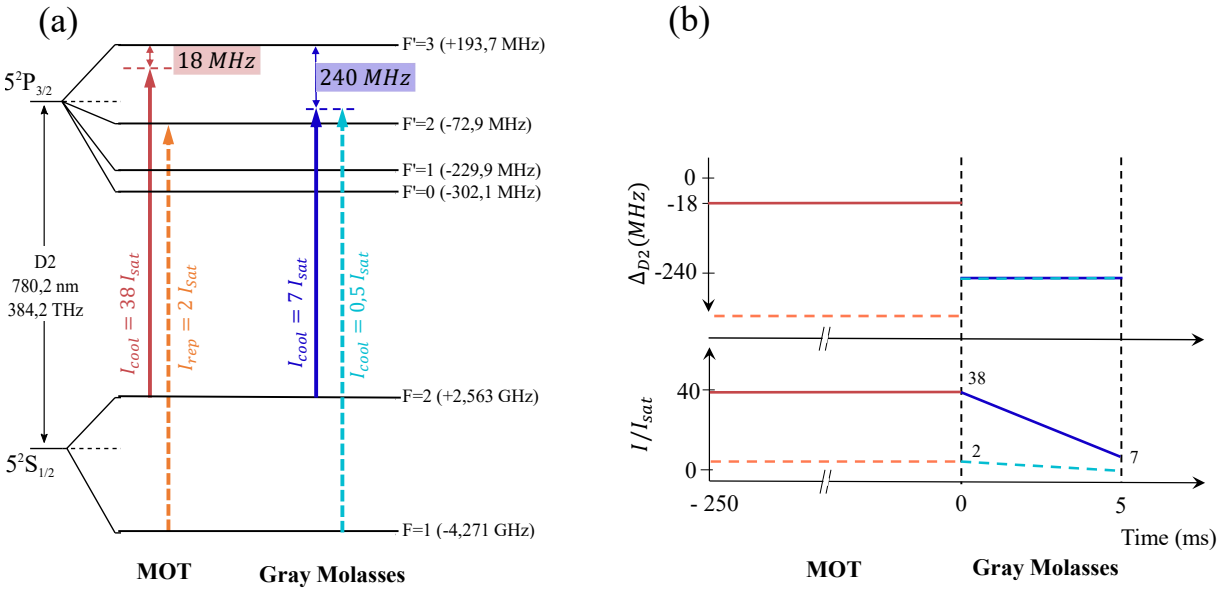

Figure 2.10: ***Gray molasses cooling sequence for*** ^{87}***Rb*** *- (a) Hyperfine structure and laser configuration during the MOT and Gray Molasses stages. (b) Schematic view of the cooling sequence. The solid and dashed lines correspond, respectively, to the Cooling and Repumper frequencies on the D_2 transition. All the intensities mentioned here take into account the contribution from the 6 beams.*

transition and adjusting the Repump frequency to satisfy the Raman resonance condition. The detuning of these two frequencies, expressed with respect to the $|F = 1, 2\rangle \rightarrow |F' = 3\rangle$ transitions for convenience, is set to 240 MHz. The total intensity on the atoms is approximately 7 I_{sat} with an intensity ratio of $I_{rep}/I_{cool} = 0.1$. This sequence leads to the production of a 7 μK atomic sample.

2.4 Dipole trap and ultra-cold atoms

So far, we have presented cooling methods that provide what we call "thermal" samples, or "cold" sources. Indeed, they are based on radiation pressure force, limiting the minimum achievable temperature. Therefore, it is necessary to explore other complementary techniques if we want to lower the temperature by several orders of magnitude. This stage is crucial for the realization of long-time-of-flight atomic interferometry.

The strategy adopted in ICE was to implement an all optical crossed dipole trap in order to employ evaporative cooling, taking advantage of the dipolar force induced by a far-detuned laser beam with large optical power. This type of trapping is one of the techniques referred to as "optical tweezers". In this section, we provide a brief theoretical background on this type of cooling and describe in detail the procedure we use. Our approach is original in several aspects as it combines loading through gray molasses and spatial modulation of dipole beams. As we will see, this method has allowed us to achieve the regime of quantum degeneracy (Bose-Einstein condensation) for rubidium both in the standard gravity regime and in the microgravity regime. We were also able to load potassium atoms in our crossed dipole trap, paving the way to obtaining ultra-cold mixture of potassium and rubidium.

2.4.1 The dipole potential

The interaction between the electromagnetic field of the laser and an atom, modeled as a two-level system, leads to an interaction between an electric field given by $E(\vec{r}, t) = \vec{E}_0(\vec{r})e^{-i\omega t} + \vec{E}_0(\vec{r})e^{i\omega t}$ and an induced dipole, which potential U_{dip} can be mathematically expressed as[[57]]:

$$U_{dip}(\vec{r}) = \frac{-1}{2\epsilon_0 c}\,\mathrm{Re}(\alpha) I(\vec{r}) \tag{2.15}$$

with $I(\vec{r})$ the light intensity given by $I(\vec{r}) = 2\epsilon_0 c\|\vec{E}_0(\vec{r})\|^2$ and $\alpha(\omega)$ being the complex atomic polarizability, which is written as

$$\alpha(\omega) = \frac{6\pi\epsilon_0 c^3 \Gamma}{\omega_0^2(\omega_0^2 - \omega^2 - i\frac{\omega^3}{\omega_0^2}\Gamma)} \tag{2.16}$$

with ω_0 the resonance frequency i.e. the optical transition when considering a two-level atom. This gives the following expressions for the dipole potential and dipole force :

$$U_{dip}(\vec{r}) = \frac{-3\pi c^2}{2\omega_0^3}\left(\frac{\Gamma}{\omega_0 - \omega} + \frac{\Gamma}{\omega_0 + \omega}\right) I(\vec{r}) \tag{2.17}$$

$$\vec{F}_{\mathrm{dip}}(\vec{r}) = -\vec{\nabla}U_{\mathrm{dip}} = -\frac{3\pi c^2}{2\omega_0^3}\left(\frac{\Gamma}{\omega_0 - \omega} + \frac{\Gamma}{\omega_0 + \omega}\right)\vec{\nabla} I(\vec{r}) \tag{2.18}$$

These relationships demonstrate that a gradient of light intensity induces a force on atoms. When considering $\Delta \ll \omega, \omega_0$, the sign of the detuning $\Delta = \omega - \omega_0$ is an important feature of dipole traps : if the laser frequency is in the red side of the atomic transition ($\Delta < 0$), the atoms will be attracted to the intensity maxima. Conversely, operating in the blue side of the

transition ($\Delta > 0$) will result in the atoms being drawn towards the intensity minima [3]. In this work, we will use the dipole trap to produce an attractive potential at the waist of the laser beam : we will use a large detuning in the red side of the transition.

With this approximation, one can simplify the expression in the rotating wave approximation leading to

$$U_{\text{dip}}(\vec{r}) = \frac{3\pi c^3}{2\omega_0^3}\frac{\Gamma}{\Delta}I(\vec{r}) \tag{2.19}$$

Here another aspect of the dipole trap can be noted : the relationship between the scattering rate Γ_{sc} and the depth of the dipole potential.

$$\Gamma_{\text{sc}}(\vec{r}) = \frac{3\pi c^3}{2\hbar\omega_0^3}\left(\frac{\Gamma}{\Delta}\right)^2 I(\vec{r}) \tag{2.20}$$

As the photons scatter, they supply energy to the trapped atoms, which counteracts the cooling process. While the potential depth scales linearly with the ratio of $\frac{\Gamma}{\Delta}$, the scattering rate scales as its square. To mitigate this effect and minimize optically induced heat, far-off-resonance traps (FORTs) were devised. FORTs aim to achieve comparable trap depths while reducing the scattering rate. However, it's important to note that using larger detunings in FORTs requires higher laser powers to maintain the potential depth at a similar value.

Dipole trap with a gaussian beam

Trap depth (dipole potential)

First, we examine the dipole potential induced by a single focused Gaussian beam propagating along the y direction. Denoting P as the laser power and w_0 as the beam waist, the intensity profile is given by:

$$I(x,y,z) = \frac{2P}{\pi w^2(y)}\exp\left(-2\frac{x^2+z^2}{w^2(y)}\right) = I_0\left(\frac{w_0}{w(y)}\right)^2\exp\left(-2\frac{x^2+y^2}{w^2(y)}\right) \tag{2.21}$$

where I_0 and $w(y)$ are respectively the maximum intensity and the $1/e^2$ radius of the beam, given by:

$$I_0 = \frac{2P}{\pi w_0^2} \quad \text{and} \quad w(y) = w_0\sqrt{1+\left(\frac{y}{l_R}\right)^2} \tag{2.22}$$

where $l_R = \frac{\pi w_0^2}{\lambda}$ is the Rayleigh length and λ is the wavelength.

The dipole potential induced by this intensity profile can be expressed using equation 2.15:

$$U_{\text{dip}}(x,y,z) = -\frac{\text{Re}(\alpha)P}{\epsilon_0 c\pi w_0^2 w^2(y)}\exp\left(-2\frac{x^2+z^2}{w^2(y)}\right) = \frac{U}{w^2(y)}\exp\left(-2\frac{x^2+z^2}{w^2(y)}\right) \tag{2.23}$$

by introducing the trap depth U:

$$U = \frac{\text{Re}(\alpha)P}{\epsilon_0 c\pi w_0^2} \tag{2.24}$$

If we also consider the presence of a gravitational field g oriented along the z-axis, then the gravitational potential is given by: $U_{\text{grav}} = -mgz$, and the resulting potential is:

$$U_{\text{tot}}(x,y,z) = U_{\text{dip}}(x,y,z) - mgz$$

[3] It is also worth noting that this dipole force is conservative: it only converts kinetic energy into potential energy or vice versa.

The potential along gravity is lowered and the atoms can escape more easily from the trap in this direction as qualitatively shown in figure 2.13. The influence of the gravitational potential can be neglected for high intensities but must be taken into account at low power to explain the displacement of the trap center and the reduction of its depth.

Trap frequencies

Generally, we aim to achieve a harmonic approximation of the potential near its center[4] to quantify the motion of atoms in the trap and associate it with a temperature.

The general form of a harmonic potential is:

$$U_{\text{harm}}(x,y,z) = \frac{1}{2}m\left(\omega_x^2 x^2 + \omega_y^2 y^2 + \omega_z^2 z^2\right) + \text{constant} \tag{2.25}$$

where ω_i is the trap frequency along the i direction.

By performing a Taylor expansion of the dipole potential (Gaussian) around its center, we obtain:

$$U_{\text{dip}}(x,y,z) = -U\left[1 - 2\left(\frac{x^2+z^2}{w_0^2}\right) - \left(\frac{y}{l_R}\right)^2\right] \tag{2.26}$$

By identification, we can deduce the expressions (valid only when the atoms have low energy compared to the trap depth and remain near its center) for the trap frequencies along the transverse axes:

$$\omega_x = \omega_z = \sqrt{\frac{4U}{mw_0^2}} \tag{2.27}$$

and along the propagation axis:

$$\omega_y = \sqrt{\frac{2U}{ml_R^2}} \tag{2.28}$$

The presence of the gravity field has an effect on the trap potential that can be expressed in terms of trap frequency. The gravity sag moves the position of the center of the trap i.e. the minimum of the potential U_{tot}:

$$z_{sag} = -\frac{g}{\omega_z^2} \tag{2.29}$$

Crossed dipole trap

On our setup, two beams form a crossed optical configuration, with an angle of 70° imposed by the geometry of our vacuum chamber. A simulation of the dipolar potential is presented in figure 2.11.This permits high trapping frequencies in all directions by superimposing the two potentials of the Gaussian beams. Interference patterns are avoided by crossing the polarization of the beams.

The light coming from the amplified fiber laser at $\lambda_D = 1550$ nm delivering up to 23 W is recycled using two retroreflecting mirrors with the configuration presented in section 1.2.9, to form a "butterfly" configuration. The optical system shapes the beam profile to obtain a beam waist $w_0 = 45$ μm at the location of the atoms.

[4]This approximation is possible if we consider the energy of the atoms is small compared to the trap depth

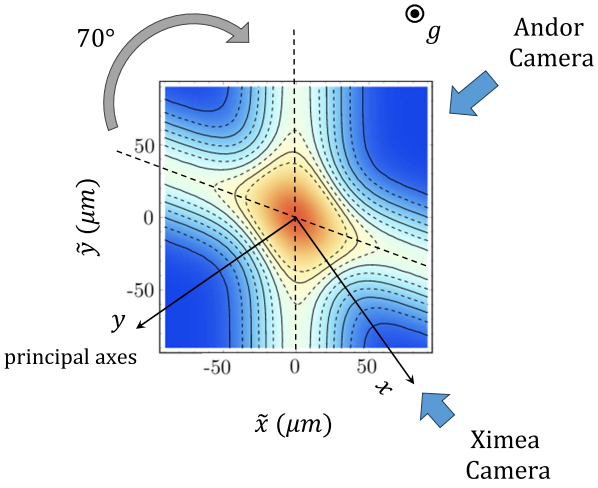

Figure 2.11: ***Simulated profile of a crossed beam dipole trap with an angle of 70°*** *- with an arbitrary unit for the potential and a waist of 45 µm*

In this configuration, the principal axes of the dipole trap are not along the propagation direction and the trap frequencies are different than those computed in 2.27. Considering the potential U_{dip} as expressed in Equation 2.25, one can find the center $\mathbf{r_0} = (x_0, y_0, z_0)$ of the trap that corresponds to the annihilation of the gradient $\nabla U(\mathbf{r}) = 0$. By a second-order Taylor expansion around $\mathbf{r_0}$, we have:

$$U_{\text{dip,dl}}(\mathbf{r})|_{\mathbf{r_0}} = U_{\text{dip}}(\mathbf{r_0}) + \mathbf{r}^T \nabla U_{\text{dip}}(\mathbf{r_0}) + \frac{1}{2}\mathbf{r}^T H_e(\mathbf{r_0})\mathbf{r} \tag{2.30}$$

where $\mathbf{H}_e$ is the Hessian matrix, i.e., the matrix of second partial derivatives. Diagonalizing H_e allows us to express the potential in a harmonic form. Its eigenvectors represent the principal axes of the trap geometry, while its eigenvalues $\lambda_{\tilde{x}}, \lambda_{\tilde{y}}$, and $\lambda_{\tilde{z}}$ are directly related to the trap frequencies. The solutions for our specific configuration can be computed using the expression 2.23 by taking into account a 70° angle between the two arms and the gravitational sag in the vertical direction.
The frequencies along x and y are not affected by gravity. For z direction, gravity lowers the trap frequency. For low optical powers, the trap depth is low and the effect of gravity on the potential "opens" the potential. In this situation, it can not be approximated by a harmonic potential anymore and the method described below is not adapted to compute the trap frequencies. However, for larger optical powers, the trap frequencies tend to be equivalent with and without gravity.

Spatial modulation

We create a time-average potential by spatially modulating the optical dipole trap beams. This technique enables to control the average intensity observed at a specific point in space, as well as the effective trapping potential. In our case, we implement this modulation to broaden our harmonic potential and increase the capture volume during the trap loading stage, as described in references [[83, 37]]. In the case of a single beam modulated with an amplitude h, the trap frequencies are given by :

$$\begin{cases} \text{Along the modulation axis:} & \omega_{mod}^2 = \left(\frac{8\alpha P}{\pi m w_0^4}\right) f_\omega(h/w_0) \\ \text{Along the transverse axes:} & \omega_\perp^2 = \left(\frac{8\alpha P}{\pi m w_0^4}\right) f_U(h/w_0) \\ \text{Along the propagation of the beam :} & \omega_z^2 = \left(\frac{4\alpha P}{\pi m w_0^2 z_R^2}\right) f_\omega(h/w_0) \end{cases} \tag{2.31}$$

where the functions $f_U(h/w_0)$ and $f_\omega(h/w_0)$ are the fractional reduction factors due to the spatial modulation of the beam. Their expressions can be found in [[83, 37]]. The capture volume is then proportional to h^2. The trap depth U of the potential is then :

$$U = \left(\frac{2\alpha P}{\pi w_0^4}\right) f_U(h/w_0) \tag{2.32}$$

The modulation function that we implement on the AOM in order to generate a harmonically modulated potential has the shape presented in section 1.2.9. The detailed calculations leading to the analytical expression of the modulation can be found in [[83]]. The modulated intensity $\tilde{I}$ for several modulation amplitudes is presented in figure 2.12.

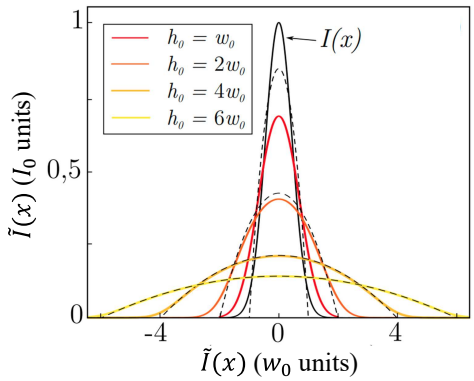

Figure 2.12: ***Simulations of the modulated intensity in 1D*** *- The simulations are made by finding the analytical solutions leading to a harmonic average potential on the atoms. The modulated intensity is presented when considering the instant potential has a gaussian shape (solid line) or a Dirac (dashed line). We note that the higher the modulation amplitude, the closer to a parabolic profile[[83]].*

The optimal modulation frequency and amplitude were found to be $f_{mod} = 280$ kHz, which corresponds to a much greater frequency than that of the trap, and $2h_0 = 600\mu$m, which correspond to the maximum angle achievable with our AOM.

Let's note that as the diffraction efficiency of the AOM is linear only around the center frequency of 40 MHz and the response $\delta x = f(V_{mod})$ is not linear, the modulation profile is slightly flattened, leading to non perfect harmonic modulation.

2.4.2 Evaporative cooling

Evaporative cooling in optical dipole traps is a powerful technique for achieving ultracold temperatures.
As presented in Figure 2.13, evaporation in the dipole trap relies on the selective removal of high-energy atoms from a trapped sample, resulting in a significant reduction in temperature and the possible formation of a condensed state.
On ICE experiment, evaporative cooling is achieved by placing the atoms within a confining potential associated with an optical trap. The depth of this potential well, denoted as U, plays a central role as it defines the "threshold" energy at which atoms can escape from the trap.

To achieve efficient cooling, the process of removing the most energetic atoms must be accompanied by thermalization of the remaining atomic ensemble. This redistribution of energy occurs through elastic collisions between particles. However, this thermalization process has its own characteristic timescales, which are influenced by the collisional properties of the species being

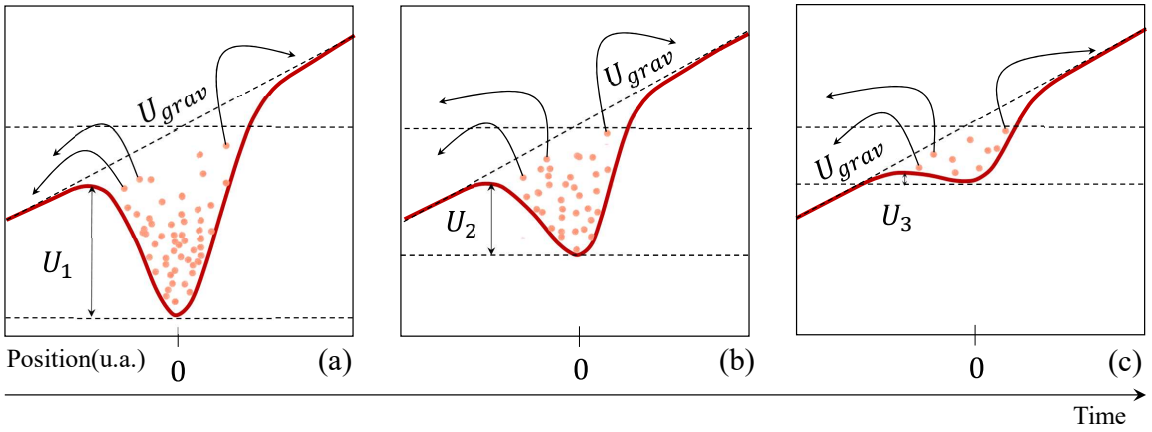

Figure 2.13: ***Principle of forced evaporative cooling*** *- Evolution of the trapping potential due to the laser and gravitational sag. The gradual reduction of the trap depth U allows for the continuous removal of the most energetic atoms. The thermalization of the remaining atomic ensemble then leads to a population of the lowest velocity classes.*

cooled. Evaporative cooling is therefore a relatively "slow" process that takes place over typical durations of several seconds.

If we consider a constant trap depth U during the process, the evaporation rate slows down exponentially over time. As the temperature of the ensemble decreases, collision processes become increasingly challenging in providing the threshold energy for a particle to escape the trap.

To counteract this phenomenon, a commonly used technique is the "forced evaporation" procedure, which involves gradually lowering the height of the potential barrier as presented in figure 2.13, with the different U_i). This maintains the efficiency of the evaporation process during the temperature descent. To have a more quantitative approach of the phenomenon, one must describe the collision processes in the trap and the resulting losses in terms of number of trapped atoms.

Collision Processes

The energy redistribution relies on elastic collisions between particles, which, by definition, conserve the total kinetic energy of the system. Other types of collisions, called "inelastic" collisions, also occur and disrupt the cooling process by inducing internal energy changes in one or more of the involved particles [[39]].

Elastic Collisions

The thermalization dynamics are governed by the rate of elastic collisions, expressed as:

$$\gamma_{\text{el}} = \bar{\rho}\sigma_{\text{el}}\bar{v}_{\text{r}} \tag{2.33}$$

where $\bar{\rho} = \frac{\rho_0}{2\sqrt{2}}$ is the average density of atoms in the trap, $\sigma_{\text{el}} = 8\pi\xi_s^2$ is the cross-section for collisions at low temperature (ξ_s^2 being the scattering length linked to the atom[5]), and $\bar{v}_{\text{r}} = \sqrt{\frac{16k_B\mathcal{T}}{\pi m}}$ the average relative velocity between particles.

[5] $\xi_s = 100 \times a_0$, a_0 being the Bohr radius

It is these elastic collisions that also allow some atoms to acquire sufficient energy to escape the trap. The rate of elastic collisions, therefore, influences the evaporation dynamics. The relationship between the temperature $\mathcal{T}$ of the trapped atoms and the depth of the potential U can be expressed using a dimensionless parameter η defined as

$$\eta = \frac{U}{k_B \mathcal{T}} \tag{2.34}$$

The particle expulsion rate can then be quantified as:

$$\frac{dN}{dt}\Big|_{\text{el}} = -N\gamma_{\text{el}}\sqrt{2\eta e^{-\eta}} \tag{2.35}$$

where N is the total number of atoms in the trap.

Inelastic Collisions

Several types of inelastic collisions can lead to particle losses and disturb the cooling process. The main types of inelastic collisions that can occur are as follows:

- **Collisions with background pressure:** Even in an ultra-high vacuum regime, the science chamber still contains a residual pressure of untrapped atoms at ambient temperature, making them highly energetic. These atoms can collide with the trapped atoms and induce losses through heating. These losses depend solely on the vacuum quality within the chamber, rather than the density of trapped atoms. With ρ_{bg} is the density of atoms associated with the residual vacuum, the reference [[11]] gives collision rates $\gamma_{\text{bg}}/\rho_{\text{bg}}$ of 6.3×10^{-9} for rubidium and 7.5×10^{-9} for potassium. These values take into account the Rb-Rb and K-K collisions, but in the case of a trap containing both species the Rb-K interactions will have to be taken into account.

- **Two-body collisions:** In the absence of near-resonant light, inelastic two-body collisions often involve a change in hyperfine state [[54, 95]]. If at least one of the two particles that collide is in the $|5S_{1/2}, F = 2\rangle$ state before the collision, both atoms end up in the $|5S_{1/2}, F = 1\rangle$ state. Due to this loss of internal energy, the total kinetic energy of the system increases by an amount corresponding to the hyperfine transition energy $\bar{h}\omega_{\text{HF}}$. This energy is significantly higher than typical trap depths[6], ensuring the ejection of the affected atoms. However, it should be noted that this parasitic process can be easily avoided by depumping all atoms into the $|5S1/2, F = 1\rangle$ state, which is the case on our experiment.

- **Three-Body Collisions** : Following a collision, two atoms can form a molecular structure if a third body is located close enough to capture the released energy. This atom then receives a significantly high kinetic energy to be expelled from the trap. As for the newly formed molecule, it no longer experiences trapping forces and also escapes. The loss rate associated with these three-body collisions is given by:

$$\gamma_{3b} = \frac{K_{3b}}{N} \int \rho^3(\vec{r}) d^3\vec{r} \tag{2.36}$$

  with ρ the density of the cloud. In [[26]], the factor K_{3b} was experimentally estimated for a non condensed gas of ultra-cold rubidium atoms to be $\approx 4 \times 10^{-29}\,\text{cm}^6/\text{s}$, and $\approx 6 \times 10^{-30}\,\text{cm}^6/\text{s}$ for potassium.

[6] around 100 mK in the case of ^{87}Rb, a few mK for ^{39}K

Overall Evolution

Finally, the overall evolution of the number of trapped atoms under the influence of collisions can be expressed as:

$$\frac{dN}{dt} = \frac{dN}{dt}\Big|_{\text{el}} + \frac{dN}{dt}\Big|_{\text{inel}} \quad = -\left(\gamma_{\text{el}}\sqrt{2\eta e^{-\eta}} + \gamma_{\text{bg}} + \gamma_{3b}\right) N \quad = -(\Gamma_{\text{ev}} + \Gamma_{\text{loss}})N \tag{2.37}$$

where $\Gamma_{\text{ev}} = \sqrt{\gamma_{\text{el}}/2\eta e^{-\eta}}$ and $\Gamma_{\text{loss}} = \gamma_{\text{bg}} + \gamma_{3b}$ represent the evaporation and loss rates, respectively. The term γ_{2b} has been deliberately omitted here as we assume pre-pumping into the $|F = 1\rangle$ state.

Scaling laws

During the forced evaporation process, the most energetic atoms are selectively removed by progressively lowering the trap depth. This lowering must be done sufficiently slowly compared to the characteristic thermalization time, which itself depends on the elastic collision rate γ_{el} introduced earlier.

We derive scaling laws for thermodynamic quantities in a 3D harmonic trap. The reader can refer to numerous sources [[34, 71]] for a more comprehensive and quantitative approach.
We consider a system at temperature $\mathcal{T}$ composed of N particles.
The application of the equipartition theorem allows us to express the average energy of a particle in the system as:

$$\bar{\epsilon} = 3k_B\mathcal{T} \tag{2.38}$$

and we assume that this average energy remains much smaller than the trap depth $U = \eta k_B\mathcal{T}$, with η being the dimensionless parameter defined in the previous section.
The total energy of the system E can be written very generally as:

$$E = \frac{3}{2}Nk_B\mathcal{T} \tag{2.39}$$

When a number dN of atoms amongst the most energetic atoms leave the trap, the energy carried out is $dN\eta k_B\mathcal{T}$. The total energy of the atomic ensemble is decreased by :

$$dE = dN(\eta - \frac{3}{2})k_B\mathcal{T} \tag{2.40}$$

Through energy conservation, one can derive the temperature variation of the atomic ensemble in the trap and deduce the scaling law, that shows the relative rate of change between average temperature $\mathcal{T}$ and number of atoms N remaining in the trap:

$$\alpha = \frac{\dot{\mathcal{T}}/\mathcal{T}}{\dot{N}/N} \tag{2.41}$$

where $\dot{N}$ and $\dot{\mathcal{T}}$ are the time derivatives of the number of trapped atoms and the temperature of the system, respectively. The coefficient α is :

$$\alpha = \frac{\eta}{3} - 1 \tag{2.42}$$

The integration of this differential equation finally leads to the scaling law describing the temperature evolution $\mathcal{T}(t)$ as a function of the number of atoms $N(t)$ during evaporation:

$$\frac{\mathcal{T}(t)}{\mathcal{T}(0)} = \left(\frac{N(t)}{N(0)}\right)^{\alpha} \tag{2.43}$$

where $\mathcal{T}(0)$ and $N(0)$ are the initial conditions for the temperature and the number of atoms in the system.
However, we have considered here the ideal case of evaporation occurring without any losses due to inelastic collisions. By taking into account the loss rate Γ_{loss} from the previous section, α should rather be replaced by [[81]]:

$$\alpha' = \frac{\Gamma_{\text{ev}}}{\Gamma_{\text{ev}} + \Gamma_{\text{loss}}}\alpha \tag{2.44}$$

The value of this parameter completely determines the efficiency of cooling as it defines the temperature gain per atom lost in the process. Thus, we understand that evaporative cooling will be more effective when the rate of elastic collisions is much larger than the rate of inelastic collisions.

2.4.3 Bose-Einstein condensation

When decreasing the temperature of a gas of bosonic particles to reach ultra-low temperatures, a phase transition towards the quantum degeneracy regime called Bose-Einstein Condensate (BEC) occurs. This state of matter was first predicted by Satyendra Nath Bose and Albert Einstein as early as in the 1920s and later experimentally observed in dilute atomic gases in 1995[[4]].

At room temperature, a gas of atom can be pictured classically as moving particles than have a certain velocity distribution, directly linked to the temperature of the gas. When the temperature decreases, the de Broglie wavelength given by equation 2.45 increases and is not negligible in comparison to the inter-atomic distance.

$$\lambda_{dB} = \frac{\hbar}{\sqrt{2\pi m k_b \mathcal{T}}} \tag{2.45}$$

Below a certain temperature threshold, $\mathcal{T}_c$, the wave functions of atoms overlap, and they lose their individuality. This leads to collective behavior of the gas, influenced by its bosonic nature: atoms can simultaneously occupy the same quantum state, specifically, the lowest energy state. All the bosons in the gas are described by a single atomic wave function, resulting in a new state of matter with unique properties.
The relevant physical quantity for evaluating the progress of this process is the atomic density in phase space, or PSD (Phase Space Density). The PSD $\tilde{\rho}$ is defined as the number of particles contained in a volume box of size $\hbar^3$ in phase space. It is expressed as follows:

$$\tilde{\rho} = \rho\lambda_{dB}^3 \tag{2.46}$$

where $\rho = \frac{N}{V}$ is the spatial density of particles.

It is often useful to express the PSD in terms of the parameters of the trapping potential. If we consider a conservative trap of harmonic and isotropic type, then the trapping potential can be written as:

$$U(r) = \frac{1}{2}m\omega^2 r^2 \tag{2.47}$$

where r is the distance from the center of the trap, and ω is the average trap frequency.

The spatial density is given by:

$$\rho(r) = \frac{N}{V_e} e^{-\frac{U(r)}{k_b T}} \tag{2.48}$$

where V_e is the effective volume of the cloud, given by:

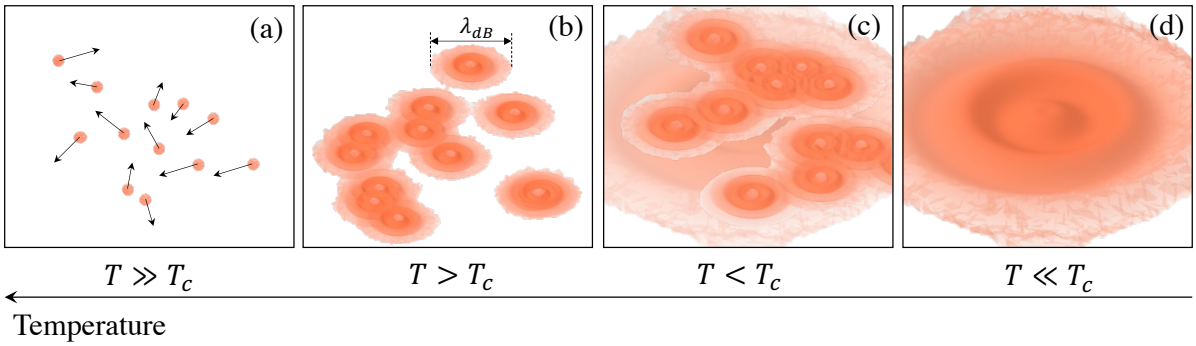

Figure 2.14: ***Principle of Bose-Einstein Condensation*** *- (a) The behavior of atoms can be treated in a classical manner : a gas of particles with different velocities due to thermal agitation (b) The wave nature of matter begins to manifest itself, but the average distance d between two particles remains much larger than the typical coherence length of a wave packet λ_{dB}. (c) Atomic wave functions start to overlap, and some particles condense into the ground state : close to the critical temperature $\mathcal{T}_c$, the Bose Einstein Condensate appears but part of the atoms remain thermal (d) The majority of particles have condensed into the ground state: a pure Bose-Einstein condensate is obtained.*

$$V_e = \int e^{-\frac{U(r)}{k_b T}} 4\pi r^2 dr \tag{2.49}$$

which leads to:

$$\rho(r) = \frac{N}{(\pi^{\frac{3}{2}} R^3)} e^{-(\frac{r}{R})^2} \tag{2.50}$$

where we have introduced the "harmonic radius" of the cloud $R = \sqrt{\frac{2k_b T}{m\omega^2}}$, a parameter representing the distance from the trap center at which the density has dropped by a factor of $1/e$.

The spatial density ρ at the center of the trap is then given by:

$$\rho = \rho(r = 0) = N \left(\frac{\hbar\omega}{k_b T} \right)^3 \tag{2.51}$$

When the evaporation brings the cloud under the critical temperature $\mathcal{T}_C$, the Bose-Einstein condensation occurs. It is associated with the saturation of excited energy levels, the atoms preferentially occupying the lowest energy state. The phenomenon described here is in fact more subtle as accumulation can occur at any temperature, more comprehensive models can be found for example in [[39]]. The macroscopic fraction of the population in the ground state is commonly referred to as the Bose-Einstein condensate or the condensed fraction, while the remaining population in the excited states is termed the thermal cloud.

The number atoms in the condensed part of the cloud is N_0 and ρ_0 is the density corresponding to the ground state. The above expression allows us to determine another scaling law, analogous to equation 2.43, involving these new quantities. It can be shown that:

$$\frac{\rho}{\rho_0} = \left(\frac{N}{N(0)} \right)^{1-\frac{3\alpha}{2}} \tag{2.52}$$

The critical temperature, $\mathcal{T}_c$, can then be expressed using the density ρ and the Riemann zeta function $\zeta(3/2)$.

$$\mathcal{T}_c = \left(\frac{\rho}{\zeta(3/2)}\right)^{1/3} \frac{2\pi\hbar^2}{mk_B} \tag{2.53}$$

Similarly, the critical density in phase space, $\tilde{\rho}_C$, can be defined as :

$$\tilde{\rho}_C = \zeta(3/2) \approx 2.612 \tag{2.54}$$

In the trap, we have the relationship between the temperature $\mathcal{T}$ of the background thermal atoms and the number of thermal atoms $N - N_0$:

$$\frac{\mathcal{T}}{\mathcal{T}_c} = \left(\frac{N - N_0}{N}\right)^{2/3} \tag{2.55}$$

These scaling laws will enable us to characterize our evaporation process and study condensation within the trap.

2.5 Implementation of loading and evaporative cooling in standard gravity

The concepts presented in the previous section are implemented on our experimental setup. In this section, the characterization of our dipole trap in the case of standard gravity is presented.

2.5.1 Lightshift due to the dipole trap

When considering the real internal structure of the atoms, one must study the effect of the dipole trap on the different sub-levels. The dipolar interaction creates a lightshift, also called "AC stark-shift" : a displacement of the energy levels due to the oscillating light electro-magnetic field of the laser. This effect is stronger when the power of the laser is higher.

The calculations leading to the energy displacements due to the dipole trap can be found in [[83]], based on the formalism of [[57, 61]].

An estimation of the light shift can however be obtained by deriving the equivalent trap depth due to the effect of the dipole trap on a specific transition, using equation 2.23. To take into account the modulation that tends to reduce the peak laser intensity seen by the atoms, one can refer to equation 2.32.

Rubidium

In the case of a FORT at 1550 nm on the ^{87}Rb D_2 line, the laser is close to a transition between the $5P_{3/2} \rightarrow 4D_{3/2}$ transition, leading to an important lightshift of the $5P_{3/2}$ state in comparison to the $5S_{1/2}$ state. The internal structure of the atom with the effect of the Gaussian beam of the dipole trap for an optical power of 10 W (2×5 W in the crossed dipole trap) is presented in figure 2.15 [[36]].
This has the effect of rendering the molasses completely ineffective in the overlapping region of the MOT beams and the dipole beam. However, this configuration is compatible with a specific gray molasses scheme in which a dark state persists despite the lifting of degeneracy. In our spatially modulated potential, atoms still have a strong probability to be cooled and pumped into the non-coupled state because the pumping rate ($\sim$ 6 MHz) is much larger than the modulation frequency of 280 kHz. Thanks to the time-average potential, the gray molasses

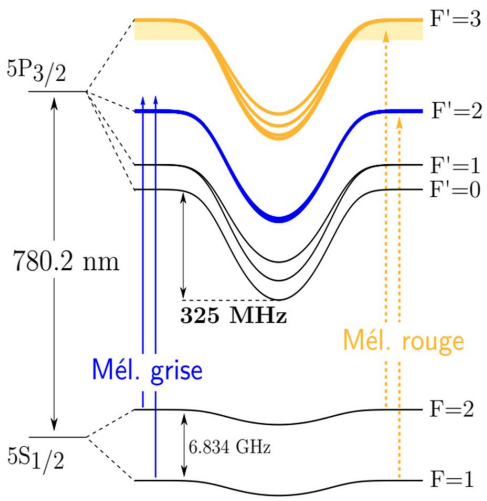

Figure 2.15: ***Lightshift due to the FORT on the D_2 transition of Rb*** *- Level structure of Rb including the lightshift due to the ODT, for an optical power of 2×5 W. The shift of the excited level is 325 MHz. In blue is the gray molasses configuration, where the beams never cross the level $|F = 2\rangle$. In yellow is the red molasses configuration. In this case, inside the trap, the cooling beams are located in the blue of the transition towards $|F = 3\rangle$.*

can operate where the atoms do not 'see' the dipole trap beam and its resulting lightshift.

Furthermore, gray molasses operating on the blue side of the cooling transition never allows for a crossing of the transition due to the light shift, thereby preventing any induced induced heating as is the case with a red molasses scheme.

Potassium

In the case of ^{39}K, the lightshifts can be computed using the same method for the D_1 line.

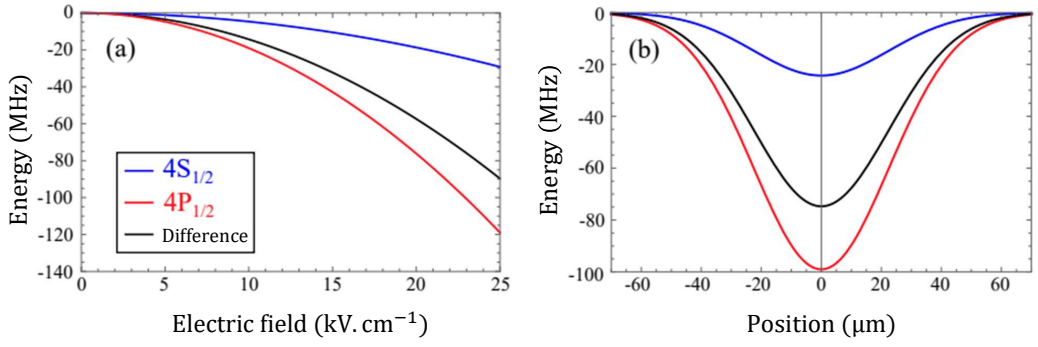

Figure 2.16: ***Lightshift due to the FORT on the D_1 transition of K*** *- (a) Calculation of the energy shift of the fundamental level (in blue) and the excited level (in red), and their difference (in black) as a function of the electric field amplitude at 1550 nm. (b) Profiles of potentials induced by a single passage of our unmodulated dipole beam when it is at its maximum power (23W).*

We find that these energy shifts occur in the same direction as for rubidium and that they are

once again more significant in the excited level than in the ground level. However, it is observed that the light-induced shifts caused by the dipole beams are considerably smaller for potassium compared to rubidium (typically by a factor of 10 for the excited level).

2.5.2 Loading rubidium and potassium in the dipole trap

Rubidium

The loading stage of the dipole trap begins immediately after the red molasses stage we described in Section 2.2. This initial sub-Doppler cooling phase allows us to produce a sample of 5×10^7 atoms at a temperature of approximately 7 µK.

The switching to the gray molasses configuration is performed by detuning the Cooler frequency to the blue side of the transition $|F = 2\rangle \rightarrow |F' = 2\rangle$, and adjusting the Repumper frequency to resonate with the Raman condition. The detuning of these two frequencies, expressed with respect to the transitions $|F = 1, 2\rangle \rightarrow |F' = 3\rangle$, is $\Delta_{F'=3} = 240$ MHz.

The total intensity on the atoms is approximately 7 I_{sat} with an intensity ratio $\frac{I_{\text{rep}}}{I_{\text{cool}}} = 0.1$. Throughout the loading step, which lasts 150 ms, the dipole trap beams are switched on at a power P of 2×4 W and modulated with an amplitude $h_0 = 300$ µm at the atom level.

The efficiency when loading the atoms from the gray molasses with the modulated dipole trap can be estimated by comparing the number of atoms in the gray molasses and in the dipole trap after the loading step, as presented in figure 2.17.

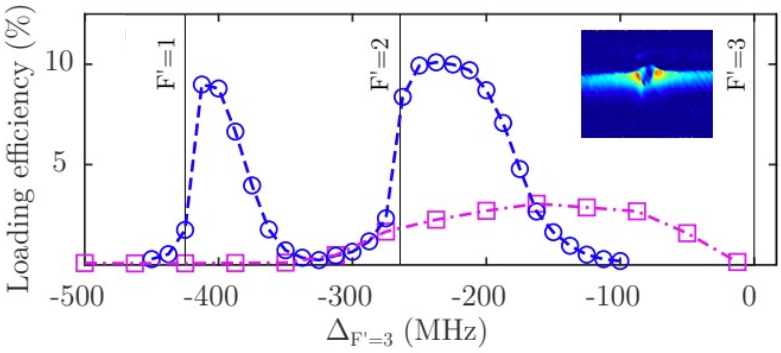

Figure 2.17: ***Loading efficiency as a function of the detuning for*** ^{87}***Rb*** *- The detuning is relative to the* $|F = 2\rangle \rightarrow |F' = 3\rangle$ *transition. The efficiency is measured for red molasses (pink squares) and gray molasses (blue circles)*

We note that the efficiency is much higher for gray molasses than for red molasses. For gray molasses, we can see the two peaks in the efficiency corresponding to the laser being resonant with the transition from the ground state to the excited levels $|F' = 1\rangle$ and $|F' = 2\rangle$.

Our method of loading the dipole trap with gray molasses results in a sample of approximately 5×10^6 atoms at a temperature of 15 µK. At this stage, the phase space density is evaluated to be 2×10^{-4}, and it is estimated that over 90% of the atoms are in the $|F = 2\rangle$ state. To avoid losses due to two-body collisions and increase the efficiency of our cooling, the atoms are immediately depumped to the $|F = 1\rangle$ state through a 500 µs laser pulse tuned to the transition $|F = 2\rangle \rightarrow |F' = 2\rangle$. To perform the so-called "blast" pulse, we use the MOT beams without

the Repumper frequency, with an effective intensity on the atoms of approximately $1I_{sat}$. The parameters of the dipole trap (power and modulation) remain unchanged during this step.

Potassium

The results on ^{39}K in the dipole trap are preliminary results and are still ongoing on the experiment.

Compressed MOT

In order to improve the loading efficiency of our dipole trap, it is important to maximize the initial density of the atomic cloud. In a magneto-optical trap (MOT), this density is typically limited by multiple scattering processes and light-assisted collisions, which induce a repulsive force between the atoms. We apply a technique called compressed MOT (CMOT)[[90, 49]] just after the MOT in the sequence by turning on both the laser on the D_2 and on the D_1 transition. The "main" laser frequency addresses the blue side of the transition $|F = 2\rangle \rightarrow |F' = 2\rangle$ of the D_1 line, while the "auxiliary" laser frequency is tuned to the red side of the transition $|F = 1\rangle \rightarrow |F' = 2\rangle$ of the D_2 line. By combining D_1 and D_2 transitions we obtain a pumping of atoms into a state with weak coupling to light, which helps limit the undesirable processes mentioned earlier. The basic idea is to take advantage of naturally occurring dark states on the "main" D1 transition. In this configuration, the "main" frequency enables gray molasses cooling at the center of the magneto-optical trap (where the magnetic field is weak), while the "auxiliary" frequency (on the red side of a transition of the form $|F\rangle \rightarrow |F + 1\rangle$) generates a restoring force in the presence of the magnetic field, thus providing the trapping function.

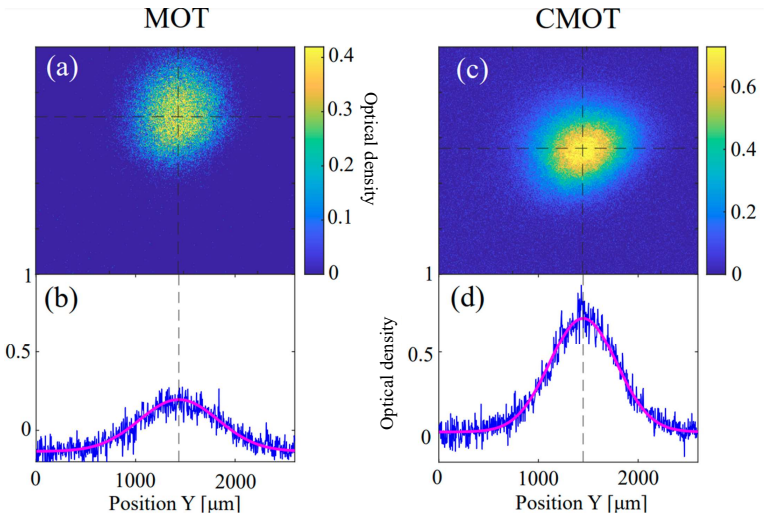

Figure 2.18: ***^{39}K compressed MOT*** *- Comparison of absorption images (a) and (c) and optical density cross-sectional views (b) and (d) obtained after a standard MOT step and after a compressed MOT step. These images were taken after a 200 μs time-of-flight.*

In our case, this compressed MOT step lasts for 10 ms. We implement it experimentally by setting the "main" frequency at resonance and detuning the "auxiliary" frequency by 22.6 MHz with respect to their respective transitions. We apply the maximum available power in the "main" frequency to increase the capture velocity and maximize the cloud density. The total intensities

associated with the two beams are then $I_{main} = 12\ I_{sat}$ and $I_{aux} = 22\ I_{sat}$. The detunings and laser intensities are kept constant throughout this step. The magnetic field gradient used is the same as that used in the standard MOT step.

As illustrated in Figure 2.18, this compression step allows for an increase in the density at the center of the MOT by a factor greater than 2 while maintaining a temperature and number of atoms equivalent to those obtained in a standard magneto-optical trap.

Loading in the dipole trap

Loading of the dipole trap occurs immediately after the compressed MOT. The dipole trap is turned on with maximum power and modulation. The D_1 laser is in gray molasses configuration during loading, while the D_2 laser is turned off. This step lasts for 8 ms. A depump pulse, performed with the D_2 laser, follows the loading, and a 50 ms holding step of the dipole trap allows non-trapped atoms to fall to the bottom of the chamber. The trapped atoms can then be detected either by fluorescence using the PMT or by absorption imaging (when this study was done on the experiment, the fluorescence imaging was not implemented). Figure 2.19 shows the number of atoms after loading in the dipole trap as a function of the detuning Δ_{cool} of the D_1 laser. We can see the two peaks in the efficiency corresponding to the laser being resonant with the transition from the ground state to the excited levels $|F' = 1\rangle$ and $|F' = 2\rangle$.

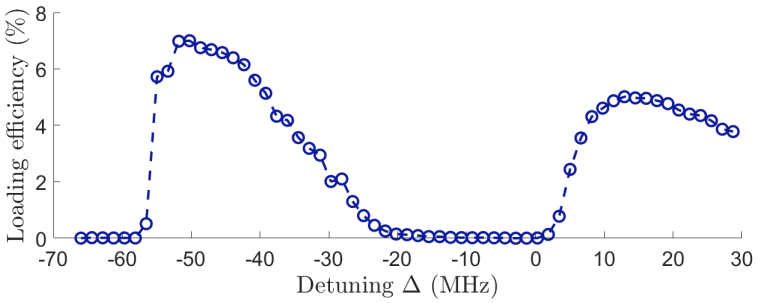

Figure 2.19: ***Loading efficiency in the dipole trap as a function of the detuning Δ_{cool} of the D_1 laser*** *- The detuning Δ_{cool} with respect to the $|F = 2\rangle \rightarrow |F' = 2\rangle$ transition is scanned and the loading efficiency in the dipole trap is computed by comparing the detected atom number after a 5 ms time of flight for a gray molasses and after the loading step.*

Figure 2.20 presents absorption images of Rb and K trapped in the dipole trap.

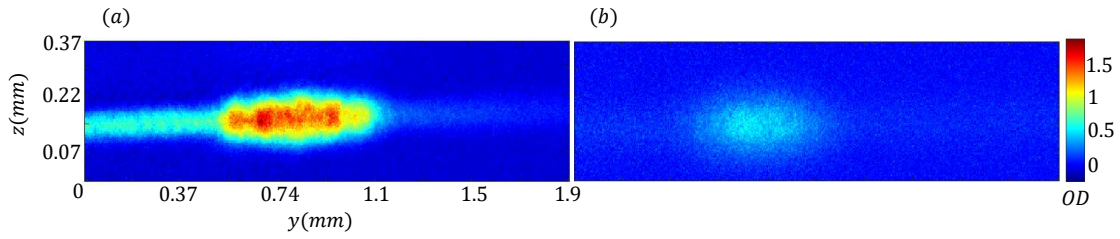

Figure 2.20: ***Absorption images of ^{87}Rb and ^{39}K in the dipole trap*** *- (a) Trapped atoms of rubidium after 1 ms time of flight. (b) Trapped atoms of potassium after 1 ms time of flight.*

In the current conditions, this sequence results in loading approximately 3×10^5 potassium atoms into the crossed dipole trap in just 8 ms. This corresponds to approximately 7% of the total number of atoms captured in the gray molasses. Without the CMOT, this percentage goes down

to 3.2%. The loading efficiency is therefore comparable to that of ^{87}Rb, which we estimate to be around 10%.
We were also able to successfully load the two species simultaneously in the dipole trap. A trade-off was made to obtain similar numbers of atoms in the trap was found : rubidium was loaded in the MOT for 500 ms and potassium for 2 s, and the dipole trap power was set to its maximum which is the optimum for potassium.

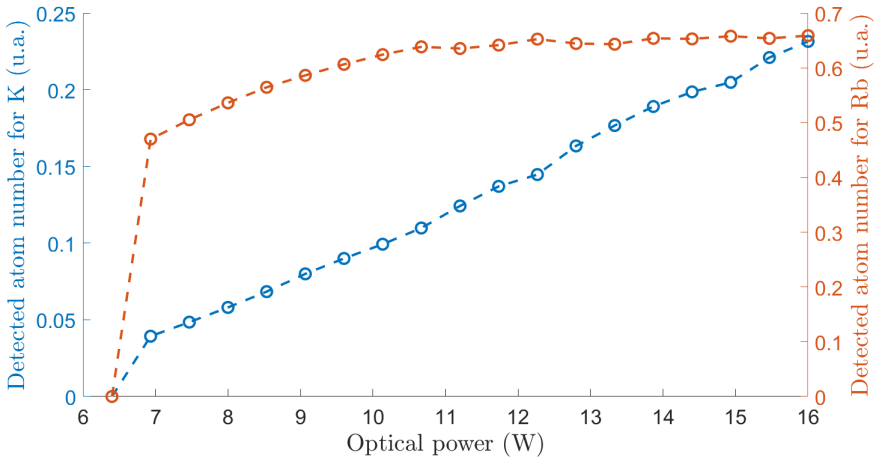

Figure 2.21: ***^{87}Rb and ^{39}K loaded in the dipole trap as a function of the optical power*** *- Fluorescence signal for rubidium and postassium detected with a PMT after loading the two species simultaneously in the dipole trap for 20 ms, for different values of the optical power in the dipole trap.*

Figure 2.21 depicts the fluorescence signals for rubidium and potassium, detected with a PMT after simultaneously loading both species into the dipole trap for 20 ms, at various optical power levels within the dipole trap. It's worth noting that the number of atoms loaded into the dipole trap for rubidium saturates when the optical power exceeds 10 W, whereas for potassium, it continues to increase without saturation.

2.5.3 Evaporation in standard gravity

Rubidium

We describe here the experimental sequence that leads to BEC in the crossed dipole trap. The laser powers, trap depth and trap frequency at each steps are presented in table 2.1.

Step	Duration (ms)	Optical Power (W)	Trap depth (μK)	Trap frequency (Hz) (f_x, f_y, f_z)	N_{at} $\times 10^3$	$\mathcal{T}$ (μK)
DT Load	50	2×10	/	/	1.5×10^3	15
DT Hold	250	2×16	/	/	/	/
Compression	150	2×7.5	237	$\approx$ (600,900,1000)	/	140
Evaporation 1	400	2×1	31	$\approx$ (200,300,400)	300	3
Evaporation 2	600	2×0.092	2.9	$\approx$ (70,100,120)	140	1.2
Evaporation 3	1000	2×0.046	1.45	$\approx$ (50,70,90)	50	0.04

Table 2.1: ***Different steps of evaporative cooling****- The trap frequencies are not given for the two first step because the dipole trap beam is spatially modulated.*

- **DT Hold :** Before starting the evaporation, a holding step is performed in the trap, during which the power of the dipole beams is slightly increased from 2×10 W to 2×16 W while keeping the same modulation parameters. However, the cooling beams of the MOT are completely turned off, causing the atoms not trapped by the dipole potential to fall under the influence of gravity. At the end of this step, 90% of the atoms are in the $|F = 2\rangle$ state. The atoms are depumped in the $|F = 1\rangle$ state using the MOT beams to avoid two-bodies collisions.

- **Adiabatic compression :** The large spatial modulation amplitude used at the beginning of our cooling sequence provides a large capture volume but results in a relatively uncompressed trap. It is necessary to increase the elastic collision rate before starting the evaporation process to enhance its efficiency. For this purpose, an adiabatic compression step is performed by gradually reducing the amplitude of the spatial modulation of the beam. This adiabatic compression simultaneously leads to an increase in temperature and spatial density while preserving the phase space density.

  The adiabaticity criterion imposes two conditions on the compression of the harmonic trap. Firstly, the increase rate of the trap frequencies must be negligible compared to the characteristic oscillation period of an atom in the trap. This condition can be expressed as:

  $$\dot{\omega} \ll \omega^2 \tag{2.56}$$

  where $\omega = (\omega_x \omega_y \omega_z)^{1/3}$ is the geometric mean of the trap frequencies, and $\dot{\omega}$ is its temporal derivative.

  Secondly, the rethermalization of the cloud must be faster than the variation of the trap frequencies, ensuring a good redistribution of energy along the three axes of the trap. This thermodynamic criterion can be mathematically expressed as:

  $$\dot{\omega} \ll \gamma_{el} \omega \tag{2.57}$$

  Experimentally, the trap is compressed by linearly decreasing the modulation amplitude until complete cutoff. This step lasts a total of 150 ms and increases the average trap frequency from approximately 125 to 900 Hz.

- The evaporation step begins immediately after the adiabatic compression and consists of three successive ramps on the laser power control voltage. The evolution of several parameters during the evaporation are presented in Figure 2.22. The durations and slopes of each ramp have been experimentally optimized so that the reduction in trap depth compensates for the decrease in the evaporation rate during the process.

  We also sought to quantify the efficiency of the evaporation by studying the evolution of temperature and PSD as a function of atom number. It is expected that these three thermodynamic quantities follow the scaling laws 2.43 and 2.52 that we introduced earlier. The logarithmic plots presented in 2.23 confirm the expected behaviors and allow us to extract the parameters α.

  The linear fit of the curve $\log(T) = f(\log(N))$ gives an estimate for α of 1.8 in the x direction and 1.5 in the y direction. The curve $\log(PSD) = f(\log(N))$ gives an estimate of 2.07. The discrepancy between the two values is likely due to three-body collision losses [[24]].

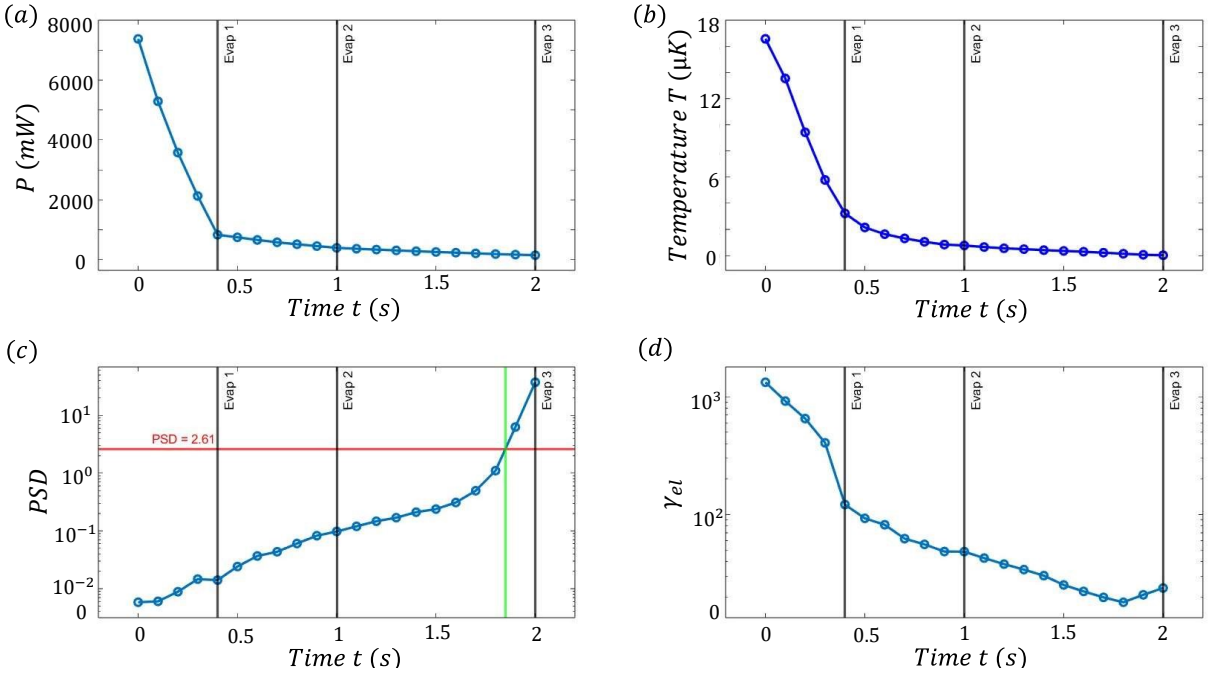

Figure 2.22: ***Temporal evolutions during the process of forced evaporation****- (a) Dipole trap power during evaporation. Three portions of ramps enable to create a decrease in the power with a shape mimicking an exponential decrease. (b) Evolution of the temperature during evaporation. The temperatures were estimated using time of flight method. (c) PSD evolution during evaporation. The PSD xas computed with the estimated atom number, temperature and trap frequency using equation 2.51 (d) Evolution of the rate of elastic collision estimated using equation 2.33*

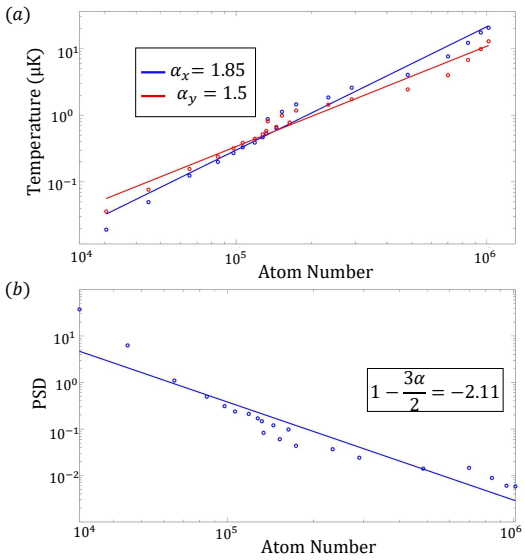

Figure 2.23: ***Efficiency of evaporation in 1 g*** *- (a) Cloud temperature and (b) Phase space density as a function of the number of atoms on a log-log scale during the evaporation trajectory.*

The cooling procedure described above allows us to produce a Bose-Einstein condensate containing 4×10^4 atoms. The critical condensation temperature is estimated to be 140 nK. The velocity dispersion of this condensate corresponds to a temperature of 40 nK. The condensation threshold is observed after 1.8 s of forced evaporation, highlighted by the emergence of a double structure when imaging the condensate, as presented in Figure 2.24.

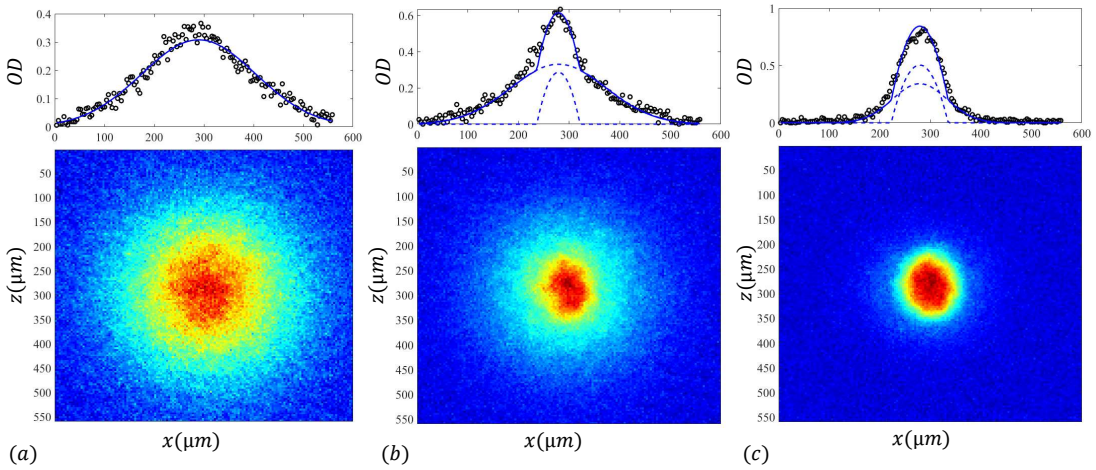

Figure 2.24: ***Absorption image of atoms for different stages of evaporation****- Image and cross-section of optical density, and fitting for different evaporation durations. The thermal part of the cloud is fitted with a Gaussian, and the condensed part with an inverted parabola. This allows us to determine the condensed part for each evaporation step. (a) The optical power is lowered to $P = 2 \times 92$ mW. We estimate that we have 140000 atoms in the thermal phase at 1.2 μK (b) The optical power is lowered to $P = 2 \times 60$ mW. We estimate that we have 108000 atoms in the thermal phase at 90 nK and 12000 atoms in the condensed part (c) The optical power is lowered to $P = 2 \times 46$ mW. We estimate that we have 30000 atoms in the thermal phase and 30000 atoms in the condensed part*

In the BEC, if the interaction energy is not negligible compared to the kinetic energy, we enter the Thomas-Fermi regime. In this regime, the cloud's density profile can be approximated by an inverted parabola. To fit such atomic clouds, we typically perform a two-component fit: a Gaussian Fit for the thermal part of the cloud, representing high-energy atoms, and an inverted parabola for the condensed part of the cloud, representing low-energy, ground state atoms. The first line of figure 2.24 shows this two-component fit for different evaporation stages.

Trap frequencies measurement

To characterize our dipole trap and verify the theoretical trap frequencies, we performed trap frequencies measurement using the atoms. The principle is based on sinusoidal excitation of the cloud through laser intensity modulation. It can be shown that for low modulation amplitudes, the heating rate of the cloud exhibits resonances at frequencies equal to twice the trap frequencies [[92]]. This heating is also accompanied by atomic losses due to the finite depth of the potential. The following sequence is used: the dipole trap is loaded, and then we perform evaporation to obtain a BEC. The power in the dipole trap laser is then suddenly set to the value for which we want to measure the trap frequency. The laser intensity is then temporally modulated around this average value for 500 ms using the AOM, with an amplitude on the order of a few milliwatts. We then detect the signal emitted by fluorescence of the atoms after a time of flight.
Figure 2.25 shows an example of measurement obtained using this method called parametric heating. We plotted the detected fluorescence signal as a function of the frequency of the

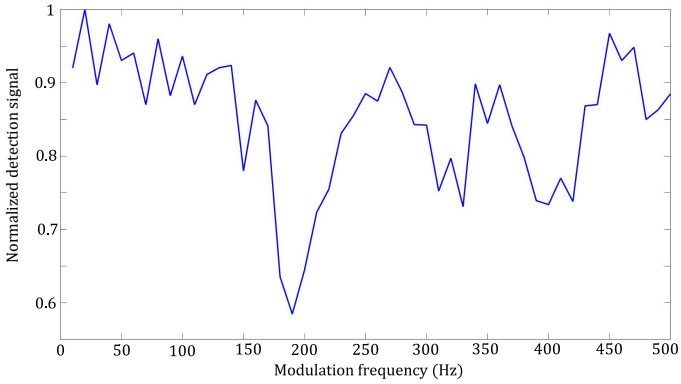

Figure 2.25: ***Parametric heating method for trap frequency measurement*** *- The trap is heated by modulation of the optical power at a varying frequency from 0 to 500 Hz. We identify three peaks corresponding to the x, y and z frequencies.*

modulation applied to the AOM. We can observe dips in the curve corresponding to resonance frequencies at which the atoms are heated and therefore the detected atom number is decreased for long times of flight. Each dip corresponds to a principal axis of the trap. By comparing the numerical model considering a waist on the atoms of 60µm and the measured trap frequencies, we obtain the results presented in Figure 2.27.

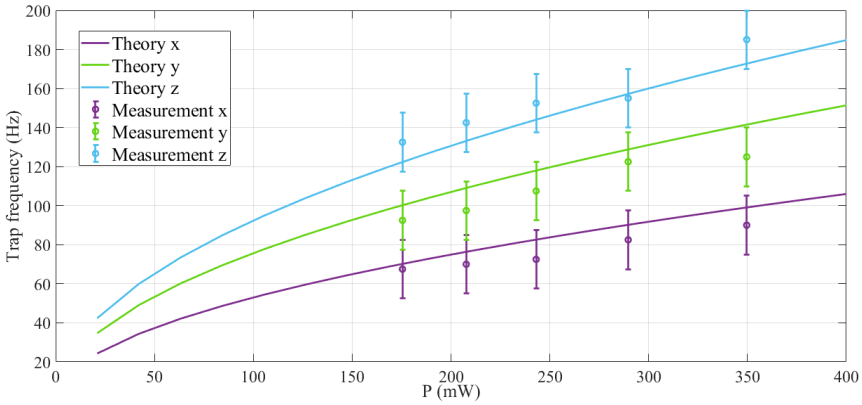

Figure 2.26: ***Trap frequencies*** *- Results of parametric heating measurements providing access to the three trap frequencies represented by circles symbols with their uncertainty. The solid lines represent the numerically simulated frequencies obtained by diagonalizing the potential's Hessian matrix.*

The main uncertainty on the theoretical trap frequencies are the waist of the laser on the atoms and the optical power. Due to our mechanical setup, it is possible that the waists of the two dipole trap beams are not perfectly overlapped, leading to a lower power on the atoms and a larger beam diameter.

Lifetime measurement

The BEC lifetime in the dipole trap is a good indicator of the quality of the ultra-high vaccuum in our science chamber. We maintain the atoms in the trap after evaporation by keeping the optical tweezer at a constant power value, and collect the fluorescence of the atoms for different durations.

We observe on Figure 2.27 an exponential decay of the atom number with the holding time, with an estimated time constant of approximately 6.8 s. The measured loss rate is therefore compatible with future atomic interferometry experiments, where expansion times are on the order of a few hundred milliseconds.

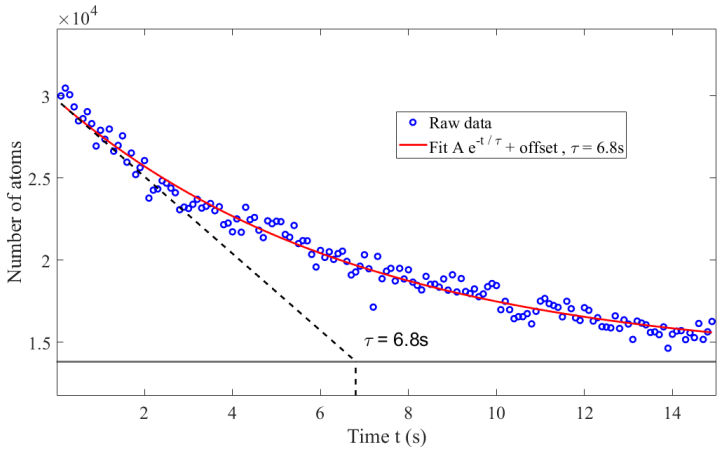

Figure 2.27: ***BEC Lifetime****- Following the evaporation ramp, the power of the dipole trap is maintained for a duration ranging from 0 to 15 seconds. The measured number of atoms is plotted as a function of this holding time (blue dots) and fitted with a decreasing exponential function (red). The slope of this curve at the origin provides the time constant associated with the atom number decrease:* $\tau = 6.8$ *seconds.*

Potassium

The next step towards achieving an ultracold source involves the forced evaporation of potassium within our conservative trap. This presents a significant challenge due to the unique collisional properties of this atomic species. Specifically, ^{39}K has a negative scattering length which complicates the thermalization of the cloud, significantly hampers the efficiency of evaporation and doesn't enable the condensation of the cloud. The cold atom community commonly resorts to the use of Feshbach resonances to reach the regime of quantum degeneracy [[89]]. In our case we would prefer to avoid relying on methods requiring intense magnetic fields because it would necessitate significant modifications to our experimental setup and jeopardize operation in the zero-gravity plane. In particular, the use of water-cooling techniques for magnetic coils is complicated to set up.

Instead, we intend to leverage sympathetic cooling with ^{87}Rb to achieve the lowest possible temperatures. Mixtures of rubidium and potassium exhibit intra- and inter-species collisional Feshbach resonances[[62]]. These resonances allow for the continuous adjustment of collisional interaction strength by applying an external magnetic field. This strategy has already been implemented between ^{41}K and ^{87}Rb isotopes to achieve the quantum degenerate regime[[76]], as well as with ^{39}K and ^{87}Rb[[27, 86]]. Recently, ultra-cold gases of ^{39}K at 350 nK and ^{87}Rb were produced on the ISS[[46]] on the CAL experiment using microwave evaporation on a chip, benefiting from the strong confinement of the cloud that results in high collision rates. A common limitation of the sympathetic cooling with different isotopes is the differential gravity sag between both species due to their large difference in mass. As the center of the traps are not perfectly overlapped, the efficiency of the sympathetic cooling is limited. Operating in microgravity is an opportunity to overcome this problem and would pave the way to future dual species BEC

in an optical dipole trap for dual-species interferometry.

While previous results regarding the cooling of potassium to very low temperatures are promising, investigating the feasibility within the specific context of our experiment will require additional work.

2.6 Ultra-cold atoms of ^{87}Rb in microgravity

During my thesis, I had the opportunity to operate the experiment on two microgravity platforms. Our microgravity simulator in the laboratory offers 500 ms which is too short to perform the evaporative cooling sequence described in the previous section. However, it is a precious tool to study the behaviour of ultra cold atoms in microgravity thanks to its high repetition rate and accessibility. The study of the evaporation process in microgravity is central when preparing for future space missions and requires longer free-fall times. In March 2022 and March 2023, we took part in the CNES flight campaigns onboard the Zero-G aircraft and performed all-optical evaporative cooling of rubidium down to 100 nK. This section presents the methods and results to obtain ultra-cold atomic samples in microgravity on both platforms.

In microgravity, the evaporation process is different because of the absence of gravitational sag. Very low temperatures of atoms can be obtained, as demonstrated in table 2.2, which gives an overview of the state of the art concerning ultra-cold atoms in microgravity.

Project	Ref	Platform	Technique	Min. Temperature
MAIUS	[[20]]	Sounding rocket	Atom chip	BEC
QUANTUS	[[43]]	Drop tower	Atom chip	38 pK
CAL	[[10]]	ISS	Atom chip	230 pK
ICE	[[37]]	Einstein Elevator	All-optical	35 nK
PRIMUS	[[103]]	Drop tower	All-optical	28 μK

Table 2.2: ***Summary of Projects and Achieved Minimum Temperatures***

Except for PRIMUS, the experiments presented in Table 2.2 use atom chips to reach Bose-Einstein Condensation. However, to the best of our knowledge, the production of a Bose-Einstein condensate through all-optical evaporative cooling in microgravity remains unaccomplished. We note that in the case of the BEC obtained on our Einstein Elevator, the evaporation process does not occur in microgravity.

2.6.1 Condensation on the microgravity simulator

The method to obtain ultra-cold atom sources of rubidium on our Einstein Elevator is explained in previous work [[83, 37]].

In order to fully utilize the microgravity phase for interferometry, the ultra-cold atomic source needs to be prepared prior to microgravity. Therefore, we implemented a strategy involving completing the evaporation process during platform motion, specifically during the hypergravity phases preceding the parabola [[36]]. The experimental sequence and different signals acquired during the sequence are presented in Figure 2.28.
We take advantage of the 12-second downtime between two trajectories to load the MOT, establish the dipole trap, perform depumping and trap compression, and initiate evaporation. At the end of the second evaporation ramp, specifically 900ms after the start of evaporation, a trigger signal is sent to the simulator. At this moment, we emphasize that the power in each dipole beam is 92 mW, resulting in a trap depth of 2.9 µK. At this stage, we estimate we have the same

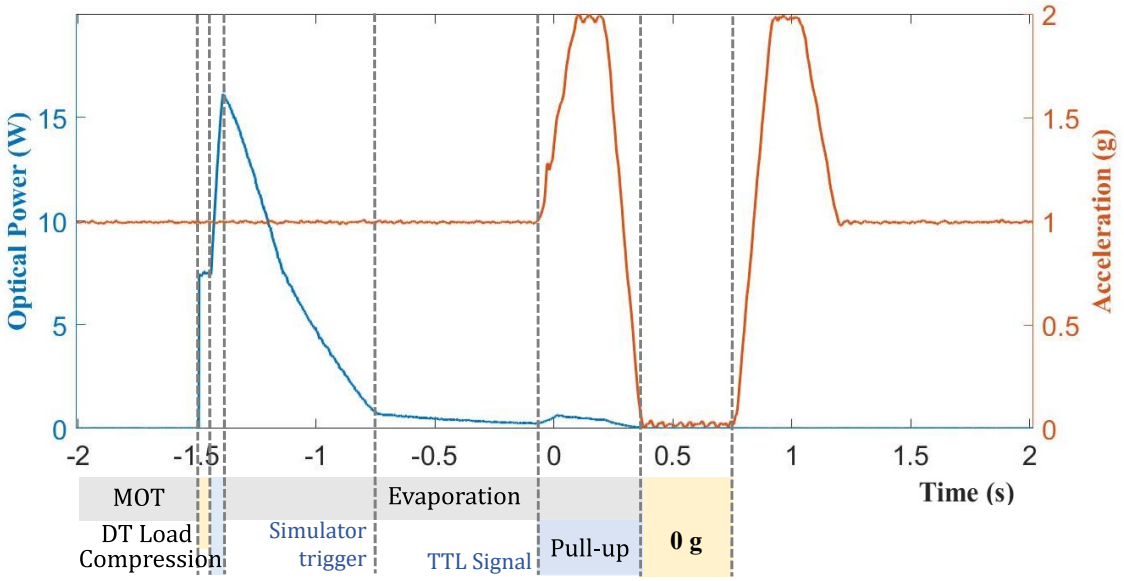

Figure 2.28: ***Experimental sequence for ultra-cold atoms on the microgravity simulator*** *- The red line is the signal along z of the mechanical accelerometer placed on the reference mirror : we distinguish the different gravity regimes. The solid blue line is the optical power seen by the atoms in the crossed dipole trap. During the hypergravity phases, the power of the laser is increased to maintain the atoms in the trap.*

number of atoms and temperature as the end of 'Evaporation 2' in standard gravity : 140000 atoms at 1.2 µK.

When the platform motion begins and we receive the TTL signal indicating its start around 80 ms later, we conclude the ramp. However, since the vertical acceleration varies during the trajectory, both the trap depth and frequencies are significantly affected compared to the standard evaporation trajectory due to gravitational sag. To address this issue, we modify the evaporation ramp as follows (see Figure 2.29), aiming to optimize the temperature and atom number at the end of the trajectory: at the beginning of the motion when the acceleration exceeds 1 g, the trap is adiabatically compressed by linearly increasing the power to 215 mW (per beam) within 80 ms. This ensures a sufficient depth (4 µK) to retain the atoms in the trap during the 2 g phase. Subsequently, evaporation continues and is completed in two steps until the microgravity phase. A first linear ramp lasting 200 ms extends until the end of the 2 g phase, followed by a second ramp of 165 ms leading up to the end of the injection phase and resulting in a power of 30 mW.
When the microgravity phase begins, the power of the dipole trap is further reduced to 10 mW within 40 ms to reach the minimum depth required to retain the atoms in the trap. This decompression is accompanied by a reduction in the velocity spread of the condensate, equivalent to a temperature of 35 nK, and a loss of atoms, resulting in a total of 4×10^4 atoms.

Note that for time-of-flight measurements, a command is applied to the polarization tee of the dipole beam modulation system to spatially shift the beams relative to the cloud. This is necessary because the extinction rate of the acousto-optic modulator (AOM) is not infinite, and the minimum achievable power is 2 mW, at the output of the first pass. In 0 g, since the atoms remain within the beam region even after time-of-flight, this procedure is required. The trap decompression could be pushed further by reducing the power and reactivating spatial modulation,

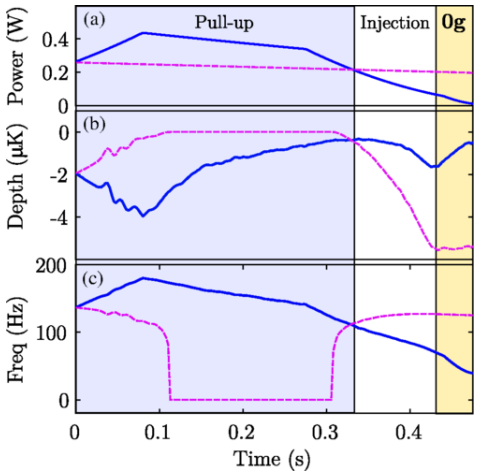

Figure 2.29: ***Experimental sequence for ultra-cold atoms on the microgravity simulator during the pull-up phase*** *- Adapted parameters during the pull-up, injection, and 0 g phases (blue solid line). The parameters are calculated using the calibration of the optical dipole trap (ODT) power and the measured acceleration. Calculations were validated by measuring the trap frequencies at three different times during the sequence: two in 1g and one in 0 g. (a) ODT optical power. (b) Evolution of the ODT depth. (c) Average ODT frequency taking into account the acceleration sag. For comparison, a sequence using parameters appropriate for 1 g (pink dashed line) shows vanishing trap depth and frequency because of the increased sag during the pull-up phase. Figure extracted from [[37]].*

but it would limit the useful duration of microgravity. Additionally, cooling using a delta-kick method[[3]] could potentially reach sub-nanokelvin temperatures.

However, these results were obtained before the modification of the mechanical structure of the sensor-head (change of the main breadboard). After this change, we observed strong misalignments on the simulator that degraded the atomic cloud in terms of number of atoms and temperature. The change in gravity during the parabola translates to different mechanical constraints on the sensor head which in turn leads to a misalignment of the crossed dipole trap. By lightening the experiment with a carbon fiber breadboard, we altered the mass distribution on the sensor head, thereby affecting the system's response to various acceleration regimes. If the two paths of the dipole trap are overlapped along the vertical (z) axis while the simulator is on the ground, it is no longer the case in 2g and 0g phases. Thanks to a remotely controlled motorised mirror, we are able to realign the dipole trap "by hand", but this correction does not compensate for the misalignment in real time. A large number of atoms thus leave the trap when the simulator takes off and we are not able to reach the condensation threshold anymore.

Through strategic placement of weights (about 10 kg) on both the main breadboard and the 'L'-shaped breadboard, which was specifically designed to minimize misalignments, we successfully mitigated these alignment issues. While we do not directly observe the splitting of the dipole trap into two paths during the various phases, there is a noticeable variation in the atom number. We quantified this effect by measuring the optical density, which is proportional to the number of atoms loaded into the dipole trap, and plotted it alongside the acceleration measurements. Figure 2.30(left) illustrates a decrease in optical density that correlates with the 2g phase. Additionally, Figure 2.30(right) demonstrates significant variations in the tweezer's position during the simulator's movement. We inferred that the first path is greatly influenced by changes in gravity. By adding weights, we intentionally introduced a similar misalignment on the second path to compensate for this effect. Figure 2.31 presents fluorescence images of the atomic cloud

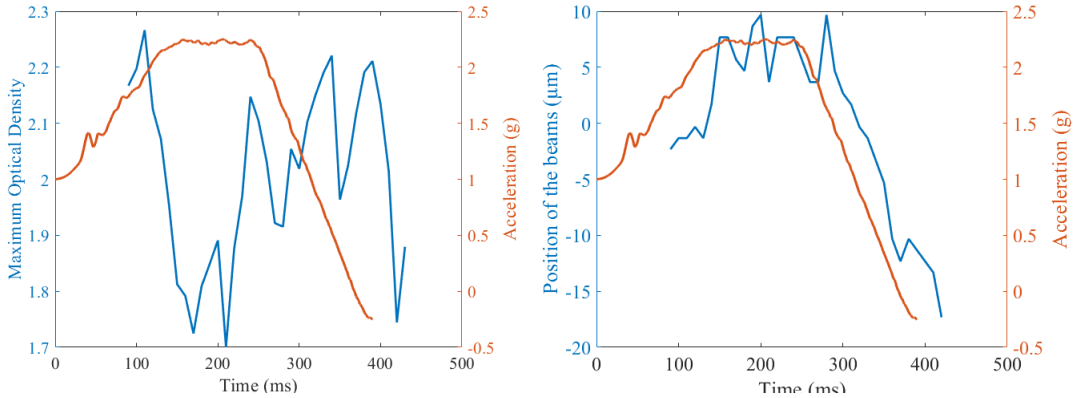

Figure 2.30: ***Atom loss and misalignment of the dipole trap during the parabola on the Einstein Elevator*** *- Left: We have plotted the acceleration data alongside the maximum optical density, derived from our absorption images of the trapped atoms in the optical tweezer. A clear correlation is observed between the signal loss and the 2g phase. Right: The position of the intersecting beams is determined by measuring absorption images during the "DT Load" step. Despite the beams remaining crossed, the acceleration-induced changes result in a displacement of the dipole trap beams with an amplitude exceeding 20 µm.*

with the Andor camera after different times of flight. Under theses conditions, we are still able to obtain ultra-cold atoms with about 10000 atoms at 100 nK, as shown by the time of flight analysis in Figure 2.32.

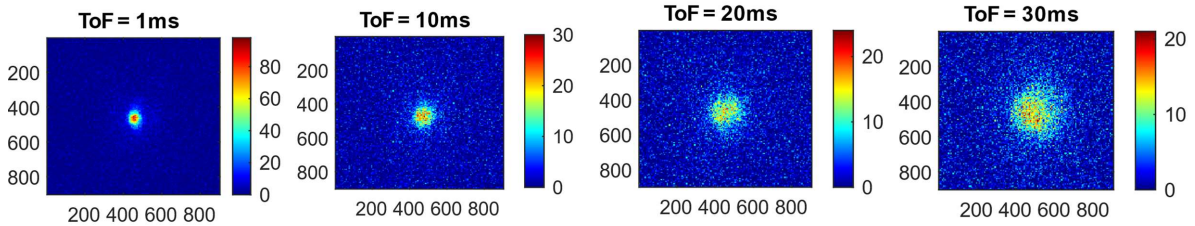

Figure 2.31: ***Fluorescence images of the atoms on the simulator*** *- The images are taken in microgravity with a varying time of flight after evaporation.*

The characterization of this source was not pursued further due to the high variability in the number of atoms observed from one shot to another on the simulator. For instance, it can vary from 5000 to 15000 between consecutive shots.

We want to retrieve sources with higher numbers of atoms and lower temperature on the Einstein Elevator. The solution we are actively pursuing involves the use of four-quadrant detectors and picomotorized mirrors to actively control the position of the dipole trap beams.

2.6.2 Ultra-cold atoms in the Zero G plane

Studying the process of forced evaporation in microgravity requires long times free fall that are not allowed by our simulator. The 22 seconds offered by the zero-G plane enabled us to evaporate in the dipole trap with different final trap depths. The results presented in this section were taken during the 62nd and 64th parabolic flight campaigns organised by the French National Centre for Space Studies (CNES) which took place in March 2022 and March 2023.

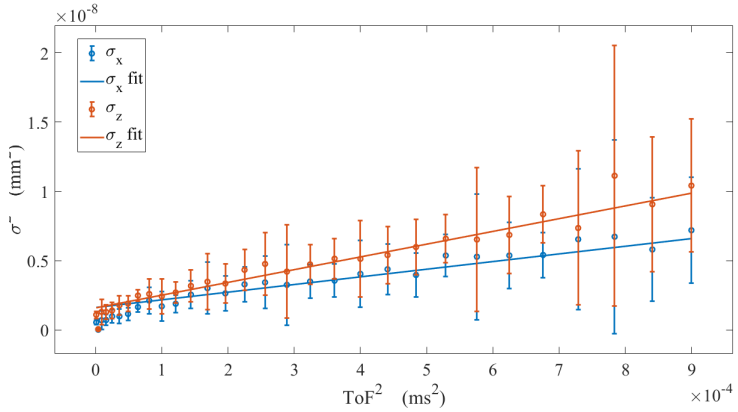

Figure 2.32: ***Temperature estimation on the simulator by time of flight method*** *- From the linear fit we deduce a temperature of 60 nK in the x direction and 100 nK in the z direction.*

As for the simulator and as mentioned in section 1.2.9, the displacement of the dipole trap during the different gravity phases is the main issue to tackle.

We use the remotely controlled motorised mirror to realign the dipole trap during the microgravity phase by looking at absorption images of the atoms trapped in the two arms of the dipole trap at the end of the 'DT Hold' step (see Table 2.1), with no time of flight. An overlap of the two clouds of trapped atoms on absorption images is a good enough starting position for evaporation. Fine tuning of the mirror's position is then achieved by maximising the number of atoms in the cloud at different stages of the evaporation process. We typically used the first five parabolas of each flight to make these adjustments.

Examples of absorption images showing the atoms trapped in the two arms of the dipole trap are visible in in Chapter 1 on figure 1.28. Here, the motorized mirror was adjusted to ensure that the two arms are well overlapped in microgravity. However, during the standard and hypergravity phases, the arms of the dipole trap are separated by more than a millimeter. To provide a more quantitative analysis, we tracked the displacements of both dipole trap beams during the parabola. When comparing these displacements to the acceleration profile, we obtained the curves presented in Figure 2.33.
We observe an anti-correlation between the positions of the first (red curve) and second paths (blue curve). Our suspicion is that misalignment in the first beam affects the reflected beam in the opposite direction. This finding suggests that implementing a servo-locking mechanism to stabilize the beam's position could enhance the loading of the dipole trap and improve the evaporation process during parabolic flights.

Furthermore, we have noted that the alignment of the dipole trap in microgravity is maintained only for a portion of the 0g phase. This phenomenon significantly impacts our data collection. Since our experiment is not synchronized with the parabolic maneuvers, we encounter substantial fluctuations in the number of trapped atoms from one shot to another.

In this section two datasets from the two flight campaigns we took part in are presented. Figure 2.34(a) and (c) shows fluorescence images of the clouds obtained for different times of flight. By releasing the atoms from the dipole trap and measuring the expansion of the BEC on fluorescence images, we find a kinetic energy equivalent to a temperature of 100 nK for the first data set (Figure 2.34(b)) and 170 nK for the data taken in 2023 (Figure 2.34(d)).
We find that a greater reduction in laser intensity is necessary to lower the temperature of the

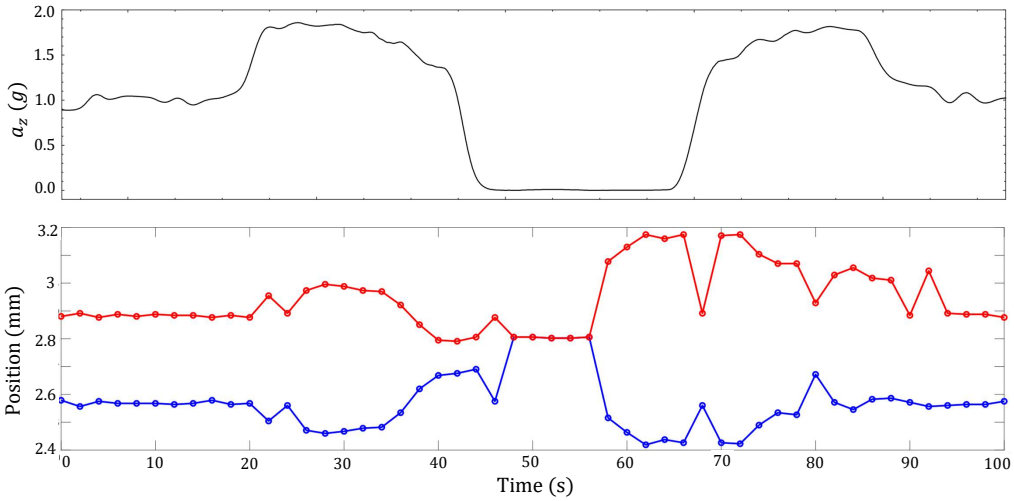

Figure 2.33: ***Acceleration profile along the z direction during the parabola and position of the dipole trap beams*** *- The acceleration data is supplied by Novespace through their measurement instruments. To determine the beam positions, we analyze the absorption images of the dipole trap captured at the conclusion of the 'DT Hold' step. This is done by taking cross-sections and fitting the beams using Gaussian profiles. The red curve represents the first traversal of the dipole trap beam within the chamber, while the blue curve corresponds to the second crossing of the dipole trap beams. Notably, the system is aligned during the microgravity phase, and we observe an anti-correlation between the two curves.*

atoms in microgravity in comparison to the situation in standard gravity.

For instance, in the dataset acquired in 2022 (first row of Figure 2.34), which corresponds to a temperature of approximately 100 nK, the optical power was reduced to less than 2×40 mW, lower than at the end of the evaporation ramp under standard gravity conditions. Despite having a similar number of atoms (about 4×10^4), the temperature is more than twice as high. This is consistent with a with a higher trap depth due to the absence of gravity in the z direction.

However, when we analyze the fit of the cloud's spatial expansion, we observe that the temperature along the x axis appears to be higher than that along the z axis. This is primarily due to the presence of atoms remaining in the 'wings' of the dipole trap. In the absence of gravity, even the weak trapping optical powers along the dipole trap beams can capture atoms, resulting in the elongation of the cloud along these beams. For this reason, we preferentially estimate the temperature of the cloud along the z axis.

Depending on the dataset, the number of atoms loaded in the dipole trap varies a lot. As several shots are necessary to have an estimation of the temperature, it is difficult to estimate the phase space density we obtained. We suspect the condensation threshold was reached for certain shots, as shown in Figure 2.35. This atom cloud remaining at the end of evaporation exhibits a characteristic double structure with a thermal part (Gaussian) and a condensed part (parabolic).

We could not detect the free atoms for time of flights longer than 200 ms as they moved out of the detection zone of the EMCCD camera (approximately 3 by 3 mm in the object plane). This is due to the residual accelerations of the plane resulting in an imperfect parabola whereas the atoms follow the path of a perfect free fall. This problem could be mitigated by choosing an imaging system with a lower magnification.

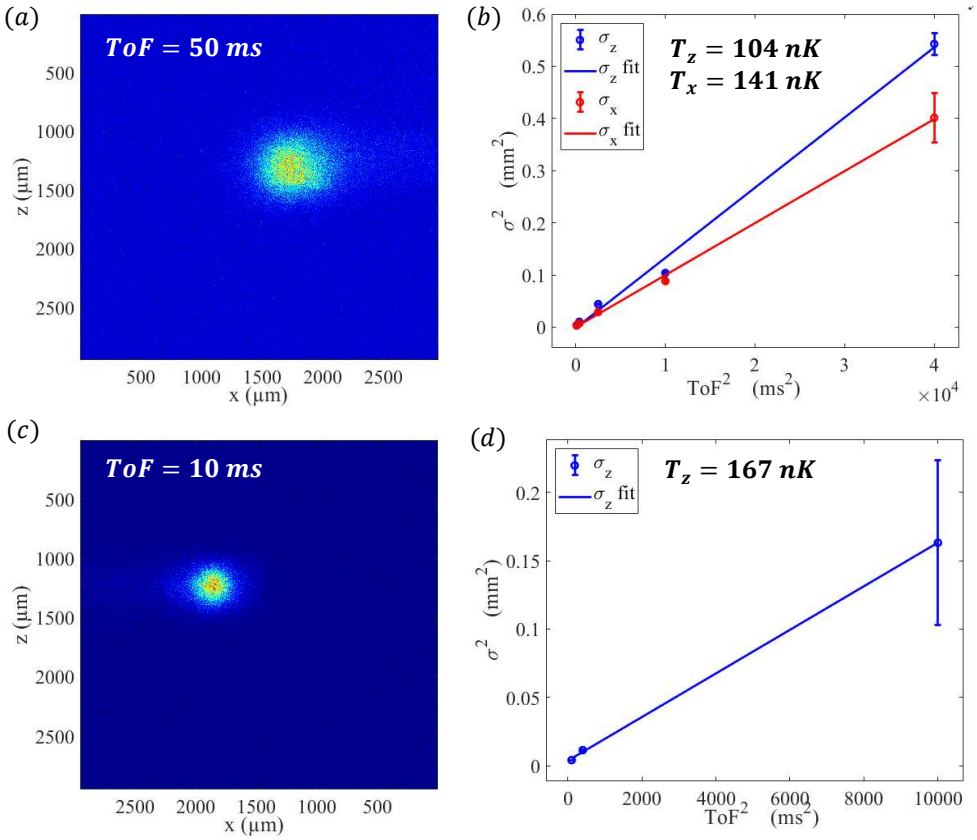

Figure 2.34: ***Fluorescence images of the ultra-cold atoms onboard the Zero-G plane*** *- (a) and (c) present fluorescence images of the atomic cloud after 50 and 100 ms time of free expansion. (b) and (c) present the expansion temperature estimation with time of flight method for two datasets taken in 2022 and 2023.*

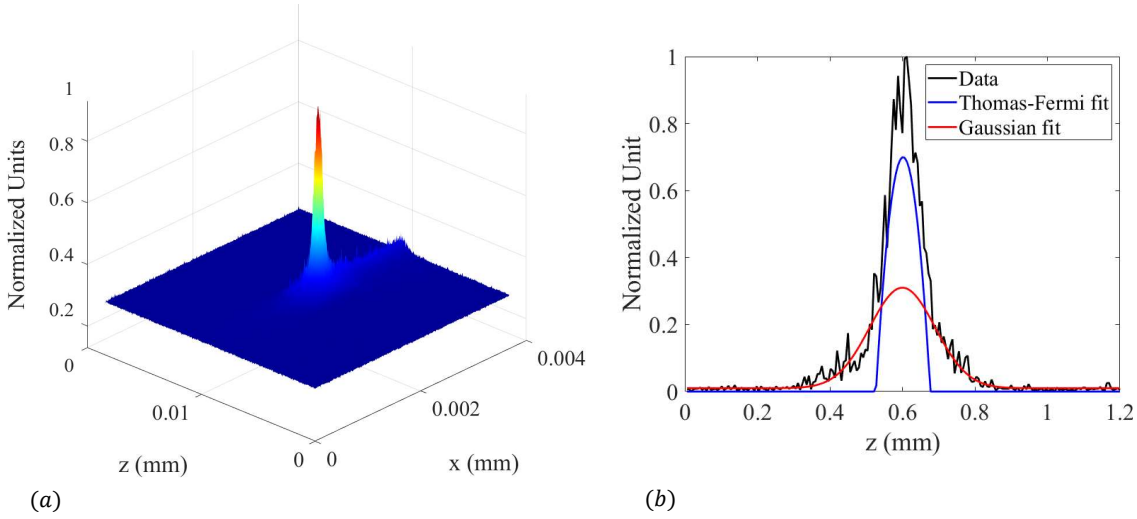

Figure 2.35: ***Ultra-cold atoms of ^{87}Rb in the Zero-G plane*** *- (a) Fluorescence of the atomic cloud after a time of flight of 10 ms. We distinguish the peak of the atomic cloud and the atoms loaded in the 'wings' of the dipole trap (b) Cross-section of the atomic cloud and two-component fit.*

For the experiments described above, at the end of evaporation, the dipole trap is turned off, and to ensure that no residual light reaches the atoms, the radio-frequency sent to the AOM is detuned to change the deflection angle. If the beam is not deflected away from the atoms, we find that the residual beam of 2×4 mW is sufficient to trap some atoms in the dipole trap, even when it is suddenly set to this minimum power just after the evaporation. During one of the parabolic flights, we observed atoms in this residual tweezer after 1 s of flight time, as depicted in the fluorescence image in Figure 2.36. The microgravity environment gives access to regimes unavailable on the ground. We are able to keep atoms trapped in a very shallow potential. The estimated number of atoms in this image is 500, and the optical power at the extinction of the AOM corresponds to a trap depth of less than 250 nK.

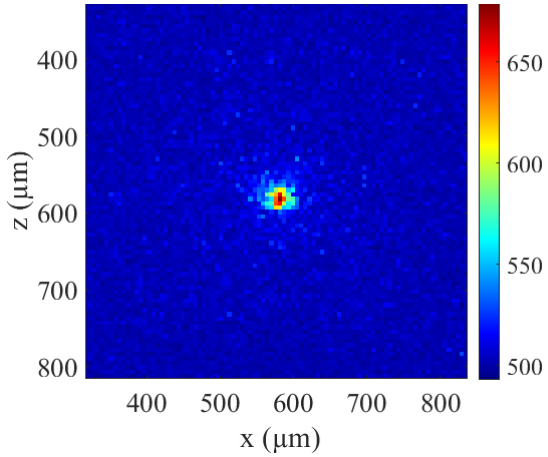

Figure 2.36: ***Fluorescence image of the residual tweezer after 1 s time of flight on the Zero G plane*** *- After the end of evaporation, the AOM is set to extinction, corresponding to less than* 2×4 *mW, and atoms remain trapped in the residual tweezer and are detected after to 1 s.*

We were able, onboard the Zero G plane, to experiment with an ultra-cold atomic source and tune parameters such as the trap depth. Despite the technical challenge of operating in these peculiar conditions, we obtained the coldest atomic cloud with an all-optical method in microgravity. The next step is to install an active correction of the dipole trap misalignment using not only one but two motorised mirrors. This solution is aimed to be tested during the next flight campaign in March 2024 in order to cool the atoms down to colder temperatures and perform interferometry.

2.7 State preparation

To perform atom interferometry, we always aim to prepare the atoms in a state insensitive to the magnetic field. Depending on the temperature and the nature of the atoms, several methods can be used. In this section, we describe the selected method for each case.

2.7.1 Microwave state preparation for ^{87}Rb cold atoms

The rubidium purification procedure involves a selective microwave pulse for coherent transfer between the states $|F = 2, m_F = 0\rangle$ and $|F = 1, m_F = 0\rangle$.
This purification sequence consists of three successive steps, as depicted in Figure 2.37. The first step, known as "repump," involves increasing the power of the Repump frequency using the light from the Raman beam for approximately 500 μs to transfer all the atoms to the $|F = 2\rangle$ state. At the end of this step, the atoms populate the five Zeeman sublevels of this state equally:

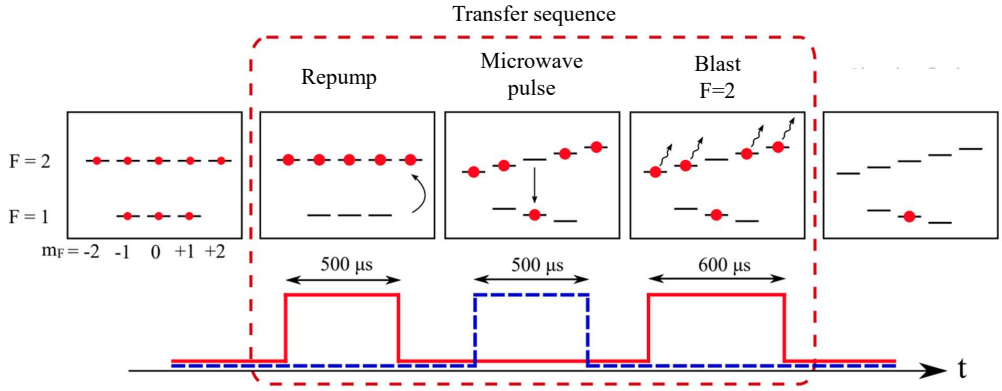

Figure 2.37: ***State preparation sequence for thermal samples of*** ^{87}***Rb*** *- The first line describes the evolution of atomic populations associated with different states. The second line presents the temporal profiles of laser power (solid red line) and microwave power (dotted blue line).*

$m_F = 0$, $m_F = \pm 1$, and $m_F = \pm 2$.

Next, we apply a magnetic field bias of approximately a hundred milligauss along the vertical axis to induce Zeeman splitting. We then apply a microwave pulse using the antenna described in Section 1.2.6. This microwave excitation, performed at the clock frequency of 6.834 GHz, is resonant only with the transition $|F = 2, m_F = 0\rangle \rightarrow |F = 1, m_F = 0\rangle$. By choosing an appropriate interaction duration, a complete population transfer from $|F = 2, m_F = 0\rangle$ to $|F = 1, m_F = 0\rangle$ is achieved. The duration of this π pulse can slightly vary, but typically falls around 500 μs.

The third and final step involves ejecting the remaining atoms in the other m_F states using a 600 μs pulse from the Push beam. This beam is tuned to the cycling transition $|F = 2\rangle \rightarrow |F' = 3\rangle$ and only affects the atoms in the $|F = 2\rangle$ state.

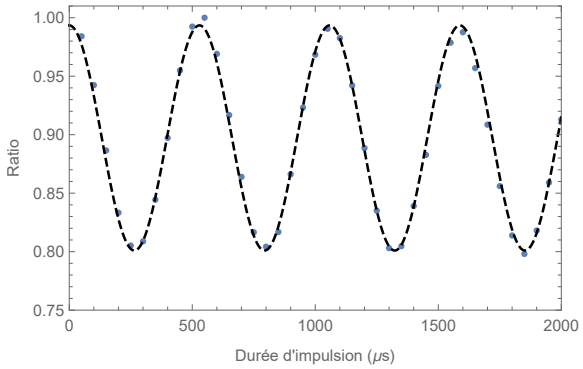

Figure 2.38: ***Rabi Oscillation due to the microwave source between the hyperfine levels*** $|F = 1\rangle$***,*** $|F = 2\rangle$ *- The duration of the π pulse to perform the transfer is 300 μs.*

This is indeed a purification sequence, rather than a transfer, as it results in the loss of 80% of the atoms (4 out of 5 Zeeman sublevels). However, this is not a problem when working with thermal samples of rubidium, as the number of atoms we retain is more than sufficient

to perform our interferometric measurement under favorable conditions. Figure 2.38 shows the Rabi oscillations of the population ratio as a function of the duration of the micro-wave pulse.

2.7.2 State preparation for ^{39}K cold atoms

For potassium, it is not possible to apply a similar method as for rubidium. The clock frequency associated with the hyperfine transition $|F = 1\rangle \rightarrow |F = 2\rangle$ is only 461.7 MHz, corresponding to a wavelength of approximately 65 cm. The dimensions of our metallic chamber, which are significantly smaller, prevent such a field from propagating within it.

The strategy developed a few years ago on the experiment is to use two-photon Raman pulses to achieve selective transfer between the states $|F = 1, m_F = 0\rangle$ and $|F = 2, m_F = 0\rangle$, as presented in Figure 2.39. In this way, it is possible to operate far from the one-photon resonance and limit sample heating due to spontaneous emission. We will describe rapidly the method here but as it was not recently operated on the experiment, the reader can refer to is described in [[32, 5]] for further details.

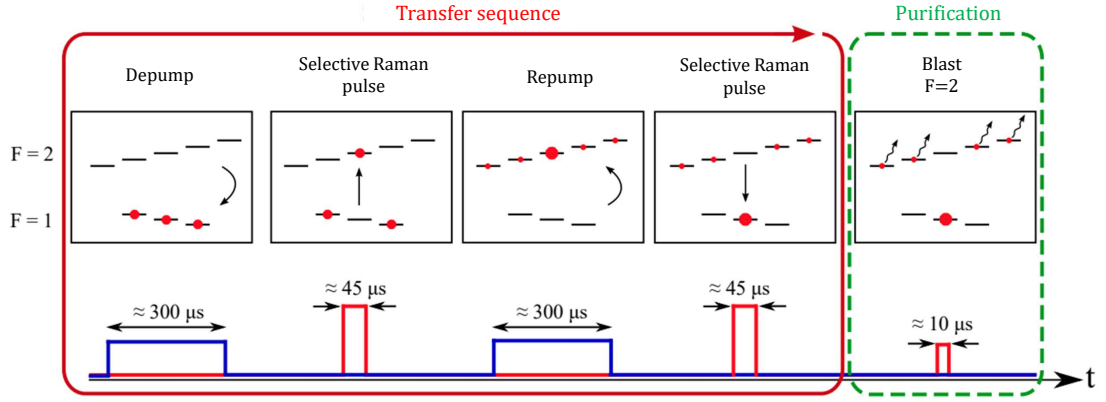

Figure 2.39: ***State preparation sequence for thermal samples of ^{39}K*** *- The first line describes the evolution of atomic populations associated with different states. The second line presents the temporal profiles of laser power tunes on the D_2 transition (red line) and on the D_1 transition (blue line)*

To be effective, this pulse must be applied in the presence of a magnetic field bias (applied along the vertical axis using the Z-compensation coils) and utilize a co-propagating beam in the σ^+ or σ^- polarization configuration. In our case, it is challenging to align the selection beam along the quantization axis since it is already used by the Raman beam, which is kept in a counter-propagating configuration with linear polarization perpendicular to each other for the interferometer. The choice was made to use another physical axis for state preparation. A detailed study on the effect of the selection beam orientation was carried out in Laura Antoni-Micollier's thesis [[5]]. The conclusion of this study is that an effective selective pulse can be achieved by orienting the selection beam at a 45° angle relative to the quantization axis.

Although these selective transfer pulses are consistently performed with the D_2 laser, the optical pumping pulses (depumping to $|F = 1\rangle$ or repumping to $|F = 2\rangle$) are carried out using the D_1 laser. The advantage of the D_1 line is the absence of a cycling transition: the atoms undergo a low number of absorption/emission cycles before falling into the desired state. Therefore, the optical pumping steps do not lead to significant sample heating.
The procedure depicted in Figure 2.39 consists of a transfer sequence, which places the majority of atoms in the sublevel $|F = 1, m_F = 0\rangle$, and a purification step used to remove particles

remaining in other magnetic sublevels. A magnetic field bias of a few hundred milligauss is applied along the vertical axis throughout the procedure, inducing a separation of a few hundred kilohertz between the different magnetic sublevels.

The sample is initially repumped to $|F = 1\rangle$ using D_1 light sent to the MOT optical access. The laser frequency must be tuned to the $|F = 2\rangle \rightarrow |F' = 2\rangle$ transition, resulting in an equal distribution of atoms among the three Zeeman sublevels. Subsequently, the atoms in the $|F = 1, m_F = 0\rangle$ state are coherently transferred to the $|F = 2, m_F = 0\rangle$ state using a co-propagating π pulse performed with the selection beam at a 45° circular polarization. The D_2 laser, detuned by 700 MHz to the red of the $|F = 2\rangle \rightarrow |F' = 3\rangle$ transition, is used to stay far from one-photon resonance and limit heating due to spontaneous emission. The Raman detuning is adjusted to a specific value, addressing only the transition between the $m_F = 0$ substates. The atoms remaining in $|F = 1\rangle$ are then repumped with the D_1 laser tuned to the $|F = 1\rangle \rightarrow |F' = 2\rangle$ transition. Due to the isotropic polarization of the light, this pulse uniformly redistributes the atoms among $|F = 2\rangle$ and increases the population of the target sublevel. Finally, a second selective Raman pulse is applied to bring the atoms back to the $|F = 1, m_F = 0\rangle$ state, ensuring that the process of accumulating atoms in $m_F = 0$ cannot be reversed by subsequent pulses.

The four steps described above constitute what is called the transfer sequence. This procedure can be repeated several times in succession to increase the population of the target state $|F = 1, m_F = 0\rangle$. However, this sequence induces a slight heating of the sample, so it may not be advantageous to perform a large number of cycles in practice.

Finally, an additional purification step is carried out to eliminate all remaining atoms in $|F = 2\rangle$. This is achieved by applying a short D2 light pulse tuned to the $|F = 2\rangle \rightarrow |F' = 3\rangle$ transition using the pusher/selection beam.

Overall, the entire preparation sequence lasts only a few hundred microseconds. Previous studies have demonstrated a preparation efficiency exceeding 95% using this method, with a temperature increase in the sample limited to a few microkelvins. It should be noted that this sequence can be adapted to prepare the sample in any Zeeman sublevel of the ground state by modifying the Raman detuning during the selective pulses to preferentially address the transition between the $m_F = +1$ or $m_F = -1$ substates.

2.7.3 Spin distillation technique for ultra-cold atoms

To achieve the state preparation on ultra cold atoms, we were inspired by a 'distillation' process involving making certain magnetic sub-levels more 'volatile' by adding a magnetic force during the evaporation process [[38]]. The idea is to introduce a magnetic field gradient during evaporation to generate different trap depths for each Zeeman sub-level without altering the center position of these three potentials, ensuring good spatial overlap and thermalization between atoms in the three sub-states. However, the trapping parameter η becomes dependent on m_F, favoring the evaporation of certain sub-species. A detailed understanding of the underlying mechanism requires studying the potential seen by each Zeeman sub-level during evaporation in the presence of the magnetic field gradient. The total potential U_{tot} experienced by the atoms is always the sum of three contributions: the dipole trapping potential U_{dip}, the gravitational potential U_{grav}, and the magnetic potential (m_F-dependent) given by $U_{\text{mag}} = m_F \mu_B g_F \|\mathbf{B}\|$, where μ_B is the Bohr magneton and g_F is the Landé factor of the relevant level. In the following, we consider a homogeneous magnetic field gradient across the entire trapping region, such that the magnetic potential varies linearly with position within the trap. For simplicity, we also take the trap center as the origin for the magnetic and gravitational potential energies.

We can first consider a situation where the gradient is in a direction transversal to gravity, in the horizontal direction. In this situation, the potentials of the different Zeeman sub levels are affected by the magnetic field as presented in Figure 2.40 (a). The gravity field has no component along the gradient axis, and the gravitational potential shows no dependence on the position along this axis. The total potential energy is then simply the sum of the dipole and magnetic potentials. It is observed that the trapping depths of the $m_F = \pm 1$ sub-species are lowered on one side or the other by the addition of this magnetic field gradient. This results in a preferential evaporation of atoms in the Zeeman sub-levels $m_F = \pm 1$ and thus a purification of the condensate in the magnetically insensitive state $m_F = 0$.
This situation is equivalent to the operation in a microgravity regime.

Now, considering a gradient along the vertical direction, we obtain the situation depicted in Figure 2.40 (b). The addition of gravitational potential energy has the effect of decreasing the trap depth seen by the Zeeman sub-level $m_F = 0$ while re-increasing the depth associated with one of the $m_F = \pm 1$ species. As a result, this sub-species becomes better trapped and will be purified during the process.

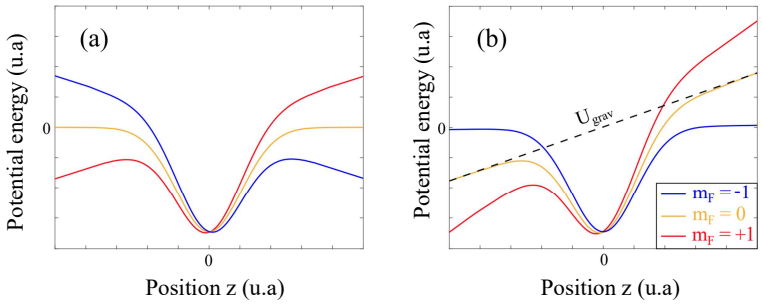

Figure 2.40: ***Principle of condensate state preparation*** *- The potential profiles associated with different Zeeman sub-levels are plotted for an applied magnetic field gradient (a) horizontally or (b) vertically with respect to the direction of gravity.*

In our case, we generate the magnetic field gradient during evaporation using our MOT coils, which are supplied with a current of over 5 A. It is worth noting that these coils have an 'anti-Helmholtz' configuration and are positioned on the chamber body such that their axis forms a 45° angle with the vertical direction. In standard gravity, we have verified that the specific magnetic sub-species purified after the process depends directly on how we position the intersection point of the dipole trap beams relative to the geometric center of the MOT. Certain well-defined positions allow us to achieve the desired preparation in the $m_F = 0$ state. This is illustrated in Figure 2.41, which shows Raman spectra before and after state preparation.
This phenomenon can be understood by considering that the vicinity of the geometric center of the MOT is a region where the magnetic field gradient is highly inhomogeneous. The effective orientation of the gradient seen by the atoms, and therefore the component of the gravitational field along its axis, is directly related to the positioning of the dipole trap. By displacing it by just a few tens of micrometers, we can approach one or the other of the 'ideal' scenarios presented earlier. It should also be noted that the magnitude of the gradient is not necessarily constant throughout the spatial extent of the trap, which may result in a slightly more complex energy landscape than described above.
The condensate produced in this way contains approximately three times fewer atoms than the one obtained in the absence of distillation. Therefore, this is indeed a filtering phenomenon, but this state preparation method proves to be significantly more efficient than the one we

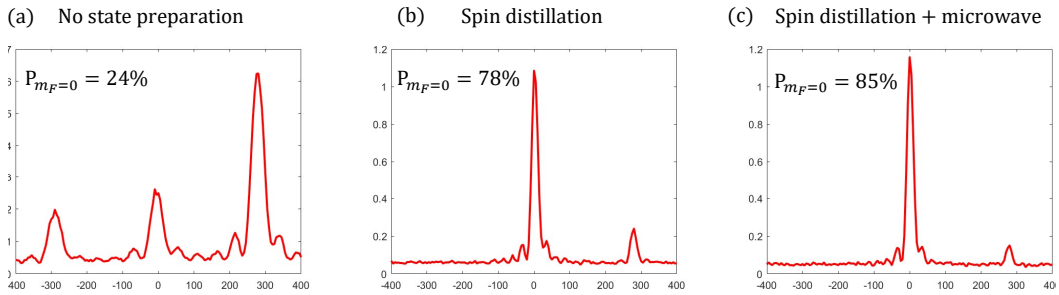

Figure 2.41: ***State preparation efficiency for ultra-cold samples of*** ^{87}***Rb*** *- Co-propagating Raman spectra performed without (a) and with (b) and (c) state preparation of the condensate. Spectrum (b) corresponds to the situation where spin distillation was performed, spectrum (c) corresponds to an additional state preparation using the microwave antenna with a modulated signal. The same magnetic field bias is applied in all cases to separate the three magnetic sublevels via the Zeeman effect. The spectrum before state preparation was taken with a Raman pulse of 20 µs duration, whereas the two other spectra with 40µs, which explains the difference in the width of the peaks. After state preparation, the majority of the atoms are in the* $m_F = 0$ *state with an efficiency of about 80 %.*

implement for thermal samples, which retains only one-fifth of the atoms. Finally, it is worth mentioning that this state preparation method is particularly suitable for operation in micro-gravity. As expected, this spatial dependence completely disappears in the absence of gravity, and the purification consistently occurs in the magnetically insensitive state.

Additional purification using a microwave pulse

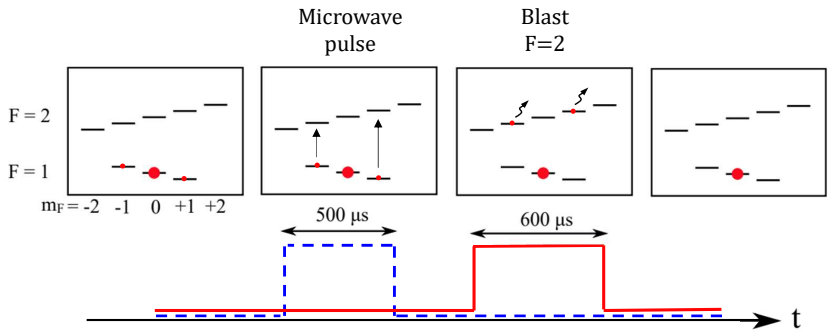

Figure 2.42: ***Additional microwave state preparation for ultra-cold*** ^{87}***Rb samples*** *- The first line describes the evolution of atomic populations associated with different states. The second line presents the temporal profiles of laser power (solid red line) and microwave power (dotted blue line).*

As we can see on the co-propagating spectrum in figure 2.41 (b), the spin distillation leaves a residual population in a sub-state that is sensitive to the magnetic field. In order to improve the state preparation, we investigated an additional purification step using a microwave pulse resonant only to the $m_F = \pm 1$ states. The sequence is presented in figure 2.42.
It consists in strongly modulating the microwave signal sent to the antenna to obtain to side-bands, as shown in section 1.3. The frequency of the modulation is tuned to have two waves

resonant to the $|F = 1, m_F = \pm 1\rangle \rightarrow |F = 2, m_F = \pm 1\rangle$ transitions when applying a magnetic field bias. For a given value of the magnetic field bias, we scan the value of the modulation to optimize the transfer from the $F = 1$ to the $F = 2$ state. Similarly to the state preparation for cold atoms, the final step involves ejecting the remaining atoms in the other m_F states using a 600 μs pulse from the Push beam. As shown in Figure 2.41, this purification enables to reduce the population of the $m_F = 1$ sub-level.

2.8 Conclusion

In conclusion, this chapter has focused on the generation of cold and ultra-cold atomic sources of rubidium and potassium. We have discussed various cooling methods, such as the magneto-optical trap and red molasses. Furthermore, the utilization of gray molasses for both rubidium and potassium has been explored. The creation of a dipole trap has allowed for evaporative cooling, leading to the achievement of Bose-Einstein condensation of ^{87}Rb. Promising results have been obtained for loading ^{39}K in the dipole trap, simultaneously with ^{87}Rb.
Additionally, the successful generation of ultra-cold atoms of ^{87}Rb in microgravity conditions has been demonstrated, both on the microgravity simulator and in the Zero G plane. State preparation techniques have also been addressed.

The obtained results lay the foundation for further investigations to obtain ultra-cold sources of rubidium and potassium in microgravity on our simulator and onboard the plane. The two main future research directions are the stabilization of the dipole trap both in the simulator and on board the aircraft, and the cooling of potassium in the optical tweezer.

The relatively low number of atoms obtained with this method and the high optical powers required raise questions about their relevance for space applications. The issues we faced regarding the misalignments of the optical dipole trap emphasize the need to study this aspect for future space missions involving evaporation in an all-optical dipole trap. However, these issues can be resolved by using an adapted optical setup, for example, by employing micro-optical benches that have demonstrated high stability even under significant accelerations and vibrations.

Chapter 3

Atom interferometry in standard gravity

Introduction

While the ultimate goal of ICE experiment is to perform inertial measurements in microgravity, the operation of the interferometer on the ground, under standard gravity conditions, proves to be essential in practice. It allows us to characterize our atomic sources, validate new methods and equipment, or simply verify the proper functioning of the experimental setup.

In this chapter, we will provide a comprehensive overview of the theory underpinning acceleration measurement using atom interferometry. We will then proceed to elucidate the experimental sequence, highlight key results, and detail the characterization performed under standard gravity conditions.

3.1 Principles of a light-pulse atom interferometer

An atomic interferometer consists in separating an incident matter wave into a coherent superposition of quantum states and then recombining them after a free evolution. The probability of presence in one of the states at the output of the interferometer then depends on the phase difference accumulated along each path of the interferometer. The structure is comparable to an optical Mach-Zehnder interferometer, the wave that interfere being an atomic cloud and the mirrors and beam splitters being laser pulses.

3.1.1 Raman transition

In order to create a coherent beam-splitter or mirror, we exploit a two-photon process that connects two distinct atomic energy levels called Raman transition[[77]]. This process allows both a momentum transfer and a change in the internal state. While other types of two-photon transitions, such as Bragg transitions, can also split the atomic cloud without altering the internal state[[72]], we opt for the Raman transition in this study because it enables us to measure the transition probability of the atoms by monitoring the populations of their internal states through fluorescence.

In our case, the Raman transitions couple the two hyperfine levels of the ground state of the rubidium or potassium atom on the D_2 line, whose energy separation corresponds respectively to a frequency ω_{HF} of 6.834 GHz and 461.7 MHz.

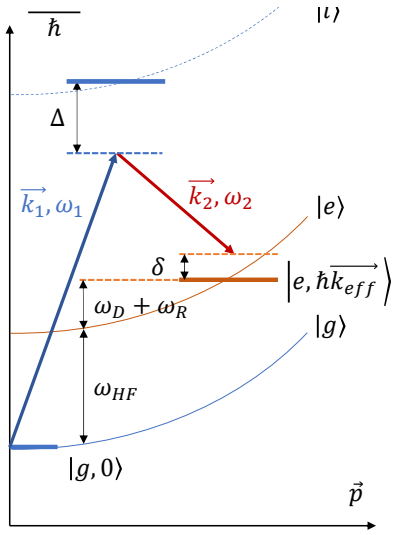

Figure 3.1: ***Energy-momentum diagram of a stimulated Raman transition*** *- An atom initially in the state $|g, \vec{p}\rangle$ is transferred to the state $|e, \vec{p}+\hbar\vec{k_{eff}}\rangle$ through a two-photon transition via the intermediate state $|i, \vec{p}+\hbar\vec{k_1}\rangle$.*

The Raman transition consists in illuminating the atoms with two lasers of different frequencies ω_1 and ω_2 which are retro-reflected on a reference mirror (see figure 3.2). The atoms interact with two pairs of laser beams and can absorb a photon at ω_1 and emit a photon into the mode of the second laser at ω_2. We can consider the atom as a three-level system ($|g, \vec{p}\rangle, |e, \vec{p}+\hbar\vec{k_{eff}}\rangle, |e, \vec{p}-\hbar\vec{k_{eff}}\rangle$), with $\vec{k_{eff}} = \vec{k_1} - \vec{k_2}$ as described in Figure 3.1. By absorbing a photon at ω_1 and emitting a photon into the mode of laser 2, the atoms change their internal state, jumping from $|g\rangle$ to $|e\rangle$. By conservation of energy and momentum, they are

accelerated by an amount corresponding to the two photon recoil: the momentum $\vec{p}$ gains $\hbar\vec{k_{eff}}$.

On our experiment, the two Raman frequencies ω_1 and ω_2 come from the Raman output of our laser system described in Section 1.1 by modulating the phase of a laser at ω_1 with a frequency corresponding to ω_{HF}. As shown in figure 3.2, the Raman collimator is located under the science chamber (see section 1.2) and a polarizer enables to have a linear polarization. The beam is retro-reflected on a reference mirror, and a quarter-wave plate enables a so called 'lin-perp-lin' polarization configuration for the two counter-propagating pairs of Raman beams. In this configuration, the incident beam has a linear polarization state, while the retro-reflected beam has a linear polarization state orthogonal to the incident one.

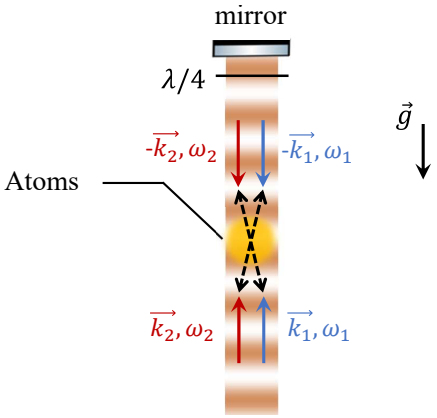

Figure 3.2: ***Diagram of the retro-reflected laser configuration used to create Raman pulses*** *- In standard gravity, due to the Doppler effect induced by the falling atoms, only one of the two counter-propagating pairs is resonant with the atomic transition.*

In this section we present the main principles of the calculation of Raman transitions in the simple case of a three-level atomic system interacting with two lasers of frequencies ω_1 and ω_2 and wavevectors $\vec{k}_1$ and $\vec{k}_2$, adapted from [[77]]. The atomic system considered is represented in Figure 3.1, and its Hamiltonian is given by:

$$\hat{H}_a = \frac{\hat{\vec{P}}^2}{2m} + \hbar\omega_g|g\rangle\langle g| + \hbar\omega_e|e\rangle\langle e| + \hbar\omega_i|i\rangle\langle i| \tag{3.1}$$

The eigenstates of the external Hamiltonian $\hat{P}^2$ are the plane waves $|p\rangle$ of de Broglie, and the atomic eigenstates are given by the tensor product of the internal state $|a\rangle$ and the external momentum $|p\rangle$: $|a,p\rangle = |a\rangle \otimes |p\rangle$. The principle of Raman transition relies on the coupling of the two stable states $|g\rangle$ and $|e\rangle$ through the intermediate level $|i\rangle$ with a finite lifetime $1/\Gamma$, Γ being the linewidth of the intermediate level. This coupling is expressed through the dipole interaction Hamiltonian:

$$\hat{H}_{\text{int}} = -\hat{\vec{d}} \cdot \vec{E} \tag{3.2}$$

where $\hat{\vec{d}}$ is the electric dipole moment operator and $\vec{E}$ is the total electric field:

$$\vec{E}(\vec{r},t) = \frac{1}{2}\vec{\varepsilon}_1 E_1 e^{i(\omega_1 t - \vec{k}_1\cdot\vec{r} + \phi_1)} + \frac{1}{2}\vec{\varepsilon}_2 E_2 e^{i(\omega_2 t - \vec{k}_2\cdot\vec{r} + \phi_2)} + \text{h.c.} \tag{3.3}$$

We consider that E_1 only couples the states $|g\rangle$ and $|i\rangle$, while E_2 couples the states $|e\rangle$ and $|i\rangle$, which is true for certain combinations of atomic structure and light polarization, according to the selection rules of atomic transitions.

In the rotating wave approximation (RWA), which consists of neglecting anti-resonant terms, and by defining the Rabi frequency as $\Omega_\alpha = -\langle\alpha|\hat{\vec{d}}\cdot\vec{\varepsilon}_n E_n|i\rangle\,\frac{1}{2\hbar}$, the interaction potential can be rewritten as:

$$\hat{H}_{\text{int}} = \hbar\Omega_g e^{i(\omega_1 t - \vec{k}_1\cdot\vec{r}+\phi_1)}|i\rangle\langle g| + \hbar\Omega_e e^{i(\omega_2 t - \vec{k}_2\cdot\vec{r}+\phi_2)}|i\rangle\langle e| + \text{h.c.} \tag{3.4}$$

Here, $\vec{\hat{d}}$ is the electric dipole moment operator, $\vec{\varepsilon}_n$ are the polarization vectors of the lasers, E_n are the electric field amplitudes, Ω_f and Ω_e are the Rabi frequencies for the transitions $|i\rangle \to |g\rangle$ and $|i\rangle \to |e\rangle$, respectively. The terms "h.c." stand for the Hermitian conjugate of the previous terms.

By performing the change of basis to the rotating frame :$C_\alpha = c_\alpha e^{i\omega_\alpha t+\phi_\alpha}$, the equation becomes:

$$i\hbar\frac{\partial}{\partial t}|\Psi_p(t)\rangle = c_g(p,t)e^{\frac{i}{\hbar}\left(\omega_g+\frac{p^2}{2m}\right)t}|g,p\rangle \tag{3.5}$$

$$+ c_i(p,t)e^{\frac{i}{\hbar}\left(\omega_i+\frac{(p+\hbar k_1)^2}{2m}\right)t}|i,p+\hbar k_1\rangle \tag{3.6}$$

$$+ c_e(p,t)e^{\frac{i}{\hbar}\left(\omega_e+\frac{(p+\hbar k_{\text{eff}})^2}{2m}\right)t}|e,p+\hbar k_{\text{eff}}\rangle \tag{3.7}$$

The total Hamiltonian is given by:

$$\hat{H} = \begin{pmatrix} \hbar\omega_g + \frac{\hat{p}^2}{2m} & \hbar\Omega_g e^{-i(\omega_1 t-\phi_1)} & 0 \\ \hbar\Omega_g^* e^{i(\omega_1 t-\phi_1)} & \hbar\omega_i + \frac{\left(\hat{p}+\hbar\vec{k_1}\right)^2}{2m} & \hbar\Omega_e e^{-i(\omega_2 t-\phi_2)} \\ 0 & \hbar\Omega_e^* e^{i(\omega_2 t-\phi_2)} & \hbar\omega_e + \frac{\left(\hat{p}+\hbar\vec{k_{eff}}\right)^2}{2m} \end{pmatrix} \tag{3.8}$$

where $\hat{p}$ is the momentum operator, m is the mass of the atom, ω_f and ω_i are the frequencies of the levels $|g\rangle$ and $|i\rangle$, respectively. The Rabi frequencies Ω_g and Ω_e are associated with the transitions $|i\rangle \to |g\rangle$ and $|i\rangle \to |e\rangle$, respectively. The symbols k_{eff}, ω_1, and ω_2 represent the effective wave vector, and the angular frequencies of the lasers.

The expression for the phase imprinted on the atoms by the laser is given by:

$$\phi_n = \vec{k}_n\cdot\vec{r}(t) - \varphi_n \tag{3.9}$$

with φ_n the phase of the laser. We then distinguish between two detunings related to the laser-atom interaction:

- The Raman detuning $\delta = (\omega_1-\omega_2)-(\omega_e-\omega_g)-(\omega_R-\omega_D)$ with respect to the transition $|g,\vec{p}\rangle \to |e,\vec{p}+\hbar\vec{k_{eff}}\rangle$.

$$\delta = \frac{p^2}{2m} + \omega_g - \frac{(\vec{p}+\hbar\vec{k}_{\text{eff}})^2}{2m} - \omega_e \tag{3.10}$$

$$= \omega_{\text{eff}} - (\omega_{HF}+\omega_R+\omega_D) \tag{3.11}$$

$$= \delta^{\text{RF}} - \omega_R - \omega_D \tag{3.12}$$

  where we have introduced the detuning $\delta^{RF} = \omega_{\text{eff}} - \omega_{HF}$, $\omega_{\text{eff}} = \omega_1 - \omega_2$, $\omega_{HF} = \omega_e - \omega_g$ representing the hyperfine splitting, $\omega_R = \frac{\vec{k}_{\text{eff}}^2}{2m}$ as the recoil frequency, and $\omega_D = \frac{\vec{p}\cdot\vec{k}_{\text{eff}}}{m}$ as the Doppler frequency.

- The large detuning Δ of ω_1 with respect to the transition $|g,\vec{p}\rangle \to |i,\vec{p}+\vec{k}_1\rangle$

3.1.2 Atomic beam-splitter and mirror

Depending on the duration τ of the Raman pulse, a fraction or all of the population may be transferred with a good control. The evolution of the population of the excited state as a function of time can be computed by writing the evolution of the coefficients c_α as a function of time using the Schrödinger equation:

$$\begin{cases} \dot{c}_g &= -i\Omega_g e^{i(\Delta t+\phi_1)}c_i \\ \dot{c}_e &= -i\Omega_e e^{i((\Delta-\delta)t+\phi_2)}c_i \\ \dot{c}_i &= -i\Omega_g^* e^{-i(\Delta t+\phi_1)}c_g - i\Omega_e^* e^{-i((\Delta-\delta)t+\phi_2)}c_e \end{cases} \tag{3.13}$$

The determination of the coefficients c_α is achieved through the adiabatic elimination of the intermediate level. This approximation assumes that the temporal variations of the intermediate level are much faster than the evolution of the fundamental levels, requiring the condition:

$$\Delta \gg |\Omega_g|, |\Omega_e|, \delta \tag{3.14}$$

This allows us to reduce the system to two equations by assuming c_g and c_e to be constant in the third equation and then substituting the expression of c_i into the first two terms. The resulting equations are as follows:

$$\begin{cases} \dot{c}_g = i\frac{|\Omega_g|^2}{2\Delta}c_g + i\frac{\Omega_{\text{eff}}}{2}e^{i(\delta t+\phi_{\text{eff}})}c_e \\ \dot{c}_e = i\frac{\Omega_{\text{eff}}^*}{2}e^{-i(\delta t+\phi_{\text{eff}})}c_g + i\frac{|\Omega_e|^2}{2\Delta}c_e \end{cases} \tag{3.15}$$

where we have defined the effective Rabi frequency and the effective phase as follows:

$$\Omega_{\text{eff}} = 2\frac{\Omega_g\Omega_e^*}{\Delta} \tag{3.16}$$

$$\phi_{\text{eff}} = \phi_1 - \phi_2 \tag{3.17}$$

This system of equations is analogous to that describing the evolution of a two-level atom interacting with an electromagnetic wave of frequency ω_{eff}, wave vector $\vec{k}_{\text{eff}}$, and phase $\phi_{\text{eff}} = \phi_1 - \phi_2$.

The choice of a parameter Δ such that $\Delta \gg \Gamma$ is justified in order to limit the spontaneous emission from the state $|i\rangle$ to the two fundamental states, which leads to a loss of coherence between $|g\rangle$ and $|e\rangle$. The rate of spontaneous emission scales as $1/\Delta^2$, and the Rabi frequency of a Raman transition scales as $1/\Delta$. Therefore, it is possible to limit the decoherence by choosing a large Δ and compensating with an increase of the laser power.

If we take the initial condition $c_g(t_0) = 1$ and $c_e(t_0) = 0$, then the probability of the transition from state $|g, \vec{p}\rangle$ to state $|g, \vec{p} + \hbar\vec{k_{eff}}\rangle$ for a pulse duration τ is given by:

$$|c_e|^2 = \left(\frac{\Omega_{\text{eff}}}{\Omega_r}\right)^2 \sin^2\left(\frac{\Omega_r\tau}{2}\right) \tag{3.18}$$

with $\Omega_r = \sqrt{|\Omega_{\text{eff}}|^2 + \delta^2}$
It corresponds to a Rabi oscillation that depends on the pulse duration and has maximal amplitude when the Raman condition $\delta = 0$ is verified.

For $\Omega_r\tau = \frac{\pi}{2}$, we have a coherent and equiprobable superposition between the two fundamental states of the atom $|g, \vec{p}\rangle$ and $|e, \vec{p} + \hbar\vec{k_{eff}}\rangle$ of different momentum. As presented in Figure 3.3, this is the equivalent of a 50/50 **optical splitter** plate for the atomic wave function. The transfer is maximum for $\Omega_r\tau = \pi$, which is equivalent to a **mirror**.

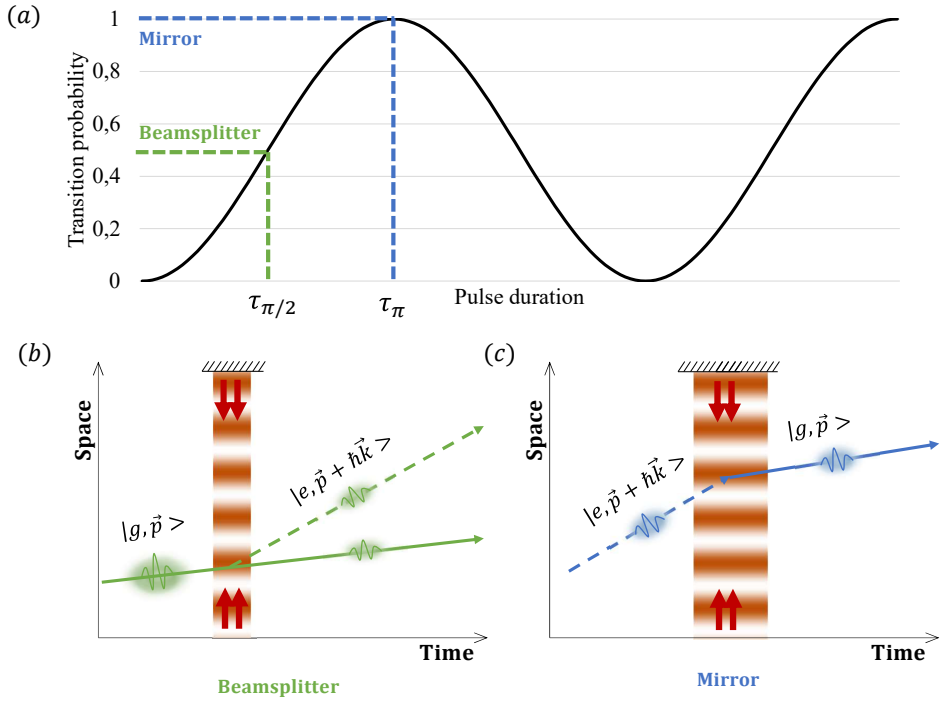

Figure 3.3: ***Atom beam splitters and mirrors*** *- (a) Rabi oscillation (b) $\pi/2$ pulse : beam splitter (c) π pulse : mirror*

3.1.3 Considering Atom Velocity in Raman Transitions

The resonance condition for Raman transitions depends on the atom's velocity through the Doppler detuning, and it is only exactly satisfied for a specific range of velocities determined by the laser frequencies. The Doppler term is maximized when the wave vectors satisfy $\vec{k_1} = -\vec{k_2}$, corresponding to counter-propagating Raman pulses. This results in a high sensitivity of Raman transitions to the targeted velocity class, which is known as selectivity in velocity. In contrast, for co-propagating Raman pulses ($\vec{k_1} = \vec{k_2}$), the Doppler term is much smaller than the hyperfine transition frequency, leading to velocity-independent transitions.
To compute the populations $P_\alpha(\delta)$ taking into account the thermal dispersion of the gas for a given laser detuning δ, we integrate equation 3.15 on ω_D :

$$P_\alpha(\delta) = \int d\omega_D \times G(\omega_D)^2 \times |[c(t,\omega_D,\delta)]_\alpha|^2 \tag{3.19}$$

where

$$G(\omega_D) = \frac{1}{(\sqrt{\pi}\sigma_{\omega_D})^{3/2}} e^{-\frac{1}{2}(\frac{\omega_D}{\sigma_{\omega D}})^2} \tag{3.20}$$

is the Gaussian distribution of the velocities with $\sigma_{\omega_D} = \sqrt{\frac{k_B \mathcal{T}}{m}} \times k_{eff}$ the standard deviation of the velocity distribution (see supplementary note 1 of [[15]]).
At a fixed duration τ, the transition probability is thus a cardinal sine function of the Raman detuning (or equivalently the atom's velocity) with a width of $1/\tau$ for a pi-pulse. Therefore, for longer pulses, the spectral width of the Raman transition becomes narrower, enhancing the selectivity in velocity (i.e., smaller velocity class width addressed). To address as many atoms as possible, shorter impulses and higher laser power are preferred. For cold atoms, the velocity distribution in an atomic cloud limits the efficiency of Raman transitions and, consequently, the interferometer's contrast. If the temperature of the atoms corresponds to a distribution smaller

than the width of the Fourier transform of the pulse duration, the Raman spectrum is a cardinal sine function and the theoretical efficiency is 100%. This highlights the importance of having the coldest atoms possible for interferometry.

3.1.4 Mach-Zehnder interferometer in the single-diffraction regime

We use atomic beam splitters and mirrors to create the atomic equivalent of the Mach-Zehnder photonic interferometer, as depicted in Figure 3.4. The interferometer is thus sensitive to any effect modifying the phase difference of the Raman lasers between the first and third pulse. In the following, we will call $\Phi_{\text{Raman}} = \phi_{eff,1} - 2\phi_{eff,2} + \phi_{eff,3}$ the interferometric phase shift associated with the Raman pulses, with $\phi_{eff,i}$ the phase imprinted on the atoms by the i^{th} laser pulse.

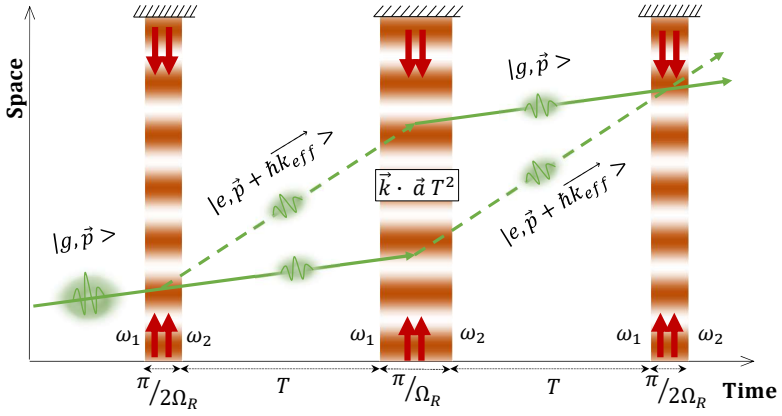

Figure 3.4: ***Mach-Zehnder interferometer in the single diffraction regime*** *- A sequence of $\pi/2 - \pi - \pi/2$ laser pulses enables to split, reflect and recombine the wave packet to create an interference pattern*

The phase shift in an atomic interferometer determines the probability of observing the atom in a specific momentum state after the sequence of $\pi/2 - \pi - \pi/2$ light pulses.

The proportion of atoms in state $|e\rangle$ is measured as:

$$P_e = \frac{N_e}{N_g + N_e} = P_0 + A\cos\Phi \tag{3.21}$$

where N_e (resp. N_g) is the number of atoms detected in state $|e\rangle$ (resp. $|f\rangle$), and P_0 and A are the offset and amplitude of the interference fringes, respectively. The fringe contrast is given by $C = 2A$. By measuring P_e and employing a model providing the expression of the interferometric phase Φ_{tot}, valuable information about the measured inertial effect can be obtained. To enhance the precision of a specific measurement, two key factors are necessary: increasing the interferometer's sensitivity to resolve small variations of the interferometric phase and accurately modeling all the non-inertial effects that can lead to phase shifts.

The calculation of the phase involves determining the phase difference resulting from wave propagation in free space and the phase acquired after each pulse from the initial state to the output of the interferometer. The interferometric phase can be expressed as follows[[98]]:

$$\Phi_{\text{tot}} = \Phi_{\text{Raman}} + \Phi_{\text{prop}} + \Phi_{\text{sep}} \tag{3.22}$$

With:

- Φ_{Raman}, which reflects the interaction of atomic wave packets with the different Raman pulses [[59]]
- Φ_{prop}, which is associated with the propagation of the waves in the two arms of the interferometer
- Φ_{sep}, which arises from a potential separation between the two wave packets during the final Raman pulse of recombination

The most common method for calculating the term Φ_{prop} is based on Feynman's approach to quantum mechanics in terms of path integrals [[47, 98]]. In the specific case of a Lagrangian quadratic in position and momentum, it can be shown that the terms Φ_{prop} and Φ_{sep} are either zero or exactly cancel each other out [[98]].
Therefore, in the following, we will consider Φ_{tot} to be equivalent to Φ_{Raman}.

3.1.5 Sensitivity of the interferometer to accelerations

Simple case of the response to a constant acceleration

The reference for the measurement is the retro-reflection mirror on top of the chamber. We denote $\vec{a_0}$ the constant acceleration of the atomic cloud with respect to the reference mirror.

Considering an interferometer starting at time $t = 0$ and neglecting the duration of the Raman pulses compared to the interrogation time ($T \gg \tau$), the total interferometric phase shift is written as follows:

$$\Phi_{\text{tot}} = \vec{k_{\text{eff}}} \cdot \vec{r}(0) - 2\vec{k_{\text{eff}}} \cdot \vec{r}(T) + \vec{k_{\text{eff}}} \cdot \vec{r}(2T) + \varphi_{\text{laser}} \tag{3.23}$$

With φ_{laser} the phase shift due to the laser phase difference between the successive pulses : $\varphi_{\text{laser}} = \varphi_1 - 2\varphi_2 + \varphi_3$. In the reference frame of the experiment, the equation of motion for a particular atom is given by:

$$\vec{r}(t) = \frac{1}{2}\vec{a_0}t^2 + \vec{v_0}t + \vec{r_0} \tag{3.24}$$

where $\vec{v_0}$ and $\vec{r_0}$ are the initial conditions for velocity and position, respectively. We can directly deduce the expression of the total interferometric phase shift:

$$\Phi_{\text{tot}} = \vec{k_{\text{eff}}} \cdot \vec{a_0}T^2 + \varphi_{\text{laser}} = \Phi_a + \varphi_{\text{laser}} \tag{3.25}$$

where Φ_a is the phase term arising from the relative acceleration of atoms in the Raman beams.

The scale factor of the atomic accelerometer, defined as the ratio of the phase shift to the experienced acceleration, is proportional to the wave vector magnitude $|\vec{k_{\text{eff}}}|$ and the square of the interrogation time T^2. Thus, improving the sensitivity necessarily involves increasing the spatial separation of the wave packets (using the double diffraction configuration that we will present in Chapter 4, or extending the duration of the interferometer. It is also noteworthy that interference fringes can be scanned by manipulating the term φ_{laser} experimentally.

In the presence of a gravitational field $\vec{g}$, the Raman detuning increases linearly due to the atoms' acceleration in the reference frame of the experiment. Therefore, it is necessary to apply a frequency chirp to the laser detuning to compensate for the Doppler effect and remain in resonance with the atoms at each moment of the interferometer. Denoting α as the value of this frequency ramp, it can be easily shown that a new phase term of $2\pi\alpha T^2$ is imprinted on the atomic wavefunction. The expression for the total phase shift is thus given by:

$$\Phi_{\text{tot}} = (\vec{k_{\text{eff}}} \cdot \vec{g} - 2\pi\alpha)T^2 \tag{3.26}$$

Response to phase noise

Understanding how the interferometric phase shift responds to temporal fluctuations in the laser phase is crucial. These fluctuations can originate from atom motion or be inherent to the laser beam. To investigate this behavior, the sensitivity function formalism is employed, which was initially developed for atomic clocks [[44]] and later adapted for inertial sensors. This powerful tool proves particularly valuable in assessing the interferometer's sensitivity to laser phase noise [[31]] and arbitrary acceleration profiles [[53]].

The sensitivity function, denoted as $g_s(t)$, represents the impulse response of the interferometric phase shift Φ_{tot} to an infinitesimal variation $\delta\varphi$ in the laser phase φ occurring at time t. When the laser phase experiences an elemental change $\varphi \to \varphi + \delta\varphi$, it results in a corresponding variation in the interferometric phase $\Phi \to \Phi + \delta\Phi$. Therefore, the sensitivity function can be expressed as follows:

$$g_s(t) = \lim_{\delta\varphi \to 0} \frac{\delta\Phi(\delta\varphi, t)}{\delta\varphi} \tag{3.27}$$

Its calculation can be easily performed when the laser phase jump occurs between two Raman pulses. For example, if we consider that it happens between the first and second pulse, it follows:

$$\delta\Phi = \varphi(0) - 2(\varphi(0) + \delta\varphi) + (\varphi(0) + \delta\varphi) = -\delta\varphi \tag{3.28}$$

and we deduce that $g_s(t) = -1$ in this situation. If the phase jump occurs instead between the second and third pulse, the calculation yields $\delta\Phi = +\delta\varphi$ and $g_s(t) = +1$.

If the phase jump takes place during one of the Raman pulses, it can be shown that the complete sensitivity function is expressed as follows [[30, 16]]:

$$g_s(t) = \begin{cases} -\sin(\Omega_R t) & \text{if } 0 \leq t \leq \tau \\ -1 & \text{if } \tau \leq t \leq T + \tau \\ \sin(\Omega_R(t - T - 2\tau)) & \text{if } T + \tau \leq t \leq T + 3\tau \\ 1 & \text{if } T + 3\tau \leq t \leq 2T + 3\tau \\ \sin(\Omega_R(t - T - 2\tau)) & \text{if } 2T + 3\tau \leq t \leq 2T + 4\tau \\ 0 & \text{otherwise} \end{cases} \tag{3.29}$$

With τ the duration of a $\pi/2$ pulse. Using this function, the interferometric phase shift can be calculated for any evolution of the laser phase $\varphi(t)$:

$$\Phi = \int_{-\infty}^{\infty} g_s(t) d\varphi(t) = \int_{-\infty}^{\infty} g_s(t) \frac{d\varphi(t)}{dt} dt \tag{3.30}$$

We can derive the influence of the relative phase noise of the Raman lasers on the phase φ by measuring the power spectral density of the laser phase noise, denoted as $S_\varphi(\omega)$. The variance of interferometric phase fluctuations is then given by:

$$\sigma_\Phi^2 = \int_{-\infty}^{\infty} S_\varphi(\omega) \left|\omega G(\omega)\right|^2 \frac{d\omega}{2\pi} \tag{3.31}$$

where $G(\omega)$ represents the Fourier transform of the sensitivity function.

$$G(\omega) = \int_0^{\infty} e^{-i\omega t} g_s(t) dt \tag{3.32}$$

The term $= |\omega G(\omega)|$ is defined as the transfer function of the interferometer and is thus given by:

$$H(\omega) = \frac{4\omega\Omega_R}{\omega^2 - \Omega_R^2} \sin\left(\frac{\omega(T+2\tau)}{2}\right)\left[\cos\left(\frac{\omega(T+2\tau)}{2}\right) + \frac{\Omega_R}{\omega}\sin\left(\frac{\omega T}{2}\right)\right] \tag{3.33}$$

Response function for accelerations

The sensitivity function we have defined can also be used to calculate the interferometer's response to an acceleration $\vec{a}$. It can be shown that [[16]]:

$$\Phi = \int_0^{2T+4\tau} f(t)\vec{a}(t)\vec{k}_{\text{eff}}dt \tag{3.34}$$

Where $f(t)$ is the response function of the interferometer associated with the sensitivity function, and is given by:

$$f(t) = \begin{cases} 0 & \text{if } t < 0 \\ \frac{1}{\Omega_R}(1 - \cos(\Omega_R t)) & \text{if } 0 \leq t \leq \tau \\ t - \tau + \frac{1}{\Omega_R} & \text{if } \tau \leq t \leq T + \tau \\ T + \frac{1}{\Omega_R}(1 - \cos(\Omega_R(t-T))) & \text{if } T + \tau \leq t \leq T + 2\tau \end{cases} \tag{3.35}$$

The expression of $f(t)$ in the second part of the interferometer ($T+2\tau \leq t \leq 2T+4\tau$) is obtained through symmetry from equation 3.35:

$$f(T + 2\tau + t) = f(T + 2\tau - t) \tag{3.36}$$

This formalism takes into account the phase evolution during the laser pulses. The characteristic shape of this response function is shown in Figure 3.5. We see that the atomic interferometer will be much more sensitive to an acceleration occurring in the middle of the interferometer compared to the edges.
To evaluate the interferometer's response in the frequency domain, we use the Fourier transform $H_a(\omega)$ of the response function $f(t)$. This acceleration transfer function is related to the previously defined functions G and H by: $H_a(\omega) = G(\omega)/\omega = H(\omega)/\omega^2$. The typical shape of this transfer function is shown in Figure 3.5(c). Notice the asymptotic behavior resembling a 'low-pass' filter ($H_a(\omega) \approx T^2\text{sinc}(\omega T/2)$). Using the power spectrum of acceleration fluctuations $S_a(\omega)$ and this acceleration response function $Ha(\omega)$, the variance of interferometric phase fluctuations can be expressed simply as:

$$\sigma_\Phi^2 = k_{eff}^2 \int_0^\infty |H_a(\omega)|^2 S_a(\omega) d\omega/2\pi \tag{3.37}$$

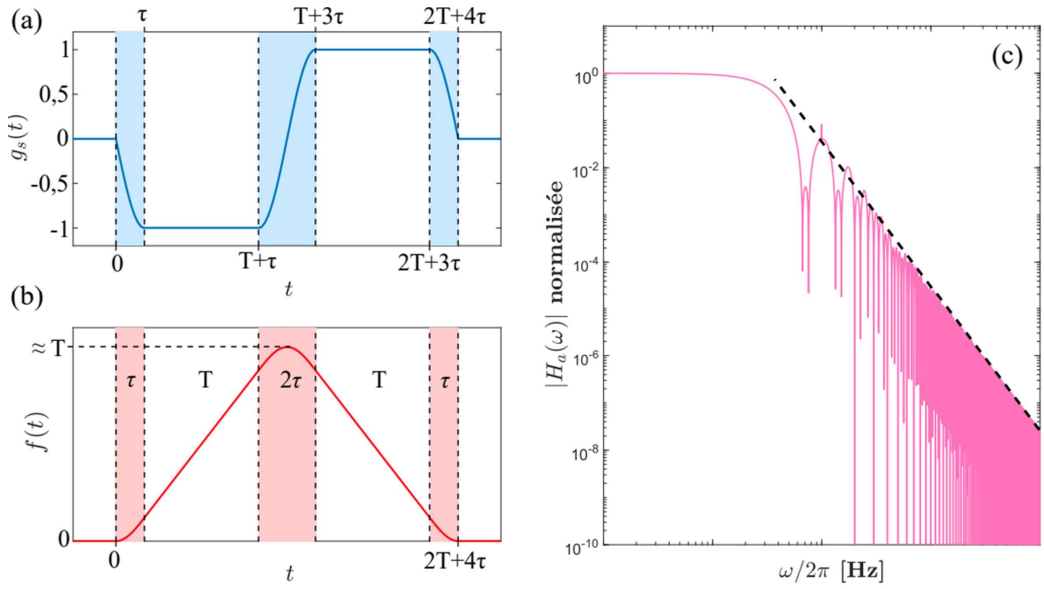

Figure 3.5: ***Response of an Atomic Mach-Zehnder Interferometer*** *- Typical shape of (a) the sensitivity function $g_s(t)$ and (b) the response function $f(t)$ of an interferometer with an interrogation time T and pulse duration $\frac{\pi}{2}$ denoted as τ. Here, the pulse durations have intentionally been exaggerated for better visualization of different segments of the functions. In practice, pulse durations are often much smaller than the interrogation time: the sensitivity and response functions can then be approximated as a double square wave and a triangle, respectively. (c) Transfer function $|H_a(\omega)|$ of the interferometer. We observe the asymptotic behavior resembling a low-pass filter.*

3.2 Experimental results and characterization of the Atom Interferometer

The ground-based experiments provide valuable insights into the experimental apparatus, data analysis procedures, and a comprehensive examination of systematic effects. It allows for the characterization of atomic sources, validation of new methods and equipment, and serves as a means to verify the proper functioning of the experimental setup. In the past, operating the double-species interferometer in gravimeter configuration even enabled a test of the equivalence principle with a statistical uncertainty on the Eötvös parameter of 7.8×10^{-8}, as we will see in Chapter 5 [[14]]. This represents the state-of-the-art for a test with cold atoms of two different atomic species.

This section will present some atom interferometry results obtained in this gravity regime. Moreover, it will introduce the methods we employ to reconstruct interference fringes and assess the atomic accelerometer's quality.

3.2.1 Raman spectroscopy and Rabi oscillations

As described in the theory section of this chapter, each pulse in the interferometer must be executed while respecting the Raman condition, ensuring that the frequency detuning $\delta = \omega_1 - \omega_2$ and duration τ are optimized to maximize the transfer and enhance the contrast.
In our experimental setup, we perform Raman spectroscopy by scanning the laser frequency difference δ_{RF} at a fixed τ. The resulting curve is a convolution product between the velocity distribution of the atomic cloud and the Fourier transform of the Raman pulse. If the pulse duration is sufficiently long such that $\Omega_r << k_{\mathrm{eff}}\sigma_v$, the measurement reflects the transition rate

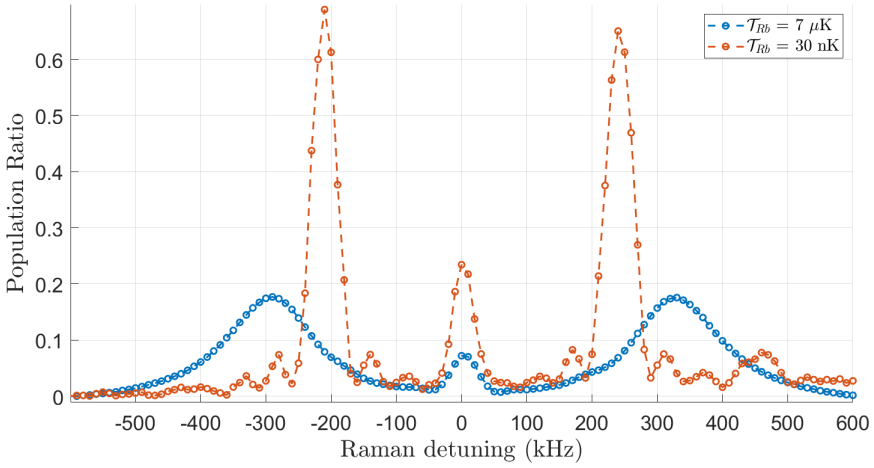

Figure 3.6: ***Counter-propagating Raman spectrum for Rb cold and ultra-cold atoms*** *- the width of the spectrum with ultra-cold atoms is limited by the duration of the pulse while the spectrum with cold atoms exhibits lower peaks enlarged by the velocity distribution within the cloud. For both spectra, the pulse duration is $\tau = 20\,\mu s$. The peaks are not at same frequencies because of a difference in the times of flight before the Raman pulses (due to the state preparation of cold atoms with the microwave)*

of each velocity class of the atomic cloud during the laser pulse. Consequently, depending on the time of flight (ToF) of the cloud, we anticipate observing in the frequency space the velocity distribution profile centered at $\delta_{\mathrm{RF}} = k_{\mathrm{eff}} g ToF + \omega_R$. Figure 3.6 presents an example of such a spectrum for a $ToF = 9$ ms for cold and ultra-cold atoms.

The frequency used in interferometry depends on the time of flight (ToF) before the first pulse. In the specific case of operation in standard gravity, a time of flight of a few milliseconds is allowed before the first interferometer pulse to lift the degeneracy between the two pairs of counter-propagating beams due to the Doppler effect caused by gravity with respect to the reference mirror. The detuning is set to a frequency corresponding to the peak of one of the Gaussians and apply a frequency chirp during the Raman pulse in the interferometer. The chirp is calculated by our control software on LabView, using the value of the peak frequency. By chosing the peak of lower or higher frequency, denoted as 'Down' and 'Up', we perform the interferometer in one direction with respect to the reference mirror or another. The chirp also changes its sign : 'Chirp Down' or 'Chirp Up'.

Once we know the pulse frequency, we proceed with Rabi oscillations by scanning the pulse duration and observing the attenuated sinusoid, as presented in Figure 3.7. We chose the $\pi-$ pulse duration to maximize the transfer to the excited state.

3.2.2 Scanning the phase of the atom interferometer

An atomic Mach-Zehnder interferometer produces a population ratio at its output that varies sinusoidally with the accumulated total phase shift Φ_{tot}. This phase includes a direct inertial phase term directly related to the relative acceleration of the atoms with respect to the reference mirror and a dependence on the laser phase fluctuation φ_{laser}. The interference fringes can be scanned through random fluctuations of accelerations imposed by the environment, or in a controlled manner, by applying a variable laser phase. In this latter case, it is referred to as an interferometer with laser phase scanning. The ability to control ϕ_{tot} with φ_{laser} provides a simple

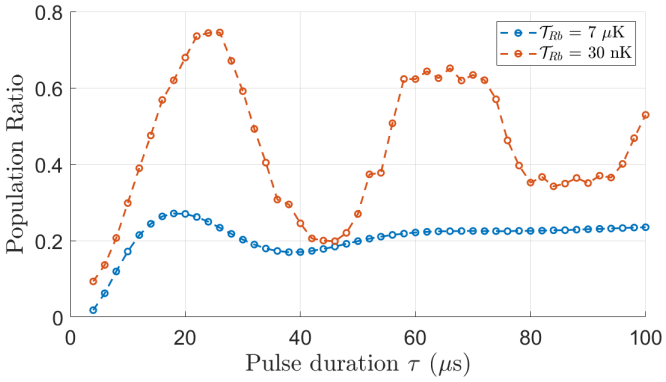

Figure 3.7: ***Counter-propagating Rabi oscillations for Rb cold and ultra-cold atoms***

and reliable way to evaluate the contrast and signal-to-noise ratio of the interferometer under given experimental conditions. The fringe pattern is obtained by repeating the experimental sequence many times and modifying the value of the laser phase term φ_{laser} at each iteration by adjusting the output phase of the Raman DDS signal (see section 1.3).
A sufficiently short interrogation time is chosen to neglect the inertial phase term and thus overcome "random" fluctuations due to vibrations. The laser frequency also undergoes a linear chirp during the interferometer to remain in resonance with the atoms. The bias field is kept on during the interferometer to ensure that $|F = 1, m_F = \pm 1\rangle \rightarrow |F = 2, m_F = \pm 1\rangle$ Raman resonances are well-separated from those involving $|F = 1, m_F = 0\rangle$.

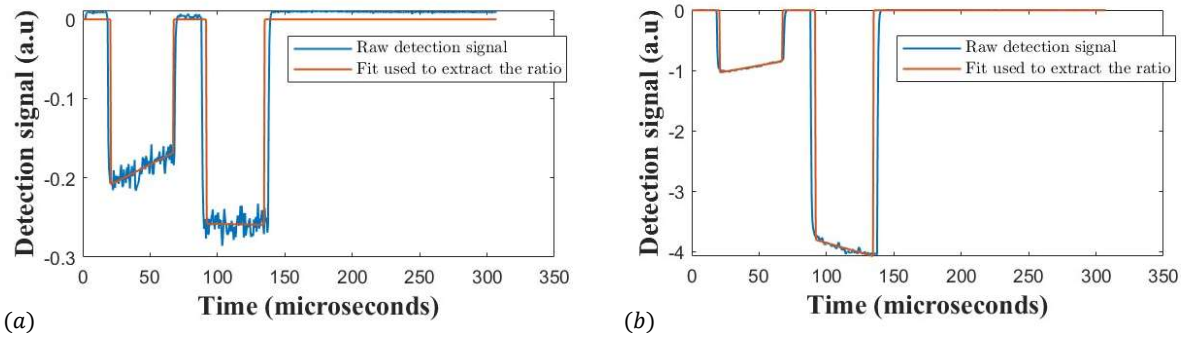

Figure 3.8: ***Detection signal for cold and ultra-cold atoms*** *- (a) Detection signal for cold atoms and (b) ultra-cold atoms, linear fit used to estimate the ratio.*

A photodiode is used for the thermal cloud, while a photomultiplier tube is used for the ultra-cold atoms due to the much lower number of atoms in the cloud. To obtain the ratio, the raw fluorescence detection signals corresponding to the number of atoms in the excited state N_2 and the total number of atoms N_{tot} are fitted with linear functions, and the average value of this fit is extracted. A background shot is taken at the beginning of the data set by performing the exact same sequence with the MOT Coils off: it corresponds to a shot without atoms, but the laser background is present. From this background shot, we extract the corresponding $N_{2,\text{background}}$ and $N_{tot,\text{background}}$, and subtract them from all the measurement points. The error on the estimation of the ratio due to the detection can be computed using the residuals of the linear fit used for N_2 and N_{tot} and propagating these errors. The principle of the ratio estimation is presented in figure 3.8. The resulting fringes and the associated error bars are presented in

Figure 3.9.

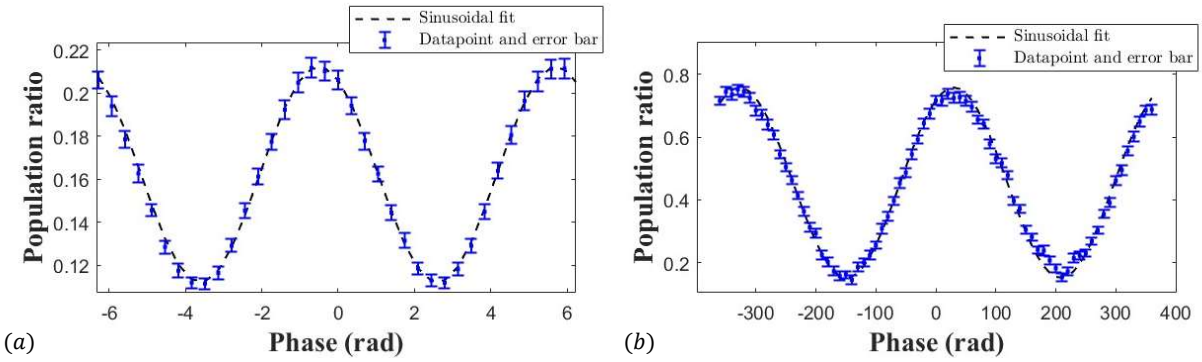

Figure 3.9: ***Phase scan for cold and ultra-cold atoms and noise due to the detection system*** *- Phase scan fringes fitted for (a) cold atoms (b) and ultra-cold atoms. The error bars are estimated using the standard deviation of linear fit residuals.*

Figure 3.10 presents two datasets obtained for cold atoms at approximately 8 μK and ultra-cold atoms (approximately 30 nK). The datasets were taken at intervals of several years, which explains the phase shift between the two datasets. The datasets are fitted with sinusoidal functions to extract the fringe contrast.

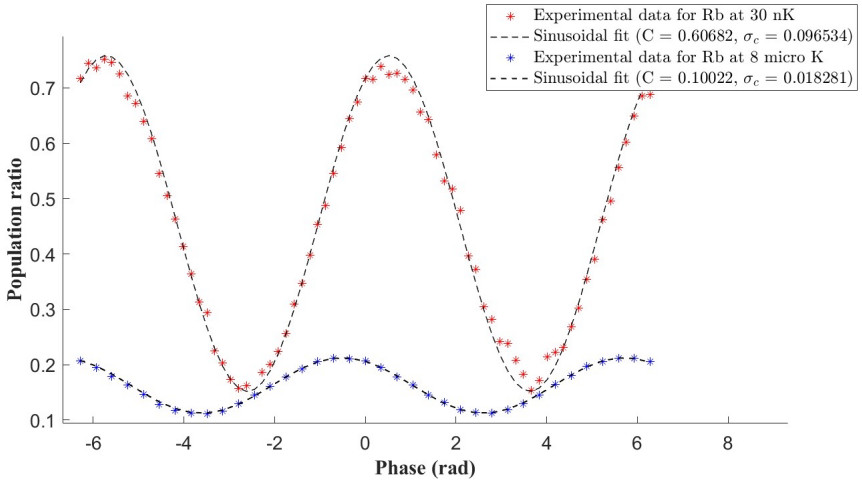

Figure 3.10: ***Atomic interferometer fringes obtained with phase scan in standard gravity with*** ^{87}***Rb*** *-for a 100 μs interrogation time in the interferometer and 20 μs π-pulse. A sinusoidal fit allows us to extract the contrast for the different atomic sources. It is observed that the ultra-cold atoms exhibit a much higher contrast than for cold atoms.*

The contrast enhancement with the ultra-cold source is substantial, as we obtain a contrast of 0.6 on the fringes for the ultra-cold atoms, whereas a contrast of 0.1 is obtained with the red molasses. Several factors affect the contrast, including the state purity (linked to the quality of the state preparation), and the temperature of the atoms.

3.2.3 Scanning the chirp of the atom interferometer

During the Raman pulses, the frequency difference between the two lasers is typically kept constant, ensuring that the atoms experience the same Raman transition at each iteration of the interferometer. However, in standard gravity, we want the atoms to remain resonant with

the Raman lasers after ToF of tens of milliseconds : we introduce a linear frequency chirp during the Raman pulses. By scanning the chirp of the Raman frequency during the pulses and measuring the resulting shift in the interference pattern, we can obtain fringes for longer times of flight.

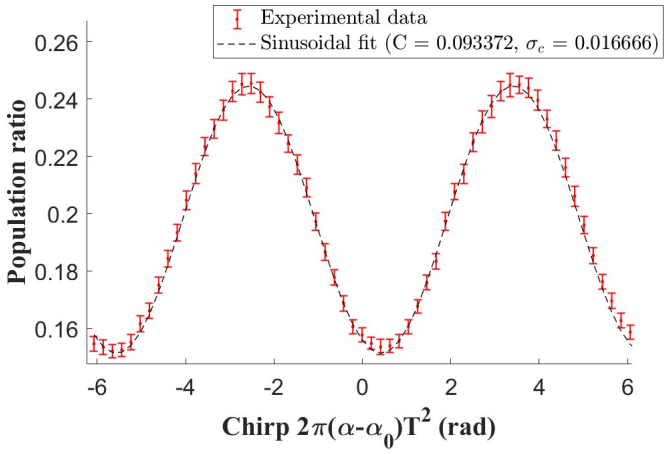

Figure 3.11: ***Atomic interferometer fringes obtained with chirp scan in standard gravity with*** ^{87}***Rb*** *-for a 1 ms interrogation time in the interferometer and 24 μs π-pulse. The experimental data points are shown with error bars, which are associated with the fitting of the raw detection signals using linear functions. A sinusoidal fit allows us to extract the contrast.*

Figure 3.11 illustrates an example of fringes obtained with a 1 ms interrogation time in the interferometer and a π-pulse duration of 24 μs. By conducting the same measurement for various interrogation times, we can for instance identify the central fringe and examine the phase shift induced by gravity. We will see in chapter 5 that this method can be used to test the weak equivalence principle in standard gravity.A so-called 'k-reversal' technique is used in order to reduce systematic errors: the measurement is made by switching the frequency from the 'Up' peak to the 'Down' peak from one shot to another. This way, the interferometer is performed in one direction and then the other, creating symmetry in the data.

3.2.4 Atomic accelerometer

As our experiment is intended to be transportable and operate on microgravity platforms that may experience vibrations, the interferometer's fringes can be affected by these inertial forces. High levels of vibration can blur the fringes. They are reconstructed using a classical accelerometer attached to the reference mirror. During each iteration of the interferometer, the sensor records the parasitic vibrations experienced by the mirror. From the measured temporal profile of acceleration, it is possible to estimate the inertial phase accumulated during the interferometer using the formalism of the response function presented in section 3.1.5. The idea is then to observe the correlation between the output of the atomic sensor, providing a measurement P of the population ratio, and that of the classical sensor, providing an estimation Φ of the inertial phase induced by the vibrations. The interferogram is formed by the set of N_m measurement pairs (P_i, Φ_i) recorded during the successive iterations of the experimental sequence (with $i = \{1, ..., N_m\}$).

The figure 3.12 illustrates the principle of this fringe reconstruction method, commonly referred to as FRAC (Fringes Reconstruction by Accelerometer Correlation) and described in [[74, 52]].

The figure 3.13 presents fringes reconstructed using this method. This dataset was acquired for

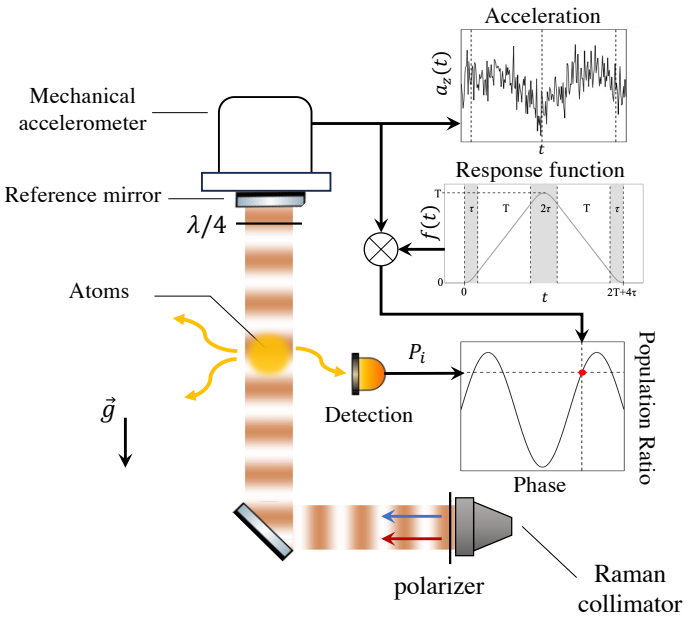

Figure 3.12: ***Principle of the FRAC method*** *- The fringes are reconstructed by measuring the temporal profile of the acceleration $a_z(t)$ of the reference mirror for each new measurement. This profile is multiplied by the interferometer's response function $f(t)$ and then integrated to estimate the interferometric phase. The correlation with the population ratio measured by detection allows the formation of the interference pattern.*

thermal atoms at 8 μK after a time of flight (ToF) of 7 ms to lift the degeneracy between the two pairs of counter-propagating beams. A sequence of $\pi - \pi/2 - \pi$ pulses with a duration of $\tau_\pi = 24\mu$s is executed, and the interrogation time T is set at 10 ms. The Raman detuning is linearly chirped to counteract the atoms' fall. For this interferometer duration, it is observed that the laboratory's ambient vibration level causes a phase excursion of several tens of radians. In the hypothetical case of an ideal correlation, the experimental data points would align perfectly along a sinusoidal curve. However, in reality, each of the classical and quantum measurements is affected by its own noise. The atomic interferometer can experience slow variations in contrast and offset due to slight instabilities in experimental conditions (e.g., optical power of the Raman laser). The atomic interferometer may also undergo significant contrast drops when subjected to excessive inertial effects. Additionally, the measurement of the population ratio is also affected by its own uncertainty, associated with the detection or imaging method used. The combination of all these disturbances constitutes what is known as "amplitude noise". On the other hand, the classical sensor also has its intrinsic limitations, well-known in the field of inertial navigation. These include the sensor's own noise, limited bandwidth, bias or scale factor instabilities, linearity defects, axis couplings, and sampling noise. Any instability in the laser phase also introduces a parasitic term that is not accounted for in this reconstruction method. All these phenomena introduce errors in the estimation of Φ and are thus the source of "phase noise." Ultimately, these two types of noise contribute to the degradation of the correlation quality, which can be evaluated by performing a large number of measurement and study the statistics.

It should be noted that the number of fringes scanned by this method is more significant when the level of parasitic vibrations is higher and when the interrogation time is longer. Consequently, this technique is not suitable for short interrogation times (typically less than a millisecond) as it does not allow for sufficient fringe scanning given the ambient vibration level. In such cases,

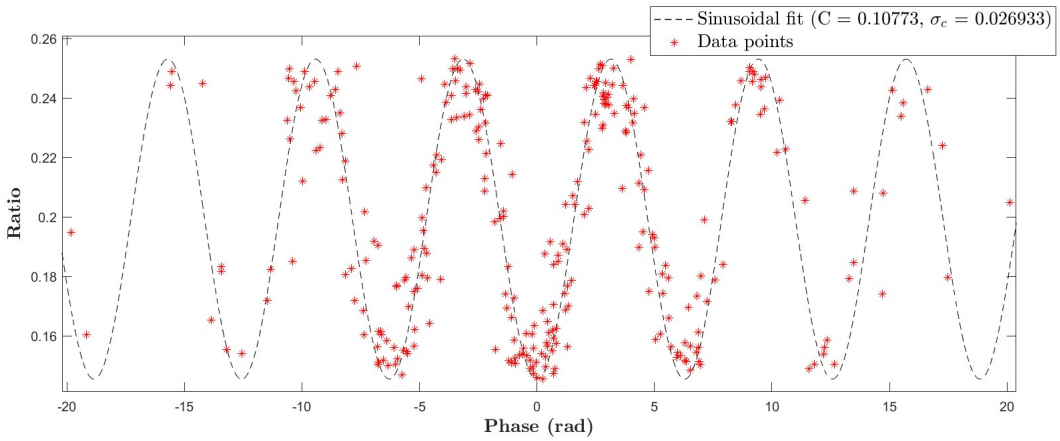

Figure 3.13: ***Atomic interferometer fringes obtained with FRAC method with*** ^{87}***Rb*** *- for a 10 ms interrogation time in the interferometer and 24 µs π-pulse. A sinusoidal fit allows us to extract the contrast.*

it is preferable to use the laser phase or chirp scanning technique. On the contrary, when the number of scanned fringes is too high, it is still possible to fold the data within the interval $[0, 2\pi]$ to facilitate their visualization. In this situation, we can study the distribution of the ratio and verify that it corresponds to the distribution of a sinusoid, with a double-shape structure. This confirms that the atoms interfere even with higher levels of vibrations. This method based on the statistical distribution is also used to study the quality of our interferometer, as it enables to separate the noises linked to the phase and amplitude. We call this method 'BAT' method, because of the shape of the studied distribution [[74]].

BAT Method

First, consider the case of an ideal measurement, unaffected by amplitude noise, associated with an offset P_0 and a contrast $C = 2A$. Each measurement P_i can then be modeled as a draw from the random variable: $P = P_0 + \frac{C}{2}\cos(\Phi)$. For a phase fluctuation Φ uniformly distributed in the interval $[0, \pi]$, it can be shown that the probability density function of P is given by:

$$f_{P(p)} = \begin{cases} \frac{1}{A\pi}\sqrt{1 - \left(\frac{P_0 - p}{A}\right)^2} & \text{if } p \in]P_0 - A, P_0 + A[\\ 0 & \text{otherwise} \end{cases} \tag{3.38}$$

As illustrated in Figure 3.14, this distribution exhibits two discontinuities at $P_0 \pm A$. This reflects the fact that it is more probable for the random variable to fall at the peak of fringes than on the flanks. By considering a Gaussian noise on the population ratio of standard deviation σ_P, the resulting probability density function writes :

$$\mathcal{F}(r) = \int_{-\infty}^{+\infty} \frac{2}{C\pi\sqrt{1 - \left(\frac{2(P_0 - r')}{C}\right)^2}} \times \frac{1}{\sigma_P\sqrt{2\pi}} \exp - \frac{(r - r')^2}{2\sigma_P^2} dr' \tag{3.39}$$

with $C = 2A$ being defined as the AI contrast. This function is characterized by three parameters: the offset P_0, the contrast C, and the amplitude noise σ_P. We show the characteristic shape of this function in Figure 3.14(b) for the case where $P_0 = 0.5$, $C = 0.2$, and $\sigma_P = 0.02$.

To construct the the histogram of the N_m measured ratios, one need to determine the number of bins N_c. This parameter must be chosen carefully, as having too many bins leads to low statistics in each bin and ultimately results in a noisy histogram. Conversely, a too small number

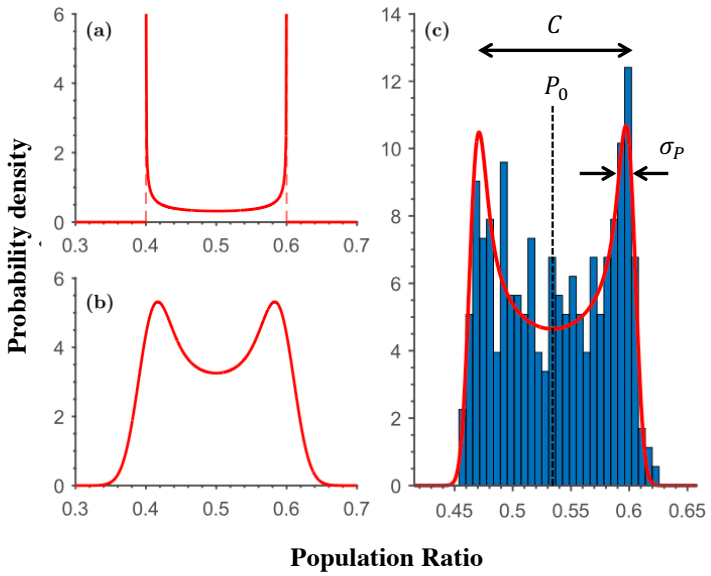

Figure 3.14: ***Principle of the BAT method*** *- (a) Probability density of a sinusoidal function characterized by an offset $P_0 = 0.5$ and a contrast $C = 0.2$. (b) Convolution with a Gaussian of standard deviation $\sigma_P = 0.02$. (c) Example histogram constructed from experimental measurements (blue) and the result of fitting with the function f_P defined in equation 4.4 (red). In this example, $N_c = 30$, $\Delta P = 0.0059$, and the parameter triplet estimated from the fit is: $P_0 = 0.534$, $C = 0.1375$, and $\sigma_P = 0.0061$.*

of bins will lead to poor sampling of the bi-modal structure and an artificial broadening of the side peaks. The choice of N_c is typically made to ensure that there are at least 5 measured data points, on average, in each bin of the histogram. It is also ensured that the width of a bin does not exceed the estimated value of the amplitude noise. When several hundred points have been measured under typical noise conditions encountered in practice, a value of $N_c = 30$ is often suitable.

Once this value N_c has been defined, the calculation of the bin width ΔP gives:

$$\Delta P = \frac{\max(P_i) - \min(P_i)}{N_c} \tag{3.40}$$

where $\max(P_i)$ and $\min(P_i)$ represent the extreme values of the measured data set. The centers of each bin are then given by:

$$\begin{aligned} c_1 &= \min(P_i) + \frac{\Delta P}{2} \\ c_2 &= c_1 + \Delta P \\ &\vdots \\ c_{N_c} &= \max(P_i) - \frac{\Delta P}{2} \end{aligned}$$

The histogram is constructed by counting the number n_l (where $l = 1, \ldots, N_c$) of measurements P_i falling within each bin and applying a normalization factor to obtain the associated probability density d_l:

$$d_l = \frac{n_l \cdot \Delta P}{N_c} \tag{3.41}$$

The offset P_0, contrast C, and amplitude noise σ_P of the atomic interferometer can be estimated by performing a least squares fit of the histogram (c_l, d_l) with $l = 1, \ldots, N_c$. The function F_P defined in Equation 3.39 is used for the fitting. An example of such fitting is provided for illustration in Figure 3.14 (c). The signal-to-noise ratio (SNR) can be calculated as

$$SNR = \frac{C}{2\sigma_P} \tag{3.42}$$

We can derive the sensitivity per shot, denoted as S, which is given by:

$$S = \frac{1}{SNR \cdot k_{\text{eff}} \cdot T^2} \tag{3.43}$$

Here, k_{eff} represents the effective wave number of the interferometer, and T is the interrogation time.

The uncertainty δS in the estimation of this sensitivity is directly linked to the uncertainties δC and $\delta\sigma_P$ in the contrast and amplitude noise obtained from the fitting process. Basic rules of uncertainty propagation lead to the expression:

$$\delta S = S\sqrt{\left(\frac{\delta C}{C}\right)^2 + \left(\frac{\delta\sigma_P}{\sigma_P}\right)^2} \tag{3.44}$$

To test the effectiveness of the BAT method, we apply it to simulated data with known parameters rather than experimental data. This enables a comparison between the estimated values of contrast, offset, and amplitude noise with the actual values defined in the simulation. Such tests confirm that the statistical efficiency of this method heavily relies on the amount of accumulated data and the signal-to-noise ratio of the dataset. It's also important to ensure that the range of randomly scanned phase is wide enough to consider a uniform distribution over the interval $[0, \pi]$ after folding. This method doesn't require measurements from the classical accelerometer to function since it uses only the measured population ratios. Therefore, it allows the separation of the two types of noise (amplitude and phase) and demonstrates the proper functioning of the atomic interferometer even when the interference fringes are significantly disturbed. However, this approach completely ignores the effects of possible atomic phase fluctuations and thus does not demonstrate control over them.

Conclusion

In this chapter, we have introduced the main principles of atomic interferometry and studied and characterized our interferometer for rubidium in standard gravity. Our experiment is an atom interferometer that has demonstrated state-of-the-art measurements while functioning as a gravimeter in standard gravity. The small dimension of the vacuum chamber is the main limitation; the experiment was designed to function in microgravity to work with longer interrogation times.

Moving forward, our focus will shift to the operation in microgravity, where atoms do not experience the gravitational fall with respect to the reference mirror. This unique scenario requires the exploration of new models of interferometry, which will be the subject of the following section.

The insights gained from this study can be extended to potassium, as the methods remain the same. We anticipate that the operation in a dual-species regime will introduce additional aspects that must be carefully considered to test the universality of free fall.

Chapter 4

Atom interferometry in microgravity

Introduction

Future tests of the Weak Equivalence Principle (WEP) demand extended interrogation times that only the space environment can provide. Therefore, the study of atom interferometry becomes crucial in the microgravity regime, wherein the entire apparatus experiences free fall onboard a satellite. In this environment, atoms undergo near zero velocity and acceleration relative to the reference mirror, we are in a so called "low velocity and low acceleration regime". The acceleration encountered by the atoms is then sufficiently low for the group velocity $\vec{v}_0$ of the atom cloud to satisfy the following condition at each moment of the interferometer operation:

$$\vec{k}_{\text{eff}} \cdot \vec{v}_0(t) < \Omega_{\text{eff}} \tag{4.1}$$

When this criterion is fulfilled, an atom can potentially resonate with the two pairs of counter-propagating Raman transitions concurrently in the present case of retro-reflected beams.
Within the low velocity and acceleration regime, two operational modes arise for the atomic interferometer. In the case of a thermal cloud, the velocity dispersion is larger than $\hbar k_{eff}$. Two regimes of atomic diffraction are possible. For the zero-velocity class $p = 0$, $|F = 1, 0\rangle$ is simultaneously coupled with both states $|F = 2, \pm\hbar k_{\text{eff}}\rangle$ leading to **Double Diffraction** (DD) [[67]]. For a velocity class $p >> \hbar k_{eff}$, the laser pulse couples simultaneously $|F = 1, p\rangle$ with $|F = 2, p + \hbar k_{\text{eff}}\rangle$ on one hand, and $|F = 1, -p\rangle$ with $|F = 2, -p - \hbar k_{\text{eff}}\rangle$ on the other hand leading to **Double Single Diffraction** (DSD) [[13]]. In the case of ultra-cold atoms, the narrow velocity distribution only allows for the Double Diffraction regime.

In this chapter, we present a theoretical investigation of this unique regime, alongside the results of numerical simulations that forecast the interferometer's behavior. Additionally, we showcase diverse experimental results obtained from our microgravity platform, which lays the groundwork for future inertial measurements in space.

4.1 Theory of Atom Interferometry in microgravity

In this section, we will extend the formalism that describes atom interferometry in standard gravity from Section 3.1 to understand the "low velocity and low acceleration" regime. Through numerical solutions of the time-dependent Schrödinger equation, we will demonstrate the capability to anticipate the characteristics of Raman spectra and Rabi oscillations in microgravity.

4.1.1 Raman transition in the low velocity and acceleration regime

The investigation of Raman transitions in the regime of low velocity and acceleration is conducted using the approach outlined in [[69]].

Theoretical analysis

In microgravity, in the absence of Doppler effect, the Raman resonance condition is the same for both pair of beams. The two counter-propagating transitions $\pm\vec{k}_{eff}$ are degenerate and simultaneously address the same velocity class. In this scheme, atoms interact with four laser waves which drive Raman transitions with effective wave vectors $\pm\vec{k}_{eff}$, with $|\vec{k}_{eff}| \simeq 2|\vec{k_1}| \simeq 2|\vec{k_2}|$. The atomic system can be reduced to a 5-level system, noted as :

$$\begin{aligned} |+2\rangle &= |g, \vec{p} + 2\hbar\vec{k}_{\text{eff}}\rangle \\ |+1\rangle &= |e, \vec{p} + \hbar\vec{k}_{\text{eff}}\rangle \\ |0\rangle &= |g, \vec{p}\rangle \\ |-1\rangle &= |e, \vec{p} - \hbar\vec{k}_{\text{eff}}\rangle \\ |-2\rangle &= |g, \vec{p} - 2\hbar\vec{k}_{\text{eff}}\rangle \end{aligned} \tag{4.2}$$

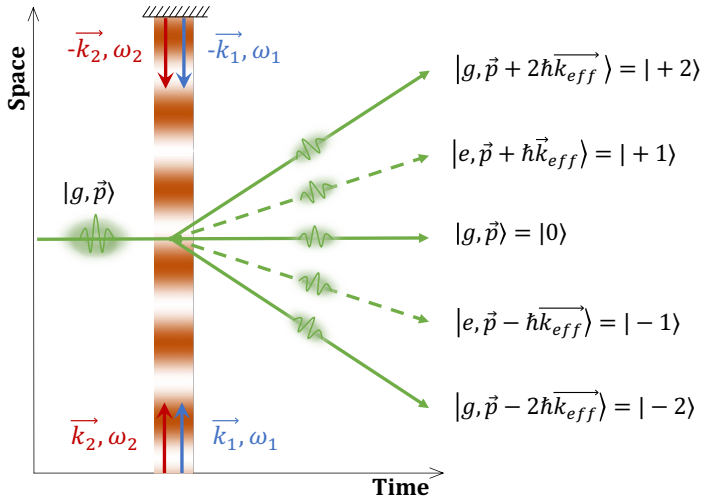

Figure 4.1: ***Diagram of the retro-reflected configuration used without Doppler effect*** *- We consider the coupling of 5 atomic energy levels.*

Figure 4.1 shows the different orders of diffraction associated with the external states. The Raman transition causes atom diffraction in both directions in microgravity, and a second order of diffraction has to be taken into account to develop a comprehensive model of the pulse. Figure 4.2 presents the energy-momentum diagram of the Raman transition in absence of Doppler effect when considering this 5-level system with an initial atomic state $|g, 0\rangle$ along with the detunings involved :

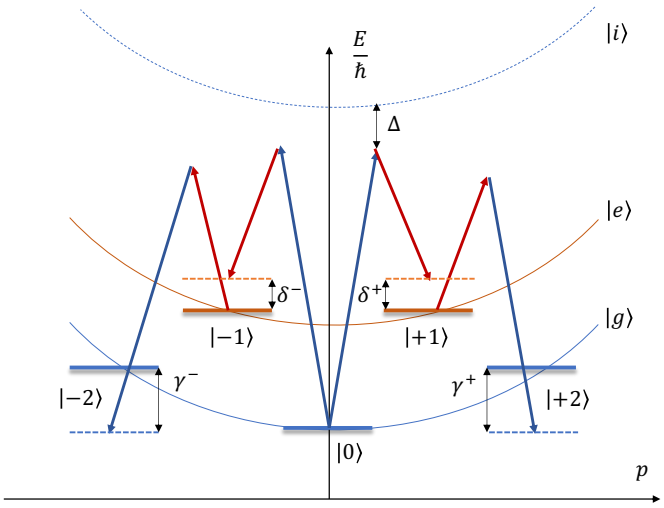

Figure 4.2: ***5-level system for a stimulated Raman transition in microgravity*** *- In this energy-momentum representation,* $\omega_D = 0$.

$$\begin{aligned}
\delta^+ &= (\omega_1 - \omega_2) - (\omega_{|+1\rangle} - \omega_{|0\rangle}) \\
\delta^- &= (\omega_1 - \omega_2) - (\omega_{|-1\rangle} - \omega_{|0\rangle}) \\
\gamma^+ &= (\omega_1 - \omega_2) - (\omega_{|+2\rangle} - \omega_{|+1\rangle}) \\
\gamma^- &= (\omega_1 - \omega_2) - (\omega_{|-2\rangle} - \omega_{|-1\rangle})
\end{aligned} \tag{4.3}$$

These states correspond to the orders of diffraction 0, ± 1 and ± 2, associated to 2 photons process and 4 photons process respectively. Thus, the conservation conditions of energy and total momentum during the interaction allow us to write :

$$\begin{aligned}
\hbar\omega_{|+2\rangle} &= \hbar\omega_g + \frac{\vec{p}^2}{2m} + 4\hbar\omega_R + 2\hbar\omega_D \\
\hbar\omega_{|+1\rangle} &= \hbar\omega_e + \frac{\vec{p}^2}{2m} + \hbar\omega_R + \hbar\omega_D \\
\hbar\omega_{|0\rangle} &= \hbar\omega_g + \frac{\vec{p}^2}{2m} \\
\hbar\omega_{|-1\rangle} &= \hbar\omega_e + \frac{\vec{p}^2}{2m} + \hbar\omega_R - \hbar\omega_D \\
\hbar\omega_{|-2\rangle} &= \hbar\omega_g + \frac{\vec{p}^2}{2m} + 4\hbar\omega_R - 2\hbar\omega_D
\end{aligned} \tag{4.4}$$

In the absence of Raman beams, the 5 considered states are eigenvectors of the Hamiltonian. Therefore, we decompose the atomic wave function in terms of these 5 states, writing:

$$|\psi(t)\rangle = \sum_{j=-2}^{2} c_{|j\rangle} e^{-i\omega_j t} |j\rangle \tag{4.5}$$

In the presence of lasers, the Hamiltonian is no longer diagonal and involves the dipole coupling term:

$$\hat{H} = \sum_{j=-2}^{2} \hbar\omega_j |j\rangle \langle j| - \vec{d} \cdot (\vec{E}_1 + \vec{E}_2) \tag{4.6}$$

The approach involves solving the Schrödinger equation by adiabatically eliminating the intermediate levels and then performing the following change of variables to bring it into a time-independent basis:

$$c_{|+2\rangle} = a_{|+2\rangle} e^{-i(\gamma_+ + \delta_+)t} \tag{4.7}$$
$$c_{|+1\rangle} = a_{|+1\rangle} e^{-i\delta_+ t} \tag{4.8}$$
$$c_{|0\rangle} = a_{|0\rangle} \tag{4.9}$$
$$c_{|-1\rangle} = a_{|-1\rangle} e^{-i\delta_- t} \tag{4.10}$$
$$c_{|-2\rangle} = a_{|-2\rangle} e^{-i(\gamma_- + \delta_-)t} \tag{4.11}$$

One can express the Hamiltonian of the system in the time independant frame :

$$\hat{H} = -\hbar \begin{pmatrix} \gamma^+ + \delta^+ & -\frac{\Omega_{eff}}{2} e^{i\phi} & 0 & 0 & 0 \\ -\frac{\Omega_{eff}}{2} e^{-i\phi} & \delta^+ & -\frac{\Omega_{eff}}{2} e^{-i\phi} & 0 & 0 \\ 0 & -\frac{\Omega_{eff}}{2} e^{i\phi} & 0 & -\frac{\Omega_{eff}}{2} e^{i\phi} & 0 \\ 0 & 0 & -\frac{\Omega_{eff}}{2} e^{-i\phi} & \delta^- & -\frac{\Omega_{eff}}{2} e^{-i\phi} \\ 0 & 0 & 0 & -\frac{\Omega_{eff}}{2} e^{i\phi} & \gamma^- + \delta^- \end{pmatrix} \tag{4.12}$$

Only one Rabi effective angular frequency Ω_{eff} is used because we consider that the effective coupling is the same among all the eigenstates. It is expressed as :

$$\Omega_{eff} = \frac{\Omega_{gi}^* \Omega_{ei}}{2\Delta} \tag{4.13}$$

with i the intermediate state involved in the two-photon process. The phase difference between the lasers is noted ϕ.

The detunings can be expressed as :

$$\begin{cases} \delta^+ = (\omega_1 - \omega_2) - (\omega_e - \omega_f) - (\omega_R + \omega_D) \\ \delta^- = (\omega_1 - \omega_2) - (\omega_e - \omega_f) - (\omega_R - \omega_D) \\ \delta^+ + \gamma^+ = 4\omega_R + 2\omega_D \\ \delta^- + \gamma^- = 4\omega_R + 2\omega_D \end{cases} \tag{4.14}$$

with

$$\begin{cases} \omega_D = \frac{\vec{p}.\vec{k}_{eff}}{M} \\ \omega_R = \frac{\hbar.|\vec{k}_{eff}|^2}{2M} \end{cases} \tag{4.15}$$

We can study the temporal evolution of the populations of the different states, solving the Schrödinger equation :

$$i\hbar \frac{d}{dt}[a(t)]_{|j\rangle} = H[a(t)]_{|j\rangle} \tag{4.16}$$

In the ideal case of a monochromatic wave packet, considering a velocity distribution infinitely narrow around zero velocity and an atomic cloud resonant with the laser beams, the duration τ_s of the beam splitter, for which all the atoms are transferred to the excited states $|+1\rangle$ and $|-1\rangle$, is related to the effective Rabi frequency Ω_{eff} is given by[[69]]:

$$\tau_s = \frac{\pi}{\sqrt{2}\Omega_{\text{eff}}} \tag{4.17}$$

Numerical simulations

Numerical simulations using Matlab software are carried out. The equation (4.16) is solved by computing the exponential of the Hamiltonian :

$$[a(t)]_{|j\rangle} = e^{-i\frac{Ht}{\hbar}}[a(0)]_{|j\rangle}, \tag{4.18}$$

where the exponential of a matrix is defined by :

$$e^A = \sum_{k\in\mathbb{N}} \frac{A^k}{k!} \tag{4.19}$$

To take into account the thermal dispersion of the gas, a Gaussian distribution of the velocities leading to a frequency width σ_{ω_D} is considered, similarly to the previous Chapter 3.

The method that has been implemented consists in computing the evolution of the populations $P_{|j\rangle}$ for a range of values of the detuning $\delta = (\omega_1 - \omega_2) - (\omega_e - \omega_g)$. Then for each value of δ, the evolutions are computed for a range of values of the Doppler detuning ω_D. We sum the equation (4.22) for every ω_D :

$$P_{|j\rangle}(\delta) = d\omega_D \times \sum_{\omega_D} G(\omega_D)^2 \times |[a(t,\omega_D,\delta)]_{|j\rangle}|^2 \tag{4.20}$$

with $G(\omega_D)$ given by equation 3.20. For both cold and ultra cold atoms, it is then possible to simulate Rabi oscillations and Raman spectra.

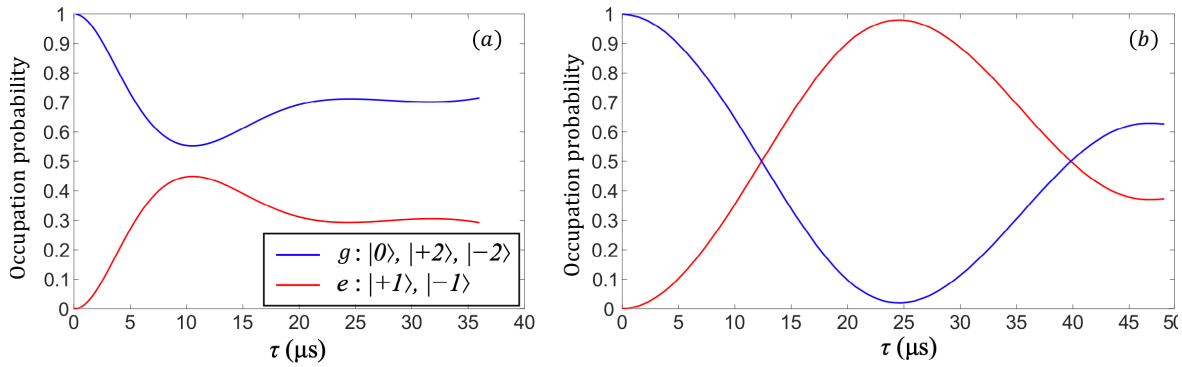

Figure 4.3: ***Numerical simulations of Rabi oscillations in the Double Diffraction regime*** *- The occupation probabilities of the different internal states ($|g\rangle$ and $|e\rangle$) are depicted in blue and red respectively, as a function of the Raman pulse duration τ. Situation (a) corresponds to that of a thermal cloud of rubidium ($T_{Rb} = 7\,\mu K$) with an effective Rabi oscillation $\Omega_{eff} = 30\,kHz$. Situation (b) corresponds to an ultracold sample ($T_{Rb} = 30\,nK$) with $\Omega_{eff} = 15\,kHz$. In both cases, the laser detuning is set to satisfy the condition for double-diffraction resonance ($\delta_{RF} = 0$).*

Figure 4.3 presents the simulated evolution of the populations of the internal ground state $|g\rangle$, which corresponds to the sum of the populations of the states $|-2\rangle$, $|0\rangle$, and $|+2\rangle$, as well as the population of the external excited state, corresponding to the states $|-1\rangle$ and $|+1\rangle$. The temporal evolution is plotted as a function of the pulse duration τ for thermal atoms at 7 μK and ultra-cold atoms at 30 nK. We observe damped Rabi oscillations for cold atoms with a maximum transfer to the excited states of less than 50 %, achieved for $\tau_s = 12\mu$s, approximately

corresponding to $\tau_s \simeq \frac{\pi}{\sqrt{2}\Omega_{\text{eff}}}$ with a value of Ω_{eff}= 30 kHz. For ultra-cold atoms at 30 nK and a Rabi frequency Ω_{eff}= 15 kHz, the damping of the oscillations is smaller, and we observe a maximum transfer of about 99% for a pulse duration of τ_s=25μs. In the case of double diffraction, the temperature of the atoms is thus a crucial parameter to enhance the efficiency of the Raman pulses.

By scanning the detuning δ_{RF} for this pulse duration τ_s, one can plot the population of the excited state, which corresponds to the Raman spectrum. Figure 4.4 (a) shows the spectra obtained for several values of the pulse duration τ_s for cold atoms, staying at the beamsplitter condition.

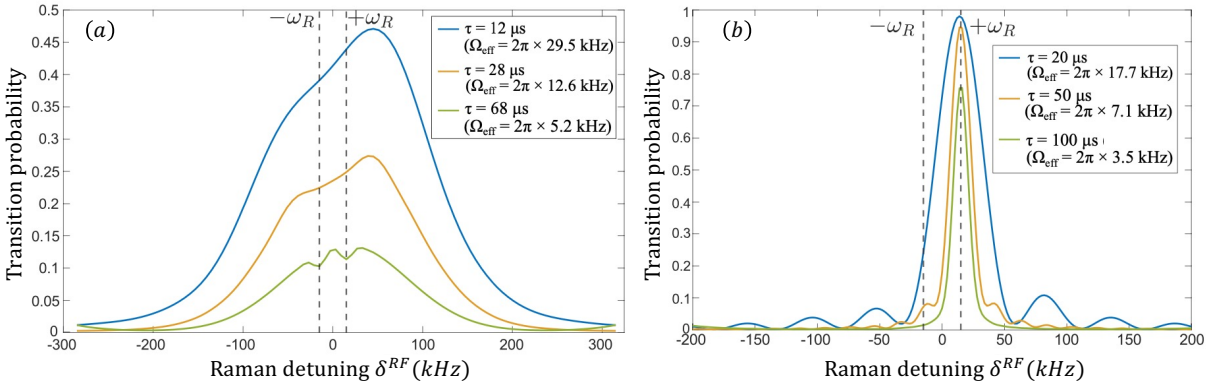

Figure 4.4: ***Simulations of Raman spectra in the regime of low velocity and low acceleration*** *- These numerical simulations were conducted using the 5-level coupled model for (a) a thermal sample of rubidium at 7 µK and (b) an ultracold sample at 30 nK. The pulse durations considered consistently match those of a beam splitter pulse.*

We obtain spectra that are characteristic of double diffraction, their interpretation can be found in [[67, 53]]. Figure 4.4 (a) shows simulations for cold atoms ($\mathcal{T} = 7$ μK) and 4.4 (b) for ultracold atoms ($\mathcal{T} = 30$ nK). For cold atoms, the gaussian envelope of the spectrum is due to the temperature of the atomic cloud. When increasing the pulse duration, the velocity selection leads to a decrease of the amplitude of the ratio because of velocity selection. Less atoms are transfered to the excited state for a fixed δ. For long pulses, two gaps appear at $+\omega_R$ and $-\omega_R$:

- In the presence of $\pm\vec{k_{eff}}$, the transition probability across the entire envelope is twice as high as in the presence of a single $\vec{k_{eff}}$. This is because atoms in the states $|g, \vec{p}\rangle$ and $|g, -\vec{p}\rangle$ satisfy the same resonance condition simultaneously to transition to $|e, \vec{p} + \vec{k_{eff}}\rangle$ and $|e, \vec{p} - \vec{k_{eff}}\rangle$. When $\delta_{RF} = \omega_R$, only the zero-velocity class ($\vec{p} = \vec{0}$) contributes to the transition probability, resulting in the dip in the Doppler envelope. This dip represents the process of double diffraction of a zero-velocity atom into the states $|e, \vec{0} \pm \vec{k_{eff}}\rangle$.
- The second dip at $\delta_{RF} = -\omega_R$ represents the existence of a process during which an atom initially in the state $|g, \pm\vec{k_{eff}}\rangle$ can transition to $|e, \vec{0}\rangle$ and be diffracted again to $|g, \mp\vec{k_{eff}}\rangle$. For an atom initially in the state $|g, -\vec{k_{eff}}\rangle$, when $\delta_{RF} = -\omega_R$, the resonance condition for the transition $|g, -\vec{k_{eff}}\rangle \rightarrow |e, 0\rangle$ through the absorption of an effective photon with momentum $+\vec{k_{eff}}$ is satisfied. Once in this state, the atom can be diffracted to $|g, +\vec{k_{eff}}\rangle$ because the resonance condition for this transition is once again $\delta_{RF} = -\omega_R$. A similar reasoning can be applied to an atom initially in $|g, +\vec{k_{eff}}\rangle$ and diffracted to$|g, -\vec{k_{eff}}\rangle$

through the successive absorption of two photons with momentum $-\vec{k_{eff}}$. We can refer to this process as a '4-photon' process.

For ultra-cold atoms, the shape of the spectrum is not influenced by the velocity distribution of the atoms but rather by the duration of the pulse: it exhibits a sinc shape, which is the Fourier transform of a square pulse with duration τ_s. The atoms are transferred predominantly around the resonance frequency at $+\omega_R$ due to the narrow initial velocity distribution. With this setup, the only feasible configuration for the Raman pulse is double diffraction. We achieve very high transfer rates at resonance, which advocates for the utilization of ultra-cold atoms in microgravity interferometry.

Taking into account the co-propagating transitions

In our experiment, the two incident beams $(\omega_1, \vec{k_1})$ and $(\omega_2, \vec{k_2})$ of respective optical frequency ω_1 and ω_2, have the same linear polarization state. In our retro-reflected configuration, after illuminating the atoms on a first pass, the beams go through a quarter wave-plate, are then reflected back by a mirror and pass again through the same wave-plate at which point the polarization of the beams is linear and perpendicular to their original polarization (lin-perp-lin configuration). Because the polarization is generally not perfectly linear, co-propagating transitions may still occur. We can extend the previous model to a 10-level system, depicted in Figure 4.5 using the energy-momentum representation.

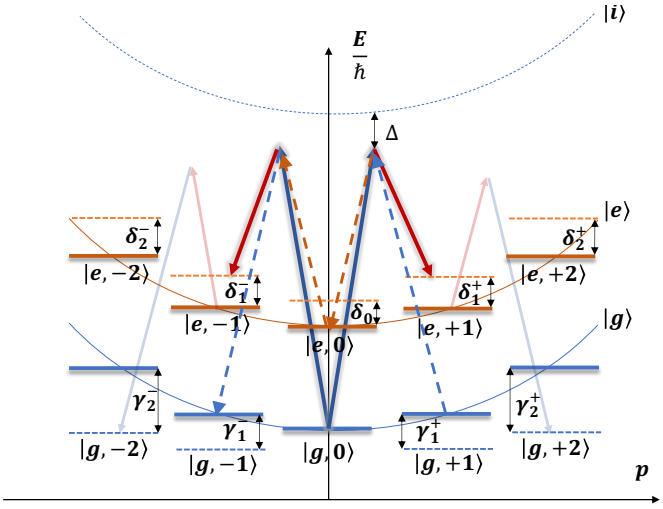

Figure 4.5: ***10-level system for a stimulated Raman transition in microgravity*** *- In this context, we consider the copropagating transitions. The double diffraction process corresponds to the solid arrow lines, the dashed lines correspond to the previously mentioned '4-photon process'. Other possible transitions are presented in transparent arrows. In this energy-momentum representation,* $\omega_D = 0$.

In this scheme, we define the detunings between the laser frequencies and the atomic levels as follows:

$$\begin{cases} \delta_0 = (\omega_1 - \omega_2) - (\omega_{|e,0\rangle} - \omega_{|g,0\rangle}) \\ \delta_1^+ = (\omega_1 - \omega_2) - (\omega_{|e,+1\rangle} - \omega_{|g,0\rangle}) \\ \delta_1^- = (\omega_1 - \omega_2) - (\omega_{|e,-1\rangle} - \omega_{|g,0\rangle}) \\ \delta_2^+ = (\omega_1 - \omega_2) - (\omega_{|e,+2\rangle} - \omega_{|g,+1\rangle}) \\ \delta_2^- = (\omega_1 - \omega_2) - (\omega_{|e,-2\rangle} - \omega_{|g,-1\rangle}) \\ \gamma_1^+ = (\omega_2 - \omega_1) - (\omega_{|g,+1\rangle} - \omega_{|e,0\rangle}) \\ \gamma_1^- = (\omega_2 - \omega_1) - (\omega_{|g,-1\rangle} - \omega_{|e,0\rangle}) \\ \gamma_2^+ = (\omega_1 - \omega_2) - (\omega_{|g,+2\rangle} - \omega_{|e,+1\rangle}) \\ \gamma_2^- = (\omega_1 - \omega_2) - (\omega_{|g,-2\rangle} - \omega_{|e,-1\rangle}). \end{cases} \tag{4.21}$$

The coupling strength $\Omega_{eff,co}$ corresponding to the co-propagating transitions is a fraction ϵ of Ω_{eff} that depends on the polarization extinction ratio (PER) : $\Omega_{eff,co} = \epsilon\Omega_{eff}$. The Hamiltonian H of the system can be derived, and the time evolution of the amplitude of probability $[a(t)]_{|j\rangle}$, with $|j\rangle \in \{|e,-2\rangle, |g,-2\rangle, |e,-1\rangle, |g,-1\rangle, |g,0\rangle, |e,0\rangle, |g,+1\rangle, |e,+1\rangle, |g,+2\rangle, |e,+2\rangle\}$ can then be computed by solving the Schrödinger equation :

$$i\hbar\frac{d}{dt}[a(t)]_{|j\rangle} = H[a(t)]_{|j\rangle}, \tag{4.22}$$

The Hamiltonian H can be expressed as the sum of a co-propagating Hamiltonian and a counter-propagating Hamiltonian : $H = H_{co} + H_{counter}$.
The detunings can then be expressed as a function of ω_D and ω_R.

$$\begin{cases} \delta_0 = (\omega_1 - \omega_2) - (\omega_e - \omega_g) \\ \delta_1^+ = (\omega_1 - \omega_2) - (\omega_e - \omega_g) - (\omega_R + \omega_D) \\ \delta_1^- = (\omega_1 - \omega_2) - (\omega_e - \omega_g) - (\omega_R - \omega_D) \\ \delta_2^+ = (\omega_1 - \omega_2) - (\omega_e - \omega_g) - (3\omega_R + \omega_D) \\ \delta_2^- = (\omega_1 - \omega_2) - (\omega_e - \omega_g) - (3\omega_R - \omega_D) \\ (\delta_2^+ + \gamma_1^+) = 4\omega_R + 2\omega_D \\ (\delta_2^- + \gamma_1^-) = 4\omega_R - 2\omega_D \\ (\delta_1^+ + \gamma_2^+) = 4\omega_R + 2\omega_D \\ (\delta_2^- + \gamma_1^-) = 4\omega_R - 2\omega_D \end{cases} \tag{4.23}$$

The total Hamiltonian can be expressed in the matrix form presented in equation 4.24:

$$
H = -\hbar \begin{pmatrix}
4\omega_R - 2\omega_D & \frac{\Omega_{eff,co}}{2} e^{i2\delta_0 t} & 0 & \frac{\Omega_{eff}}{2} & 0 & 0 & 0 & 0 & 0 & 0 \\
\frac{\Omega^*_{eff,co}}{2} e^{-i2\delta_0 t} & 4\omega_R - 2\omega_D & \frac{\Omega_{eff}}{2} & 0 & 0 & 0 & 0 & 0 & 0 & 0 \\
0 & \frac{\Omega^*_{eff}}{2} & -\delta_1^- & \frac{\Omega_{eff,co}}{2} e^{i\delta_0 t} & \frac{\Omega_{eff}}{2} & 0 & 0 & 0 & 0 & 0 \\
\frac{\Omega^*_{eff}}{2} & 0 & \frac{\Omega^*_{eff,co}}{2} e^{-i\delta_0 t} & \omega_R - \omega_D & 0 & \frac{\Omega_{eff,co}}{2} & 0 & 0 & 0 & 0 \\
0 & 0 & \frac{\Omega^*_{eff}}{2} & 0 & \frac{\Omega^*_{eff,co}}{2} & -\delta_0 & \frac{\Omega^*_{eff}}{2} & 0 & 0 & 0 \\
0 & 0 & 0 & 0 & \frac{\Omega^*_{eff}}{2} & \frac{\Omega_{eff}}{2} & \omega_R + \omega_D & \frac{\Omega^*_{eff,co}}{2} & 0 & \frac{\Omega^*_{eff}}{2} \\
0 & 0 & 0 & 0 & \frac{\Omega_{eff}}{2} & 0 & \frac{\Omega_{eff,co}}{2} e^{i\delta_0 t} & -\delta_1^+ & \frac{\Omega_{eff}}{2} & 0 \\
0 & 0 & 0 & 0 & 0 & 0 & 0 & \frac{\Omega_{eff}}{2} & 4\omega_R + 2\omega_D & \frac{\Omega^*_{eff,co}}{2} e^{-i\delta_0 t} \\
0 & 0 & 0 & 0 & 0 & 0 & \frac{\Omega_{eff}}{2} & 0 & \frac{\Omega_{eff,co}}{2} e^{i\delta_0 t} & 4\omega_R + 2\omega_D
\end{pmatrix} \tag{4.24}
$$

The simulations can be run with this new Hamiltonian by taking into account the polarization parameter ϵ. Simulation results for cold atoms are presented in Figure 4.6.

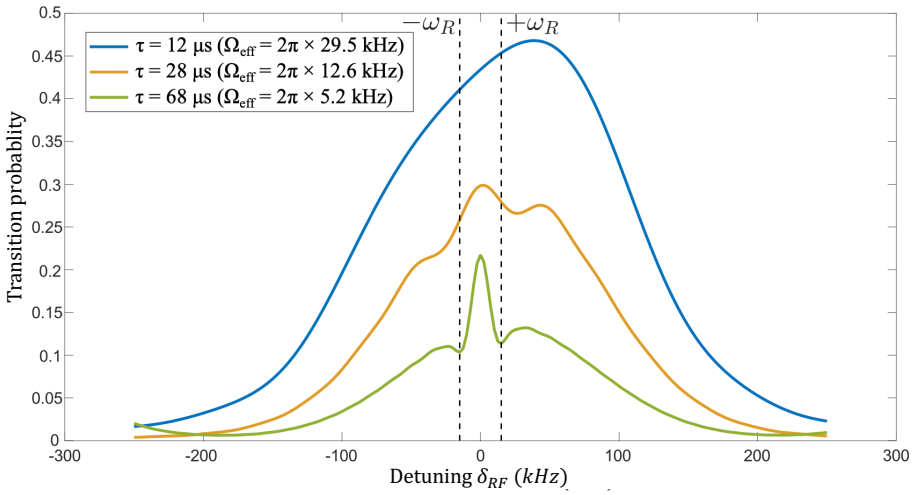

Figure 4.6: ***Simulations of Raman spectra in the regime of low velocity and low acceleration with co-propagating transitions*** *- These spectra were obtained using the 10-level model. The simulation parameters are:* $T_{Rb} = 7\mu K$ *and* $\epsilon = 10\%$.

The spectra are similar to those shown in Figure 4.4, with an additional peak emerging around $\delta_{\mathrm{RF}} = 0$. Its relative amplitude compared to the counter-propagating spectrum becomes more significant as the duration of the Raman pulse increases, as the co-propagating transition remains unaffected by the velocity selection effect.

4.1.2 Interferometry in the Double-single diffraction regime

The regime of double single diffraction exists with cold atoms when the velocity distribution of the cloud is $\sigma_v >> v_r$. By choosing a detuning δ_{RF} greater than the recoil frequency, we break the degeneracy between the two pairs of counter-propagating Raman transitions. We thus address two classes of non-zero and symmetric velocities with respect to each other. The first velocity class, associated with a momentum state $|+\vec{p}\rangle$, satisfies the Raman resonance condition with only one of the two pairs of beams. The Raman transition then allows it to be diffracted to a state like $|+\vec{p} + \hbar\vec{k}_{\mathrm{eff}}\rangle$, for example. The symmetric velocity class $|-\vec{p}\rangle$, on the other hand, resonates with the other pair of beams and can be diffracted to the state $|-\vec{p} - \hbar\vec{k}_{\mathrm{eff}}\rangle$. This regime allows simultaneously two symmetric "single-diffraction" interferometers, each addressing different atoms in the velocity distribution of the cloud (see Figure 4.7).

As presented in Chapter 3, it can be shown that the accumulated phase shifts Φ^{+}_{tot} and Φ^{-}_{tot} in each of the two interferometers can be written as[[13]]:

$$\Phi^{\pm}_{\mathrm{tot}} = \pm\Phi_a + \varphi_{\mathrm{laser}} \tag{4.25}$$

The transition probability $P_{|e\rangle}$ to the internal state $|e\rangle$ is the sum of the output probabilities from each of the two interferometers ($P_{\pm}$). Thus, we have:

$$P = \frac{P_+ + P_-}{2} = P_0 + A\cos(\Phi_a)\cos(\varphi_{\mathrm{las}}) \tag{4.26}$$

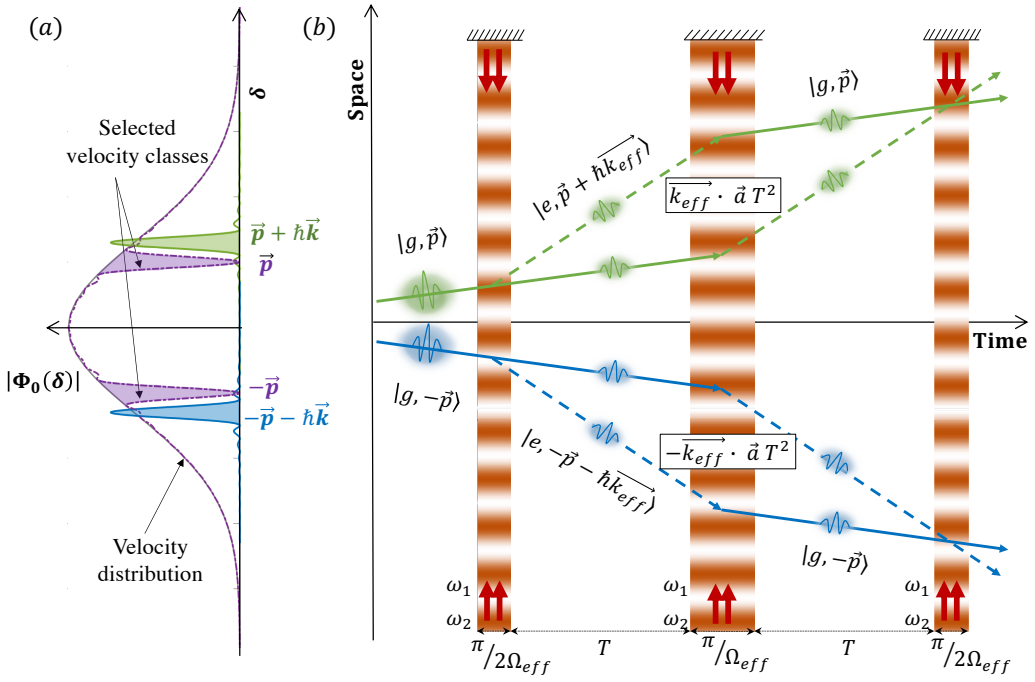

Figure 4.7: ***Space-time diagram of an interferometer in the Double Single Diffraction regime*** *- (a) Velocity distribution and selected velocity classes (b) Space-time diagram of the double single diffraction interferometer : in the absence of the Doppler effect, when choosing atoms from the non-zero velocity class ($\vec{p}$ and $-\vec{p}$), two single diffraction interferometers coexist.*

4.1.3 Interferometry in the Double Diffraction regime

The Double Diffraction regime becomes predominant when the detuning is adjusted to target atoms in the zero-velocity class. Figure 4.8 illustrates the comprehensive structure of an interferometer operated in this regime.
It includes two 'beam-splitter' pulses with a duration of τ_s and a 'mirror' pulse with a duration of τ_m, all separated by an interrogation time T. The first beam splitter pulse transfers the atom from an initial state $|g,\vec{p}\rangle$ to a coherent equiprobable superposition of states $|e,\vec{p}+\hbar\vec{k}_{\text{eff}}\rangle$ and $|e,\vec{p}-\hbar\vec{k}_{\text{eff}}\rangle$. Thus, it is not a $\pi/2$-type pulse strictly speaking, as the initial state is no longer present in the output superposition. It can be shown that the pulse duration required for this transfer is: $\tau_s = \frac{\pi}{\sqrt{2}\Omega_{\text{eff}}}$. For the same effective Rabi frequency, this duration is $\sqrt{2}$ times longer than the one typically used to split the wave packet in single-diffraction regimes.

The 'mirror' pulse consists in transferring the atoms initially in $|e,\vec{p}\pm\hbar\vec{k}_{\text{eff}}\rangle$ to $|e,\vec{p}\mp\hbar\vec{k}_{\text{eff}}\rangle$. This pulse is imperfect because atoms can transfer from $|e,\vec{p}\pm\hbar\vec{k}_{\text{eff}}\rangle$ to $|g,\vec{p}\rangle$. Figure 4.9 shows simulation results for the evolution of the populations of sublevels $|e,\vec{p}\rangle$, denoted as $|0\rangle$, and $|e,\vec{p}\pm\hbar\vec{k}_{\text{eff}}\rangle$, denoted as $|\pm1\rangle$. To simulate a mirror pulse, the atoms are initially in the $|e,\vec{p}+\hbar\vec{k}_{\text{eff}}\rangle$. In this simulation, we consider an effective Ω_{eff} so that the beam splitter condition is $\tau_s = 100$ μs and a near zero temperature distribution (300 pK, to account for an 'ideal' case).
The efficiency of theses pulses can be simulated in the presence of a residual co-propagating transition. Simulation results for a beam-splitter and a mirror pulse with a polarization parameter $\epsilon = 0.2$ are shown in Figure 4.10. The "mirror" pulse in the double diffraction regime presents its challenges. Figure 4.10 indicates that for a temperature of 30 nK, the maximal efficiency achievable is around 80 % in the ideal simulated scenario. Its efficiency decreases significantly

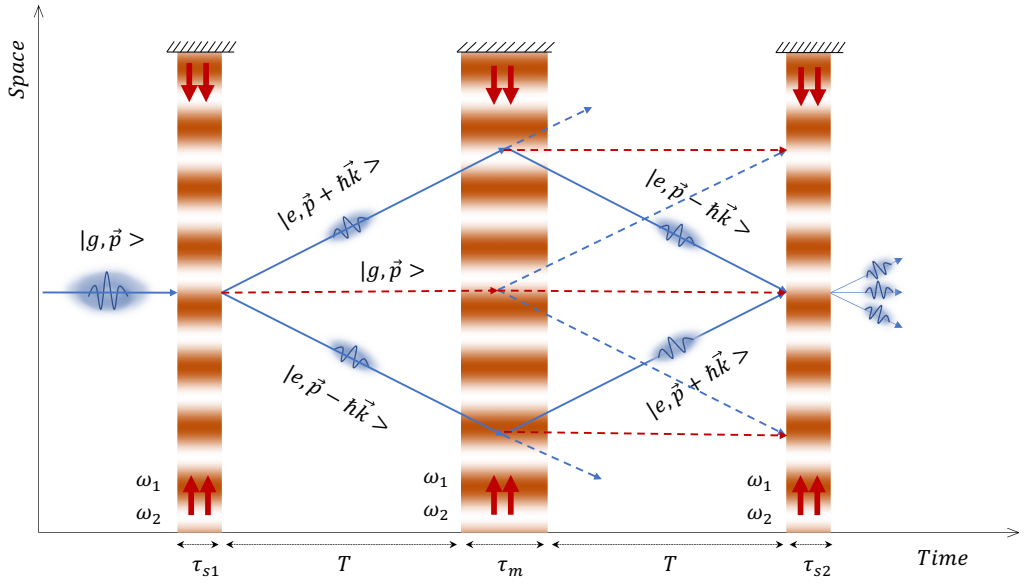

Figure 4.8: ***Space-time diagram of an interferometer in the Double Diffraction regime*** *- The wavepacket is in the initial state $|g,\vec{p}\rangle$. A sequence of $\tau_{s1}-\tau_m-\tau_{s2}$ is executed, splitting the wavepacket and then recombining it symmetrically. The imperfections of each pulse result in residual wavepackets, depicted by dashed lines.*

with an increase in temperature.
Following a second free evolution time T, the interferometer is finally closed with the last pulse. At the output, the atoms are in a superposition of the three states $|e,\vec{p}-\hbar\vec{k}_{\text{eff}}\rangle$, $|g,\vec{p}\rangle$ and $|e,\vec{p}+\hbar\vec{k}_{\text{eff}}\rangle$.

The total interferometric phase shift can be expressed[[53]]:

$$\Phi_{\text{tot}} = 2\Phi_a \tag{4.27}$$

The total phase accumulated by the interferometer is twice the phase shift of single diffraction. This is explained by the larger spatial separation between the two arms of the interferometer, differing here by a momentum amount of $2\hbar\vec{k}_{\text{eff}}$. As a result, the sensitivity to inertial effects is doubled in this regime, representing a significant advantage for our application. We also note that it is no longer possible to sweep interference fringes by varying the relative laser phase between the three Raman pulses. Indeed, the total phase shift no longer depends on the term φ_{laser}, given that the atoms evolve in the same internal state throughout the interferometer. To scan the fringes, one can move the reference mirror in a controlled manner or use the acceleration fluctuations from one measurement to another.

4.2 Experimental realization of atom interferometry in microgravity

In this section, we present the highly sensitive interferometric measurements recently conducted with thermal samples of ^{87}Rb on the microgravity simulator in the laboratory. These measurements took place in two stages: one in January 2021 before a major malfunction of our simulator, and another in December 2022 after the simulator was repaired and its structure modified. Before focusing on AI in microgravity, we first investigate the coherent manipulation of both internal and external states of the atom with 2-photon Raman and Ramsey spectroscopy

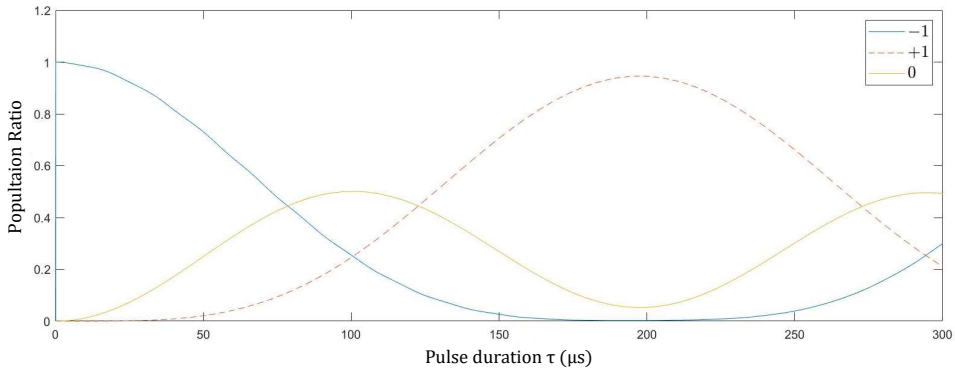

Figure 4.9: ***Simulated Rabi oscillation for a mirror pulse in double diffraction*** *- In order to simulate a mirror pulse, we initialize the atoms in the state $|e, \vec{p} + \hbar\vec{k}eff\rangle$ (blue line). The evolution of the population of $|e, \vec{p} - \hbar\vec{k}eff\rangle$ is in red dashed line, and the atoms that are transferred to the $|g, \vec{p}\rangle$ state follow the evolution of the yellow line. This simulation assumes an effective Ωeff such that the beam splitter condition is met at $\tau_s = 100\mu s$. We consider a nearly zero-temperature distribution (300 pK) to approximate an 'ideal' scenario.*

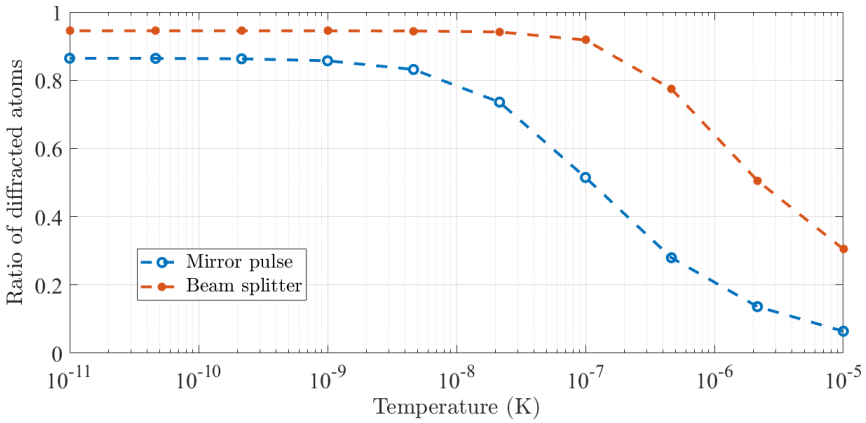

Figure 4.10: ***Simulated efficiency of atomic mirror and beam-splitter as a function of the temperature of the atoms*** *- For each temperature, we simulate a double diffraction Raman pulse and compute its maximum efficiency, taking into account a co-propagating residual of $\epsilon = 0.2$ and a 20 μs τ_s pulse.*

in microgravity. The high repeatability of our experiment allows us to produce a complete scan of the experimental parameters, thus enabling a full spectroscopy study to be performed directly in microgravity. Then, we then investigate atom interferometry on our simulator.

When operating on the microgravity simulator, a single experimental sequence is performed during each parabola. The various steps of the sequence are synchronized with the platform's movements through digital signals. It is important to note that two successive trajectories must be separated by a latency time of 13 s to ensure satisfactory cooling of the motors. Thus, the simulator fundamentally limits the repetition rate of our experiment by adding this dead time between two trajectories. Each new trajectory of the simulator is initiated by a signal from the experiment's sequencer. Loading of the Magneto-Optical Trap (MOT) and the input state preparation are executed simultaneously. After receiving the signal from the simulator indicating the start of the microgravity phase, the control system triggers the rest of the experimental sequence, including the molasses phase, state preparation, Raman pulse sequences, and the

detection or imaging step.

4.2.1 Raman spectroscopy in microgravity

Figure 4.11 presents two Raman spectra obtained in the microgravity regime with a thermal sample of ^{87}Rb initially prepared in the state $|F = 1, m_F = 0\rangle$. These are counter-propagating spectra obtained at two distinct laser intensities after the same 7 ms time of flight. The duration of the Raman pulse corresponds to that of a $\pi/2$-pulse in each case, namely 65 μs and 20 μs, respectively.

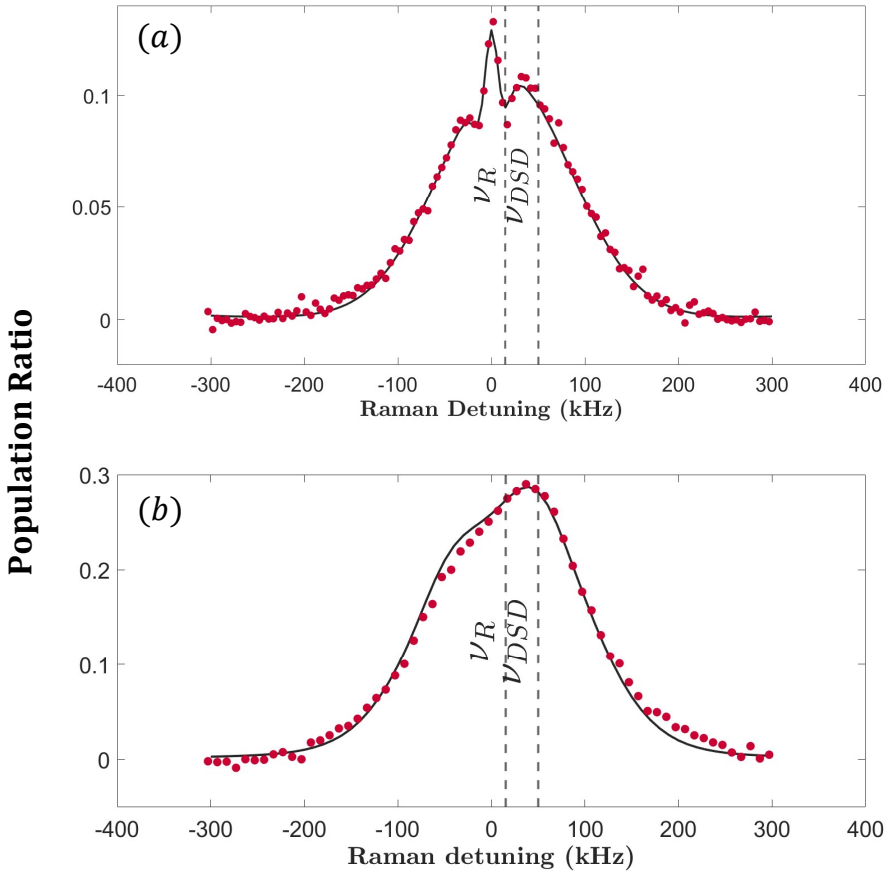

Figure 4.11: ***Raman spectra obtained in microgravity with cold ^{87}Rb and simulated spectra*** *- These counter-propagating Raman spectra correspond to pulse durations of (a) 65 μs and (b) 20 μs. The continuous lines represent the results of adjustments performed using the 10-level theoretical model, accounting for residual circular polarization effects. The sets of parameters extracted from the adjustments are: $\{\Omega_{eff} = 2\pi \times 4.5\ kHz,\ T = 7.5\ \mu K,\ \epsilon = 0.2\}$ for situation (a) and $\{\Omega_{eff} = 2\pi \times 15\ kHz,\ T = 7.5\ \mu K,\ \epsilon = 0.07\}$ for situation (b). The vertical lines indicate the two-photon recoil frequency $\nu_R \approx 15\ kHz$ and the chosen detuning value $\nu_{DSD} = 50\ kHz$ for the implementation of the interferometer in the double-simple diffraction regime.*

The experimental data points are fitted by a theoretical curve obtained from the 10-level model that accounts for residual circular polarization effects. The free parameters of the fitting include the effective Rabi frequency Ω_{eff}, the temperature T, and the parameter ϵ related to the polarization extinction ratio. The parameter combinations yielding the best fits are :
$\Omega_{\text{eff}} = 2\pi \times 4.5$ kHz, $T = 7.5\mu$K, $\epsilon = 0.2$ for $\tau_\pi = 65\mu$s, and

$\Omega_{\text{eff}} = 2\pi \times 15$ kHz, $T = 7.5\mu$K, $\epsilon = 0.07$ for $\tau_\pi = 20\mu$s.

We note that the polarization parameter ϵ found is not the same in both cases. For the larger pulse durations, the spectral resolution of the method is higher: the co-propagating peak is fitted more easily than for shorter pulses. The value we trust the most here is $\epsilon = 0.2$

The high quality of the fits validates the model and allows us to estimate the sample temperature to be around 7.5μK. The retrieved asymmetry in the spectrum is due to the 4-photon process. As expected for a short pulse, which is less velocity selective, higher transition rates and a broader resonance are observed due to a larger number of atoms being simultaneously addressed by the Raman beam.

4.2.2 Ramsey fringes in microgravity

We conduct high-resolution spectroscopy in microgravity using an interferometer in the Ramsey configuration with long interrogation times [[84]]. This involves applying a series of two Raman pulses with a duration of $\tau_{\pi/2}$ separated by the interrogation time T.

The principle of the method is presented in Figure 4.12.

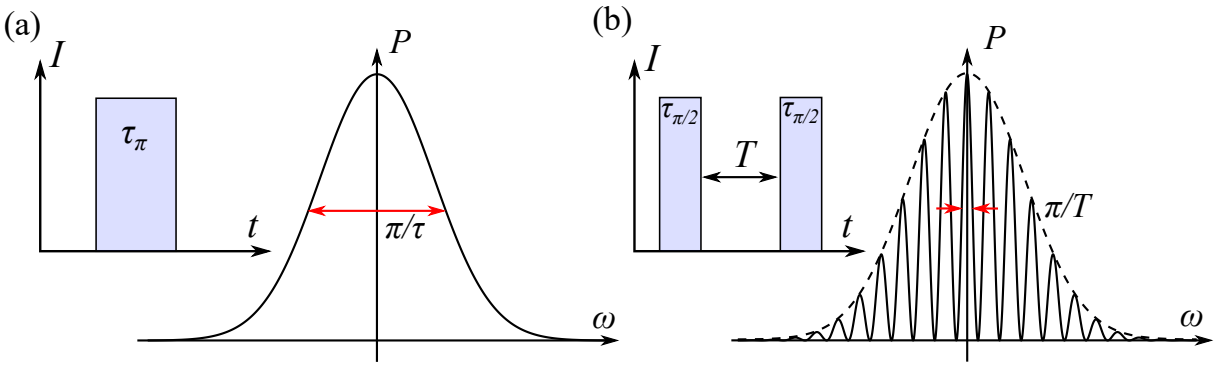

Figure 4.12: ***Principle of Ramsey fringes*** *- Transition probability plotted as a function of detuning from resonance for two types of excitations: (a) a single π-pulse and (b) two $\pi/2$ pulses spaced by a duration T [[7]].*

When the detuning δ is smaller than the effective Rabi frequency Ω_{eff}, the transition probability at the output of the interferometer is given by[[82]]:

$$P(\delta, T) = \frac{1}{2}\sin^2(\Omega_r \tau)[1 + \cos(\delta T + \phi)] \tag{4.28}$$

where $\Omega_r = \sqrt{\Omega_{eff}^2 + \delta^2}$ and ϕ represents a phase linked to the laser. In our setup, this method is applied to two-photon Raman transitions. We obtain so-called Raman-Ramsey interferometers. Such interferometers have been implemented for example in cesium jets[[23]], yielding a line width of 50Hz. Analyzing the fringes obtained through this method allows us to characterize the stability of our laser system and study systematics, such as light shifts.

In microgravity, we present the results obtained with our thermal samples of ^{87}Rb at $\mathcal{T} = 7\,\mu$K, using a pulse duration of 25 µs. The observed Ramsey fringes in microgravity for various interrogation times T are illustrated in Figure 4.13 (a) and (b).
We demonstrate state-of-the-art measurements for light-pulse Ramsey spectroscopy achieved in microgravity [[64, 70]]. We perform a sinusoidal fit on the data to estimate the contrast. The SNR of these fringes can be deduced by comparing the contrast of the fitted fringes and the

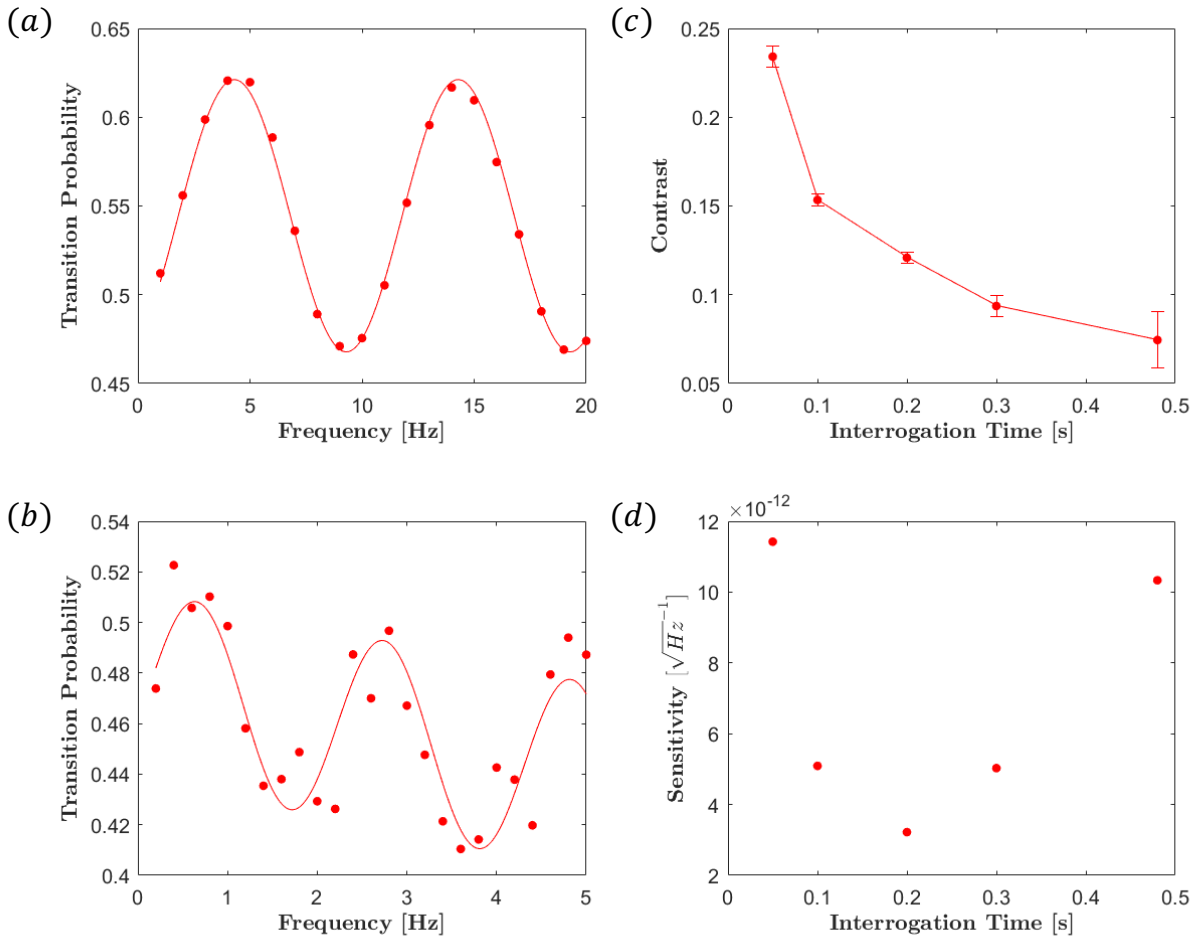

Figure 4.13: ***Ramsey fringes obtained in microgravity*** *- Examples of fringes obtained for interrogation times of (a) 100 ms and (b) 480 ms. Evolution of fringe contrast (c) and measurement sensitivity (d) as a function of interrogation time T. The sensitivity optimum ($\sigma = 3 \times 10^{-12}\sqrt{Hz}^{-1}$) is achieved for $T = 200$ ms.*

standard deviation of the residuals of the fit.

For $T = 100$ ms, light pulse Ramsey spectroscopy leads to a half-width at half-maximum (HWHM) frequency signal $\Delta\nu = 1/2T$ as low as 1 Hz. The short term sensitivity σ on the frequency measurement is given by the following expression :

$$\sigma = \frac{1}{\pi}\frac{\Delta\nu}{\nu_c}\frac{1}{\mathrm{SNR}} \tag{4.29}$$

Where ν_c is the clock frequency for ^{87}Rb. Figure 4.13 (c) shows the contrast as a function of the interrogation time T : we observe the contrast drops as T increases. The decrease in contrast can be attributed to the expansion of the thermal cloud, as presented in section 1.2.5.Moreover, with the cloud expanding, the effective Rabi frequency seen by the atoms is inhomogeneous, leading to contrast loss. The sensitivity can be plotted as a function of T using equation 4.29 as shown is figure 4.13 (d). The short term sensitivity of the measurement is limited to $\sigma = 1 \times 10^{-11}$ for $T = 480$ ms. The best sensitivity $\sigma = 3 \times 10^{-12}$ is reached for $T = 200$ ms, corresponding to the best trade-off between the SNR of the atomic fringes and the interrogation time.

4.2.3 Atom interferometry in Double Single Diffraction regime in the Einstein elevator

A sequence of $\tau_{\pi/2} - \tau_{\pi-} - \tau_{\pi/2}$ is performed in the double single diffraction (DSD) giving rise to an atom accelerometer that is a double Mach-Zehnder interferometer as presented in Figure 4.7.

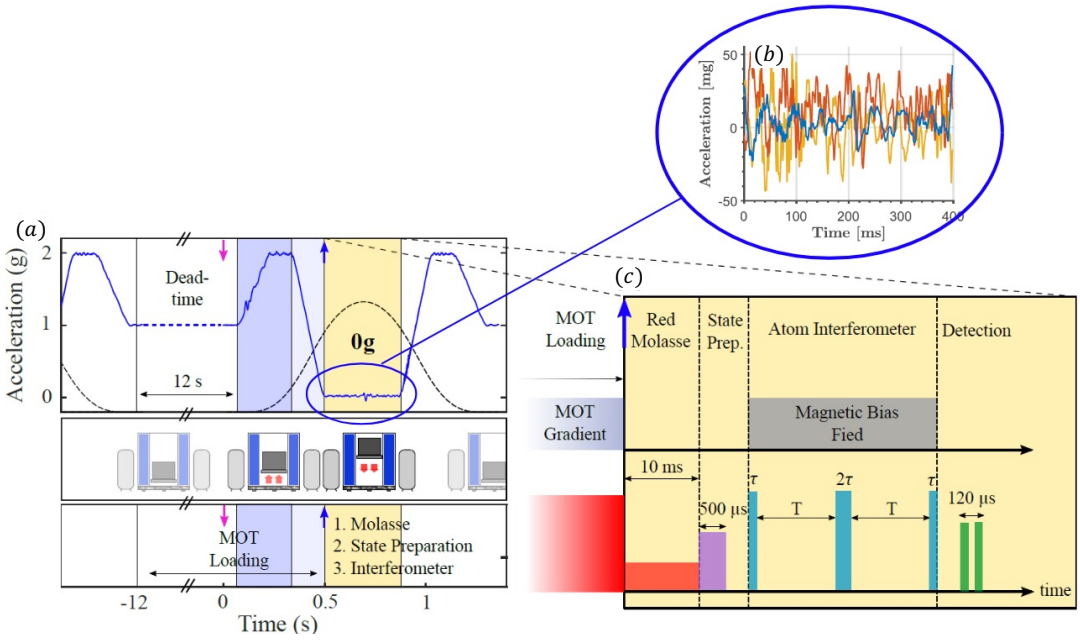

Figure 4.14: ***Experimental sequence in the Double Single Diffraction regime on the Einstein Elevator*** *- (a) Acceleration (blue) and position profiles (dashed) of a trajectory for a microgravity duration of $t = 400$ ms. (b) Residual acceleration during the microgravity phase. (c) Cold atom experimental sequence. The MOT loading starts a few seconds before the start of the movement. The molasses, the state preparation and the interferometer are performed during the microgravity phase, after receiving the trigger from the simulator controller.*

The experimental sequence is illustrated in Figure 4.14 (c). A velocity selection at a non zero velocity class is achieved by choosing $\delta_{RF} = 50$ kHz for the Raman pulses, and only a fraction

of the thermal atomic cloud participates to the upper ($+\hbar\vec{k}_{eff}$) or the lower ($-\hbar\vec{k}_{eff}$) interferometer. Each pair of wavepackets interferes after propagating over a distance of 20 cm. The parabola described by the center of mass of the double atom interferometer has an amplitude of 10 cm. After a time of flight, the position/velocity correlation leads to two spatially separated atom interferometers. For an interrogation time $T = 100$ ms, the two interferometers outputs are separated by 8 mm while measuring conjointly the acceleration Φ_a, using a single photodiode to detect both interferometers simultaneously.

Experimental results

Interference fringes for an interrogation time $T = 10$ ms and $T = 15$ ms on the Einstein elevator are presented in Figure 4.15. As only one measurement can be carried out during a EE platform's parabola, 300 cycles were performed to complete the whole interference pattern. Here, the laser phase is fixed ($\varphi_{\text{las}} = 0$) and the atomic phase shift is scanned by the vibrations of the moving platform. Fringes are reconstructed by a method consisting in correlating the output of the atom interferometer with a classical accelerometer described in section 3.2.4.

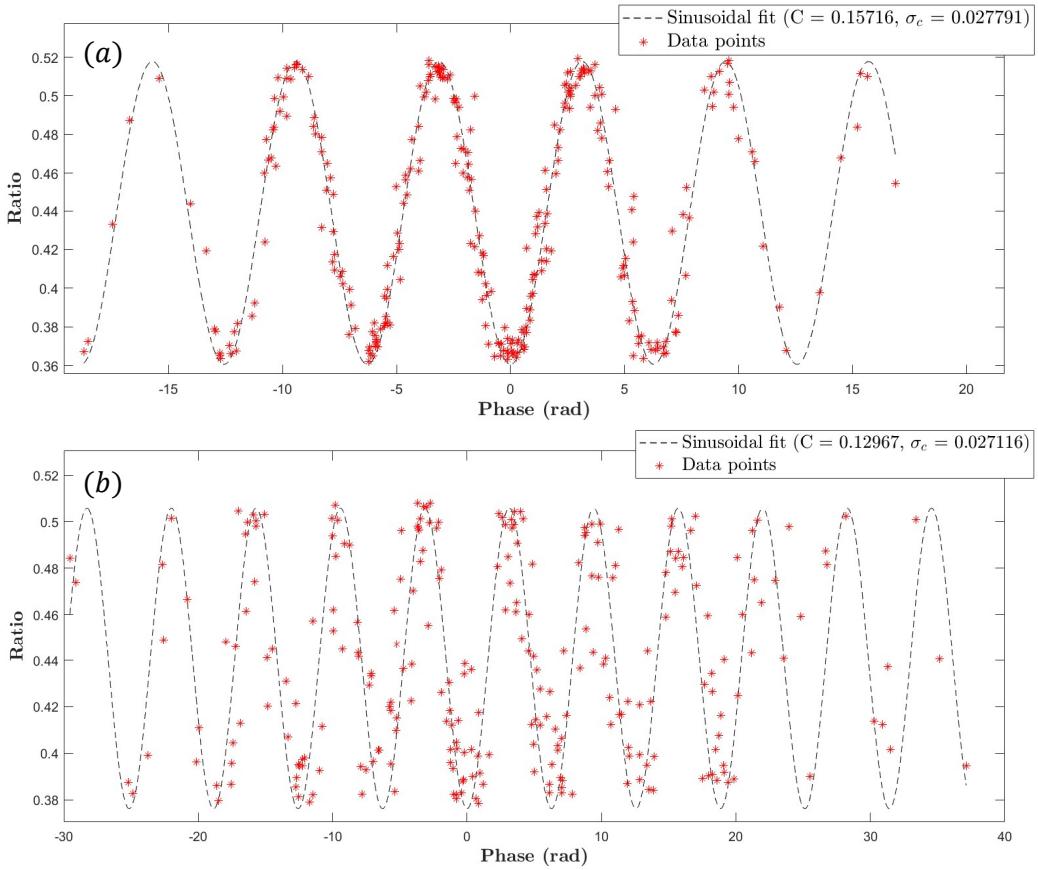

Figure 4.15: ***Results of interferometry obtained in the regime of double-single diffraction in microgravity*** *- Interference fringes reconstructed using the FRAC method for an interrogation time of (a) $T = 10$ ms and (b) $T = 15$ ms. These results were obtained with a thermal sample of rubidium while operating in the regime of double-single diffraction on the microgravity simulator. The sinusoidal fitting allows estimating the contrast at 15.7% and 13 %*

On our microgravity simulator, we take advantage of the highly repeatable nature of the vibrations for the implementation of the FRAC method. The variations in the acceleration profile

from one parabola scan the interference fringes, not the shape of the "average" vibration profile. By measuring the residual acceleration with classical accelerometers for a large number of parabola, we estimate a "shot-to-shot" variation of the phase term due to vibrations. For an interrogation time $T = 100$ ms, we estimate a scan of 100 rad.
The quality of correlations deteriorates rapidly when attempting to increase the interrogation time: beyond $T = 20$ ms, the fringes are no longer distinguishable. This interference is not linked to the atomic interferometer itself but mainly originates from the inherent noise of the classical accelerometer. On the simulator, the analog signal of the Colibrys accelerometer also appears to undergo electromagnetic disturbances induced by the linear motors, which add to the sensor's intrinsic imperfections. The noise from the accelerometer becomes predominant, preventing us from accurately estimating the phase within the fringe reconstruction procedure. We observed a significant reduction in this noise by selecting a more suitable cable for the accelerometer signal, and we added appropriate filters to diminish the impact of this noise and improve the correlations.

Despite the loss of correlations, we take advantage of the high repetition rate of our apparatus and construct the histogram of the measured population ratio after having performed a number of measurements $N_{meas} \approx 300$. We conducted measurements for extended interrogation times and analyzed the histogram of the ratio using the BAT method as described in section 3.2.4. In this context, a first set of data was collected in January 2021, covering interrogation times ranging from 10 to 100 ms, before the experiment was interrupted due to a simulator malfunction. A subsequent data collection was performed in December 2022 after the simulator was repaired, encompassing interrogation times from 10 to 150 ms. Various histograms and the sensitivity S plotted against interrogation time T for these two datasets are presented in Figure 4.16.

A clear preservation of the interferometer contrast is observed, as shown by the histograms of the measured ratios on Figure 4.16(c) and 4.16(d) which display the characteristic bimodal distribution of a sinusoidal pattern up to $T = 100$ ms.

For each dataset, the experimental histograms is fitted by the function $\mathcal{F}(r)$ expressed in Equation 3.39 to retrieve the contrast C and the amplitude noise σ_P to deduce the signal-to-noise ratio (SNR) and the measurement sensitivity S, given respectively by:

$$\mathrm{SNR} = \frac{C}{2\sigma_P} \tag{4.30}$$

and

$$S = \frac{1}{\mathrm{SNR}\, k_{\mathrm{eff}}\, T^2} \tag{4.31}$$

The relevance of the extracted parameters depends of the numbers of bins and the number of measurement.

The best sensitivity, achieved at $T = 100$ ms for the dataset of January 2021, reaches a value of 5.6×10^{-8}g per shot. This represents the highest short-term sensitivity ever achieved by an atomic accelerometer operating in a microgravity regime.

The dataset of December 2022 enables to confirm the limitation of our measurement to $T = 100$ ms interrogation times. However, the contrast of the fringes for this serie of measurement was lower than the previous one. We suspect it is due to imperfections in the state preparation.

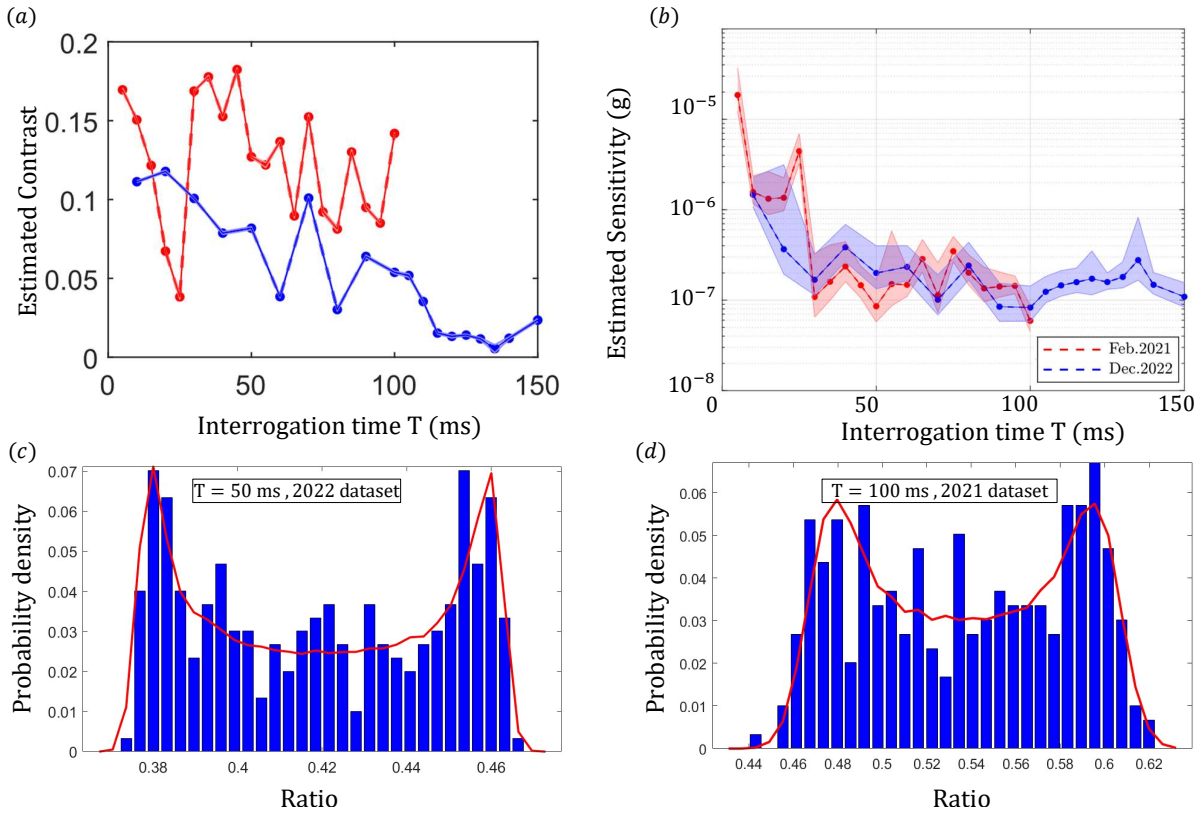

Figure 4.16: ***Sensitivity estimation using BAT method for two different datasets of interferometry in microgravity*** *- (a) Contrast for the two datasets as a function of the interrogation time. (b) Sensitivity computed for both datasets as a function of the interrogation time. The colored area are error bars corresponding to the standard deviation of the residual of the fit of the Batman (c) Example of an histogram and the fit of the Batman for $T = 50$ ms for the 2022 dataset and (d) $T = 100$ ms for the 2021 dataset.*

Contrast loss due to rotations

The contrast loss limiting the sensitivity of our measurement is first due to the relatively high temperature of our atomic samples ($\mathcal{T} \approx 7$ μK). For long interrogation times, the size of the atom cloud become significant compared to the Raman beam. It is perfectly illustrated by the contrast of the Ramsey fringes presented in section 4.13 and on Figure 4.17 (a) where a model implying a Gaussian intensity profile with a waist of 6.3 mm explains this contrast loss when the interrogation time increases significantly.

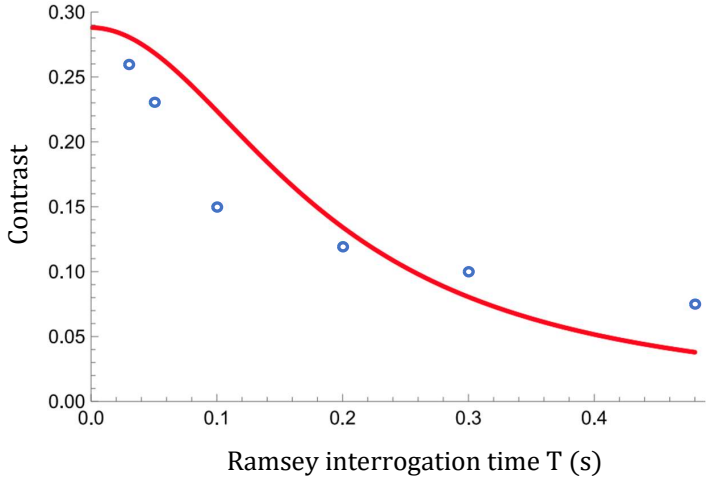

Figure 4.17: ***Contrast loss for the Ramsey fringes versus the interrogation time*** *- The data are presented with empty blue dots and a model including the finite size of the Raman beam compared to the atomic cloud is presented in red.*

On addition to the contrast loss, for both datasets, we observe significant fluctuations in the contrast as a function of interrogation times. Instead of a monotonic decrease, we observe "revivals" of contrast for longer T, for both datasets. This behavior can be explained by simulating the theoretical contrast loss caused by simulator-induced parasitic rotations.

Our model to evaluate the contrast loss due to rotation is based on the work in [[88]] which introduces the vector displacement in the phase space density:

$$\delta\vec{\chi} = \delta\vec{P} - \frac{m}{\Delta t}\delta\vec{R} \tag{4.32}$$

with $\delta\vec{R}$ and $\delta\vec{P}$ the position and momentum displacement vectors of the atomic cloud with respect to the reference mirror, and Δt the expansion time of the wave function. It leads to the contrast loss :

$$C \approx \left| \int \exp\left[\frac{i\delta\vec{\chi}\cdot\vec{r}}{\hbar}\right] |\psi(\vec{r},t)|^2 \mathrm{d}^3\tilde{\mathrm{r}} \right| \tag{4.33}$$

where $\psi(\vec{r},t)$ is the spatial wavefunction after a time of flight t. For a constant rotation rate along an orthogonal axis Ω_y with the wavevector, at first order, the displacement vector can be expressed (up to second order in T and Ω):

$$\delta\vec{\chi} = \frac{\hbar k_{eff}}{2} \begin{pmatrix} 2\Omega_y T \\ 0 \\ -3\Omega_y^2 T^2 \end{pmatrix} \tag{4.34}$$

giving a exponential contrast loss:

$$C \approx \exp\left[-\left(\frac{\sigma_r(2T)k_{eff}T}{2}\right)^2 \Omega_y^2\left[1+\frac{9}{4}T^2\Omega_y^2\right]\right] \tag{4.35}$$

In case of a time varying $\Omega(t)$ we compute numerically the orientation of the laser beams using the signal measured by the gyroscopes, and applying the 3D rotation matrix at each instant. $\vec{k^{(i)}}$ being the wavevector for the pulse i, we calculate the displacement vector:

$$\delta\vec{R} = \frac{2\hbar T}{M}\left(\vec{k^{(1)}} - \vec{k^{(2)}}\right) \tag{4.36}$$

$$\delta\vec{P} = \hbar\left(\vec{k^{(1)}} - 2\vec{k^{(2)}} + \vec{k^{(3)}}\right) \tag{4.37}$$

$$\delta\vec{\chi} = \hbar\left(\vec{k^{(1)}}\left[1-\frac{2T}{\Delta t}\right] - 2\vec{k^{(2)}}\left[1-\frac{T}{\Delta t}\right] + \vec{k^{(3)}}\right) \tag{4.38}$$

Then the contrast loss is calculated using on Eq. 4.33.

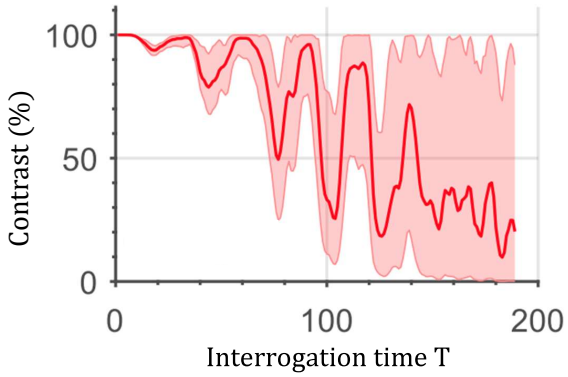

Figure 4.18: ***Estimation of the contrast loss induced by residual rotations of the simulator*** *- These contrast drops are estimated based on the rotation rates measured over the 300 successive trajectories. Thick lines represent the mean values, while the colored areas indicate the extreme values. These estimations are carried out for a sample of rubidium held at a temperature of 7 μK*

Rotation-induced contrast loss versus the interrogation time T is shown in Figure 4.18 for an atomic cloud temperature of $\mathcal{T} = 7\mu$K.

We can thus compare the fluctuations in the simulated contrast and the experimental data presented in Figure 4.16(a). While the correspondence is not perfect, there is a remarkable resemblance between the two profiles.

Limitations due to the classical accelerometer

To demonstrate the potential of our atom interferometer in terms of long term stability and accuracy and prove that the atomic phase is controlled, we want to retrieve the atomic fringes. The ability to reconstuct them using the FRAC method is limited by the self noise of the classical sensor (around 10^{-6} g) used to do the correlation.
Considering a perfect coupling between the mirror and the classical accelerometer, the sensitivity of the hybrid sensor is defined by Eq. 4.39, replacing $S_a(2\pi n f_c)$ by the self noise of the classical sensor.

$$\sigma_a^2(\tau) = \frac{k_{eff}^2}{\tau} \sum_{n=0}^{\infty} \frac{|H_\phi(2\pi n f_c)|^2}{(2\pi n f_c)^4} S_a(2\pi n f_c) \tag{4.39}$$

here $H_\phi(\omega)$ the atom interferometer transfer function which describes its response to phase noise at a frequency ω and can be derived from the Fourier transform of the sensitivity function g(t) [[31]]. $S_a(2\pi n f_c)$ is the power spectral density of the residual acceleration.

The expected phase noise σ_{self} for our current accelerometer Colybris is 19.6 rad, and 0.36 for our low noise sismo-accelerometer (Titan Nanometrics). Outside the bandwidth of the classical accelerometer, we suppose there is no reliable classical measurement and we consider the acceleration noise power spectral density.

Our calculation confirms the current limitation of the experiment due to the self noise of the Colybris accelerometer. The FRAC method requires a better accelerometer, with a lower self noise, to have an hybrid sensitivity at 10^{-8}g per shot limited by the sensitivity of the atom interferometer. Typically, an accelerometer for seismology, such as the Nanometrics Titan can almost reach such a low self noise (3×10^{-8}g.Hz$^{-1/2}$). Unfortunately, the Titan is a force balance accelerometer designed to have the best sensitivity at 1 g, and a dedicated design for microgravity is required. Moreover, the bandwidth where the sensitivity is optimal [0.1-50 Hz] doesn't match our needs. To our knowledge, no mechanical accelerometer satisfies all the criteria.

4.3 Double Diffraction in microgravity

In order to enhance both the overall duration and sensitivity of our atom interferometer, the utilization of ultra-cold atomic samples will be essential. With ultra-cold atom samples, only the double diffraction regime becomes relevant. This regime offers the significant advantage of doubling the interferometer's spatial coverage, thereby enhancing its sensitivity. In our knowledge, no reference reports on inertial measurements utilizing ultra-cold atom interferometry in the context of Double Diffraction in microgravity. Here, we present our advancements towards the realization of a Mach-Zehnder interferometer operating within the double-diffraction regime.

4.3.1 Raman spectroscopy with ultra-cold atoms in microgravity

The Figure 4.19 illustrates Rabi oscillations and a counter-propagating Raman spectrum obtained using ultra-cold atoms (with an estimated temperature of 30 nK) on the simulator. The atomic sample is prepared using the spin distillation technique detailed in section 2.6.1, with the atoms prepared in the Zeeman sub-level insensitive to the magnetic field, i.e., $m_F = 0$. By applying a Raman pulse of adjustable duration in the presence of a magnetic field bias, we optimize the transfer to the excited level. For a pulse duration of 22 μs, a maximum transfer of about 90% is observed. The Raman spectrum is obtained under theses conditions: we obtain a sinc shape centered at +15 kHz, corresponding to the recoil frequency. The error bars on the experimental data are computed from the standard deviation of 4 distinct spectra acquired under consistent experimental conditions.
The discrepancy with the simulations presented in Figure 4.4(b) may arise from imperfect state preparation or polarization of the Raman beam. Under these circumstances, we achieved an atomic beam splitter in microgravity under the double diffraction regime, as demonstrated in Figure 4.20.

A promising maximum transfer of more than 80% was observed, which is very encouraging for atom interferometry. Nevertheless, the issue of non-diffracted atoms needs to be addressed, as depicted in Figure 4.8. These undiffracted atoms can recombine at the interferometer's end, inducing a contrast degradation.

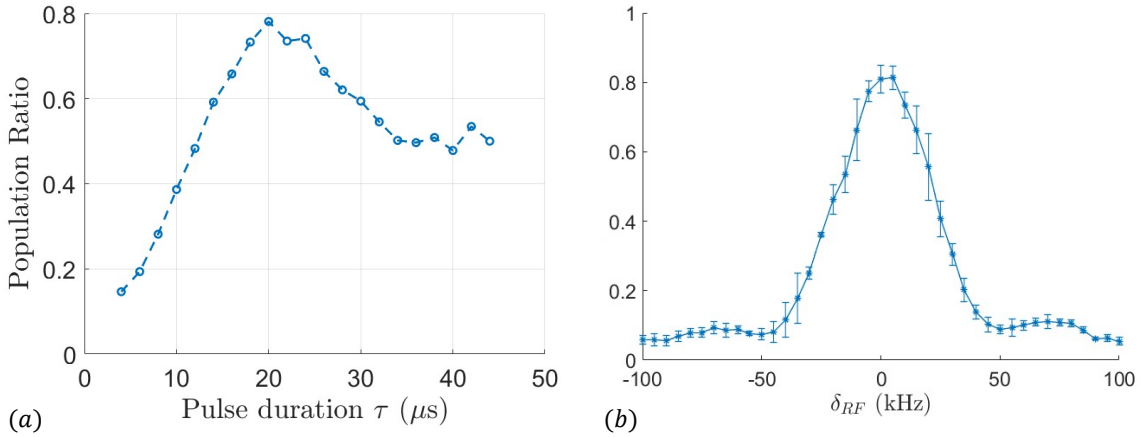

Figure 4.19: ***Rabi oscillations and Raman spectrum obtained on the simulator with ultra-cold atoms*** *- (a) Population ratio in the excited state detected as a function of the pulse duration. We observe damped Rabi oscillations and a maximum transfer for $\tau_s = 22\mu s$ (b) Spectrum obtained for ultra-cold atoms at an estimated temperature of 30 nK by averaging 4 spectra obtained in the same experimental conditions for a $22\mu s$. The error bars correspond to the standard deviation of those 4 spectra. Tha data were taken using a PMT detector.*

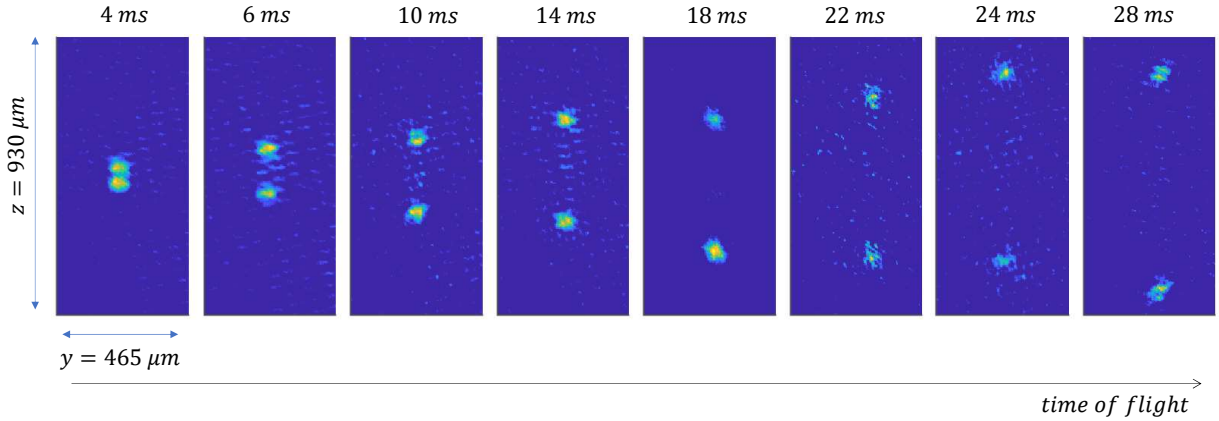

Figure 4.20: ***Absorption imaging of the diffracted atoms in microgravity as a function of the time of flight after the Raman pulse*** *- The images were taken for different times of flight after a 22 μs Raman pulse.*

The mirror pulse is the main challenge for double diffraction, as emphasized by the efficiency simulated in Figure 4.10. Our experimental Rabi oscillations presented in 4.21 reveal that, for the optimal pulse duration, at least 50% of the atoms are transferred to the ground state (after 35 μs, the ratio of atoms in the excited state corrrespond to the atoms effectively diffracted by the mirror pulse). An effective approach to enhance pulse efficiency is to lower the atom's temperature, as demonstrated in Figure 4.10. However, lowering the temperature under the order of the nK does not appear to improve the efficiency significantly.

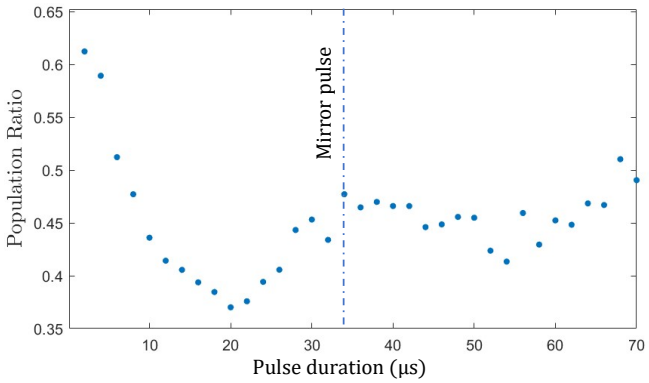

Figure 4.21: ***Rabi oscillations for a mirror pulse in double diffraction*** *- Population of the excited state detected as a function of the duration of the second Raman pulse. The atoms are prepared in the ground state $|g, m_F = 0\rangle$ with the spin distillation technique. A first 20 μs splitting pulse is performed to transfer the atoms to the excited state. Due to the imperfection of this pulse, the initial ratio is not 1. This data are taken by performing a first beam splitter pulse, then after a 6ms ToF a second pulse is performed with varying duration in increments of 2 μs.*

4.3.2 Double diffraction interferometer in the horizontal configuration

Our exploration of atom interferometry using ultra-cold atoms on the simulator encountered a setback due to the malfunction of the simulator. Consequently, we were unable to capture fringes using the ultra-cold atom sources. To continue investigating this specific regime, we adapted our setup to perform atom interrogation with the Raman beam in the horizontal direction. In doing so, for sufficiently short interrogation times in the interferometer, the atoms undergo very small free fall relative to the mirror, and we are in the double diffraction regime. In this scenario, adjusting the laser phase to scan the fringes is not possible. Nonetheless, the interferometer's phase scales as $\vec{k}_{eff} \cdot \vec{a} \cdot T^2$, where $\vec{a}$ is the acceleration due to gravity that should be null if the set up is perfectly horizontal. By tilting the Raman beam at an angle θ with respect to the horizontal plane, the phase scales as $\vec{k}_{eff} \cdot \sin(\theta) \cdot g \cdot T^2$, enabling to scan the fringes. By employing this approach, we successfully obtained fringes by varying the interrogation time T. We observe fringes with a contrast estimated around 0.18. The interference is observed up to 2T=10 ms. The fringes average value drifts down because the atoms fall in the detection area. The total signal detected N_{tot} drops and due to imperfections in our normalization, the offset varies. The contrast also decreases because the effective Rabi frequency changes when the atoms fall in the Raman beam. To improve the contrast, it is crucial to eliminate the atoms that do not undergo diffraction during each Raman pulse. Achieving this requires the removal of atoms that remain in the $|F = 1\rangle$ state after the first and second pulse, which is in practice difficult. We opted for an alternate strategy, illustrated in Figure 4.23. This approach involves starting the interferometer with atoms prepared in the $|F = 2\rangle$ state using a microwave pulse.

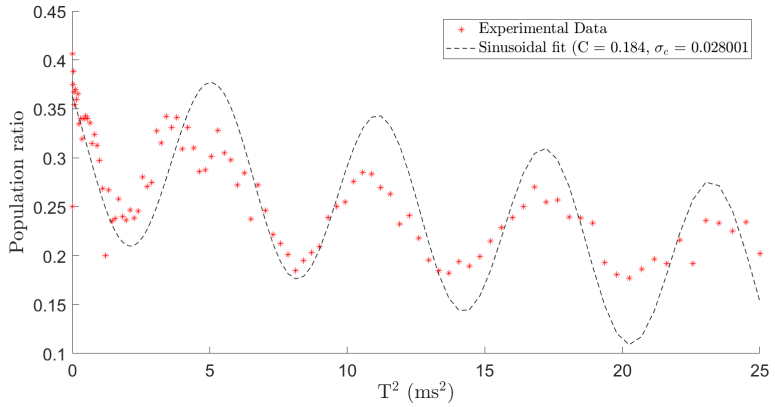

Figure 4.22: ***Double Diffraction interference fringes in the horizontal configuration*** *- The ultra-cold atoms are prepared in the $m_F = 0$ sub-state. The interrogation time is varied from 0 to 5 ms in increments of 50 μs. A sequence of $\tau_{s1} = 20\mu s$, $\tau_m = 50\mu s$ and $\tau_{s2} = 20\mu s$.*

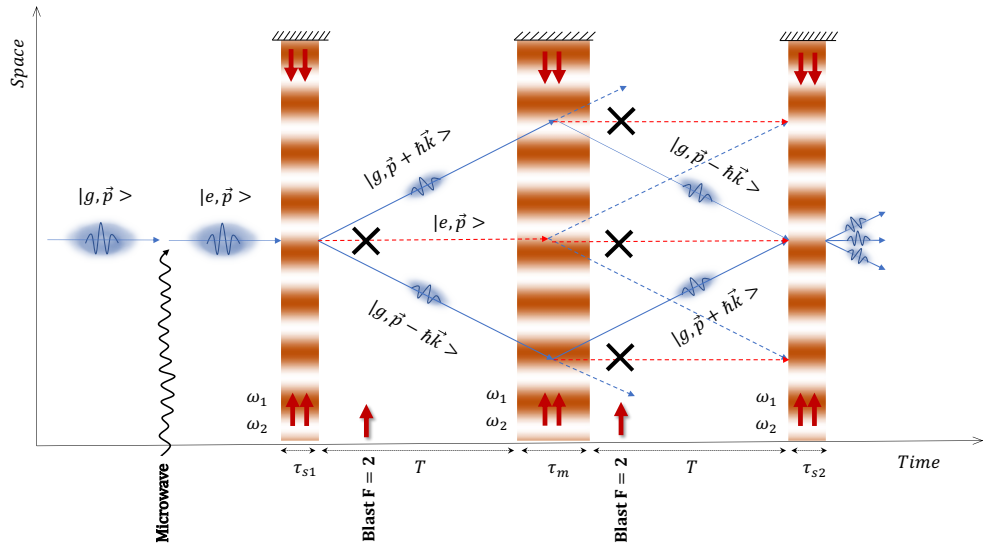

Figure 4.23: ***Space-time diagram of an interferometer in the Double Diffraction regime when starting in the F=2 excited state*** *- The wavepacket is first pumped in the F=2 state using a microwave pulse, than a sequence of $\tau_{s1} - \tau_m - \tau_{s2}$ is executed. The imperfections of each pulse result in residual wavepackets, depicted by dashed lines. laser pulses referred as "Blast" enable to get rid of the residual atoms after each pulse.*

The Raman spectrum obtained when starting in the excited state is depicted in Figure 4.24. The duration corresponding to the splitting of the wavepacket is around 22 μs.

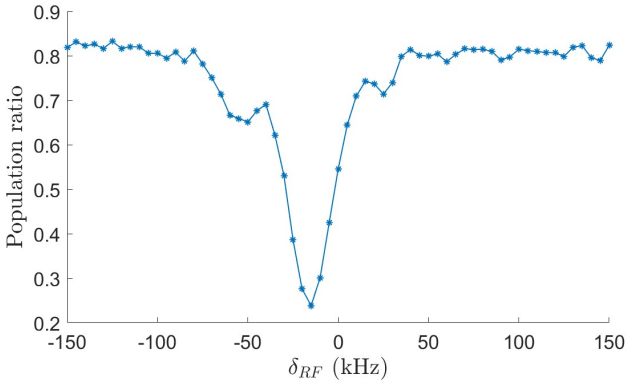

Figure 4.24: ***Raman spectrum obtained in horizontal configuration when starting the sequence in the excited state*** *- Spectrum obtained experimentally : the atoms are transferred to $|F = 2, m_F = 0\rangle$ using a microwave pulse, with an efficiency of about 80%. The peak corresponding to double diffraction is around -15kHz.*

We note that the microwave transfer to the exited state is not perfect, with a 80% efficiency. The maximum transfer achieved by the Raman pulse is about 60% : this can be due to a imperfect state preparation (spin distillation), inducing residual atoms in the m_F states that are sensitive to the magnetic field. In this setup, the remaining atoms reside in the $|F = 2\rangle$ state, and our laser set up has the capability to blast these atoms after the first and second pulses. By performing Rabi oscillations for each pulse after several ToF, we notice the optimal duration for each pulse enlarges because of the fall of the atoms in the horizontal Raman beam. To conteract this effect, the durations of the mirror pulse and the second splitting pulse are varied from 48 μs to 60 μs in 0.12 μs increments and from 28 μs to 34 μs in 0.05 μs increments, respectively. The corresponding fringes obtained under this configuration are presented in Figure 4.25.
For both Double Diffraction configurations (with and without blasting the residual atoms), we observe a contrast around 0.18, which is similar to the contrast obtained with thermal atoms. This low contrast can be explained by the presence of residual m_F in the cloud, or by the very low efficiency of the mirror pulse. We conclude that lowering the atoms' temperature, for example by evaporating during the microgravity phase, is necessary to obtain the high contrast interferometry needed for our measurements.

4.3.3 Interferometry on the simulator : latest results

As seen in Section 2.6.1, the atomic clouds obtained in the microgravity simulator after its modification have a higher temperature than the sources that enabled us to achieve the previously presented results. However, several tests for performing atom interferometry in microgravity using these sources have been conducted. We successfully split the atoms in the double diffraction regime and attempted to execute the mirror pulse in the scheme presented in Figure 4.8, (starting the interferometer in the $|F = 1\rangle$ state).
Figure 4.26 presents fluorescence images of the atomic cloud for different times of flight after the 24 μs splitting pulse and then after a 48 μs mirror pulse. The atomic clouds exhibit larger spatial expansion than those presented in Figure 4.20 due to their higher temperature, estimated to be around 100 nK. We observe a successful Double Diffraction beam splitter with residual atoms that are not diffracted by the first Raman pulse. After the mirror pulse and time of flight, the clouds appear to recombine, but it is more challenging to distinguish between the atomic

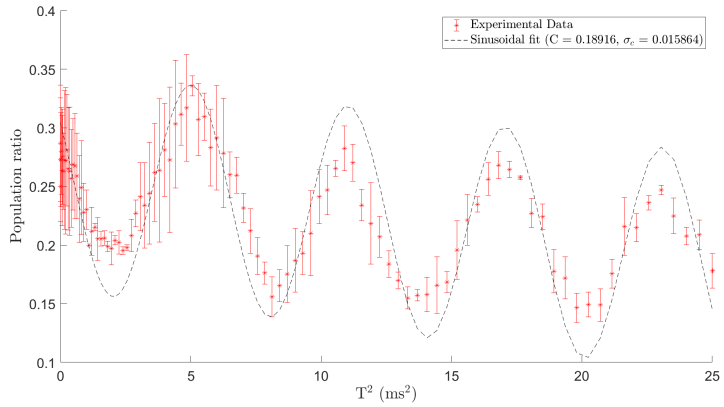

Figure 4.25: ***Double Diffraction interference fringes in the horizontal configuration when starting the sequence in the excited state*** *- The ultra-cold atoms are pumped to the excited state using a 300µs microwave pulse. The interrogation time is varied from 0 to 5 ms in increments of 50 µs. The duration of the first splitting pulse is $\tau_{s1} = 20\mu s$, while the durations of the mirror pulse and the second splitting pulse are varied from 48 µs to 60 µs in 0.12 µs increments and from 28 µs to 34 µs in 0.05 µs increments, respectively. These adjustments are made to compensate for the atoms' fall in the Raman beam. The error bars represent the standard deviation of three datasets taken under the exact same experimental conditions.*

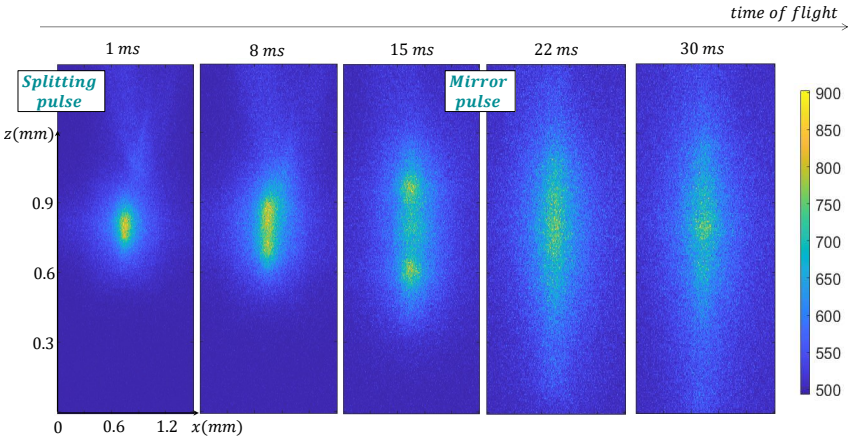

Figure 4.26: ***Absorption imaging of the diffracted atoms in 0g as a function of the time of flight after the first and second Raman pulses*** *- The images were taken for different times of flight after a 24 µs Raman pulse for the splitter, and then after a 48 µs mirror pulse. The estimated temperature of the clouds used in the experiment is approximatively 100 nK.*

paths because of the expansion of the clouds. Unfortunately, we were not able to obtain fringes or interference patterns using these sources on the simulator.

Conclusion

In this chapter, we have presented the theoretical framework of atom interferometry in a free-falling reference frame. Our experimental results conducted on our microgravity platform in the laboratory showcase a state-of-the-art setup capable of measuring inertial effects in microgravity using thermal samples. The performances are limited by the temperature of the atoms in this regime. The promising outcomes obtained with ultra-cold atoms suggest the future realization of atom interferometry in the double diffraction regime on our simulator, once we obtain samples at temperatures similar to those achieved in 2021. Although our work has been conducted with rubidium atoms, we plan to extend these investigations to potassium once we obtain ultra-cold samples of both species.

A significant advantage of our microgravity platform lies in its high repetition rate and the unrestricted access to microgravity within our laboratory. This distinctive setup, combined with the knowledge gained about atom interferometry in microgravity as demonstrated in this chapter, offers a remarkable opportunity to comprehensively study inertial measurements in a microgravity environment. This tool is set to play an important role in the development of a spaceborne atom accelerometer for geodesy purposes or for testing the weak equivalence principle.

Chapter 5

Testing the Weak Equivalence Principle with Atom Interferometry

Introduction

Testing the universality of free fall using a double-species atom interferometer represents the primary objective of the ICE experiment. As outlined in Chapter 0.1, this process entails measuring the relative acceleration between two test masses in free fall under the influence of the same gravitational field, denoted as accelerations a_1 and a_2. We characterize this test using the Eötvös parameter:

$$\eta = 2\frac{a_1 - a_2}{a_1 + a_2} \tag{5.1}$$

where $\Delta a = a_1 - a_2$ is the relative acceleration, and $a = \frac{a_1+a_2}{2}$ is the average acceleration. In the final chapter of this manuscript, we concentrate on realizing this measurement using atomic ensembles of ^{87}Rb and ^{39}K. Previous tests of this principle were carried out using the ICE experiment aboard the Zero G plane [[15]], yielding $\eta_{0g} = (0.9 \pm 3.0) \times 10^{-4}$ as the result, with the measurement primarily hampered by significant vibrations in the plane. Ground-based tests produced a value of $\eta_{1g} = (0.9 \pm 1.6) \times 10^{-6}$, also allowing for an in-depth study of systematic effects [[14]]. Table 5.1 presents some results pertaining to the test of the WEP using cold atoms as test masses :

Project	Reference	Atoms	Platform	η
Stanford Univ.	[[8]]	^{85}Rb - ^{87}Rb	8.2 m atomic fountain	$1.6 \pm 5.2 \times 10^{-12}$
Wuhan Inst. of Phys.	[[104]]	^{85}Rb - ^{87}Rb	10 m atomic fountain	$2.8 \pm 3.0 \times 10^{-8}$
LENS (Florence)	[[100]]	^{87}Sr-^{88}Sr	Ground	$0.2 \pm 1.6 \times 10^{-7}$
ATLAS (QUEST)	[[94]]	^{87}Rb - ^{39}K	Ground	$-0.3 \pm 5.4 \times 10^{-7}$
ONERA	[[22]]	^{85}Rb - ^{87}Rb	Ground	$1.2 \pm 3.2 \times 10^{-7}$
ICE	[[14]]	^{87}Rb - ^{39}K	Ground	$0.9 \pm 1.6 \times 10^{-6}$
ICE	[[15]]	^{87}Rb - ^{39}K	Zero G plane	$0.9 \pm 3.0 \times 10^{-4}$

Table 5.1: Tests of the weak-equivalence principle using dual-species atomic interferometers.

To date, most experiments involving cold atoms have utilized pairs of isotopes belonging to the same atomic element, such as ^{85}Rb and ^{87}Rb, or ^{87}Sr and ^{88}Sr. While these isotopic pairs have shown effective common-mode noise rejection in differential phase measurements, they inherently possess lower sensitivity to potential violations of the equivalence principle due to their relatively similar mass and composition. Consequently, there is an interest in conducting these experiments with two entirely distinct atomic elements. In our case, ^{87}Rb and ^{39}K exhibit

a substantial discrepancy in the number of nuclei, resulting in a mass ratio approximately equal to $m_{\mathrm{Rb}}/m_{\mathrm{K}} \approx 2.2$.
In this chapter, we will discuss various methods that have been developed to extract the differential acceleration from the dual-species interferometer. We provide a brief overview of the previous findings from ICE experiments. Additionally, we will explore potential approaches for future tests using cold atoms within our microgravity simulator. This study contributes to the envisioning of a space-based experiment aimed at examining the universality of free fall using quantum technologies.

5.1 Dual-species atomic accelerometer

In our experiment, two matter-wave sensors composed of ^{87}Rb and ^{39}K operate simultaneously, as presented in Figure 5.1.

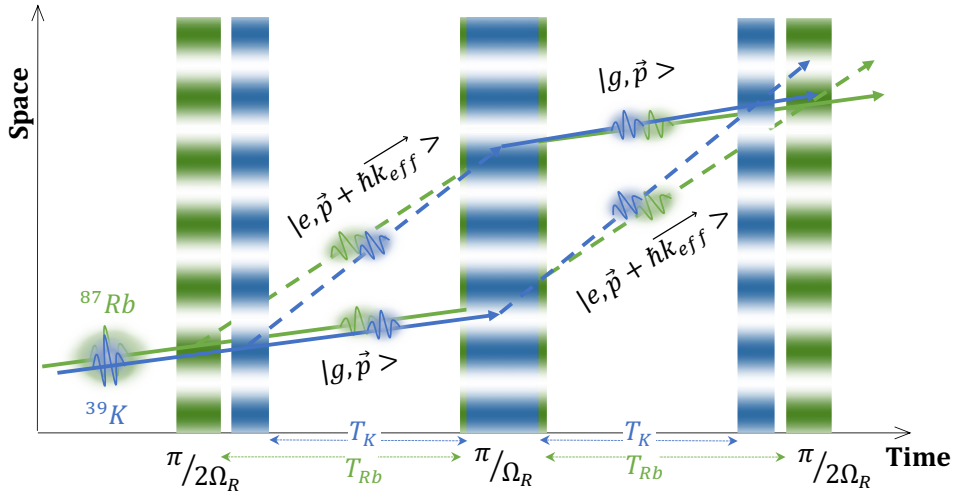

Figure 5.1: ***Principle of the simultaneous dual-species interferometer*** *- Two Mach-Zehnder interferometers with interrogation times T_{Rb} and T_K are centered around the mirror pulse.*

Here we provide a description of three methods for extracting the differential phase between the two atom interferometer [[12]].
The Eötvös parameter can be written as :

$$\eta = \frac{\Delta a}{a} \tag{5.2}$$

where $\Delta a = a_1 - a_2$ is the relative acceleration, and $a = \frac{a_1+a_2}{2}$ is the average acceleration. The output of two coupled atomic interferometers are sinusoidal :

$$\begin{cases} y_1{=}A_1\cos(S_1 a + \phi_1) + B_1 \\ y_2{=}A_2\cos(S_2 a + \phi_2) + B_2 \end{cases} \tag{5.3}$$

where a is an acceleration common to both atomic clouds, A_j is the amplitudes and B_j the offsets of the fringes obtained with sensors j.
Equations (5.3) can be normalized in the form

$$\begin{cases} n_1{=}\cos(S_1 a + \phi_1) \\ n_2{=}\cos(S_2 a + \phi_2) \end{cases} \tag{5.4}$$

with $n_j = \frac{(y_j - B_j)}{A_j}$, ϕ_j its phase shift and S_j is the scale of the j^{th} interferometer. These equation describe a Lissajous curve.
For a constant acceleration, S_j is given by :

$$S_j = S_j = k^j_{\text{eff}} \int f_j(t)dt = k^j_{\text{eff}}(T_j + 2\tau_j)\left(T_j + \frac{4\tau_j}{\pi}\right) \tag{5.5}$$

with k^j_{eff} being the effective wave vector, f_j the response function, T_j the interrogation time, and τ_j the $\pi/2$ pulse duration of interferometer j. For interrogation times much greater than the Raman pulse durations ($T_j \gg \tau_j$), we have:

$$S_j \approx k_{eff}^j T^2 \tag{5.6}$$

We consider three contributions to the phase shifts ϕ_j :

$$\phi_j = \phi_j^{laser} + \phi_j^{sys} + \phi_j^{WEP} \tag{5.7}$$

Here, ϕ_j^{laser} is the laser phase term, which is controlled, while ϕ_j^{sys} is the term related to systematic effects, which we seek to minimize (or at least estimate). Finally, ϕ_j^{WEP} is the phase shift induced by a possible violation of the WEP (Weak Equivalence Principle), which can be written as:

$$\phi_j^{WEP} = S_j(a_j - a) \tag{5.8}$$

where a_j is the absolute acceleration of species j.

In the ideal case, the total interferometer phase Φ_j contains only the shift due to the mean acceleration, $S_j a$, and a WEP violation. It then follows that :

$$\Phi_j = S_j a + \phi_j. \tag{5.9}$$

Under these ideal conditions, the total phase of each interferometer can be directly linked to the Eötvös parameter as follows:

$$\eta = \frac{\Phi_1/S_1 - \Phi_2/S_2}{a} \tag{5.10}$$

We define a common phase $\phi_c = S_2 a + \phi_2$ and a differential phase $\phi_d = \phi_1 - \kappa\phi_2$ with $\kappa = \frac{S_1}{S_2}$. The interferometer outputs can then be expressed as

$$\begin{cases} n_1(\phi_c) = \cos(\kappa\phi_c + \phi_d) \\ n_2(\phi_c) = \cos(\phi_c) \end{cases} \tag{5.11}$$

The Eötvös parameter can then be deduced from the differential phase

$$\eta = \frac{\phi_d}{S_1 a} \tag{5.12}$$

The methods used to extract the differential phase ϕ_d from the dual-species interferometer in a noisy environment are described. On ICE experiment, three methods have been studied : an improved ellipse fitting method, a general Bayesian analysis and a fringe reconstruction by accelerometer correlation method (FRAC).

5.1.1 Ellipse fitting method

The system of equations in Equation 5.11 describes the general form of a Lissajous figure. If we choose to make the scale factors between the two atom interferometers equal by properly tuning the interrogation times T_{Rb} and T_K, the scale factor κ becomes equal to 1. In this scenario, the parametric plot in a plane simplifies to that of an ellipse, with the eccentricity determined by the differential phase ϕ_d. The initial methods for extracting the differential phase involved fitting experimental data to an ellipsoidal shape [[48]]. However, a significant limitation of this method is its applicability only when scale factors are equal. It also results in a biased estimation of the differential phase ϕ_d in the presence of noise in the fringe offset or amplitude. When the signal is noisy, several different ellipses can be found by the fitting algorithm. By incorporating a noise model into the ellipse, the method can be improved [[12]] and has been used in the past in our experiment. Therefore, its use is not recommended for our specific application.

5.1.2 Generalized Bayesian Analysis

Algorithms based on a Bayesian analysis of the experimental data can be used to retrieve the differential phase from noisy data. Unlike ellipse-fitting methods, it can be used to find a solution even when the scale factors between the two species are not equal. We consider three possible noise sources : amplitude δA_j, offset δB_j and differential phase $\delta\phi_d$. The system (5.11) can thus be written as :

$$\begin{cases} n_1(\phi_c) = (1+\delta A_1)\cos(\kappa\phi_c + \phi_d + \delta\phi_d) + \delta B_1 \\ n_2(\phi_c) = (1+\delta A_2)\cos(\phi_c) + \delta B_2. \end{cases} \tag{5.13}$$

The noises are uncorrelated and follow a Gaussian probability distribution with zero mean and non zero standard deviation.

According to Bayes' theorem, the state of the knowledge of the differential phase after the i^{th} measurement can be expressed as the conditional distribution called posterior distribution

$$P(\phi_d|\{n_1,n_2\}_i) = \frac{P(\phi_d)_i L(\{n_1,n_2\}_i|\phi_d)_i}{N(\{n_1,n_2\}_i)_i}. \tag{5.14}$$

$P(\phi_d)$ is the prior probability distribution before the i^{th} measurement, the likelyhood function $L(\{n_1,n_2\}_i|\phi_d)_i$ is the probability to measure the result $\{n_1,n_2\}_i$ given the actual phase ϕ_d. $N(\{n_1,n_2\}_i)_i$ is a normalizing factor for the posterior distribution : it is the probability of measuring $\{n_1,n_2\}$ integrated on all the possible values of ϕ_d. The algorithm consists in updating the knowledge of ϕ_d on a measurement-by-measurement basis. The principle of this algorithm is presented in the schematic on Figure 5.2.

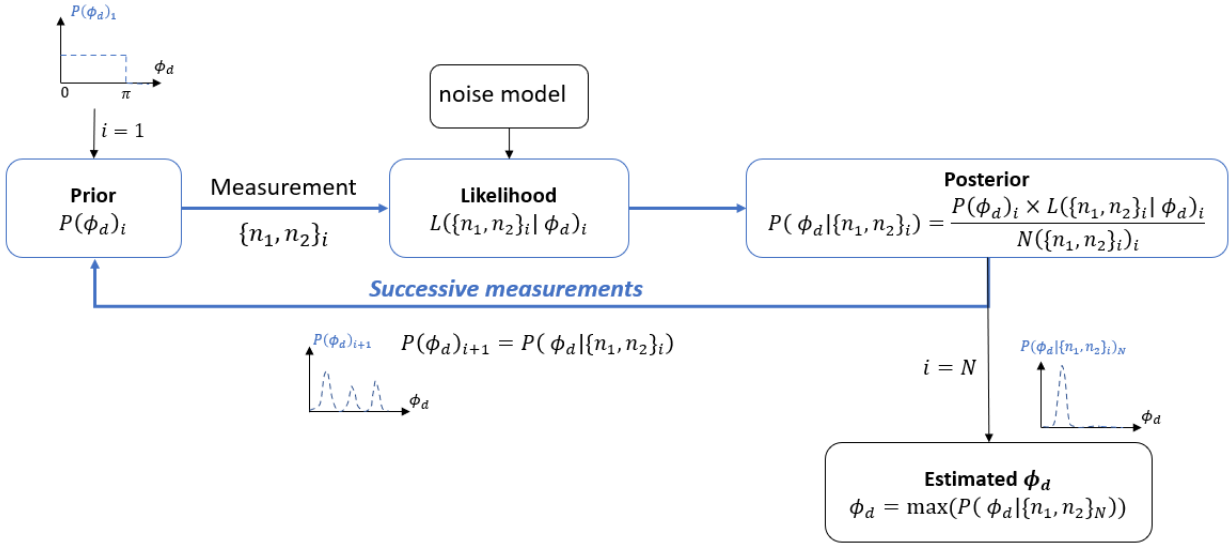

Figure 5.2: ***Principle diagram of the algorithm of Bayesian estimation of the differential phase*** ϕ_d *- The algorithm follows these main steps : (i) An initial prior distribution* $P(\phi_d)$ *is chosen (in this case, uniform distribution within the range* $\phi \in [0,\pi]$*, and zero elsewhere). (ii) A measurement is recorded and the noise model is used to calculate the likelihood* $L(\{n_1,n_2\}_i|\phi_d)_i$*. (iii) Bayes' rule is applied to compute the posterior distribution* $P(\phi_d|\{n_1,n_2\}_i)$*. (iv) The new prior distribution is set equal to previous conditional distribution. (v) Steps ii to iv are repeated for N measurements. (vi)* ϕ_d *is estimated using the maximum value of the final posterior probability distribution*

The likelihood distribution $L(\{n_1,n_2\}|\phi_d)$ is computed given the model of equations 5.13 and can be shown to be [[97]] :

$$L(\{n_1, n_2\}|\phi_d) = \sum_l \int_{-1}^{1} \frac{P(n_1|s_1)P(n_2|\{s_{2,\ell}; s_1, \phi_d\})}{\sqrt{1-s_1^2}} \tag{5.15}$$

with s_1 and $s_{2,\ell}$ the parametric curves without noise.

$$\begin{cases} s_1 = \cos(\kappa\phi_c + \phi_d) \\ s_{2,l} = \cos(\phi_c), \end{cases} \tag{5.16}$$

$P(n_1|s_1)$ and $P(n_2|\{s_{2,\ell}; s_1, \phi_d\})$ are the single-sensor conditional distributions. For each value of n_1, a number ℓ of solutions for n_2 exist due to the periodic nature of the Lissajous equations (5.11). For $s_1 = n_1$, the ℓ^{th} root of n_2 is $s_{2,\ell}$. If $\kappa = 1$, the Lissajous curve is an ellipse and only two solutions exist. If $\kappa \neq \frac{p}{q}$, p and q being prime numbers, the curve is not a closed ellipse and 0, 1 or 2 solutions can exist. It is then necessary to know the range of common phase spanned by the data : $\phi_c \in [\phi_c^{min}, \phi_c^{max}]$, which gives us the range of phase spanned by the sensor $\theta \in \kappa[\phi_c^{min}, \phi_c^{max}] + \phi_d$. For instance, in presence of vibrations, this range is estimated from the experimental data of the accelerometer. We then look for solutions by dividing this full range in π-subranges (in each subrange, the cosine can be inverted and one can find one unique solution):

$$s_{2,\ell} = \begin{array}{ll} \cos[(\cos^{-1} s_1 - \phi_d + 2\pi m_{1,\ell})/\kappa] & \text{for even } \ell \\ \cos[(\cos^{-1} s_1 + \phi_d - 2\pi m_{2,\ell})/\kappa] & \text{for odd } \ell \end{array}$$

with

$$m_{1,\ell} = \begin{cases} \text{floor}((\ell-1)/2) & \ell < -1, \\ 0 & -1 \leq \ell < 2, \\ \text{floor}(\ell/2) & \ell \geq 2, \end{cases} \tag{5.17}$$

and

$$m_{2,\ell} = \begin{cases} \text{floor}(\ell/2) & \ell < -2, \\ 0 & -2 \leq \ell < 1, \\ \text{floor}((\ell+1)/2) & \ell \geq 1, \end{cases} \tag{5.18}$$

The likelihood can then be computed using the noise models for the single sensor's probability distributions. If we consider the two noise contributions independently:

- **Offset noise** : the parameters δB_j are randomly distributed and the single-sensor conditional probabilities can be written as

$$P(n_1|s_1) \propto \exp\left(-(n_1 - s_1)^2/2\sigma_{B_1}^2\right) \tag{5.19}$$

$$P(n_2|\{s_{2,\ell}; s_1, \phi_d) \propto \exp\left(-(n_2 - s_{2,l})^2/2\sigma_{B_2}^2\}\right) \tag{5.20}$$

- **Differential phase noise** : we consider the measured value ϕ'_d in presence if a gaussian noise centered on the most likely value ϕ_d with a $\sigma\phi_d$ standard deviation : $P(\phi'_d|\phi_d) = \exp\left(-(\phi'_d - \phi_d)^2/2\sigma_{\phi_d}^2\right)$. The likelihood function can be written as

$$L(\{n_1, n_2\}|\phi'_d) = \sum_k \delta(\phi'_d - \phi_{d,k}), \tag{5.21}$$

where $\phi_{d,k}$ are all the possible solutions in the range $\phi_c \in [\phi_c^{min}, \phi_c^{max}]$. Two possible solutions exist within each π interval of the phase range :

$$\phi_{d,k}^{(\pm)} = \cos^{-1}(n_1) \pm \kappa[\cos^{-1}(n_2) - 2\pi m_k], \tag{5.22}$$

with $m_k = (-1)^k floor((|k|+1)/2)$. Finally, this result is convolved with the gaussian model:

$$L(\{n_1, n_2\}|\phi_d) \propto \int_{-\infty}^{\infty} L(\{n_1, n_2\}|\phi'_d) P(\phi'_d|\phi_d) d\phi'_d \tag{5.23}$$

$$L(\{n_1, n_2\}|\phi_d) = \sum_k \exp[-(\phi_d - \phi_{d,k}^{(\pm)})^2 / 2\sigma_{\phi_d}^2] \tag{5.24}$$

The inputs of the final algorithm are the experimental data to analyse, the noise parameters, and the common phase scanned by the vibrations. This last input is deduced from the accelerometer measurement using the transfer function of the interferometer. The outputs are the estimated differential phase, the statistical uncertainty and the systematic error.

This technique was demonstrated in [[12]] by deducing ϕ_d from both simulated data and experimental data from the K–Rb interferometer. The principle is described in Figure 5.3.

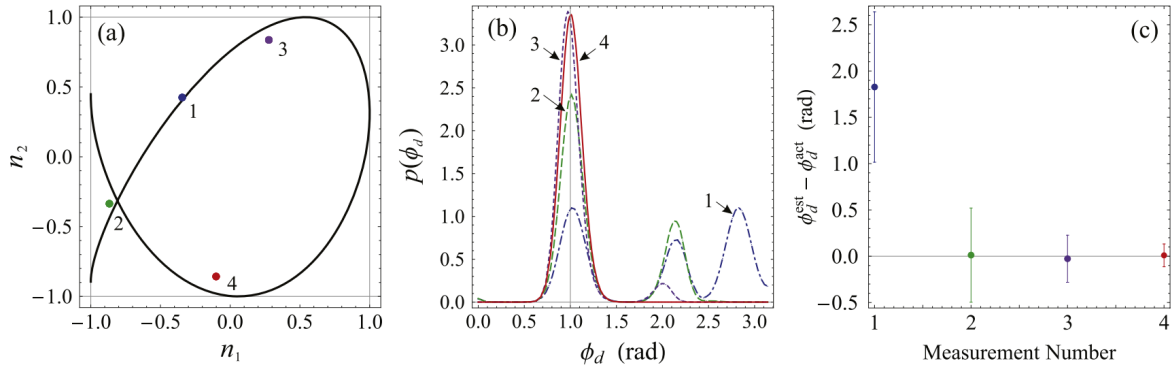

Figure 5.3: ***Bayesian estimation of the differential phase from data following a Lissajous curve*** *- The figure is extracted from [[12]]. (a) Randomly selected points, labeled 1–4, following equations 5.13, while introducing Gaussian offset noise to n_1 and n_2. Actual Lissajous curve (black curve) plotted for $\kappa = 0.8$ and 1 rad for an actual differential phase ϕ_d^{act} for the sake of illustration. (b) The prior probability distribution, as computed using Bayes' algorithm after each measurement, is displayed. The vertical solid line marks the differential phase employed in the simulation.(c) Error in the Bayesian estimate after successive measurements. The points indicate the the systematic error between ϕ_d^{Bayes} and ϕ_d^{True}, where ϕ_d^{Bayes} is the Bayesian estimate derived from the maximum likelihood value of the corresponding prior distribution. The error bars denote the statistical uncertainty, calculated based on the standard deviation of the prior distributions in (b).*

The key advantage of employing this estimation technique lies in the rapid convergence of uncertainty in ϕ_d, as seen in Figure 5.3 (c). Consequently, fewer data points are needed to attain a specified level of sensitivity. However, there are certain drawbacks associated with the Bayesian analysis approach. Firstly, it necessitates a priori knowledge of the noise characteristics within the system. Secondly, it can be computationally demanding due to the requirement to evaluate a large number of integrals.

5.1.3 Differential FRAC method

The differential FRAC method consists of applying the method described in chapter 3.2.4 to each of the two atomic sensors. This procedure can be straightforwardly extended to any number of correlated atomic interferometers, offering several notable advantages in the context of

testing the WEP.

This approach provides a precise and unbiased estimation of ϕ_d since it relies on a sinusoidal fitting of each set of fringes individually. Unlike the Bayesian method, it does not require any a priori information about the noise affecting the system. It also does not necessitate the two interferometers to be temporally superimposed. The synchronization details can be freely chosen, provided that the time interval over which accelerations are measured encompasses the temporal location of the two interferometers.

This method is simple, fast, and demands low computational resources, allowing for real-time usage. The primary drawback of differential FRAC is the same as that of "classical" FRAC, namely its sensitivity to the measurement noise of conventional accelerometers (see chapter 3.2.4). The method's efficiency is thus fundamentally limited by the performance level of the conventional sensors used and the quality of their coupling with the reference mirror. In the specific case where both interferometers are implemented simultaneously and where the sensor's intrinsic noise remains reasonable, it can nonetheless be demonstrated that the differential measurement allows one to surpass the sensor's intrinsic noise by common-mode rejection [[45]]. A strong coupling between the two interferometers enables to reduce the uncertainty on the estimation of the differential phase thanks to the high correlation of the two measurements[[12]].

5.2 Weak Equivalence Principle test on ICE

Previous measurement campaigns using the ICE experiment have enabled to test the WEP, proving the concept of the method both onboard the harsh environment of the Zero G plane and on the ground. Here, we provide a brief summary of these two measurements and offer an overview of the systematic effects study published in [[14]].

5.2.1 WEP test onboard the Zero G aircraft

This section presents the experimental sequence and results obtained in 2016 with thermal samples of rubidium and potassium by previous team members of the ICE experiment presented in [[15]]. The purpose of this summary is to provide an overview of the concept of the WEP test onboard the plane and to discuss its limitations.

Experimental sequence for the dual-species interferometer

During the flight campaign, the apparatus operates in both steady flight phases (standard gravity) and during the microgravity phases. In steady flight conditions, the matter-wave inertial sensors acts as a gravimeters, following the configuration described in Section 3.2.4. The detuning between the two frequencies contained in the retro-reflected Raman pulse is chirped to compensate for the Doppler shift due to the gravitational fall of the atoms. In this single-diffraction regime, because of the counter-propagating configuration of the Raman beams, the interferometer can be operated with the atoms diffracted with a wave vector $\vec{k}_{eff}$ or $-\vec{k}_{eff}$. For each direction of momentum transfer, the output of the interferometer is then given by:

$$P^{\pm} = P_0 - \frac{C}{2}\cos(\Phi^{\pm}) \tag{5.25}$$

where P_0 is the mean probability of finding the atom in one of the interferometer output ports, C is the fringe contrast, $\Phi^{\pm}$ is the total interferometer phase corresponding to the momentum transfer direction $\pm k_{\text{eff}}$. Its contributions include gravitational acceleration $\phi^{\text{acc}} = k_{\text{eff}} a T^2$, with a the relative mirror-atom acceleration, T the free-fall time. The term $-\alpha T^2$ is added when the frequency chirp compensates for gravity in 1g. Other terms participate in the total interferometer phase : the phase shift due to vibrations $\phi^{\text{vib}} = \int f(t)a(t)dt$ with f the response function of

the interferometer, the laser phase ϕ^{las}, the systematic effects ϕ^{sys}, and a phase related to the potential equivalence principle violation $\phi^{\text{WEP}_{K;Rb}} = k_{\text{eff}_{K;Rb}}(a_{K;Rb} - a)T^2$ for either atomic species.

During parabolic flight in standard gravity, the measurement is performed in single diffraction with only one output port. In weightlessness, the measurement is performed in the Double Single Diffraction (DSD) regime described in section 4.1.2, by selecting the Raman detuning δ^{RF} near the half-maximum—simultaneously selecting two symmetric velocity classes with opposite signs[1]. The two symmetric interferometers of opposite area sum up to yield the output signal for a specific internal state :

$$P_{\text{DSD}} = P^+ + P^- = 2P_0 - C\cos(\Sigma\Phi)\cos(\Delta\Phi) \tag{5.26}$$

This signal is a product of two cosine terms: one involving the half-sum $\Sigma\Phi = \frac{1}{2}(\Phi^+ + \Phi^-)$, which includes only non-inertial contributions and direction-independent systematics; the other with the half-difference $\Delta\Phi = \frac{1}{2}(\Phi^+ - \Phi^-)$, which includes all inertial contributions, such as gravitational effects and direction-dependent systematics. The advantage of this setup is that it effectively separates non-inertial and inertial contributions, allowing for the maximization of fringe contrast $2C\cos(\Sigma\Phi)$ and scanning of fringes through the inertially sensitive phase $\Delta\Phi$. Consequently, the DSD interferometer simultaneously rejects direction-independent systematics during each experiment shot, leading to a significantly reduced systematic phase shift per shot compared to the single-diffraction configuration. The same systematics are rejected by using the k-reversal technique described in Chapter 3.

Onboard the aircraft, the dominant source of interferometer phase noise is caused by vibrations of the reference mirror, which serves as the inertial phase reference for both ^{87}Rb and ^{39}K sensors. Hence, the atomic signal caused by its motion is indistinguishable from motion of the atoms. To make this distinction, we use the FRAC method described in 3.2.4 by measuring the mirror motion with a mechanical accelerometer from which we compute the vibration-induced phase (ϕ^{vib}) and correlate it with the normalized output population of each species. Furthermore, since the two pairs of Raman beams follow the same optical pathway and operate simultaneously, the vibration noise is common mode and can be highly suppressed from the differential phase between interference fringes.

Results and discussion

Several datasets are taken for different interrogation times. For each output of the interferometers, interference fringes can be reconstructed in 0g and 1g and the differential phase can be extracted using the differential FRAC method. The relative acceleration between potassium and rubidium atoms is determined by correcting the relative FRAC phase shift for systematic effects (see Methods of [[15]]), resulting in the isolation of the differential phase attributable to a potential WEP violation:

$$\phi_d^{WEP} = \phi_K^{WEP} - \kappa\phi_{Rb}^{WEP} = k^{eff,K}T^2(a_K - a_{Rb}) \tag{5.27}$$

Here, κ is the ratio of interferometer scale factors when T is much larger than the Raman pulse durations. The Eötvös parameter (η) is then obtained from

$$\eta = \frac{\phi_d^{WEP}}{k_{eff,K}a^{\text{eff}}T_K^2} \tag{5.28}$$

where a^{eff} is the average projection of the gravitational acceleration vector $\vec{a}$ along the z-axis during the measurements. This acceleration is not exactly equal to g because of the rotations of the plane during the microgravity phase.

[1] During microgravity phases, the frequency chirp is disabled

An Eötvös parameter of $\eta_{1g} = (-0.5 \pm 1.1) \times 10^{-3}$ is measured during steady flight. This sensitivity is limited by the interrogation time in the interferometer in standard gravity. The uncertainty is a combination of statistical ($\delta\eta_{\text{stat,1g}} = 4.9 \times 10^{-5}$) and systematic ($\delta\eta_{\text{sys,1g}} = 1.1 \times 10^{-3}$) errors, primarily due to direction-independent phase shifts from the quadratic Zeeman effect. Because we don't use the k-reversal technique, these systematic effects are not compensated. Similarly, thanks to the microgravity regime, a sensitivity of $\eta_{0g} = (0.9 \pm 3.0) \times 10^{-4}$ is obtained, with statistical ($\delta\eta_{\text{stat0g}} = 1.9 \times 10^{-4}$) and systematic ($\delta\eta_{\text{sys0g}} = 2.3 \times 10^{-4}$) errors. The systematic uncertainty in microgravity improved significantly, roughly by a factor of 5 compared to measurements in standard gravity, due to the reduced sensitivity of the DSD interferometer to direction-independent systematic effects. Both measurements are consistent with $\eta = 0$.

The main limitations of this measurement are linked to the high levels of vibrations and rotations due to aircraft motion effects. Mirror vibrations induce interference contrast loss due to Doppler shifts, necessitating strict confinement within the spectral width of Raman transitions. During parabolic maneuvers, the aircraft's rotation leads to contrast loss, which can be addressed by counter-rotating the retro-reflection mirror, as investigated by my predecessor R. Arguel in [[7]], or by employing ultra-cold atoms.

5.2.2 WEP test in standard gravity and study of the systematic errors

This paragraph presents the results of a WEP test performed under standard gravity conditions in our laboratory published in [[14]].

Experimental sequence for the dual-species interferometer

On ground, the experimental sequence for testing the WEP consists in performing the single-diffraction interferometer when using the k-reversal technique. The principle of the measurement is to obtain the Eötvös parameter

$$\eta = \frac{a_K - a_{Rb}}{g} \tag{5.29}$$

where a_S is the gravitational acceleration of species S (Rb, K) relative to the reference frame defined by the retro-reflection mirror, and g is the known local gravitational acceleration. The output of each atom interferometer is a sinusoidal fringe pattern:

$$P_S^{\pm} = Y_S^{\pm} - \frac{C_S^{\pm}}{2} \cos(\Phi_S^{\pm}) \tag{5.30}$$

where $+$ (resp. $-$) represents momentum transfer in the forward (resp. backward) z-direction. The fringe parameters Y_S and C_S are the offset and contrast, and the phase shift $\Phi_S^{\pm}$ includes the inertial phase, a control phase from the Raman laser, a deterministic phase shift from mirror vibrations, and systematic effects. The effective interrogation time T_{eff} is identical for both species. It can be shown that for a square Raman pulse with Rabi frequency Ω_{eff} a $\pi/2$ pulse au duration τ, it is given by[[31]]:

$$T_{eff}^2 = \int f(t)dt = (T + 2\tau) \left[T + \frac{2}{\Omega_{eff}} \tan\left(\frac{\Omega_{eff}\tau}{2} \right) \right] \tag{5.31}$$

With $f(t)$ the atom interferometer response function. The ratio of interferometer scale factors is $\kappa = \frac{k_K}{k_{Rb}} \approx 1.017657$.

The k-reversal technique is used to simultaneously scan the chirp for the K and Rb interferometers, helping reject non-inertial systematic effects. The accelerometer data is recorded and used for post-correction of vibrational motion using FRAC method.

Results analysis

- **FRAC method**

  For short interrogation times, the differential FRAC method can be applied to extract the differential phase. The chirp frequency α_S is adjusted for each species and a vibration phase correction is applied:

$$\tilde{\alpha}_S = \alpha_S + \tilde{\phi}_S^{\text{vib}}/T_{\text{eff}}^2 \tag{5.32}$$

  where $\tilde{\phi}_S^{\text{vib}}$ estimates the vibration phase. Fringes are reconstructed shot-to-shot using $\tilde{\alpha}_S$. The central fringe is found by varying T and locating the common dark fringe, and the corresponding chirp rates $\alpha_{\pm S}$ is extracted :

$$\alpha_S^{\pm} = \pm k_S a_S + \frac{\phi_S^{\pm,\text{sys}}}{T_{eff}^2} \tag{5.33}$$

  One can then estimate the value η^{raw}:

$$\eta^{\text{raw}} = \eta + \eta^{\text{sys}} = \frac{1}{g}\left[\frac{\alpha_K^+ - \alpha_K^-}{2k_K} - \frac{\alpha_{Rb}^+ - \alpha_{\text{Rb}}^-}{2k_{\text{Rb}}}\right] \tag{5.34}$$

  With this method, statistical uncertainties yield $\delta\eta^{\text{raw}} \approx 3\times10^{-7}$ for a 20 ms interrogation time T for each measurement of the Eötvös parameter. This performance is limited by the signal-to-noise ratio (SNR), primarily for ^{39}K that operates with at least 5-times fewer atoms.

  The differential FRAC method intrinsically correlates the two atomic sensors as a consequence of using a single source of information, the mechanical accelerometer, to reconstruct the two interference fringe. We reach a long-term sensitivity associated with a statistical uncertainty of $\delta\eta^{\text{raw}} = 7.8\times10^{-8}$ after 24000 s of integration time.

- **Bayesian method**

  Here we perform the method described in section 5.1.2 on the same dataset. The differential phase $\phi_d^{\pm}$ is calculated as $\phi_K^{\pm} - \kappa\phi_{Rb}^{\pm}$, where κ is the scale factor ratio. The differential inertial phase, known laser phase, and differential systematic phase $\phi_d^{\pm,sys}$ are the components of $\phi_d^{\pm}$. The phase linked to vibrations is canceled in ϕ_d, because the same timings are used for both interferometers. By computing the half-difference $\phi_d = \frac{1}{2}(\phi_d^+ - \phi_d^-)$, direction-independent systematics are removed, and the Eötvös parameter η_{raw} is computed as :

$$\eta_{\text{raw}} = \frac{\phi_d}{k_K g T_{\text{eff}}^2} \tag{5.35}$$

  To estimate $\phi_d^{\pm}$, Bayesian analysis is employed, marginalizing over the likelihood distribution for $n^{\pm\kappa}$ and $n_{Rb}^{\pm}$, which both implicitly depend on the common phase ϕ_c. As $\kappa \neq 1$, the algorithm requires an approximate range for ϕ_c to estimate $\phi_d^{\pm}$. This phase range is determined by considering the sum of the laser phase ($\alpha_{Rb}^{\pm}T_{eff}^2$) and the vibration phase ($\tilde{\phi}_{Rb}^{\text{vib}}$) estimated from the mechanical accelerometer. Accurate noise parameter estimates for each interferometer are also necessary. A single-measurement uncertainty of $\delta\phi_d^{\pm} \approx 33$ mrad is achieved for each momentum transfer direction, corresponding to $\delta\eta_{\text{raw}} \approx 3.7\times10^{-7}$ for an interrogation time of $T = 20$ ms. When integrating the data on longer measurement times, the measured sensitivities at long term are consistent within their respective uncertainties with those obtained using the differential FRAC method.

Systematic effects

When performing a WEP test, it is necessary to have an extensive knowledge of the systematic effects that affect the measurement. Table 5.2 presents the contributions of all the systematics studied in this work.

Systematic effect	$\eta(\times 10^{-6})$	$\delta\eta(\times 10^{-6})$
Wavefront aberration	0.00	1.21
2nd-Order Zeeman	-1.44	0.69
AI asymmetry	1.05	0.56
Beam misalignment	3.92	0.42
Parasitic lines	6.11	0.19
Two-photon light shift	0.15	0.14
One-photon light shift	< 0.01	0.06
Wavefront curvature	0.14	0.02
Coriolis force	0.03	< 0.01
Magnetic force	-0.06	< 0.01
Gravity gradient	< 0.01	< 0.01
Total systematics	9.90	1.58
Raw measurement	10.79	0.08
Final measurement	0.89	1.58

Table 5.2: Contributions of systematic effects to the measurement.

- **Second-order Zeeman effect**
  Despite the absence of a 1st-order Zeeman shift, the most substantial contribution to the measurement of η is the 2nd-order Zeeman effect. In the presence of a spatial gradient ∇B, atoms following the two trajectories associated with $\pm k_S$ experience slightly different magnetic fields, preventing the phase shift to be perfectly canceled out when reversing the direction of momentum transfer.

  The 2nd-order Zeeman shift for the clock transition $|F = 1, m_F = 0\rangle \rightarrow |F = 2, m_F = 0\rangle$ is represented by $\Delta\omega_{BS} = 2\pi K_S B^2$, where K_S is a constant that relies on Landé g-factors and the hyperfine ground-state splitting $\Delta\omega_S^{HS}$:

$$K_S = \frac{(g_J - g_I)^2 \mu_B^2}{\Delta\omega_S^{HS}} \tag{5.36}$$

  For ^{87}Rb, $\Delta\omega_{HFS}$ is about 575.15 Hz/G^2, and for ^{39}K, it is significantly higher: 8513.75 Hz/G^2. The phase shift on the atom interferometers due to the 2nd-order Zeeman effect is deduced from:

$$\phi^S_{\text{Zeeman}} = 2\pi K_S \int g_S(t)(B_S^{\pm}(t))^2 dt \tag{5.37}$$

  Here, $g_S(t)$ represents the sensitivity function, and $B_S^{\pm}(z(t))$ is the time-varying magnetic field experienced by species $S = Rb, K$ along the two center-of-mass trajectories associated with opposite momentum transfer. To evaluate this phase shift, the magnetic field profile is directly measured using simultaneous two-photon Raman spectroscopy with both species. The magnetic field profile is measured as a function of time-of-flight (TOF), and the Breit-Rabi equation is solved to obtain the magnetic field at each time.

  The field profiles during the interferometer, $B_S^{\pm}(z(t))$, are then determined from a model described in [[58]] by considering the shift in the center-of-mass position due to the photon recoil during the interferometer.

- **Parasitic lines**
  This systematic effect is present only in ^{87}Rb due to the use of an electro-optic phase modulator (PM) to generate the second Raman frequency. The PM generates a comb of laser lines with an electric field

$$E(t) = E_0 e^{i\omega_0 t} \sum_n i^n J_n(\beta) e^{in\Delta\omega t} \tag{5.38}$$

  where $J_n(\beta)$ is a Bessel function with modulation depth β, and the modulation frequency $\Delta\omega = 2\pi \times 6.834$ GHz is the hyperfine splitting in ^{87}Rb. These additional laser frequencies separated by the two-photon resonance that can diffract the atoms along parasitic trajectories which experience a different phase shift and close to form an interferometer. If these trajectories lie within the coherence length of the interference pattern, their phase shifts add a bias to the interferometer. Each nearest-neighbor pair of lines is simultaneously resonant with a counter-propagating Raman transition. The Raman coupling parameter associated with each pair of lines (one traveling upward and its conjugate traveling downward) is proportional to the product of their electric field amplitudes and inversely proportional to the detuning. As a result, the atoms see a spatially-varying Rabi frequency due to the interference between different coherent Raman transitions. The total phase shift due to parasitic laser lines in a three-pulse Mach-Zehnder interferometer is calculated using the relative intensity of parasitic lines and the relative position between the atoms and the mirror. The uncertainties on this shifts are constrained by our understanding of the initial velocity, the distance between atoms and the mirror, and the average Rabi frequency for each species.

- **Two-photon lightshift**
  The two-photon light shift (TPLS) is a velocity-dependent frequency shift affecting counter-propagating Raman transitions due to neighboring off-resonant transitions. It can be separated into two components: one from counter-propagating transitions and another from residual co-propagating transitions between specific atomic states.

$$\omega^{\pm,TPLSS}(t) = \omega_S^{\pm,counter}(t) + \omega_S^{\pm,co}(t) \tag{5.39}$$

  It can be shown[[51]] that these frequency shift correspond to :

$$\omega_S^{\pm,TPLS}(t) = \frac{1}{4}\left(\frac{(\Omega_S^{\text{eff}})^2}{2\omega_S^{\pm,D}} + \frac{(\Omega_S^{\text{eff}})^2}{2\omega_S^{\pm,D} + 4\omega_S^{\text{rec}}}\right) + \frac{(\Omega_S^{\text{co}})^2}{4(\omega_{DS}^{\pm} + \omega_S^{\text{rec}})} \tag{5.40}$$

  The phase shift due to TPLS is computed using the sensitivity function:

$$\phi_S^{\pm,\text{TPLS}} = \int g_S(t)\omega_S^{\pm,\text{TPLS}}(t)dt \tag{5.41}$$

  and assuming TPLS remains constant during Raman pulses, the phase shift can be expressed in terms of the effective Rabi frequencies during these pulses:

$$\phi_S^{\pm,\text{TPLS}} = \frac{\omega_{S,3}^{\pm,\text{TPLS}}}{\Omega_{S,3}^{\text{eff}}} \tan\left(\frac{\Omega_{S,3}^{\text{eff}}\tau}{2}\right) - \frac{\omega_{S,1}^{\pm,\text{TPLS}}}{\Omega_{S,1}^{\text{eff}}} \tan\left(\frac{\Omega_{S,1}^{\text{eff}}\tau}{2}\right) \tag{5.42}$$

  where where $\Omega_{S,i}^{\text{eff}}$ the effective Rabi frequency during the i^{th} pulse.

- **One-photon lightshift**
  The one-photon light shift (OPLS), also called the differential AC Stark shift, is a shift between ground states due to far off-resonant Raman beams. The shift depends on the optical intensity and detuning from each excited state, and the total OPLS is a sum of shifts from each optical field. For rubidium, the OPLS can be suppressed by adjusting the

intensity ratio between two beams, because we meet the condition that the large detuning $\Delta < \omega^{HF}$. For potassium, this condition cannot be met because of the low clock frequency, the OPLS has to be taken into consideration. The Mach-Zehnder interferometer geometry primarily detects variations in OPLS. Measurement of OPLS is done by performing a comprehensive range of spectra obtained by varying laser intensities and free-fall durations. It enables us to derive the frequency shifts occurring during each instance of the interferometer. We then estimate the phase shift due to the OPLS using the sensitivity function :

$$\phi_S^{\mathrm{OPLS}} = \frac{\omega_{S,3}^{\mathrm{OPLS}}}{\Omega_{S,3}^{\mathrm{eff}}} \tan\left(\frac{\Omega_{S,3}^{\mathrm{eff}}\tau}{2}\right) - \frac{\omega_{S,3}^{\mathrm{OPLS}}}{\Omega_{S,3}^{\mathrm{eff}}} \tan\left(\frac{\Omega_{S,1}^{\mathrm{eff}}\tau}{2}\right) \tag{5.43}$$

where $\omega_{S,i}^{\mathrm{OPLS}}$ is the frequency shift of the counter-propagating resonance during the i^{th} Raman pulse. This phase shift is canceled out in both momentum directions using the k-reversal method, but it's not perfect due to fluctuations in laser intensity, atom cloud size, and temperature.

- **Wavefront aberration and curvature**
  Imperfections in the optics along the Raman beams introduce phase distortions due to wavefront curvature (WC) and wavefront aberrations (WA). These phase distortions result in systematic shifts in the interferometer measurements. The WC-induced phase shifts are related to the divergence of the Raman beams :

  $$\phi^{\pm,\mathrm{WCS}} = \pm k_S \frac{(\sigma_{\mathrm{vel},S} T_S)^2}{R_S} \tag{5.44}$$

  Wavefront aberrations are challenging to measure precisely but are estimated by measuring the wavefront profile using a Shack-Hartmann analyzer. In this study, the wavefront imperfections were smaller than the precision of the wavefront sensor used for the measurment : we estimate a maximum value for the aberration.

- **Coriolis force**
  When atoms possess an initial velocity orthogonal to the Raman beam (in the plane of the interferometer), the rotations causes the interferometer arms to enclose a spatial area. In our case , this phase shift is due to the Coriolis effect caused by Earth's rotation and introduces a bias for each species. This Coriolis effect-induced bias can be expressed as :

  $$\phi_S^{\pm,\mathrm{Cor}} = \pm k_S a_{\mathrm{Cor}} T^2, \tag{5.45}$$

  and is determined by the atom's transverse velocity, the Coriolis acceleration $a_{\mathrm{Cor}} = 2v \times \Omega$ (with v the atomic velocity and Ω the rotation rate), and the angle between the rotation vector and the x-axis.

- **Gravity gradient**
  The gravity gradient can introduce a phase shift in the atom interferometer due to the modification of the atom's free-fall trajectory compared to a parabolic path.

  In this case, the phase shift is proportional to the wavevector magnitude and is not eliminated by the k-reversal technique. However, for the relatively short interrogation times used in the experiment, the gravity gradient-induced phase shifts are negligible, and their uncertainties are mainly associated with initial cloud position and velocity knowledge errors. Nonetheless, for longer interrogation times, these effects can become significant, and a technique involving modifications to the k-vector during the π-pulse has been proposed to cancel out this phase shift[[88]].

- **AI asymmetry**
  In the atom interferometer, the effective Rabi frequency decreases over time due to the cloud expansion, with a specific effect on Rb because of spatial modulation of the effective Rabi frequency caused by parasitic lines. When there exists an imbalance in the Rabi frequencies during the 1st and 3rd Raman pulses ($\Omega_{S,1}^{eff}$ and $\Omega_{S,3}^{eff}$), an asymmetry in the interferometer occurs, leading to velocity-dependent terms.

$$\phi_S^{\pm,\text{asym}} = \mp k_S \Delta v_S^{\pm} \left[1 - \frac{\Omega_{S,3}^{\text{eff}}}{\Omega_{S,1}^{\text{eff}}} \tan(\Omega_{S,3}^{\text{eff}} \tau^2) \right] \tag{5.46}$$

  This velocity shift ($\Delta v_S^{\pm}$) can result from factors like the two-photon light shift and the velocity-selectivity of the detection system. The estimation of this phase shift is also limited by uncertainties in initial velocity, atom-mirror distance, and mean Rabi frequency.

This study reveals that the main limitations arise from potassium, which exhibits significant systematic effects as well as lower contrasts compared to rubidium. The key result lies in the fact that, thanks to a strong correlation between the two species, the systematic effects have been thoroughly identified and quantified.

This study on systematic effects results in a final measurement of the Eötvös parameter: $\eta = 0.9(1.6)^{\text{sys}}(0.078)^{\text{stat}} \times 10^{-6}$, which is primarily limited by the short interrogation times reachable in standard gravity. The systematic effects also limit this measurement but have been well quantified. The use of ultra-cold atoms has the potential to significantly reduce the contributions of several of the aforementioned systematics. For instance, due to the smaller spatial expansion of an ultra-cold atomic cloud, the uncertainty on the position and velocity can be reduced. The impact of wavefront aberrations can be decreased for low spatial frequency aberrations. Performing the interferometer in the double-diffraction regime may further reduce some systematic errors, as the atoms undergo the same internal transitions along both paths, potentially mitigating the effects of two-photon light shifts (TPLS) and one-photon light shifts (OPLS).

5.3 Strategy for a test on the simulator

Taking advantage of the high repetition and long cumulative microgravity times on our simulator, a WEP test using thermal samples of rubidium and potassium will be performed in the near future. The performance demonstrated in section 4.2 coupled the Bayesian analysis, opens the way for a state-of-the-art test of the WEP.

To evaluate our ability to extract the differential phase from experimental data for long interrogation times, I performed a simulation in the form of equation 5.13. By adding offset and phase noise at a level similar to the expected experimental conditions, I study the convergence of the Bayesian method and the error on the estimated differential phase under several parameters. In this simulation, the offset noise contains both the offset and amplitude noise : the contrast loss is also contained in this parameter. A typical value for the offset noise can be derived from the BAT results obtained in section 4. In this context, an optimistic SNR of 100 is assumed, with $\sigma_{\text{off}} = 0.01$. However, further investigations will be conducted to assess the impact of this parameter. The method employed to estimate the noise in the differential phase is detailed in [[14]], Appendix C. For this analysis, I have adopted a value of $\sigma_{\phi_d} = 50$ mrad, which aligns with previous measurements conducted on the ICE experiment.

We consider two cases for the scale factor ratio: $\kappa = 1$ corresponding to the case where the scale factors of the two interferometers are made equal, and $\kappa = 1.018$ corresponding to a WEP test with Rb and K and the same interrogation time for both species $T_{Rb} = T_K$. The simulated

data set is generated from common phases chosen randomly within a specific scanned phase range. This range corresponds to the phase scanned by the vibrations of the simulator during the interferometer operation. To fully benefit from the microgravity phase provided by our simulator, we can perform an interferometer with an interrogation time of up to $2T = 380$ ms. The corresponding phase range can be found in section 4: $[-150; +150]$ rad, accounting for the simulator's vibration levels. This interrogation is a long term goal for the test of the WEP on the simulator. When using cold rubidium atoms on the simulator, we have demonstrated optimal sensitivity for $2T = 200$ ms, corresponding to a phase scan within the range of $[-50, +50]$ rad. In this analysis, I examine both this more realistic scenario for an imminent test and the maximum interrogation time achievable on this platform.

5.3.1 Case $\kappa = 1$

We first apply the method to a case where the interrogation times T_{Rb} and T_K are tuned so that the scale factor $\kappa = 1$.The main drawback of this configuration is that, since the interrogation times are not equal, the interferometers do not experience the same accelerations throughout the interferometric sequence. This discrepancy leads to higher differential phase noise caused by vibrations.

This case corresponds also to the use of two spatially separated interferometers as a gradiometer, with only one species involved. In this particular situation, the differential phase noise σ_{ϕ_d} is considered to be 0 which makes the method even more robust to a large phase scan and thus long interrogation times.

Figure 5.4(a) presents the simulated experimental data points as black dots. The red curve corresponds to the Lissajous curve for a given differential phase ϕ_d computed over the phase scan range from equations 5.11 in the ideal case (no noises). Here, the chosen scanned phase range is $[-150; +150]$ rad, which represents the maximum phase range for our experiment. The Lissajous curve forms an ellipse, and the differential phase can be retrieved using an ellipse-fitting technique. However, we apply the Bayesian method to this simulated dataset to demonstrate the method's high robustness.

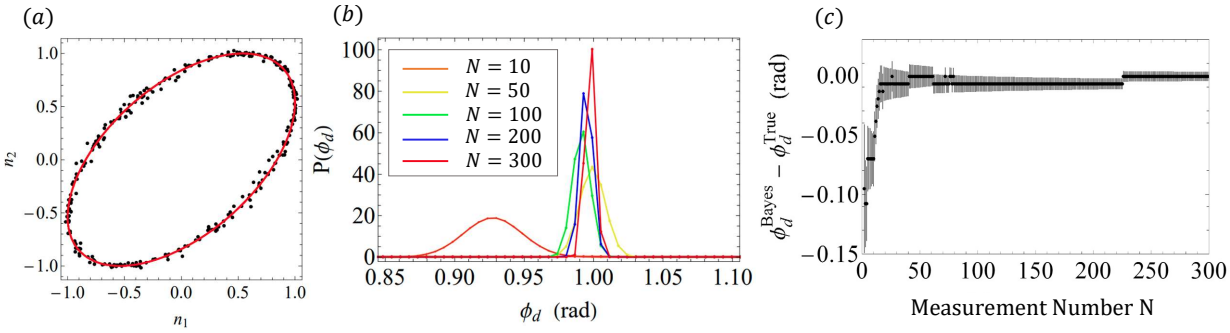

Figure 5.4: ***Bayesian method on simulated data for*** $\kappa = 1$ *- (a) The black dots correspond to 300 simulated data points, with a common phase range randomly chosen in* $[-150; +150]$ *rad, a differential phase noise* $\sigma_{\phi_d} = 50$ *mrad, and a differential phase* $\phi_d = 1$ *rad. The red curve represents the parametric curve of* n_1 *and* n_2 *without the noise contribution.(b) Probability distributions for several measurement numbers, N. The width of the probability distribution is here limited by the resolution of the* ϕ_d *vector (c) Error on the estimate as a function of the number of measurements. After N=100, the error is less than 10 mrad, and becomes less than 5 mrad for* $N > 250$.

We consider varying numbers of measurement points, N, ranging from 1 to 300. For each mea-

surement number, the algorithm updates the probability distribution that reaches its maximum value for the Bayesian estimate $\phi_d^{\text{Bayes}}(N)$, as shown in Figure 5.4(b). The error on this value $\phi_d^{\text{Bayes}}(N) - \phi_d^{\text{True}}(N)$ is a bias that leads to a systematic error on the WEP. To this value, we can associate a standard deviation, $\delta\phi_d^{\text{Bayes}}(N)$, linked to the width of the distribution. This uncertainty leads to statistical error on η. It is to be noted that the resolution of the probability distribution is a parameter of the simulation, that limits the estimate. In this section, we use a 6 mrad resolution to avoid having too long computation times. As depicted in Figure 5.4 (d), we can study the convergence by plotting the bias on the estimate, $\phi_d^{\text{Bayes}}(N) - \phi_d^{\text{True}}(N)$, along with their respective uncertainty (width of the probability distribution), $\delta\phi_d^{\text{Bayes}}(N)$.

This process can then be repeated M times to study the statistical and systematic errors of the method. The statistical error for each measurement is calculated as the average of $\delta\phi_d^{\text{Bayes}}(N)$ over all M samples, denoted as $\epsilon_{\text{stat}}^d = \langle\delta\phi_d^{\text{Bayes}}(N)\rangle$. Similarly, the systematic error is defined as $\epsilon_{\phi_d}^{\text{sys}}(N) = \langle|\phi_d^{\text{Bayes}}(N) - \phi_d^{\text{True}}(N)|\rangle$. The results are presented in figure 5.5.

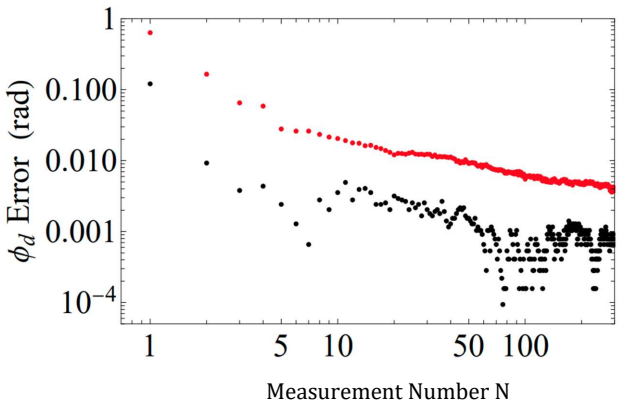

Figure 5.5: ***Statistical and systematic error in the Bayesian phase estimator as a function of the number of measurements N for*** $\kappa = 1$ *- The differential phase* $\phi_d^{True} = 1$ *rad and* $M = 50$ *are used. Red dots represent the statistical uncertainty* $\epsilon_{stat}^d(n)$ *and black dots indicate the systematic error* $\epsilon_{\phi_d}^{sys}(N)$

For this configuration, a large span is not a problem because the two atomic scale factors are the same $\kappa = 1$ and the Lissajous figure is an ellipse. The Bayesian method always applies despite the strong vibration levels and high phase and offset noises. Consequently, Figure 5.5 shows that the algorithm finds the good differential phase with a statistical error better than 10 mrad (1.8×10^{-9}) and a systematic error below 1 mrad (0.2×10^{-9}).

5.3.2 Case $\kappa = 1.018$

In the case where $T_{Rb} = T_K$, the Lissajous curves described by the data are not elliptical anymore, as seen in Figures 5.6.
The first row corresponds to a scanned phase range of $[-150; +150]$ rad, (estimated phase scanned for an interrogation time $2T = 380$ ms), and the second row depicts a situation where the phase span is reduced to $[-50; +50]$ rad (estimated phase scanned for an interrogation time $2T = 200$ ms). Because of the non unitary scale factor, a very high number of crossings in the curve arise from the large phase scans. In the case of Figure 5.6(c), the phase scan is smaller by a factor three, making the curve less messy. However, in both cases, ellipse-fitting methods

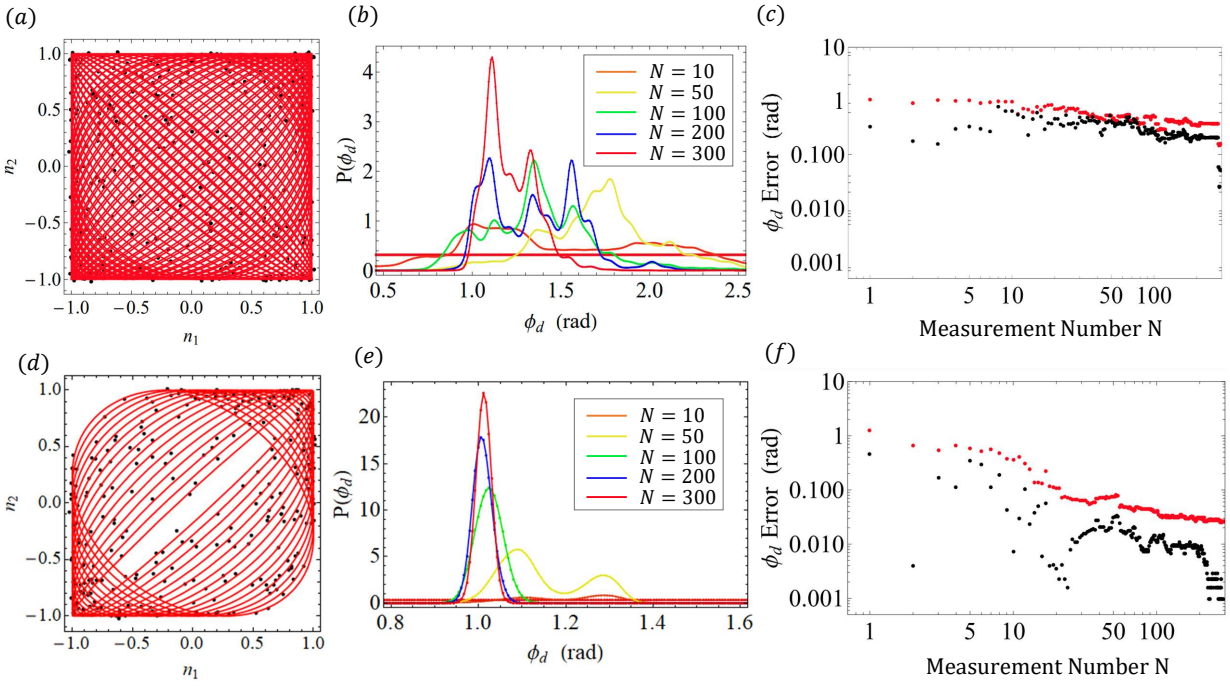

Figure 5.6: ***Bayesian simulations to extract the differential phase ϕ_d and errors on the estimation for two interrogation times*** *- for a scale factor $\kappa = 1.018$, a differential phase $\phi_d^{True} = 1$ rad and the noise model : $\sigma_{\Phi_d} = 50$ mrad, $\sigma_{off} = 0.01$ (a) Lissajous figure (red) and simulated data points (black) for a common phase range of [-150;+150] rad, corresponding to the level of vibrations on the 0g simulator and an interrogation time 2T=380 ms. (b) Probability distributions for several measurement numbers N with $\phi_c \in$[-150;+150] rad (c) Statistical uncertainty (red points) and systematic error (black points) in the Bayesian phase estimate for the scanned phase range of [-150;+150] rad, with M=10 trials (d) Lissajous figure (red) and simulated data points (black) for a scanned phase range of [-50;+50] rad, corresponding to the level of vibrations on the 0g simulator and an interrogation time 2T=200 ms. (e) Probability distributions for several measurement numbers N with $\phi_c \in$[-50;+50] rad (f) Statistical uncertainty (red points) and systematic error (black points) in the Bayesian phase estimate for the scanned phase range of [-50;+50] rad , with M=10 trials.*

seem unrealistic.

The second column of this figure illustrates the convergence of our Bayesian algorithm for estimating the differential phase. For the largest scanned phase range, the algorithm estimates the differential phase with a significant error of about 0.4 rad even for a large number of measurements. In this scenario, conducting the test of the WEP is not feasible.

The differential phase extraction can be retrieved if we reduce the scanned phase range by a factor 3, corresponding to an interrogation time of 2T=200 ms. In this case, we can reach a statistical error better than 30 mrad (1.9×10^{-8}) and a systematic error below 10 mrad (6.3×10^{-9}). This analysis can be performed for larger number of measurements N to have a possible decrease of the statistical error and perform a test with a sensitivity at the 10^{-9} order of magnitude.

5.3.3 Convergence of the algorithm as a function of the common phase range

We have seen that increasing the common phase scanned by the two species' interferometers makes it more difficult for the algorithm to converge with low bias and uncertainty. Here we test the algorithm for N= 300 simulated data points with a common phase randomly chosen in $[0;+\phi_c^{Right}]$, with ϕ_c^{Right} varying between 0 and 100 π rad, with 5π steps. The results are presented in Figure 5.7.

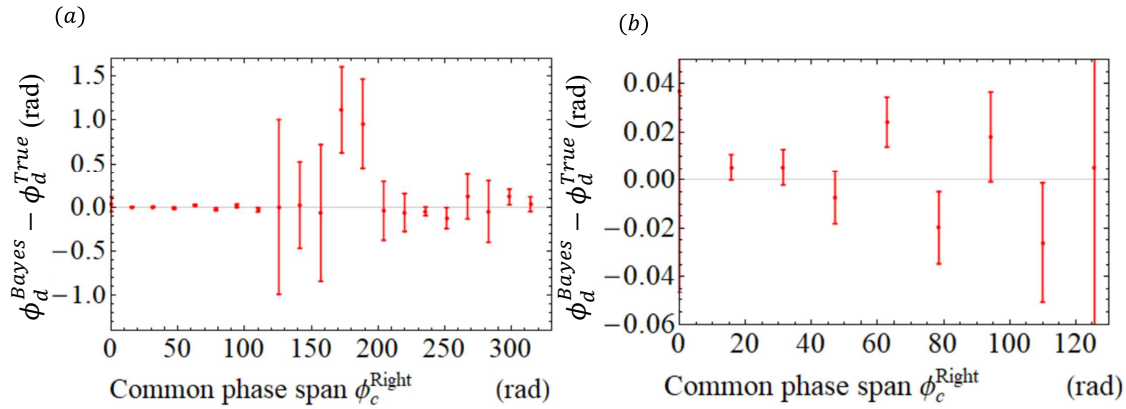

Figure 5.7: ***Error on the Bayesian estimate as a function of the common phase scanned by the simulated data*** *- The common phase is randomly chosen in* $[0;+\phi_c^{Right}]$*, with* ϕ_c^{Right} *varying between 0 and 100* π *rad, with* 5π *steps. The scale factor is* $\kappa = 1.018$*, the measurement number N is 300, the differential phase noise is 50 mrad, the offset noise is 0.01 and the true differential phase is 1 rad. The simulation is performed for one data set (M=1) (a)* ϕ_c^{Right} *is varied between 0 and* 100π *(b) Same results with a focus on the [0-35* π*] range. The dots correspond to a systematic error on the estimation and the error bars to the statistical error.*

To keep the bias and the uncertainty on the estimate below 50 mrad with the noise model considered here, the phase scan must remain under 100 rad. Increasing this phase span significantly affects the algorithm's ability to converge, resulting in a significant bias and a wide probability distribution.

5.3.4 Impact of the phase noise

The noise model provided to the Bayesian algorithm is based on typical experimental data obtained from our experiment. Here we study the convergence of the algorithm for different values of this phase noise.
The simulation are conducted with 300 measurement points, one trail (M=1), a common phase span of 100 rad, and an offset noise of $\sigma_b = 0.01$ rad.

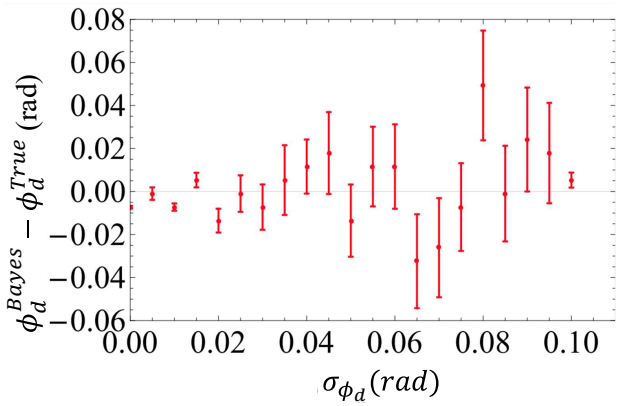

Figure 5.8: ***Error on the Bayesian estimate as a function of the differential phase noise*** *- The differential phase noise is scanned between 0 and 0.1 rad. The scale factor is $\kappa = 1.018$, the measurement number N is 300, the common phase scanned is [-50; +50] rad, the offset noise is 0.01 rad and the differential phase is 1 rad.*

Figure 5.8 illustrates the results of a phase noise scan ranging from 0 to 0.1 rad. For each phase noise level, the final estimate (systematic error) is plotted along with the standard deviation of the final probability density (statistical error). It is observed that for a phase noise level below 0.06 rad, the estimation error remains under 20 mrad. Even for higher phase noise, the error remains below 100 mrad, providing confidence in the feasibility of a WEP test using this method.

The same study will be performed to estimate the influence of the offset noise σ_b, that corresponds to the SNR of our fringes.

5.3.5 Importance of the knowledge of the phase scan

The scanning of the phase common to both intrefrometers represents a crucial input parameter for the algorithm, especially in the case of a scale factor ratio $\kappa = 1.018$. It is essential to quantify the necessary knowledge of the phase span for this method, which in turn sets the requirements for the classical accelerometer.
We can assess the algorithm's ability to converge when there is uncertainty in our knowledge of the scanning phase range. Figure 5.9 displays the simulation results when we introduce uncertainty into our knowledge of the scanning phase range for different scale factor ratios. To do so, we simulate N=300 experimental points with a common phase randomly chosen between -50 rad and +50 rad (conditions of a 2T=200 ms interrogation time on the simulator), and the noise model parameters are $\sigma_b = 10$ mrad and $\sigma_{\phi_d} = 50$ mrad. To emulate an error on the phase scan that would be due to a bias of the mechanical accelerometer, the phase scan given as an input parameter to the Bayesian algorithm is $\phi_c^{\text{Est}} \in [-50; 50 + \phi_{c,\text{Right}}]$, with $\phi_{c,\text{Right}}$ corresponding to the error on the common phase, scanned between -5π and $+5\pi$.

For $\kappa = 1.018$, it appears that the bias and uncertainty remain under 50 mrad if the phase scan is known at about $\pm 2\pi$.

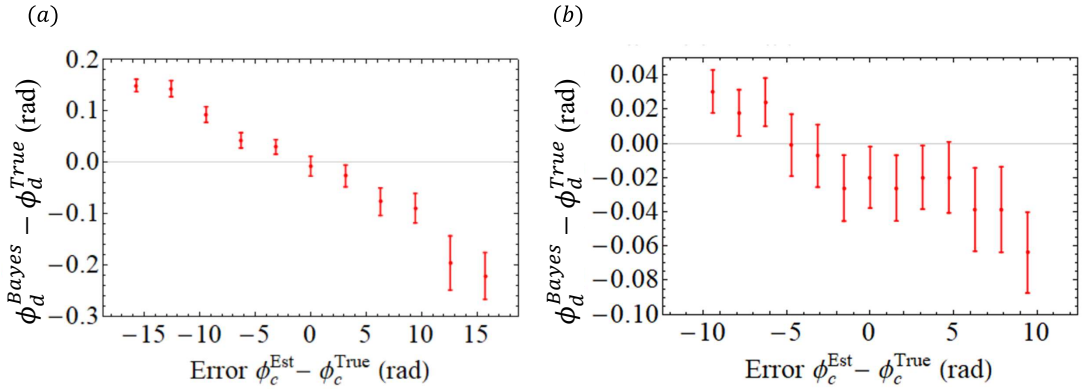

Figure 5.9: ***Error on the Bayesian estimate as a function of the unknown part of the scanning phase range*** *- The final error on the estimate and the width of the final probability distribution of the differential phase for N=300 simulated measurements, M=1 trial are plotted. The common phase is randomly chosen for each measurement point in the interval* $\phi_c^{True} \in [-50; 50]$*. The input parameter given to the Bayesian algorithm for the phase span is* $\phi_c^{Est} \in [-50; 50+\phi_{c,Right}]$*, with* $\phi_{c,Right}$ *corresponding to the error on the common phase, scanned between (a)* -5π *and* $+5\pi$ *with* π *steps. The graph in (b) presents another simulation under the exact same conditions with the error scanned between* -3π *and* $+3\pi$ *with* $\pi/2$ *steps. The noise model parameters are* $\sigma_b = 10$ *mrad and* $\sigma_{\phi_d} = 50$ *mrad and the scale factor is* $\kappa = 1.018$*.*

For $\kappa = 1$, similar simulations show a bias in the estimate of about 6 mrad and an uncertainty of less than 10 mrad, regardless of the error in the phase range. The phase resolution of the probability distribution in the simulation is 6 mrad, which explains the bias on the estimation.

Conclusion

In this section, we have presented previous results of the ICE experiment that have led to the very first WEP test using cold atoms in microgravity. On ground, we have demonstrated our ability to evaluate all the systematic effects, which is essential for such a test.

The Bayesian analysis presented in this final chapter sets the stage for a Weak Equivalence Principle (WEP) test with $\delta\eta \approx 10^{-10}$.

With our current experimental setup and thermal atoms, we've demonstrated that we can perform interferometry with a reasonable SNR for interrogation times up to $2T = 200\,\text{ms}$. Using the Bayesian method, we can accurately determine the differential phase between the two correlated interferometers with a bias of less than 30 mrad and an uncertainty better than 10 mrad, with just 300 measurements (equivalent to approximately one hour of measurements on our simulator). This translates to $\delta\eta^{\text{sys}} = 1.9 \times 10^{-8}\,\text{g}$ and $\delta\eta^{\text{stat}} = 6.3 \times 10^{-9}\,\text{g}$.
Increasing the number of measurements to $N = 1000$, for example, could potentially improve these values by more than a factor of two, based on the interpolation of the results presented in this chapter. The long-term stability of our experiment renders it entirely feasible.

The interrogation time is primarily limited by the temperature of the atoms, which makes them sensitive to rotations. By using ultra-cold atoms in this setup, we can achieve interrogation times up to $2T = 380\,\text{ms}$, limited by our microgravity platform. However, in this scenario,

we have observed that the Bayesian method struggles to converge due to the large common phase scanned by the interferometers. One solution is to dampen the vibrations of the reference mirror to reduce this phase scan to a smaller range. If we expect a threefold reduction in the phase span, we can achieve the same bias and uncertainty in the differential phase as previously presented. For this interrogation time, it results in $\delta\eta^{\mathrm{sys}} = 5.2 \times 10^{-9}$ and $\delta\eta^{\mathrm{stat}} = 1.7 \times 10^{-9}$. Further increasing the number of measurements would allow us to surpass the 10^{-10} threshold on the Eötvös parameter.

Conclusion

The work presented in this thesis is the result of three years of collective effort by the ICE team, aimed at advancing our understanding of ultra-cold source production and interferometry in microgravity. In the context of preparing for future space missions to test the Weak Equivalence Principle (WEP) and the pathfinder missions preceding them, our demonstrator serves as a valuable tool. Our results have achieved a state-of-the-art status by producing ultra-cold atoms using all-optical evaporative cooling in microgravity and conducting extended time-of-flight experiments with an atom accelerometer.

The experimental setup presented in the first chapter is versatile, designed for both laboratory operations and use aboard the Zero G aircraft. It facilitates the creation of ultra-cold sources of rubidium and potassium, as well as dual-species atom interferometry. The all-fibered architecture adds robustness and transportability, a significant challenge for a precision measurement experiment.
The second chapter has allowed me to present novel findings related to the production of rubidium and potassium sources. Achieving the first ultra-cold rubidium sources in the challenging environment of the Zero G plane represents a remarkable feat, showcasing the lowest temperatures attained through all-optical evaporation in microgravity.
The chapters on our interferometer present a comprehensive exploration of acceleration measurements using cold and ultra-cold atoms in both standard gravity and the microgravity regime. Results obtained with cold sources on our unique microgravity simulator, along with a thorough investigation of the double diffraction regime using ultra-cold atoms, pave the way for highly sensitive measurements.
The final chapter of this manuscript outlines the prospect of extending these interferometry capabilities to two atomic species. We have demonstrated in-depth understanding of the systematic effects affecting our correlated dual-species interferometer. Conducting ultra-cold atom dual-species interferometry on our simulator will enable us to perform a WEP test at better than 10^{-10}, a significant achievement for the ICE project and the culmination of the efforts of generations of researchers involved in this project.

Looking ahead, several areas will be explored using this apparatus. The top priority is implementing servo-locking of the dipole trap beam to enhance the quality of ultra-cold sources in microgravity, both on the plane and the simulator. This improvement will allow for interferometry on the simulator, capitalizing on its high accessibility and repetition rate to extensively study the double diffraction regime—a key feature of the CARIOQA space mission. The work on loading and evaporating potassium in the dipole trap must continue to achieve interferometry in the double diffraction regime with this additional atomic species. Only then can we conduct the aforementioned WEP test, representing the ultimate goal of the ICE project and a significant accomplishment for the generations of PhD students, postdocs and the permanent researchers involved on this project.

However, the potential of our apparatus extends far beyond the WEP test. For instance, the Einstein Elevator and our knowledge of all-optical dipole traps open the door to the study of new

shapes of optical dipole traps. Geometries like BEC bubbles are of great interest due to their unique topological properties, and theoretical studies are already underway. Our transportable apparatus, alongside the Einstein Elevator, represents a unique tool for investigating the physics of ultra-cold atoms in microgravity.

Bibliography

[1] D. Aguilera et al. “STE-QUEST - Test of the Universality of Free Fall Using Cold Atom Interferometry”. In: *Classical and Quantum Gravity* 31.11 (June 2014), p. 115010. ISSN: 0264-9381, 1361-6382.

[2] H. Ahlers et al. *STE-QUEST: Space Time Explorer and QUantum Equivalence principle Space Test*. 2022.

[3] H. Ammann and N. Christensen. “Delta Kick Cooling: A New Method for Cooling Atoms”. In: *Physical Review Letters* 78.11 (Mar. 1997), pp. 2088–2091.

[4] M. H. Anderson et al. “Observation of Bose-Einstein Condensation in a Dilute Atomic Vapor”. In: *Science* 269.5221 (July 1995), pp. 198–201.

[5] L. Antoni-Micollier et al. “Generation of high-purity, low-temperature samples of 39K for applications in metrology”. In: *Physical Review A* 96.2 (Aug. 2017), p. 023608. ISSN: 2469-9926, 2469-9934.

[6] L. Antoni-Micollier. “Interféromètre à atomes froids de 39K et 87Rb pour tester le principe d’équivalence en micropesanteur”. PhD thesis. Université de Bordeaux, 2016.

[7] R. Arguel. “Interféromètre à ondes de matière ultra-froides pour le test du principe d’équivalence faible en micropesanteur”. Thèse de doctorat dirigée par Bouyer, Philippe et Battelier, Baptiste Lasers, Matière et Nanosciences Bordeaux 2022. PhD thesis. 2022.

[8] P. Asenbaum et al. “Atom-interferometric test of the equivalence principle at the 10 - 12 level”. In: *Physical Review Letters* 125.19 (Nov. 2020), p. 191101. ISSN: 0031-9007, 1079-7114.

[9] A. Aspect. *Einstein et les révolutions quantiques*. CNRS Editions/ De Vive Voix, 2019.

[10] D. C. Aveline et al. “Observation of Bose–Einstein condensates in an Earth-orbiting research lab”. en. In: *Nature* 582.7811 (June 2020), pp. 193–197. ISSN: 1476-4687.

[11] S. Bali et al. “Quantum-diffractive background gas collisions in atom-trap heating and loss”. In: *Physical Review A* 60.1 (July 1999), R29–R32.

[12] B. Barrett et al. “Correlative methods for dual-species quantum tests of the weak equivalence principle”. en. In: *New Journal of Physics* 17.8 (Aug. 2015), p. 085010. ISSN: 1367-2630.

[13] B. Barrett et al. “Dual Matter-Wave Inertial Sensors in Weightlessness”. In: *Nature Communications* 7 (2016), pp. 2041–1723.

[14] B. Barrett et al. “Testing the universality of free fall using correlated 39K–87Rb atom interferometers”. In: *AVS Quantum Science* 4.1 (2022), p. 014401.

[15] B. Barrett et al. “Dual matter-wave inertial sensors in weightlessness”. en. In: *Nature Communications* 7.1 (Dec. 2016), p. 13786. ISSN: 2041-1723.

[16] B. Barrett et al. “Mobile and remote inertial sensing with atom interferometers”. en. In: (2014), p. 64.

[17] B. Barrett et al. “Testing the Universality of Free Fall using correlated 39K-87Rb interferometers”. en. In: *arXiv:2110.13273 [gr-qc, physics:physics, physics:quant-ph]* (Oct. 2021).

[18] B. Battelier et al. “Exploring the Foundations of the Physical Universe with Space Tests of the Equivalence Principle”. en. In: *Experimental Astronomy* (2021).

[19] D. Becker et al. “Space-borne Bose-Einstein condensation for precision interferometry”. In: *Nature* 562.7727 (Oct. 2018), pp. 391–395. ISSN: 0028-0836, 1476-4687.

[20] D. Becker et al. “Space-borne Bose–Einstein condensation for precision interferometry”. In: *Nature* 562.7727 (2018), pp. 391–395. ISSN: 0028-0836.

[21] J. Bobroff. *Bienvenue dans la nouvelle révolution quantique : Ordinateur, cryptographie, Internet, spatial, etc. : pourquoi le xxie siècle sera quantique*. Flammarion, 2022.

[22] A. Bonnin et al. “Simultaneous dual-species matter-wave accelerometer”. In: *Phys. Rev. A* 88 (4 Oct. 2013), p. 043615.

[23] P. Bouyer et al. “Microwave signal generation with optical injection locking”. EN. In: *Optics Letters* 21.18 (Sept. 1996), pp. 1502–1504. ISSN: 1539-4794.

[24] J.-P. Brantut. “Manipulation d’atomes froids dans des potentiels lumineux”. fr. PhD thesis. Université Paris Sud - Paris XI, 2009.

[25] L. de Broglie. “Recherches sur la théorie des Quanta”. Theses. Migration - université en cours d’affectation, Nov. 1924.

[26] E. A. Burt et al. “Coherence, Correlations, and Collisions: What One Learns about Bose-Einstein Condensates from Their Decay”. In: *Phys. Rev. Lett.* 79 (3 July 1997), pp. 337–340.

[27] R. L. D. Campbell et al. “Efficient production of large ^{39}K Bose-Einstein condensates”. In: *Phys. Rev. A* 82 (6 Dec. 2010), p. 063611.

[28] O. Carraz et al. “Phase shift in an atom interferometer induced by the additional laser lines of a Raman laser generated by modulation”. en. In: *Physical Review A* 86.3 (Sept. 2012), p. 033605. ISSN: 1050-2947, 1094-1622.

[29] Y. Castin and R. Dum. “Bose-Einstein Condensates in Time Dependent Traps”. In: *Phys. Rev. Lett.* 77 (27 Dec. 1996), pp. 5315–5319.

[30] P. Cheinet. “Conception et réalisation d’un gravimètre à atomes froids”. fr. PhD thesis. Université Pierre et Marie Curie - Paris VI, 2006.

[31] P. Cheinet et al. “Measurement of the Sensitivity Function in a Time-Domain Atomic Interferometer”. In: *IEEE Transactions on Instrumentation and Measurement* 57.6 (June 2008), pp. 1141–1148. ISSN: 1557-9662.

[32] L. Chichet. “Interférométrie atomique embarquée double espèce, 87Rb et 39K, appliqué au test du principe d’équivalence faible et à la navigation inertielle”. fr. PhD thesis. Université de Bordeaux, 2017.

[33] S. Chu et al. “Three-dimensional viscous confinement and cooling of atoms by resonance radiation pressure”. In: *Phys. Rev. Lett.* 55 (1 July 1985), pp. 48–51.

[34] C. Cohen-Tannoudji. “Atomes ultrafroids - Piègeage non dissipatif et refroidissement évaporatif.” fr. Collège de France, 1996.

[35] C. Cohen-Tannoudji. “Atomes ultrafroids, approches statistiques et perspectives nouvelles - Etude d’un modèle simple combinant effet Sisyphe et refroidissement subrecul”. fr. Collège de France, 1994.

[36] G. Condon et al. “All-Optical Bose-Einstein Condensates in Microgravity”. In: *Phys. Rev. Lett.* 123 (24 Dec. 2019), p. 240402.

[37] G. Condon et al. “All-Optical Bose-Einstein Condensates in Microgravity”. en. In: *Physical Review Letters* 123.24 (Dec. 2019), p. 240402. ISSN: 0031-9007, 1079-7114.

[38] A. Couvert. “Production et étude de lasers à atomes guidés, et de leur interaction avec des défauts contrôlés”. fr. PhD thesis. Université Pierre et Marie Curie - Paris VI, 2009.

[39] J. Dalibard. “Collisional dynamics of ultra-cold atomic gases”. In: *Bose-Einstein Condensation in Atomic Gases* (1999), pp. 321–349.

[40] J. Dalibard and C. Cohen-Tannoudji. “Laser cooling below the Doppler limit by polarization gradients: simple theoretical models”. In: *J. Opt. Soc. Am. B* 6.11 (Nov. 1989), pp. 2023–2045.

[41] J. Dalibard. *Une brève histoire des atomes froids*. fr. 2014.

[42] C. Davisson and L. H. Germer. “Diffraction of Electrons by a Crystal of Nickel”. In: *Phys. Rev.* 30 (6 Dec. 1927), pp. 705–7 40.

[43] C. Deppner et al. “Collective-Mode Enhanced Matter-Wave Optics”. In: *Phys. Rev. Lett.* 127 (10 Aug. 2021), p. 100401.

[44] G. J. Dick. “Local Oscillator Induced Instabilities in Trapped Ion Frequency Standards”. en. In: (1987), p. 16.

[45] F. P. Dos Santos. “Differential phase extraction in an atom gradiometer”. In: *Physical Review A* 91.6 (June 2015), p. 063615.

[46] E. R. Elliott et al. “NASA’s Cold Atom Lab (CAL): system development and ground test status”. en. In: *npj Microgravity* 4.1 (Aug. 2018), pp. 1–7. ISSN: 2373-8065.

[47] R. P. Feynman. “Space-Time Approach to Non-Relativistic Quantum Mechanics”. In: *Reviews of Modern Physics* 20.2 (Apr. 1948), pp. 367–387.

[48] G. T. Foster et al. “Method of phase extraction between coupled atom interferometers using ellipse-specific fitting”. EN. In: *Optics Letters* 27.11 (June 2002), pp. 951–953. ISSN: 1539-4794.

[49] L. Fouche. “Gaz quantiques de potassium 39 à interactions contrôlables”. fr. PhD thesis. Institut d’Optique Graduate School, 2015.

[50] G. Galilei. *Discourses and Mathematical Demonstrations Relating to Two New Sciences*. 1638.

[51] A. Gauguet et al. “Off-resonant Raman transition impact in an atom interferometer”. en. In: *Physical Review A* 78.4 (Oct. 2008), p. 043615. ISSN: 1050-2947, 1094-1622.

[52] R. Geiger et al. “Detecting inertial effects with airborne matter-wave interferometry”. en. In: *Nature Communications* 2.1 (Sept. 2011), p. 474. ISSN: 2041-1723.

[53] R. Geiger. “Senseur inertiel à ondes de matière aéroporté”. fr. PhD thesis. Université Paris Sud - Paris XI, 2011.

[54] S. D. Gensemer et al. “Ultracold 87Rb ground-state hyperfine-changing collisions in the presence and absence of laser light”. In: *Physical Review A* 62.3 (), p. 030702.

[55] V. Gokhroo et al. “Sub-Doppler deep-cooled bosonic and fermionic isotopes of potassium in a compact 2D $^{+}$ –3D MOT set-up”. en. In: *Journal of Physics B: Atomic, Molecular and Optical Physics* 44.11 (June 2011), p. 115307. ISSN: 0953-4075, 1361-6455.

[56] P. A. Gominet. “Accéléromètre atomique double espèce 87Rb/39K aéroporté pour un test du principe d’équivalence”. fr. PhD thesis. Université de Bordeaux, 2015.

[57] R. Grimm, M. Weidemüller, and Y. B. Ovchinnikov. “Optical dipole traps for neutral atoms”. en. In: *arXiv:physics/9902072* (Feb. 1999).

[58] Q.-Q. Hu et al. “Mapping the absolute magnetic field and evaluating the quadratic Zeeman-effect-induced systematic error in an atom interferometer gravimeter”. In: *Phys. Rev. A* 96 (3 Sept. 2017), p. 033414.

[59] M. Kasevich and S. Chu. “Atomic interferometry using stimulated Raman transitions”. In: *Physical Review Letters* 67.2 (July 1991), pp. 181–184.

[60] A. Keshet and W. Ketterle. “A Distributed GUI-based Computer Control System for Atomic Physics Experiments”. en. In: *Review of Scientific Instruments* 84.1 (Jan. 2013), p. 015105. ISSN: 0034-6748, 1089-7623.

[61] F. L. Kien, P. Schneeweiss, and A. Rauschenbeutel. “Dynamical polarizability of atoms in arbitrary light fields: general theory and application to cesium”. en. In: *The European Physical Journal D* 67.5 (May 2013), p. 92. ISSN: 1434-6060, 1434-6079.

[62] C. Klempt et al. “40K 87Rb Feshbach Resonances: Modeling the interatomic potential”. In: *Physical Review A* 76.2 (Aug. 2007).

[63] M. Landini et al. “Sub-Doppler laser cooling of potassium atoms”. en. In: *Physical Review A* 84.4 (Oct. 2011), p. 043432. ISSN: 1050-2947, 1094-1622.

[64] M. Langlois et al. “Differential phase extraction in dual interferometers exploiting the correlation between classical and quantum sensors”. In: (2017).

[65] P. Lemonde. “PHARAO: Étude d’une horloge spatiale utilisant des atomes refroidis par laser; réalisation d’un prototype”. fr. PhD thesis. Université Pierre et Marie Curie - Paris VI, 1997.

[66] T. Lévèque et al. “CARIOQA: definition of a Quantum Pathfinder Mission”. In: *International Conference on Space Optics — ICSO 2022*. Ed. by K. Minoglou, N. Karafolas, and B. Cugny. Vol. 12777. International Society for Optics and Photonics. SPIE, 2023, p. 127773L.

[67] T. Lévèque et al. “Enhancing the Area of a Raman Atom Interferometer Using a Versatile Double-Diffraction Technique”. In: *Physical Review Letters* 103.8 (Aug. 2009), p. 080405.

[68] T. Lévèque et al. “Gravity Field Mapping Using Laser Coupled Quantum Accelerometers in Space”. In: *Journal of Geodesy* 95.1 (Jan. 2021), p. 15. ISSN: 0949-7714, 1432-1394.

[69] T. Lévèque. “Développement d’un gyromètre à atomes froids de haute sensibilité fondé sur une géométrie repliée”. fr. PhD thesis. Université Pierre et Marie Curie - Paris VI, Sept. 2010.

[70] L. Liu et al. “In-orbit operation of an atomic clock based on laser-cooled 87Rb atoms”. en. In: *Nature Communications* 9.1 (July 2018), p. 2760. ISSN: 2041-1723.

[71] O. J. Luiten, M. W. Reynolds, and J. T. M. Walraven. “Kinetic theory of the evaporative cooling of a trapped gas”. In: *Physical Review A* 53.1 (Jan. 1996), pp. 381–389.

[72] P. J. Martin et al. “Bragg scattering of atoms from a standing light wave”. In: *Physical Review Letters* 60.6 (Feb. 1988), pp. 515–518.

[73] D. Mattingly. “Modern tests of Lorentz invariance”. en. In: (Feb. 2005).

[74] V. Ménoret. “Accéléromètre à atomes froids aéroporté pour un test du Principe d’Equivalence”. fr. PhD thesis. Université Paris Sud - Paris XI, 2012.

[75] S. Merlet et al. “Comparison between two mobile absolute gravimeters: optical versus atomic interferometers”. In: *Metrologia* 47.4 (June 2010), p. L9.

[76] G. Modugno. “Bose-Einstein Condensation of Potassium Atoms by Sympathetic Cooling”. In: *Science* 294.5545 (2001), pp. 1320–1322. ISSN: 0036-8075.

[77] K. Moler et al. “Theoretical analysis of velocity-selective Raman transitions”. en. In: *Physical Review A* 45.1 (Jan. 1992), pp. 342–348. ISSN: 1050-2947, 1094-1622.

[78] H. Müntinga et al. “Interferometry with Bose-Einstein Condensates in Microgravity”. In: *Physical Review Letters* 110.9 (Feb. 2013), p. 093602. ISSN: 0031-9007, 1079-7114.

[79] D. S. Naik et al. “Loading and Cooling in an Optical Trap via Hyperfine Dark States”. en. In: *Physical Review Research* 2.1 (Feb. 2020), p. 013212. ISSN: 2643-1564.

[80] A. Peters, K. Y. Chung, and S. Chu. “High-precision gravity measurements using atom interferometry”. In: *Metrologia* 38.1 (Feb. 2001), p. 25.

[81] C. J. Pethick and H. Smith. *Bose–Einstein Condensation in Dilute Gases*. 2nd ed. Cambridge: Cambridge University Press, 2008. ISBN: 978-0-521-84651-6.

[82] P.-E. Pottie. “Etude du refroidissement laser en cellule : contribution au développement d’une horloge atomique miniature A 133 Cs”. These de doctorat. Paris 6, Jan. 2003.

[83] M. Rabault. “Condensation de Bose-Einstein tout-optique en microgravité pour l’interférométrie atomique”. fr. PhD thesis. Université de Bordeaux, 2019.

[84] N. F. Ramsey. “A Molecular Beam Resonance Method with Separated Oscillating Fields”. In: *Physical Review* 78.6 (June 1950), pp. 695–699.

[85] M. Raudonis et al. “Microgravity facilities for cold atom experiments”. In: *Quantum Science and Technology* 8.4 (Aug. 2023), p. 044001.

[86] G. Roati et al. “39K Bose-Einstein Condensate with Tunable Interactions”. In: *Phys. Rev. Lett.* 99 (1 July 2007), p. 010403.

[87] E. Rocco et al. “Fluorescence detection at the atom shot noise limit for atom interferometry”. en. In: *New Journal of Physics* 16.9 (Sept. 2014), p. 093046. ISSN: 1367-2630.

[88] A. Roura, W. Zeller, and W. P. Schleich. “Overcoming loss of contrast in atom interferometry due to gravity gradients”. en. In: *New Journal of Physics* 16.12 (Dec. 2014), p. 123012. ISSN: 1367-2630.

[89] G. Salomon et al. “All-optical cooling of K 39 to Bose-Einstein condensation”. en. In: *Physical Review A* 90.3 (Sept. 2014), p. 033405. ISSN: 1050-2947, 1094-1622.

[90] G. Salomon et al. “Gray molasses cooling of 39K to a high phase-space density”. en. In: *EPL (Europhysics Letters)* 104.6 (Dec. 2013), p. 63002. ISSN: 0295-5075, 1286-4854.

[91] C. Sanner et al. “Optical clock comparison for Lorentz symmetry testing”. en. In: *Nature* 567.7747 (Mar. 2019). ISSN: 1476-4687.

[92] T. A. Savard, K. M. O’Hara, and J. E. Thomas. “Laser-noise-induced heating in far-off resonance optical traps”. In: *Phys. Rev. A* 56 (2 Aug. 1997), R1095–R1098.

[93] S. Schlamminger et al. “Test of the Equivalence Principle Using a Rotating Torsion Balance”. In: *Physical Review Letters* 100.4 (Jan. 2008), p. 041101. ISSN: 0031-9007, 1079-7114.

[94] D. Schlippert et al. “Quantum Test of the Universality of Free Fall”. In: *Physical Review Letters* 112.20 (May 2014), p. 203002. ISSN: 0031-9007, 1079-7114.

[95] S.-Q. Shang, Z.-T. Lu, and S. J. Freedman. “Comparison of the cold-collision losses for laser-trapped sodium in different ground-state hyperfine sublevels”. In: *Physical Review A* 50.6 (Dec. 1994), R4449–R4452.

[96] D. A. Steck. *Rubidium 87 D Line Data*. Oct. 2003.

[97] J. K. Stockton, X. Wu, and M. A. Kasevich. “Bayesian estimation of differential interferometer phase”. In: *Physical Review A* 76.3 (Sept. 2007), p. 033613.

[98] P. Storey and C. Cohen-Tannoudji. “The Feynman path integral approach to atomic interferometry. A tutorial”. en. In: *Journal de Physique II* 4.11 (Nov. 1994), pp. 1999–2027. ISSN: 1155-4312, 1286-4870.

[99] B. D. Tapley et al. “The gravity recovery and climate experiment: Mission overview and early results”. In: *Geophysical Research Letters* 31.9 (2004).

[100] M. G. Tarallo et al. “Test of Einstein Equivalence Principle for 0-Spin and Half-Integer-Spin Atoms: Search for Spin-Gravity Coupling Effects”. In: *Physical Review Letters* 113.2 (July 2014), p. 023005.

[101] T. G. Tiecke. *Potassium Properties.pdf*. 2019.

[102] P. Touboul et al. “MICROSCOPE”. In: *Physical Review Letters* 129.12 (2022). ISSN: 0031-9007.

[103] C. Vogt et al. “Evaporative cooling from an optical dipole trap in microgravity”. In: *Phys. Rev. A* 101 (1 Jan. 2020), p. 013634.

[104] L. Zhou et al. “Test of Equivalence Principle at 10 -8 Level by a Dual-species Double-diffraction Raman Atom Interferometer”. en. In: *Physical Review Letters* 115.1 (July 2015), p. 013004. ISSN: 0031-9007, 1079-7114.